Finite nuclei under extreme conditions of mass, isospin and temperature : a relativistic Hartree-Fock-Bogoliubov description

Jia Jie Li

Université Paris-Sud

Ecole Doctorale 517:
Particules, Noyaux et Cosmos

Institut de Physique Nucléaire d'Orsay

Discipline : Physique Nucléaire Théorique

Thèse de doctorat

Soutenue le 21 Septembre 2015 par

Jia Jie Li

Finite nuclei under extreme conditions of mass, isospin and temperature

- a relativistic Hartree-Fock-Bogoliubov description -

Directeur de thèse :	Prof. Jérôme Margueron	Chargé de recherche CNRS, IPN Lyon
Composition du jury :		
Président du jury :	Prof. Elias Khan	Professeur, Université Paris-Sud, Orsay
Rapporteurs :	Prof. Armen Sedrakian	Professeur, J. W. Goethe University, Germany
	Prof. Xavier Viñas	Professeur, University of Barcelona, Spain
Examinateurs :	Prof. Wen Hui Long	Professeur, Lanzhou University, China
	Prof. Nguyen Van Giai	Directeur de recherche émérite CNRS, IPN Orsay

Abstract

The covariant density functional (CDF) theory with a few number of parameters has been successfully employed to describe ground-state and excited-states of nuclei over the entire nuclear landscape for $A > 12$. It describes finite nuclear systems with a universal hadronic Lagrangian, which is solved considering the relativistic Hartree-Fock-Bogoliubov (RHFB) approach. This model is also employed for the study of compact stars, since it can be extended to high densities where special relativity cannot be ignore. This model can also be extended to include the contribution of hyperons and as well as other exotic particles. In this work, the description and some predictions based on RHFB approach for nuclei under extreme conditions of mass, isospin and temperature are presented.

In the first part, we explore the occurrence of spherical shell closures for superheavy nuclei, where shell closures are characterized in terms of two-nucleon gaps. The results depend slightly on the effective Lagrangians used, but the magic numbers beyond ^{208}Pb are generally predicted to be $Z = 120$ and 138 for protons, and $N = 172$, 184, 228, and 258 for neutrons. Shell effects are sensitive to various terms of the mean-field, such as the spin-orbit coupling, the scalar and the effective masses, as well as the Lorentz-tensor interaction. These terms have different weights in the effective Lagrangians employed, explaining the (relatively small) variations in the predictions. Employing the most advanced RHFB model, we found that the nuclide ^{304}120 is favored as being the next spherical doubly-magic nucleus beyond ^{208}Pb.

In the second part, we investigate the formation of new shell gaps in intermediate mass neutron-rich nuclei, and analyze the role of the Lorentz pseudo-vector and tensor interactions. Based on the Foldy-Wouthuysen transformation, we discuss in detail the role played by the different terms of the Lorentz pseudo-vector and tensor interactions in the appearance of the $N = 16$, 32 and 34 shell gaps. The nuclei ^{24}O, ^{48}Si and ^{52,54}Ca are predicted with a large shell gap and zero (^{24}O, ^{52}Ca) or almost zero (^{48}Si, ^{54}Ca) pairing gap, making them candidates for new magic numbers in neutron rich nuclei. We find that the Lorentz pseudo-vector and tensor interactions induce very specific evolutions of single-particle energies, which could clearly sign their presence and reveal the need for relativistic approaches with exchange interactions.

In the last part, we study the phase transitions and thermal excitations of both stable and weakly-bound nuclei. The predictions of various relativistic Lagrangians and different pairing interactions are discussed. The critical temperature of the pairing transition is found to depend linearly on the zero-temperature pairing gap, and this dependence is similar for a zero-range or a finite-range pairing interaction. The present calculations show interesting features of the pairing correlations at finite temperature, such as the pairing persistence and pairing re-entrance phenomena. Also, we analyze the thermal response of some nuclei.

In conclusion, the work presented in this thesis shown interesting and new results for three of the most important questions in nuclear physics: the quest for a new island of stability in the superheavy region, the appearance of new magic numbers in exotic nuclei, and the response of finite-systems to thermal excitations.

Résumé

La théorie covariance de la fonctionnelle de la densité (CDF), basée sur un petit nombre de paramètres ajustables, a été utilisée avec succès pour décrire état fondamental et les états excités des noyaux de la carte nucléaire, pour $A > 12$. Cette approche permet de décrire les systèmes nucléaires finis avec un Lagrangien hadronique universel résolu dans le cadre de l'approche relativiste Hartree-Fock-Bologuibov (RHFB). Ce modèle est également utilisé pour l'étude des étoiles compactes, car il peut être étendu à des densités élevées où la relativité restreinte ne peut pas être ignorer. Ce modèle peut également être étendu pour inclure la contribution des hypérons et ainsi que d'autres particules exotiques. Dans ce travail, la description et des prédictions basées sur l'approche RHFB pour les noyaux dans des conditions extrêmes de la masse, d'isospin et de température sont présentés.

Dans la première partie de cette thèse, nous explorons l'apparition de nouvelles fermeture de couches sphériques pour des noyaux super-lourds, où les fermetures de couches sont caractérisées en termes de gap à deux nucléons. Les résultats dépendent légèrement des Lagrangians effectifs utilisés, mais les nombres magiques au-delà de ^{208}Pb sont prédit pour un nombre de protons $Z = 120$ et 138, et pour un nombre de neutrons $N = 172$, 184, 228, et 258. Les effets de couche sont sensibles à différents termes de champ de moyen, tels que le couplage spin-orbite, la masse scalaire et la masses effective, ainsi que l'interaction de tensorielle de Lorentz. Ces termes ont des poids différents dans les Lagrangians effectifs employées, expliquant les variations, somme toute petites, dans leurs prédictions. Employant le modèle RHFB le plus avancé, nous avons trouvé que le nucléide ^{304}120 est favorisée comme étant le prochain noyau sphérique doublement magique au-delà de ^{208}Pb.

Dans la deuxième partie de cette thèse, nous étudions l'apparition de nouveaux nombres magiques pour les noyaux de masse intermédiaire riches en neutrons, et nous analysons le rôle des interactions pseudo-vecteur et de tensorielle de Lorentz. Basé sur la transformation de Foldy-Wouthuysen, nous discutons en détail le rôle joué par les différents termes des interactions pseudo-vecteur et de tensorielle de Lorentz. Dans l'apparition des nouveaux nombres magiques $N = 16$, 32 et 34. Les noyaux ^{24}O, ^{48}Si et ^{52,54}Ca sont prédits avec un grand gap au niveau de Fermi et un gap d'appariement zéro (^{24}O, ^{54}Ca) ou quasi-nul (^{48}Si, ^{54}Ca), les rendant candidats pour de nouveaux nombres magiques des noyaux riches en neutrons. Nous constatons que les interactions de Lorentz pseudo-vecteur et tensorielle induisent des évolutions très spécifiques des énergies à une particule, ce qui pourrait signer la présence et la nécessité d'approches relativistes avec des interactions d'échanges de mesons.

Dans la dernière partie de cette thèse, nous étudions les transitions de phase et excitations thermiques des deux noyaux stables et faiblement liés. Les prédictions de divers Lagrangiens relativistes et des différentes interactions d'appariement sont discutées. La température critique de la transition d'appariement dépend linéairement du gap d'appariement à température nulle, et cette dépendance est similaire pour une interaction de portée nulle ou bien finie. Les calculs présentés montrent des caractéristiques intéressantes des corrélations d'appariement à température finie, comme la persistance d'appariement et les phénomènes de re-entrance superfluide. En outre, nous analysons la réponse thermique de certains noyaux.

En conclusion, le travail présenté dans cette thèse montre des résultats très intéressants et nouveaux pour trois des questions les plus importantes en physique nucléaire: la quête d'un nouvel îlot de stabilité dans la région des super-lourds, l'apparition de nouveaux nombres magiques dans les noyaux exotiques, et la réponse d'un système finis aux excitations thermiques.

Contents

List of Figures

List of Tables

Chapter 1

Introduction

Before I came here I was confused about this subject. Having listened to your lecture I am still confused. But on a higher level.

Enrico Fermi, 1901-1954

The atomic nuclei are self-bound many-body systems which have to be treated with the many-body quantum theory. They exhibit a rich variety of phenomena due to density, spin, isospin and eventually strangeness degrees of freedom of the strong interaction. In addition, the correlations induced by various symmetry breaking such as deformation and pairing for instance, make atomic nuclei a very interesting and complex system. The exploration of nuclei far from stability represents a new frontier in our understanding of nuclear structure and nuclear astrophysics. In this thesis, we will explore the system located at the limit of stability for very large masses (superheavy nuclei), very large isospin asymmetries (exotic nuclei) and for thermally excited nuclei (hot nuclei).

Theoretical approaches

Nuclei are described by nuclear structure theories at different levels of refinement, from the phenomenological methods, such as for instance the microscopic-macroscopic (Mic-Mac) model [1–3], through shell-model (SM) calculations [4–6], self-consistent mean-field (SCMF) approaches [7–9] up to several ab-initio techniques [10–12] employing a given nucleon-nucleon interaction. In the following, we discuss these methods and justify our choice to employ the self-consistent mean-field approach.

The Mic-Mac model, in which the nuclear energy is calculated with an empirical mass formula with quantum effects added as corrections, has for a long time been successfully applied to the problem of nuclear binding energy or fission [13–15]. In this method, one calculates the single particle energies in a given potential which is phenomenologically adjusted to nuclear data. This method disregards, however, the self-consistent effects: particles create the potential in which they are bounded, and the potential influences back their motion. This effect is expected to be more and more important as one is considering systems far from stability.

The truncated SM employing configuration interaction (CI) has been extended to medium-heavy nuclei. This model constructs a model space within which valence particle interact through an effective interaction (two-body matrix elements). Even though the latter is often taken from G-matrix calculations using realistic microscopic forces, certain combinations of its matrix elements are partly refitted on experimental data in a given configuration space for each mass region. Proceeding in this way, spectroscopic properties within the favorable configuration space are described with an excellent accuracy [5, 6]. Since the size of the model space rapidly grows up as nuclei become heavier, the application of such method is still limited in the medium-mass region.

The most fundamental techniques keep as much as possible a connection with the bare two- and three-body interactions which reproduce nucleon-nucleon scattering phase shifts in free space. Until now, considerable efforts have been devoted to ab-initio calculations. However, due to the numerical complexity increasing with the size of the system, approximations lead to models that gradually lose the connection with the bare force. For instance, in the case of very light nuclei, Green's function Monte-Carlo (GFMC) [16, 17] can describe the fully correlated few-body problem starting from realistic two- and three-body force, using the exact evolution operator, but this is restricted to local potentials. Coupled cluster (CC) theory [18,19], which constructs the correlated state from a product state using a cluster expansion of the many-body operator, truncated to a few-body operator, renders possible calculations up to $A \sim 50$ in the vicinity of (sub)shell closures [20, 21]. The same is true for the self-consistent Green's function method [12,22] that is currently being extended to open-shell nuclei [23,24]. Notice that all these methods, while giving essentially exact results, still use a truncation, while preserving an explicit connection with the vacuum interaction. Thus, fully microscopic methods are presently not used for large-scale nuclear structure calculations neither to describe the crust of neutron stars.

The density functional theory (DFT), often referred to as "self-consistent mean-field method" (SCMF) [7], is the only microscopical method at present which can be applied throughout the entire nuclear landscape, except very light nuclei, and for describing dense matter properties (uniform and non-uniform matter in neutron stars and supernova). It is worth emphasizing that the DFT for nuclear structure represents an approximate implementation of the general concept proposed by Kohn and Sham in molecular and condensed state physics [25, 26]. The key ingredient of DFT is the energy density functional which often derives from an effective in-medium interaction. However, the exact form of the functional is difficult to determine. A universal energy density functional for nuclear many-body system is thus adjusted phenomenologically to experimental data for finite nuclei and the in-medium effects (many-body correlations) are re-summed through the use of an effective potential. Over the past decades, non-relativistic and relativistic (covariant) DFT's have been developed and successfully applied to the description of a large variety of nuclear phenomena, from light to heaviest elements, from the valley of β-stability to the drip lines, and from ground-states to excited-states, with great success. There are three widely used kind of functionals: the Skyrme energy functional [9, 27, 28], the finite range Gogny/BCP/M3Y energy functional [29–34], and the relativistic energy functional [35–37]. The present manuscript is focused on the latter class of models and discuss the interest in implementing a self-consistent relativistic Hartree-Fock model [38–40].

Covariant density functional theory

The covariant density functional (CDF) is usually formulated in terms of a hadronic Lagrangian. At the low energy regime, it is assumed that the nucleons interact through the exchange of mesons with spin J and isospin T. Such an assumption is consistent with one-boson-exchange potentials fitted to nucleon-nucleon scattering at low energies. However, the heavy-meson exchange is just a convenient representation of the effective nuclear interaction. Moreover, a quantitative treatment of nuclear matter and finite nuclei needs a medium dependence of effective interactions, which can be introduced by including nonlinear meson self-interaction terms in the Lagrangian or by assuming explicit density dependence of the meson-nucleon couplings.

The CDF are of particular interest in nuclear physics. Here we illustrate some of the advantages: (1) They exploit basic properties of QCD at low energies, in particular, symmetries and the separation of scales; (2) They provide a consistent treatment of the spin degree of freedom and its isospin-dependence, and include the complicated interplay between the large Lorentz scalar and vector self-energies induced on the QCD level by the in-medium changes of the scalar and vector quark condensates; (3) In addition, these functionals include nuclear magnetism, i.e., a consistent description of currents and time-odd mean fields, induced by the spatial parts of the vector self-energies; (4) Furthermore, the tensor force, which has gained renewed interest recently, can be included if the Fock

diagram is considered.

Superheavy Nuclei

One of the most important motivation behind the superheavy element research is to explore the limits of nuclear stability in mass and charge and the limitation on the number of chemical elements. The limit on stability in superheavy nuclei (SHN) is essential for understanding not only the nuclear properties, but also the structure of the stars and the evolution of the universe.

There is a considerable activity in the study of SHN. These studies, however, are characterized by a number of critical challenges. From the experimental side, these challenges are related to the very low production cross sections (a few atoms per week), and to the detection and analysis of these few events with half lives of the order of milliseconds. The most heavy charge element ever reported until now is $Z = 118$. The decay chains observed so far for SHNs suggest the existence of a region of enhanced stability, induced by shell effects. These experimental results cannot however confirm or reject the theoretical predictions for the next proton/neutron magic number. This domain is very much pushed forward, e.g., at the GSI, the DUBNA group and others.

On the theoretical side, the challenges one has to face are the predictions of the position of the SHN island of stability. Shell closure and the interplay of the spin-orbit term play an important role in the stability of SHN. As mentioned before, the predictions are presently performed by Mic-Mac and SCMF methods. These models are employed, e.g., to confirm experimental data and to make predictions for valuable informations of interest, e.g., binding energies, decay modes, regions of higher stability. The Mic-Mac approach, despite its great success in predicting nuclear binding energies for exotic nuclei, can hardly be extrapolated towards very new regions where experimental data are extremely scarce. The stability of nuclei is mostly driven by shell effects and therefore, SCMF methods are probably the best conceptual tool to explore the superheavy region.

Exotic Nuclei

With the developments on the radioactive ion beam (RIB) facilities, the nuclei far from stability (exotic nuclei) have become one of the forefront of nuclear science, and have intensively challenged our understanding on the nature of nuclei.

Experiments with RIB have disclosed a wealth of structure phenomena in exotic nuclei. On one hand, near the neutron drip-line, the outermost neutrons start to diffuse out, leading to the coupling to continuum, the formation of the neutron skins and halos. It has also been shown that the single-particle (s.p.) spectra in exotic nuclei result with the shell quenching effects at extreme values of the isospin. On the other hand, a topic of particular interest is the evolution of the shell structure in exotic nuclei. That is, the traditional magic numbers may change dramatically depending on the N/Z ratio when we move away from the valley of stability. For instance, it is rather commonly accepted that the $N = 8$ and 20 harmonic oscillator (HO) shell closures are suppressed in neutron-rich nuclei, and the new magic numbers like $N = 14$, 16, and 32 emerge. This change has been explained by the strong isospin-dependent interaction, originating from the one boson exchange potential. Therefore, the nuclear shell structure and magic numbers remain to be systematically investigated and may be revised in the case of exotic nuclei. These results provided the evidence that magic numbers are not immutable. It also triggers a large number of experimental and theoretical work devoted to study the nature of the magicity far from the valley of stability.

Such study is important not only due to the expected variation in properties of nuclei but also for the understanding of nucleon-nucleon interaction in neutron rich systems present in nuclear astrophysics. The availability of experimental data in exotic nuclei thus provide a new criterion to

constrain the properties of different components of the nucleon-nucleon interaction, especially, the isovector channel.

Hot Nuclei

The thermodynamical properties of excited nuclei have drawn over the last decades a renewed attention due to the advanced accurate measurements of level densities at low excitation energies. Pairing correlations play an essential role in many fermion systems and have thus a strong influence on nuclear structure at low excitation energies. Thus, special attention was paid to the influence of pairing on the low-temperature behavior of the specific heat in the isotopes extracted from the level density. By increasing the temperature, nucleons are excited from levels below the Fermi surface to levels above, resulting in level blocking, and hence pairing correlations disappear. It is the so called "pairing phase transitions". Experimental evidence has been found in the *s*-shaped curve of heat capacity as a function of excitation energy.

Pairing correlations in finite systems such as nuclei or Wigner-Seitz (WS) cells, and in infinite ones such as in neutron star matter, may exhibit different behaviors reflected in the specific heat and the level density. Very neutron-rich nuclei offer the opportunity to study pairing phenomena in systems with strong density variations. Because their properties determine the astrophysical conditions for the formation of stable isotopes, the study of hot nuclei close to the neutron drip-line has important applications in nuclear astrophysics

Moreover, the phase transition is a complex and rich phenomenon, where pairing re-entrance in asymmetric matter, in odd-nuclei, rotating nuclei, and even in doubly magic nuclei close to the drip line may occur. The interplay between temperature and shell effects in superfluid systems, giving rise to re-entrance or its opposite phenomenon —suppression— still remains to be studied.

Outline

This work concentrates on the self-consistent description of nuclei under extreme conditions of mass, isospin and temperature, in terms of the CDF approach. The present document is organized as follows:

- In Chapter 2 we give a short overview on the CDF model, and its generalization to the finite temperature (FT) case. The boundary condition for the description of neutron star inner crust is discussed.
- In Chapter 3 we investigate the superheavy nuclides covering $Z = 110-140$ aiming at the possible magic shells in this region. We compare the predictions of relativistic Hartree-Fock-Bogoliubov (RHFB) with those of relativistic Hartree-Bogoliubov (RHB) results where Fock terms are not explicitly considered, and the underlying mechanisms are discussed.
- In Chapter 4 the formation of new shell gaps in intermediate mass neutron-rich nuclei is investigated within the RHFB theory, and the role of the Lorentz pseudo-vector and tensor interactions is analyzed.
- In Chapter 5 we perform systematic FT-RH(F)B calculations for several semi-magic isotopic/isotonic chains, comparing the predictions of a large number of Lagrangians. The interesting features of the pairing correlations at finite temperature and in finite systems such as pairing re-entrance and pairing persistence are discussed.
- In the end, the conclusions and perspectives are given in Chapter 6.

Chapter 2

Relativistic Hartree-Fock approach and its extensions

It doesn't matter how beautiful your theory is, it doesn't matter how smart you are. If it doesn't agree with experiment, it is wrong.

Richard P. Feynman, 1918-1988

2.1 Relativistic Hartree-Fock approach

2.1.1 Effective Lagrangian and Hamiltonian

As the theoretical starting point, the Lagrangian density $\mathcal{L}$ of relativistic Hartree-Fock (RHF) approach is constructed on the one-boson exchange diagram of the NN interaction, which contains the degrees of freedom associated with the nucleon ψ, minimal mesons ϕ and photon A. The $\mathcal{L}$, therefore, consists of three parts:

$$\mathcal{L} = \mathcal{L}_N + \mathcal{L}_M + \mathcal{L}_{\rm int}. \tag{2.1}$$

The first term $\mathcal{L}_N$ describes free baryons as relativistic point particles with rest mass M,

$$\mathcal{L}_N = \bar{\psi}(i\gamma_\mu\partial^\mu - M)\psi, \tag{2.2}$$

where $\bar{\psi} = \psi^\dagger\gamma^0$. The $\mathcal{L}_M$ term represents free mesons and photons. The meson degrees of freedom are selected according to their relevant quantum properties (J^π, T) with spin J, intrinsic parity π and isospin T, which are listed in Table 2.1. The mesons that we consider are (including the photon field A):

$$\mathcal{L}_\sigma = +\frac{1}{2}\partial^\mu\sigma\partial_\mu\sigma - \frac{1}{2}m_\sigma^2\sigma^2, \tag{2.3a}$$

$$\mathcal{L}_\delta = +\frac{1}{2}\partial^\mu\boldsymbol{\delta}\partial_\mu\boldsymbol{\delta} - \frac{1}{2}m_\delta^2\boldsymbol{\delta}^2, \tag{2.3b}$$

$$\mathcal{L}_\pi = +\frac{1}{2}\partial^\mu\boldsymbol{\pi}\cdot\partial_\mu\boldsymbol{\pi} - \frac{1}{2}m_\pi^2\boldsymbol{\pi}^2, \tag{2.3c}$$

$$\mathcal{L}_\omega = -\frac{1}{4}\Omega^{\mu\nu}\Omega_{\mu\nu} + \frac{1}{2}m_\omega^2\omega^\mu\omega_\mu, \tag{2.3d}$$

$$\mathcal{L}_\rho = -\frac{1}{4}\boldsymbol{R}^{\mu\nu}\cdot\boldsymbol{R}_{\mu\nu} + \frac{1}{2}m_\rho^2\boldsymbol{\rho}^\mu\boldsymbol{\rho}_\mu, \tag{2.3e}$$

$$\mathcal{L}_A = -\frac{1}{4}F^{\mu\nu}F_{\mu\nu}, \tag{2.3f}$$

Table 2.1: Quantum numbers of mesons.

Meson	π	σ	δ	ω	ρ
J^π	0^-	1^+	0^+	1^-	0^-
T	1	0	1	0	1

with tensor quantities for the vector fields,

$$\Omega^{\mu\nu} \equiv \partial^\mu \omega^\nu - \partial^\nu \omega^\mu, \tag{2.4a}$$
$$\boldsymbol{R}^{\mu\nu} \equiv \partial^\mu \boldsymbol{\rho}^\nu - \partial^\nu \boldsymbol{\rho}^\mu, \tag{2.4b}$$
$$F^{\mu\nu} \equiv \partial^\mu A^\nu - \partial^\nu A^\mu. \tag{2.4c}$$

Here, $m_{\sigma,\delta,\omega,\rho,\pi}$ are the rest masses of the mesons, the bold face symbols denote vectors in the isospin space.

The meson- (photon-) nucleon interaction is described by the third term of 2.1, which have the simplest possible form consistent with the Lorentz and isospin structure,

$$\begin{aligned}\mathcal{L}_{\text{int}} = \bar{\psi}\Big(&- g_\sigma \sigma - g_\delta \boldsymbol{\delta}\cdot\boldsymbol{\tau} - g_\omega \gamma^\mu \omega_\mu - g_\rho \gamma^\mu \boldsymbol{\rho}_\mu \cdot \boldsymbol{\tau} - \frac{f_\pi}{m_\pi}\gamma_5 \gamma^\mu \partial_\mu \boldsymbol{\pi}\cdot\boldsymbol{\tau} \\ &- \frac{f_\omega}{2M}\sigma^{\mu\nu}\partial_\mu \omega^\nu - \frac{f_\rho}{2M}\sigma^{\mu\nu}\partial_\mu \boldsymbol{\rho}^\nu \cdot \boldsymbol{\tau} - e\gamma^\mu \frac{1}{2}(1+\tau_3)A^\mu\Big)\psi,\end{aligned} \tag{2.5}$$

where $\sigma^{\mu\nu} = \frac{i}{2}[\gamma^\mu, \gamma^\nu]$. The isospin Pauli matrices are given by $\boldsymbol{\tau}$, τ_3 being its third component. The mesons couple to the nucleons with the strengths of the coupling constants $g_{\sigma,\delta,\omega,\rho}$ and $f_{\omega,\rho,\pi}$,which are to be determined from experimental data and by fitting nuclear matter and finite nuclei ground-state properties.

Starting from the energy-momentum tensor of the system:

$$\mathcal{T}^{\mu\nu} \equiv \frac{\partial \mathcal{L}}{\partial(\partial_\mu \phi_i)}\partial^\nu \phi_i - g^{\mu\nu}\mathcal{L}, \tag{2.6}$$

which obeys the continuity law $\partial_\mu \mathcal{T}^{\mu\nu} = 0$, one can formally obtain the Hamiltonian density through the general Legendre transformation,

$$\mathcal{H} = \mathcal{T}^{00} = \frac{\partial \mathcal{L}}{\partial \dot{\phi}_i}\dot{\phi}_i - \mathcal{L}. \tag{2.7}$$

Here ϕ_i represents the field operators, $\dot{\phi}_i$ being their conjugate momenta. The Hamiltonian density is obtained as

$$\mathcal{H} = \mathcal{H}_N + \mathcal{H}_M + \mathcal{H}_{\text{int}}, \tag{2.8}$$

with a pure nucleonic part

$$\mathcal{H}_N = \bar{\psi}[-i\boldsymbol{\gamma}\cdot\nabla]\psi, \tag{2.9}$$

meson (photon) field contributions

$$\mathcal{H}_\sigma = +\frac{1}{2}\sigma^2 + \frac{1}{2}\nabla\sigma\cdot\nabla\sigma + \frac{1}{2}m_\sigma^2\sigma^2, \tag{2.10a}$$
$$\mathcal{H}_\delta = +\frac{1}{2}\boldsymbol{\delta}^2 + \frac{1}{2}\nabla\boldsymbol{\delta}\cdot\nabla\boldsymbol{\delta} + \frac{1}{2}m_\delta^2\boldsymbol{\delta}^2, \tag{2.10b}$$
$$\mathcal{H}_\pi = +\frac{1}{2}\boldsymbol{\pi}^2 + \frac{1}{2}\nabla\boldsymbol{\pi}\cdot\nabla\boldsymbol{\pi} + \frac{1}{2}m_\pi^2\boldsymbol{\pi}^2, \tag{2.10c}$$
$$\mathcal{H}_\omega = -\frac{1}{2}\Omega^{0\nu}\omega_\nu + \frac{1}{2}\Omega^{i\nu}\partial_i\omega_\nu - \frac{1}{2}m_\omega^2\omega^\mu\omega_\mu, \tag{2.10d}$$

$$\mathcal{H}_\rho = -\frac{1}{2}\boldsymbol{R}^{0\nu}\cdot\boldsymbol{\rho}_\nu + \frac{1}{2}\boldsymbol{R}^{i\nu}\cdot\partial_i\boldsymbol{\rho}_\nu - \frac{1}{2}m_\rho^2\boldsymbol{\rho}^\mu\boldsymbol{\rho}_\mu, \tag{2.10e}$$

$$\mathcal{H}_A = -\frac{1}{2}F^{0\nu}A_\nu + \frac{1}{2}F^{i\nu}\partial_i A_\nu, \tag{2.10f}$$

and the interaction between nucleon and mesons (photon)

$$\begin{aligned}\mathcal{H}_{\rm int} = \bar\psi\Big(&- g_\sigma\sigma - g_\delta\boldsymbol{\delta}\cdot\boldsymbol{\tau} - g_\omega\gamma^\mu\omega_\mu - g_\rho\gamma^\mu\boldsymbol{\rho}_\mu\cdot\boldsymbol{\tau} - \frac{f_\pi}{m_\pi}\gamma_5\gamma^\mu\partial_\mu\boldsymbol{\pi}\cdot\boldsymbol{\tau} \\ &- \frac{f_\omega}{2M}\sigma^{\mu\nu}\partial_\mu\omega^\nu - \frac{f_\rho}{2M}\sigma^{\mu\nu}\partial_\mu\boldsymbol{\rho}^\nu\cdot\boldsymbol{\tau} - e\gamma^\mu\frac{1}{2}(1+\tau_3)A^\mu\Big)\psi.\end{aligned} \tag{2.11}$$

One may notice that $\mathcal{H}_{\rm int}$ has a form identical to $\mathcal{L}_{\rm int}$.

The stationarity condition of the action-integral $\int\mathcal{L}(x)dx$ with respect to the variations of the physical fields leads to the Euler-Lagrange equations, from which one can deduce the equations of motion for the meson, photon and nucleon fields. The meson and photon fields obey inhomogeneous Klein-Gordon equations and Proca equations with source terms, respectively,

$$(\Box + m_\sigma^2)\sigma = -g_\sigma\rho_s, \tag{2.12a}$$

$$(\Box + m_\delta^2)\boldsymbol{\delta} = -g_\delta\boldsymbol{\rho}_s, \tag{2.12b}$$

$$\partial_\mu\Omega^{\mu\nu} + m_\omega^2\omega^\nu = g_\omega j^\nu - \frac{f_\omega}{2M}\partial_\mu j^{\mu\nu}, \tag{2.12c}$$

$$\partial_\mu\boldsymbol{R}^{\mu\nu} + m_\rho^2\boldsymbol{\rho}^\nu = g_\rho\boldsymbol{j}^\nu - \frac{f_\rho}{2M}\partial_\mu\boldsymbol{j}^{\mu\nu}, \tag{2.12d}$$

$$(\Box + m_\pi^2)\boldsymbol{\pi} = \frac{f_\pi}{m_\pi}\partial_\mu\boldsymbol{j}^{5\nu}, \tag{2.12e}$$

$$\partial_\mu F^{\mu\nu} = ej_c^\nu. \tag{2.12f}$$

where $\Box = \partial_\mu\partial^\mu$ and the various densities and currents are defined as follows:

$$\rho_s = \bar\psi\psi, \tag{2.13a}$$

$$j^\nu = \bar\psi\gamma^\nu\psi, \tag{2.13b}$$

$$j^{\mu\nu} = \bar\psi\sigma^{\mu\nu}\psi, \tag{2.13c}$$

$$j^{5\nu} = \bar\psi\gamma^5\gamma^\nu\psi, \tag{2.13d}$$

$$j_c^\nu = \frac{1}{2}\bar\psi(1+\tau_3)\gamma^\nu\psi, \tag{2.13e}$$

Because of the current conservation conditions, i.e., $\partial_\nu j^\nu = 0$ and $\partial_\mu\partial_\nu j^{\mu\nu} = 0$, the Proca equations thus reduce to Klein-Gordon equations. Solving these equations, one then gets the solutions formally expressed as (taking σ, ω meson as representatives)

$$\sigma(x) = -\int d^4y D_\sigma(x,y)\bar\psi(y)\psi(y), \tag{2.14a}$$

$$\omega^\mu(x) = +\int d^4y D_\omega(x,y)\bar\psi(y)\gamma_\nu\psi(y) + \frac{f_\omega}{2M}\int d^4y D_\omega(x,y)\partial^\mu\bar\psi(y)\sigma_{\mu\nu}\psi(y), \tag{2.14b}$$

where D_σ and D_ω are the σ and ω meson propagator, which satisfy the equations

$$(\Box + m_\sigma^2)D_\sigma(x,y) = \delta(x-y), \tag{2.15a}$$

$$(\Box + m_\omega^2)D_\omega(x,y) = \delta(x-y). \tag{2.15b}$$

For the isovector mesons one can deduce expressions similar to Eqs. (2.14) with the corresponding propagators D_δ, D_ρ and D_π.

A similar procedure for the baryon field yields the Dirac equation with source term,

$$(-i\gamma^\mu\partial_\mu + M + \Sigma)\psi(x) = 0. \tag{2.16}$$

The Σ is the so called self-energy. This equation cannot, however, be solved exactly and one has to treat it in some appropriate scheme, like the Hartree or Hartree-Fock approximations.

2.1.2 Hartree-Fock approximation and energy functional

We now construct the Hamilton operator in nucleon space, i.e., we eliminate the meson fields in the Dirac equation. With the aid of the explicit expression of the meson field operators, one can obtain the Hamiltonian in terms of nucleon fields ψ only,

$$H = \int d\boldsymbol{r}\left[\bar{\psi}(\boldsymbol{r})(-i\boldsymbol{\gamma}\cdot\boldsymbol{\nabla}+M)\psi(\boldsymbol{r})\right] + \frac{1}{2}\int d\boldsymbol{r}d\boldsymbol{r}'\sum_{\phi}\bar{\psi}(\boldsymbol{r})\bar{\psi}(\boldsymbol{r}')\Gamma_{\phi}(\boldsymbol{r},\boldsymbol{r}')D_{\phi}(\boldsymbol{r},\boldsymbol{r}')\psi(\boldsymbol{r})\psi(\boldsymbol{r}'), \quad (2.17)$$

where Γ_ϕ represents the NN interaction vertices,

$$\Gamma_{\sigma}^{S} \equiv -g_{\sigma}(\boldsymbol{r})g_{\sigma}(\boldsymbol{r}'), \quad (2.18a)$$
$$\Gamma_{\delta}^{S} \equiv -g_{\delta}\boldsymbol{\tau}(\boldsymbol{r})\cdot g_{\delta}\boldsymbol{\tau}(\boldsymbol{r}'), \quad (2.18b)$$
$$\Gamma_{\omega}^{V} \equiv \left(g_{\omega}\gamma^{\mu}\right)_{\boldsymbol{r}}\left(g_{\omega}\gamma_{\mu}\right)_{\boldsymbol{r}'}, \quad (2.18c)$$
$$\Gamma_{\rho}^{V} \equiv \left(g_{\rho}\gamma^{\mu}\boldsymbol{\tau}\right)_{\boldsymbol{r}}\cdot\left(g_{\rho}\gamma_{\mu}\boldsymbol{\tau}\right)_{\boldsymbol{r}'}, \quad (2.18d)$$
$$\Gamma_{\omega}^{T} \equiv \left(\frac{f_{\omega}}{2M}\sigma_{\mu\nu}\partial^{\mu}\right)_{\boldsymbol{r}}\left(\frac{f_{\omega}}{2M}\sigma^{\lambda\nu}\partial_{\lambda}\right)_{\boldsymbol{r}'}, \quad (2.18e)$$
$$\Gamma_{\rho}^{T} \equiv \left(\frac{f_{\rho}}{2M}\boldsymbol{\tau}\sigma_{\mu\nu}\partial^{\mu}\right)_{\boldsymbol{r}}\cdot\left(\frac{f_{\rho}}{2M}\boldsymbol{\tau}\sigma^{\lambda\nu}\partial_{\lambda}\right)_{\boldsymbol{r}'}, \quad (2.18f)$$
$$\Gamma_{\omega}^{VT} \equiv \left(\frac{f_{\omega}}{2M}\sigma_{\mu\nu}\partial^{\mu}\right)_{\boldsymbol{r}}\left(g_{\omega}\gamma^{\mu}\right)_{\boldsymbol{r}'} + \left(g_{\omega}\gamma^{\nu}\boldsymbol{\tau}\right)_{\boldsymbol{r}}\left(\frac{f_{\omega}}{2M}\boldsymbol{\tau}\sigma_{\mu\nu}\partial^{\mu}\right)_{\boldsymbol{r}'}, \quad (2.18g)$$
$$\Gamma_{\rho}^{VT} \equiv \left(\frac{f_{\rho}}{2M}\boldsymbol{\tau}\sigma_{\mu\nu}\partial^{\mu}\right)_{\boldsymbol{r}}\cdot\left(g_{\rho}\gamma^{\nu}\boldsymbol{\tau}\right)_{\boldsymbol{r}'} + \left(g_{\rho}\gamma^{\nu}\boldsymbol{\tau}\right)_{\boldsymbol{r}}\cdot\left(\frac{f_{\rho}}{2M}\boldsymbol{\tau}\sigma_{\mu\nu}\partial^{\mu}\right)_{\boldsymbol{r}'}, \quad (2.18h)$$
$$\Gamma_{\pi}^{PV} \equiv -\left(\frac{f_{\pi}}{m_{\pi}}\boldsymbol{\tau}\gamma_{5}\gamma_{\mu}\partial^{\mu}\right)_{\boldsymbol{r}}\cdot\left(\frac{f_{\pi}}{m_{\pi}}\boldsymbol{\tau}\gamma_{5}\gamma_{\nu}\partial^{\nu}\right)_{\boldsymbol{r}'}, \quad (2.18i)$$
$$\Gamma_{A}^{V} \equiv \left(e\frac{1-\tau_3}{2}\gamma_{\mu}\right)_{\boldsymbol{r}}\left(e\frac{1-\tau_3}{2}\gamma^{\mu}\right)_{\boldsymbol{r}'}. \quad (2.18j)$$

In general, the time component of the four-momentum carried by mesons in Eq. (2.17) is neglected at the level of the instantaneous approximation. It has no consequence on the direct (Hartree) terms, but for the exchange (Fock) terms it amounts to neglecting retardation effects thus omitting any state dependence of the interactions in the exchange terms. The meson propagators are, therefore, of the Yukawa form:

$$D_{\phi}(\boldsymbol{r},\boldsymbol{r}') = \frac{1}{4\pi}\frac{e^{-m_{\phi}|\boldsymbol{r}-\boldsymbol{r}'|}}{|\boldsymbol{r}-\boldsymbol{r}'|}. \quad (2.19)$$

As noted before, an approximate Dirac equation, more specifically a self-energy, is needed in order to obtain solutions for the baryon wave functions. We take here the Hartree-Fock approximation that contains only second order corrections to the free baryon. The Hartree (direct) and Fock (exchange) contributions to the self-energy Σ can be separated as

$$\Sigma(\boldsymbol{r},\boldsymbol{r}') = \Sigma_{H}(\boldsymbol{r})\delta(\boldsymbol{r}-\boldsymbol{r}') - \Sigma_{F}(\boldsymbol{r},\boldsymbol{r}'). \quad (2.20)$$

To quantize the Hamiltonian (2.17), the nucleon field operators ψ and $\psi^\dagger$ are expanded on the set of creation and annihilation operators defined from the stationary solutions of the Dirac equation

$$\psi(x) = \sum_{i}\left[f_{i}(\boldsymbol{x})e^{-i\varepsilon_{i}t}c_{i} + g_{i}(\boldsymbol{x})e^{i\varepsilon_{i}'t}d_{i}^{\dagger}\right], \quad (2.21a)$$
$$\psi^{\dagger}(x) = \sum_{i}\left[f_{i}^{\dagger}(\boldsymbol{x})e^{i\varepsilon_{i}t}c_{i}^{\dagger} + g_{i}^{\dagger}(\boldsymbol{x})e^{-i\varepsilon_{i}'t}d_{i}\right], \quad (2.21b)$$

where $f_i(\boldsymbol{x})$ and $g_i(\boldsymbol{x})$ are complete sets of Dirac spinors. $(c_i^\dagger, c_i)$ are creation and annihilation operators for nucleons in the state i, while $(d_i^\dagger, d_i)$ are the corresponding operators for antinucleons in the state i.

In the no-sea approximation, the nuclear terms are evaluated by restricting to positive energy states only, i.e., the $(d_i^\dagger, d_i)$ terms in the expansions (2.21) will be omitted in the following. For a full relativistic description, one would have to include the negative states. However, this would lead to divergent terms which can be removed by a cumbersome renormalization procedure. Actually, if the vacuum polarization is taken into count, the parameter sets of the effective Lagrangian would have to be readjusted, leading to new parameter sets with approximately the same results as in the case when the vacuum polarization is neglected. Therefore, the no-sea approximation is widely used in relativistic modelling and practical applications in nuclear systems, and the vacuum polarization effects are thus supposed to be effectively contained in the parameter sets of the model.

Inserting the expansion (2.21) and the retarded propagator (2.19) into the Hamilton operator (2.17), the Hamiltonian consequently takes the form

$$H = T + \sum_i V_i, \tag{2.22}$$

where

$$T = \int d\boldsymbol{r} \sum_{\alpha\beta} c_\alpha^\dagger c_\beta \bar{f}_\alpha(\boldsymbol{r})(i\boldsymbol{\gamma}\cdot\nabla + M) f_\beta(\boldsymbol{r}), \tag{2.23a}$$

$$V_i = \int d\boldsymbol{r} d\boldsymbol{r}' \sum_{\alpha\beta,\beta'\alpha'} c_\alpha^\dagger c_\beta^\dagger c_{\beta'} c_{\alpha'} \bar{f}_\alpha(\boldsymbol{r}) \bar{f}_\beta(\boldsymbol{r}') \Gamma_i(1,2) D_i(\boldsymbol{r},\boldsymbol{r}') f_{\beta'}(\boldsymbol{r}') f_{\alpha'}(\boldsymbol{r}). \tag{2.23b}$$

In the Hartree-Fock (HF) approximation, the ground state of the nuclear many-body system is approximated by a Slater determinant,

$$|\Phi_0\rangle = \prod_\alpha c_\alpha^\dagger |0\rangle \tag{2.24}$$

where $|0\rangle$ represents the nucleon vacuum, and α is restricted to the single-particle (s.p.) states with positive energies in the Fermi sea. The energy functional is then obtained by taking the expectation value of the Hamiltonian (2.22) on the HF ground state

$$\begin{aligned} E &= \langle\Phi_0|H|\Phi_0\rangle \\ &= \sum_\alpha \langle\alpha|(-i\boldsymbol{\alpha}\cdot\nabla + \beta M)|\alpha\rangle + \frac{1}{2}\sum_{i;\alpha\beta}\langle\alpha\beta|V_i|\beta\alpha\rangle - \frac{1}{2}\sum_{i;\alpha\beta}\langle\alpha\beta|V_i|\alpha\beta\rangle. \end{aligned} \tag{2.25}$$

In particular, the expectation value of the potential energy operator generates two types of contributions: the direct (Hartree) and exchange (Fock) terms.

The nucleon equations of motion are derived by requiring that the total energy of the system E is stationary with respect to norm-conserving variations of the Dirac spinors f_a,

$$\delta\left[E - \sum_a E_a \int d\boldsymbol{r} f_a^\dagger f_a\right] = 0, \tag{2.26}$$

with Lagrange multipliers E_a. It turns out that the E_a are the s.p. energies including the nucleon mass.

2.1.3 Infinite nuclear matter

For the description of nuclear matter, the Coulomb field is neglected, and the momentum representation is generally adopted for the Hamiltonian. A single-particle baryon state is specified by the set of quantum numbers

$$\alpha = (p_a, s_a, \tau_a) \tag{2.27}$$

where $\tau_a = 1$ for neutron (ν) states and $\tau_a = -1$ for proton (π) states.

From the Euler-Lagrange field equation for the baryon field ψ, we obtain the Dirac equation:

$$[i\gamma_\mu \partial^\mu - M - \Sigma]\psi = 0, \tag{2.28}$$

where Σ is the nucleon self-energy. Because of the requirement of translational and rotational invariance, hermiticity, parity conservation, and time-reversal invariance, the most general form of the Lorentz structure of the self-energy is

$$\Sigma(p) = \Sigma_S(p) + \gamma_0 \Sigma_0(p) + \boldsymbol{\gamma} \cdot \hat{\boldsymbol{p}} \Sigma_V(p), \tag{2.29}$$

where $\hat{\boldsymbol{p}}$ is the unit vector along p, and the scalar component Σ_S, time component Σ_0, and space component Σ_V of the vector potential are functions of the four-momentum p of the nucleon. It is convenient to define the following effective quantities:

$$\boldsymbol{p}^* = \boldsymbol{p} + \hat{\boldsymbol{p}} \Sigma_V, \tag{2.30a}$$

$$M^* = M + \Sigma_S, \tag{2.30b}$$

$$E^* = E - \Sigma_0, \tag{2.30c}$$

which lead the relativistic mass-energy relation

$$E^{*2} = \boldsymbol{p}^{*2} + M^{*2}. \tag{2.31}$$

One can now introduce the quantities as $\hat{P}$ and $\hat{M}$ by:

$$\hat{P} \equiv \frac{\boldsymbol{p}^*}{E^*} \equiv \cos\eta(p), \qquad \hat{M} \equiv \frac{M^*}{E^*} \equiv \sin\eta(p). \tag{2.32}$$

Using the general form of the self-energy (2.29) in Eq. (2.28), the Dirac equation in nuclear matter can be written as

$$(\boldsymbol{\gamma} \cdot \boldsymbol{p}^* + M^*) u(p, s, \tau) = \gamma^0 E^* u(p, s, \tau), \tag{2.33}$$

with positive energy solutions

$$u(p, s, \tau) = \left[\frac{E^* + M^*}{2E^*}\right]^{1/2} \begin{pmatrix} 1 \\ \frac{\boldsymbol{\sigma} \cdot \boldsymbol{p}^*}{E^* + M^*} \end{pmatrix} \chi_s \chi_\tau, \tag{2.34}$$

where χ_s and χ_τ, denote the spin and isospin wave functions, respectively.

For uniform nuclear matter, the ground state is obtained by filling energy levels with spin-isospin degeneracy γ up to the Fermi momentum k_F. The Fermi momentum is related to the baryon density ρ_b by

$$\rho_b \equiv \frac{\gamma}{6\pi^2} k_F^3, \tag{2.35}$$

where the degeneracy factor is 4 for symmetric matter and 2 for pure neutron matter.

At the level of the HF approximation, the contributions to the self-energy $\Sigma(p)$ consist of a sum of direct terms

$$\Sigma_S^D = -\frac{g_\sigma^2}{m_\sigma^2}\rho_s - \frac{g_\delta^2}{m_\delta^2}\rho_s^{(3)}, \tag{2.36a}$$

$$\Sigma_0^D = +\frac{g_\omega^2}{m_\omega^2}\rho_b + \frac{g_\rho^2}{m_\rho^2}\rho_b^{(3)}, \tag{2.36b}$$

$$\Sigma_V^D = 0, \tag{2.36c}$$

Table 2.2: Functions A_ϕ, B_ϕ, C_ϕ and D_ϕ.

ϕ	A_ϕ	B_ϕ	C_ϕ	D_ϕ
σ_S	$g_\sigma^2\Theta_\sigma$	$g_\sigma^2\Theta_\sigma$	$-2g_\sigma^2\Phi_\sigma$	-
δ_S	$g_\delta^2\Theta_\delta$	$g_\delta^2\Theta_\delta$	$-2g_\delta^2\Phi_\delta$	-
ω_V	$2g_\omega^2\Theta_\omega$	$-4g_\omega^2\Theta_\omega$	$-4g_\omega^2\Phi_\omega$	-
ω_T	$-(f_\omega/2M)^2m_\omega^2\Theta_\omega$	$-3(f_\omega/2M)^2m_\omega^2\Theta_\omega$	$4(f_\omega/2M)^2m_\omega^2\Lambda_\omega$	-
ω_{VT}	-	-	-	$12(f_\omega g_\omega 2M)\Pi_\omega$
ρ_V	$2g_\rho^2\Theta_\rho$	$-4g_\rho^2\Theta_\rho$	$-4g_\rho^2\Phi_\rho$	-
ρ_T	$-(f_\rho/2M)^2m_\rho^2\Theta_\rho$	$-3(f_\rho/2M)^2m_\rho^2\Theta_\rho$	$4(f_\rho/2M)^2m_\rho^2\Lambda_\rho$	-
ρ_{VT}	-	-	-	$12(f_\rho g_\rho/2M)\Pi_\rho$
π_{PV}	$-f_\pi^2\Theta_\pi$	$-f_\pi^2\Theta_\pi$	$2f_\pi^2/m_\pi^2\Psi_\pi$	-

with

$$\rho_s \equiv \langle\bar{\psi}\psi\rangle = \sum_{i=n,p}\frac{1}{\pi^2}\int_0^{k_F,i} p^2dp\hat{M}, \tag{2.37a}$$

$$\rho_s^{(3)} = \langle\bar{\psi}\tau_3\psi\rangle = \sum_{i=n,p}\tau_i\frac{1}{\pi^2}\int_0^{k_F,i} p^2dp\hat{M}, \tag{2.37b}$$

$$\rho_b \equiv \langle\psi^\dagger\psi\rangle = \sum_{i=n,p}\frac{1}{3\pi^2}k_{F,i}^3, \tag{2.37c}$$

$$\rho_b^{(3)} = \langle\psi^\dagger\tau_3\psi\rangle = \frac{1}{3\pi^2}k_{F,n}^3 - \frac{1}{3\pi^2}k_{F,p}^3, \tag{2.37d}$$

and exchange terms

$$\Sigma_S^E(p,\tau) = \frac{1}{(4\pi)^2p}\sum_{\phi,\tau'}\tau_\phi^2\int_0^{k_F} p'dp'\Big[\hat{M}(p')B_\phi(p,p') + \frac{1}{2}\hat{P}(p')D_\phi(p,p')\Big], \tag{2.38a}$$

$$\Sigma_0^E(p,\tau) = \frac{1}{(4\pi)^2p}\sum_{\phi,\tau'}\tau_\phi^2\int_0^{k_F} p'dp'A_\phi(p,p'), \tag{2.38b}$$

$$\Sigma_V^E(p,\tau) = \frac{1}{(4\pi)^2p}\sum_{\phi,\tau'}\tau_\phi^2\int_0^{k_F} p'dp'\Big[\hat{P}(p')C_\phi(p,p') + \frac{1}{2}\hat{M}(p')D_\phi(p,p')\Big], \tag{2.38c}$$

where k_F is the baryon Fermi momentum and τ_ϕ is the isospin factor at the meson-N vertex in the Fock diagram. The details of the functions A_ϕ, B_ϕ, C_ϕ and D_ϕ in Eqs. (2.38) are explicitly given in Table 2.2, where the following functions are used:

$$\Theta_i(p,p') \equiv \ln\frac{m_i^2+(p+p')^2}{m_i^2+(p-p')^2}, \tag{2.39a}$$

$$\Phi_i(p,p') \equiv \frac{1}{4pp'}(p^2+p'^2+m_i^2)\Theta_i(p,p') - 1, \tag{2.39b}$$

$$\Psi_i(p,p') \equiv (p^2+p'^2-m_i^2/2)\Phi_i(p,p') - pp'\Theta_i(p,p'), \tag{2.39c}$$

$$\Lambda_i(p,p') \equiv (p^2+p'^2)\Phi_i(p,p') - pp'\Theta_i(p,p'), \tag{2.39d}$$

$$\Pi_i(p,p') \equiv p\Theta_i(p,p') - 2p'\Phi_i(p,p'). \tag{2.39e}$$

In the present work, we ignore the retardation effects, i.e., we drop the energy transfer between interacting baryons, which gives at most a few percent contribution to the self-energy [35].

Finally, the scalar component Σ_S, time component Σ_0, and space component Σ_V of the vector potential can be obtained as

$$\Sigma_S(p) = \Sigma_S^D + \Sigma_S^E(p), \tag{2.40a}$$

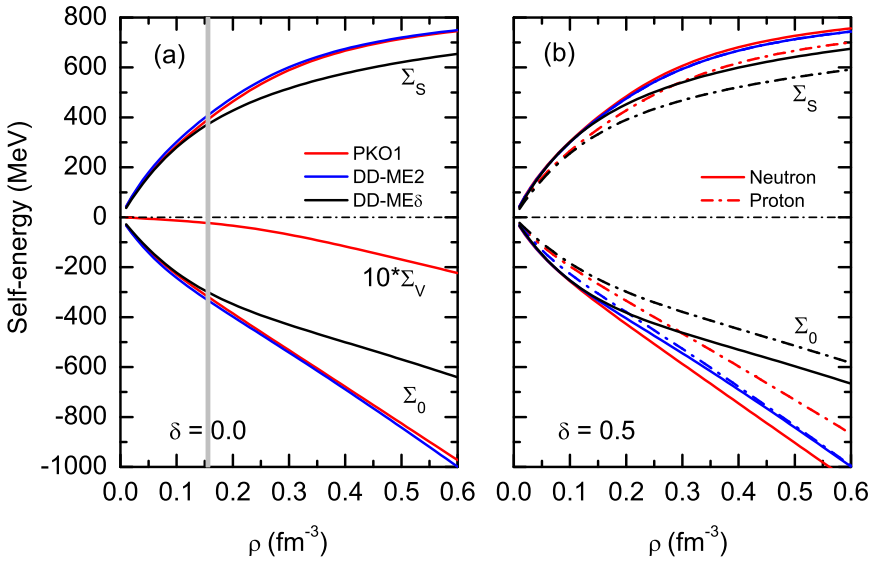

Figure 2.1: The scalar and vector self-energies in symmetric nuclear matter (a) and asymmetric matter (b), calculated in the RHF approach with PKO1. The results calculated in the RH approach with DD-ME2 and DD-MEδ are given for comparison.

$$\Sigma_0(p) = \Sigma_0^D + \Sigma_0^E(p) + \Sigma_R(p), \tag{2.40b}$$

$$\Sigma_V(p) = \Sigma_V^E(p), \tag{2.40c}$$

from which the starred and the hatted quantities (2.30-2.32) can be obtained. The rearrangement term Σ_R appearing in the self-energy Σ_0 can be written as

$$\Sigma_R^\phi(p) = \sum_\phi \frac{\partial g_\phi}{\partial \rho_b} \sum_\tau \frac{1}{\pi^2} \int p^2 dp \big[\hat{M}(p)\Sigma_{S,\tau}^\phi(p) + \Sigma_{0,\tau}^\phi(p) + \hat{P}(p)\Sigma_{V,\tau}^\phi(p)\big]. \tag{2.41}$$

One may notice that the scalar density (2.37a) is smaller than the baryon density (2.37c) due to the factor $\hat{M}$, which is an effect of Lorentz contraction. Thus, the contribution of rapidly moving baryons to the scalar source is significantly reduced.

Therefore, for nuclear matter with given baryonic density ρ_b and neutron-proton ratio N/Z, one can proceed by a self-consistent iteration to investigate their properties: With the trial self-energies one can determine the starred and hatted quantities, then calculate the scalar density, get the new self-energies, and proceed to the next iteration until final convergence is obtained.

In Fig. 2.1 are shown the scalar and vector self-energies in symmetric and asymmetric nuclear matter, corresponding to PKO1, DD-ME2, and DD-MEδ. The RH model DD-MEδ differs from others by the inclusion of the δ-meson which-as we will see-lead to different proton and neutron Dirac masses. In addition, the parameters of the DD-MEδ are largely based on microscopic Brueckner calculations in nuclear matter. In spite of the deviations in the large density region, we only give here two comments on the present calculation: (1) From the panel (a) in Fig. 2.1, we notice that the space component of vector self-energies, Σ_V is small at low density. However, it grows rapidly above $\rho > 0.2$ fm-3. Thus, it is expected to be important and cannot be ignored in dense matter. (2) From the panel (b) in Fig. 2.1, one can remark a splitting between the neutron and proton self-energies, not only for the vector self-energies but also for the scalar ones. Since the isospin dependence of the scalar self-energy Σ_S can be induced by the Fock terms or the isovector δ-meson.

The equations of state (EoS) calculated by RHF with PKA1, PKO1, and PKO2 are shown in Fig.2.2, for symmetric nuclear matter and pure neutron matter. The results calculated by RH with DD-ME2, and DD-MEδ are also shown for comparison. As can be seen from this figure, identical

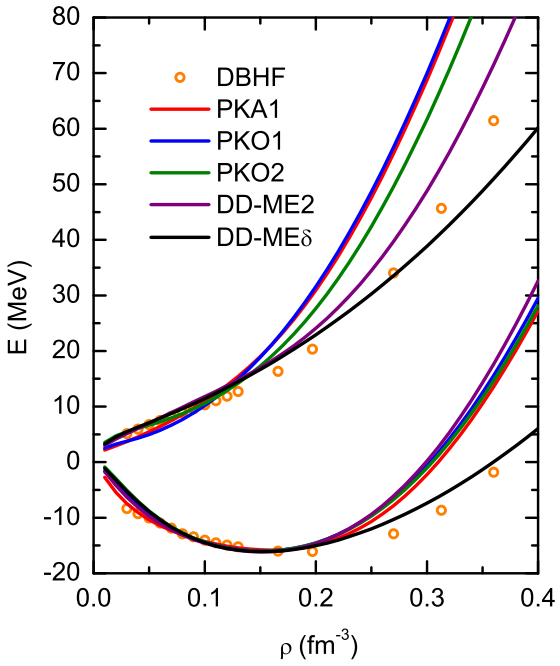

Figure 2.2: The binding energy per particle E/A in symmetric nuclear matter and in neutron matter as a function of the baryonic density ρ, calculated in the RHF approach with PKA1, PKO1, PKO2, and RH approach with DD-ME2 and DD-MEδ. The results calculated by microscopic DBHF [41] are shown for comparison.

behaviors of the EoS are obtained with all the effective interactions in the low-density region $\rho \leq \rho_0$ but in the high-density region pronounced deviations exist among different effective interactions. This feature is not surprising since the density inside nuclei are $\rho \leq \rho_0$ and these effective interactions reproduce equally the gross properties of nuclei.

2.1.4 RHF for spherical nuclei

We now generalize the results of the preceding subsection to the case of finite nuclei. Since the system now has finite spatial extent, the physical fields are spatially dependent. We first restrict ourselves to spherically symmetric nuclei, so that the meson fields depend only on the radius.

In spherically symmetric systems, a single-particle baryon state is specified by the set of quantum numbers

$$\alpha \equiv (a, m_a) = (\tau_a, n_a, l_a, j_a, m_a) \tag{2.42}$$

where $\tau_a = 1$ for neutron (ν) states and $\tau_a = -1$ for proton (π) states. The single-particle Dirac spinor is thus explicitly expressed as

$$\psi_\alpha(\boldsymbol{r}) = \frac{1}{r}\begin{pmatrix} iG_a(r) \\ F_a(r)\boldsymbol{\sigma}\cdot\hat{\boldsymbol{r}} \end{pmatrix} \mathscr{Y}_a(\hat{\boldsymbol{r}})\chi_{\frac{1}{2}}(\tau_a), \tag{2.43}$$

where $\chi_{\frac{1}{2}}(\tau_a)$ is the isospinor, G_a and F_a correspond to the radial parts of the upper and lower components, respectively, $\mathscr{Y}_a(\hat{\boldsymbol{r}})$ is the spherical spinor defined as

$$\mathscr{Y}_a(\hat{\boldsymbol{r}}) = \sum_{\mu_a, s_a} C^{j_a m_a}_{l_a \mu_a \frac{1}{2} s_a} Y_{l_a \mu_a}(\hat{\boldsymbol{r}})\chi_{\frac{1}{2}}(s_a) \tag{2.44}$$

where $Y_{l_a\mu_a}(\hat{\boldsymbol{r}})$ are spherical harmonics. The spinors ψ_α are normalized according to

$$\int d\boldsymbol{r}\psi^\dagger_\alpha(\boldsymbol{r})\psi_\alpha(\boldsymbol{r}) = \int dr\left[G^2_a(r) + F^2_a(r)\right] = 1. \tag{2.45}$$

In the spherical symmetry case, the Yukawa-type meson propagators in Eq. (2.19) can be expanded in terms of modified Bessel functions combined with spherical harmonics,

$$D(m;\boldsymbol{r},\boldsymbol{r}') = \sum_{L=0}^{\infty} R_{LL}(m;r,r')\boldsymbol{Y}_L(\hat{\boldsymbol{r}})\cdot\boldsymbol{Y}_L(\hat{\boldsymbol{r}}'). \tag{2.46}$$

The definition of $R_{LL}(m;r,r')$ and the gradients of $D(m;\boldsymbol{r},\boldsymbol{r}')$ can be found in Remark 1.

The variational procedure (2.26) with respect to the Dirac spinors ψ (2.43) leads to the Dirac HF equation

$$\int d\boldsymbol{r}' h(\boldsymbol{r},\boldsymbol{r}')\psi(\boldsymbol{r}') = \varepsilon\psi(\boldsymbol{r}), \tag{2.47}$$

where ε is the single-particle energy (including the rest mass), and the single-particle Dirac Hamiltonian $h(\boldsymbol{r},\boldsymbol{r}')$ contains the kinetic h^K, the direct (Hartree) local potential h^D, and exchange (Fock) nonlocal potential h^E,

$$h^K(\boldsymbol{r},\boldsymbol{r}') = \big[\boldsymbol{\alpha}\cdot\boldsymbol{p}+\beta M\big]\delta(\boldsymbol{r}-\boldsymbol{r}'), \tag{2.48a}$$
$$h^D(\boldsymbol{r},\boldsymbol{r}') = \big[\Sigma_T(\boldsymbol{r})\gamma_5+\Sigma_0(\boldsymbol{r})+\beta\Sigma_S(\boldsymbol{r})\big]\delta(\boldsymbol{r}-\boldsymbol{r}'), \tag{2.48b}$$
$$h^E(\boldsymbol{r},\boldsymbol{r}') = \begin{pmatrix} Y_G(\boldsymbol{r},\boldsymbol{r}') & Y_F(\boldsymbol{r},\boldsymbol{r}') \\ X_G(\boldsymbol{r},\boldsymbol{r}') & X_F(\boldsymbol{r},\boldsymbol{r}') \end{pmatrix}. \tag{2.48c}$$

In the above expressions, the local self-energies Σ_S, Σ_0, and Σ_T contain the contributions from the direct (Hartree) terms and the rearrangement terms, and can be written as follows:

$$\Sigma_S(\boldsymbol{r}) = \Sigma_\sigma^S(\boldsymbol{r}) + \Sigma_\delta^S(\boldsymbol{r})\tau_3, \tag{2.49a}$$
$$\Sigma_0(\boldsymbol{r}) = \Sigma_\omega^V(\boldsymbol{r}) + \Sigma_{0,\omega}^{VT}(\boldsymbol{r}) + \Big[\Sigma_\rho^V(\boldsymbol{r}) + \Sigma_{0,\rho}^{VT}(\boldsymbol{r})\Big]\tau_3 + \frac{1}{2}(1+\tau_3)\Sigma_A^V(\boldsymbol{r}), \tag{2.49b}$$
$$\Sigma_T(\boldsymbol{r}) = \Sigma_\omega^T(\boldsymbol{r}) + \Sigma_{T,\omega}^{VT}(\boldsymbol{r}) + \Big[\Sigma_\rho^T(\boldsymbol{r}) + \Sigma_{T,\rho}^{VT}(\boldsymbol{r})\Big]\tau_3. \tag{2.49c}$$

The nonlocal self-energies $X_{G(F)}$ and $Y_{G(F)}$ come from the exchange (Fock) terms,

$$X_{G_a}^{(\phi)}(r,r') = \sum_b \mathscr{T}_{ab}^{\phi}\hat{j}_b^2(g_\phi F_b)_r\mathscr{R}_{ab}^{X_G}(m_\phi;r,r')(g_\phi G_b)_{r'}, \tag{2.50a}$$
$$X_{F_a}^{(\phi)}(r,r') = \sum_b \mathscr{T}_{ab}^{\phi}\hat{j}_b^2(g_\phi F_b)_r\mathscr{R}_{ab}^{X_F}(m_\phi;r,r')(g_\phi F_b)_{r'}, \tag{2.50b}$$
$$Y_{G_a}^{(\phi)}(r,r') = \sum_b \mathscr{T}_{ab}^{\phi}\hat{j}_b^2(g_\phi G_b)_r\mathscr{R}_{ab}^{Y_G}(m_\phi;r,r')(g_\phi G_b)_{r'}, \tag{2.50c}$$
$$Y_{F_a}^{(\phi)}(r,r') = \sum_b \mathscr{T}_{ab}^{\phi}\hat{j}_b^2(g_\phi G_b)_r\mathscr{R}_{ab}^{Y_F}(m_\phi;r,r')(g_\phi F_b)_{r'}. \tag{2.50d}$$

In these expressions, $\mathscr{T}_{ab}^{\phi}$ denotes the isospin factors: δ_{ab} for isoscalar channels and $(2-\delta_{ab})$ for isovector channels, $\hat{j}_b^2 = 2j_b+1$ is the degeneracy number of the corresponding energy level, g_ϕ represents the coupling constants, and $\mathscr{R}_{ab}$ denote the multipole expansions of meson propagators. More detailed expressions of the Hartree and Fock potentials can be found in Appendix A.

In spherical coordinates one has

$$\boldsymbol{\alpha}\cdot\boldsymbol{p} = \alpha_r\big(p_r + \frac{i}{r}\beta\hat{\kappa}\big) \tag{2.51}$$

with

$$\alpha_r = \boldsymbol{\alpha}\cdot\hat{\boldsymbol{r}}, \qquad p_r = -i\big(\frac{\partial}{\partial r}+\frac{1}{r}\big), \qquad \hat{\kappa} = \beta(\boldsymbol{\Sigma}\cdot\boldsymbol{l}+1), \tag{2.52}$$

and

$$\alpha_r = \begin{pmatrix} 0 & \sigma_r \\ \sigma_r & 0 \end{pmatrix}, \qquad \alpha_r\beta = \begin{pmatrix} 0 & -\sigma_r \\ \sigma_r & 0 \end{pmatrix}. \tag{2.53}$$

The radial equation for the Dirac spinor (2.43) can be reduced as

$$\varepsilon_a \begin{pmatrix} G_a(r) \\ F_a(r) \end{pmatrix} = \begin{pmatrix} M + \Sigma_S(r) + \Sigma_0(r) & -\frac{d}{dr} + \frac{\kappa_a}{r} + \Sigma_T(r) \\ \frac{d}{dr} + \frac{\kappa_a}{r} + \Sigma_T(r) & -[M + \Sigma_S(r) - \Sigma_0(r)] \end{pmatrix} \begin{pmatrix} G_a(r) \\ F_a(r) \end{pmatrix} + \begin{pmatrix} Y_a(r) \\ X_a(r) \end{pmatrix}, \tag{2.54}$$

which is a coupled integro-differential equation due to the non-local Fock terms X_a and Y_a.

We thus introduce the effective local potentials $X_{G(F)}$ and $Y_{G(F)}$, by the definitions

$$X_\alpha(r) = \frac{G_a(r)X_\alpha(r)}{G_a^2(r) + F_a^2(r)} G_a(r) + \frac{F_a(r)X_\alpha(r)}{G_a^2(r) + F_a^2(r)} F_a(r) \equiv X_{\alpha,G_a}(r)G_a(r) + X_{\alpha,F_a}(r)F_a(r), \tag{2.55a}$$

$$Y_\alpha(r) = \frac{G_a(r)Y_\alpha(r)}{G_a^2(r) + F_a^2(r)} G_a(r) + \frac{F_a(r)Y_\alpha(r)}{G_a^2(r) + F_a^2(r)} F_a(r) \equiv Y_{\alpha,G_a}(r)G_a(r) + Y_{\alpha,F_a}(r)F_a(r). \tag{2.55b}$$

The exchange potentials are now written as

$$\begin{pmatrix} Y_\alpha^{(\phi)} \\ X_\alpha^{(\phi)} \end{pmatrix}_r = \int dr' \begin{pmatrix} Y_{G_\alpha}^{(\phi)} & Y_{F_\alpha}^{(\phi)} \\ X_{G_\alpha}^{(\phi)} & X_{F_\alpha}^{(\phi)} \end{pmatrix}_{(r,r')} \begin{pmatrix} G_\alpha^{(\phi)} \\ F_\alpha^{(\phi)} \end{pmatrix}_{r'}, \tag{2.56}$$

and thus the radial equation (2.54) becomes

$$\varepsilon_a \begin{pmatrix} G_a(r) \\ F_a(r) \end{pmatrix} = \begin{pmatrix} M + \Sigma_S(r) + \Sigma_0(r) + Y_{G_a}(r) & -\frac{d}{dr} + \frac{\kappa_a}{r} + \Sigma_T(r) - Y_{F_a}(r) \\ \frac{d}{dr} + \frac{\kappa_a}{r} + \Sigma_T(r) + X_{G_a}(r) & -[M + \Sigma_S(r) - \Sigma_0(r) - X_{F_a}(r)] \end{pmatrix} \begin{pmatrix} G_a(r) \\ F_a(r) \end{pmatrix}, \tag{2.57}$$

which are local, just as in the RH approach. The equations (2.57) are formally coupled differential equations which can be solved numerically like in RH by the shooting method.

The meson and photon field equations (2.12) simply become radial Laplace equations of the form

$$\Big(-\frac{d^2}{dr^2} + \frac{2}{r}\frac{d}{dr} + m_\phi^2 \Big)\phi(r) = s_\phi(r) \tag{2.58}$$

where m_ϕ are the meson masses (m_ϕ is zero for the photon). The source terms are

$$s_\phi(r) = \begin{cases} -g_\sigma \rho_s(r) & \phi = \sigma \\ -g_\delta \rho_s^{(3)}(r) & \phi = \delta \\ g_\omega \rho_v(r) & \phi = \omega \\ g_\rho \rho_v^{(3)}(r) & \phi = \rho \\ e\rho_c(r) & \phi = A \end{cases}. \tag{2.59}$$

The densities appearing in the source terms, which have been defined in Eqs. (2.13), can be expressed as,

$$\rho_v^{(\text{n or p})} = \frac{1}{4\pi r^2} \sum_\alpha^{\text{n or p}} \hat{j}_a^2 \big[G_a^2(r) + F_a^2(r)\big], \qquad \rho_v \equiv \rho_v^{(\text{n})} + \rho_v^{(\text{p})}, \qquad \rho_v^{(3)} \equiv \rho_v^{(\text{n})} - \rho_v^{(\text{p})}; \tag{2.60a}$$

$$\rho_s^{(\text{n or p})} = \frac{1}{4\pi r^2} \sum_\alpha^{\text{n or p}} \hat{j}_a^2 \big[G_a^2(r) - F_a^2(r)\big], \qquad \rho_s \equiv \rho_s^{(\text{n})} + \rho_s^{(\text{p})}, \qquad \rho_s^{(3)} \equiv \rho_s^{(\text{n})} - \rho_s^{(\text{p})}; \tag{2.60b}$$

$$\rho_t^{(\text{n or p})} = \frac{1}{4\pi r^2} \sum_\alpha^{\text{n or p}} \hat{j}_a^2 \big[2G_a(r)F_a(r)\big], \qquad \rho_t \equiv \rho_t^{(\text{n})} + \rho_t^{(\text{p})}, \qquad \rho_t^{(3)} \equiv \rho_t^{(\text{n})} - \rho_t^{(\text{p})}, \tag{2.60c}$$

where the sums run over filled orbitals. In practice, we choose $\rho_c = \rho_v^{(\mathrm{p})}$.

Finally, the total energy for closed shell nuclei can be expressed in terms of single particle energies and potential energies,

$$E_{\mathrm{hf}} = \sum_a \hat{j}_a \varepsilon_a - \sum_\phi \left(E_\phi + 2E_{R,\phi}\right). \tag{2.61}$$

The detailed expressions of the potential energies E_ϕ can be found in Appendix A.

In order to compare with the experimental binding energy of a nucleus, we need to, at least, include the center-of-mass (CM) corrections and the pairing correlation energy for open shell nuclei. The binding energy of a nucleus, therefore, can be expressed as:

$$E_B = E_{\mathrm{hf}} + E_{\mathrm{cm}} + E_{\mathrm{pair}}. \tag{2.62}$$

For the CM motion, we take the microscopic two-body CM correction

$$E_{\mathrm{cm}} = \frac{1}{2MA}\langle \mathcal{P}^2 \rangle \tag{2.63}$$

where $\mathcal{P}^2$ is the classical centre-of-mass momentum. Notice that E_{cm} is calculated after variation with the wave functions of the self-consistent solution. In general, the pairing correlations in open-shell nuclei are considered within the BCS or Bogoliubov schemes.

2.2 Effective interactions in RHF approach

The existing classes of RHF models are used in literatures: the nonlinear meson nucleon coupling model (NL) and the density-dependent meson-exchange model (DD).

Early attempts to investigate the structure of nuclear matter and finite nuclei in the RHF approximation have been made [38, 42]. In the framework of the linear effective Lagrangians, they gave satisfactory descriptions of the binding energies and densities for doubly magic nuclei but failed on the incompressibility K. Thus the main problem of the linear RHF approach is that it brings a high value of K. Then, different types of self-interaction Lagrangians have been considered in the literature up to now. Initially, by introducing the nonlinear self-couplings of the σ-field involving σ^2 and σ^4 terms, better agreement with the experiment and significant improvement on compression modulus K were obtained [43]. Later on, the nonlinear self-couplings of the ω-field ω^4 and $\sigma^2\omega^2$ terms were introduced [39]. In these cases, however, the nonlinear terms discover the chiral symmetry. To recover the chiral symmetry, the nonlinear self-interaction of the σ-field with zero-range limit is introduced in [44]. With this approximation, the nonlinear self-couplings are expressed in terms of the products of six and eight nucleon spinors, and their exchange contributions can be evaluated by the Fierz transformation. It is shown that, the σ self-interactions which are explicitly isovector-independent, generate a strong density dependence of the self-energies.

We remind here that the nonlinear self-interaction is known to play a very essential role in the RH models [36] to obtain, for instance, the proper value of the incompressibility and symmetry energy in nuclear matter.

The density-dependent meson-nucleon couplings were first introduced in Refs. [45, 46]. The nucleon self-energy obtained from the Dirac Brueckner-Hartree-Fock (DBHF) calculation was parameterized by introducing density-dependent coupling strengths of isoscalar mesons in the RHF approach. The RHF calculations with density-dependent coupling strengths not only reproduce the nuclear matter saturation properties, but also provide a good starting point to study finite nuclei properties. However, the rearrangement terms [47], which have been pointed out that are necessary for the energy-momentum conservation, are missing in these works.

In the last ten years, the appropriate effective Lagrangians with density-dependent meson-nucleon couplings for the RHF approach have been proposed [40, 48, 49]. This approach does not break the chiral symmetry nor increase the complexity of the theory itself. It brings significant improvements

to the quantitative description of nuclear phenomena with a similar accuracy of the same level as the RH approach.

In the present work, the RHF approach with density-dependent meson-nucleon couplings will be discussed. The density-dependent couplings are designed to account in an economical manner for the many-body corrections that arise beyond the mean-field approximation. Such density dependencies of the coupling constants thus describe the influence of the medium on the interaction of baryons. In this approach, the explicit density dependence is introduced into the meson-nucleon couplings which are functions of the baryonic density ρ_b. Following the experience and success in the density-dependent RH theory, the ansatz for isoscalar and isovector meson-nucleon coupling channels, is chosen of the following form:

$$g_\phi(\rho_b) = g_\phi(\rho_0) f_\phi(x), \tag{2.64}$$

where $x = \rho_b/\rho_0$ with ρ_0 being the nuclear matter saturation density, and the function f_ϕ chosen to be

$$f_\phi(x) = a_\phi \frac{1 + b_\phi(x + d_\phi)^2}{1 + c_\phi(x + e_\phi)^2}. \tag{2.65}$$

In addition, several constraints, $f_\phi(1) = 1$, $f''_\phi(0) = 0$ and $f''_\sigma(1) = f''_\omega(1)$, $e_{\sigma(\omega)} = d_{\sigma(\omega)}$, are introduced to reduce the number of free parameters. Then, the 10 parameters related to the density dependence of the σ-S and ω-V couplings are reduced to 3 free parameters, and the 10 parameters related to the density dependence of the δ-S and ρ-V couplings are reduced to 6 free parameters. For simplicity, an exponential density dependence is adopted for the tensor terms, f_ρ and f_π:

$$f_\rho(x) = f_\rho(0) e^{-a_\rho x}, \tag{2.66a}$$
$$f_\pi(x) = f_\pi(0) e^{-a_\pi x}. \tag{2.66b}$$

According to the spirit of effective field theory (EFT), the masses and the couplings strengths corresponding to the RHF effective Lagrangian in Eq. (2.1) have been developed by fitting the masses of reference nuclei, and the bulk properties of symmetric nuclear matter at the saturation point [40,48,49].

The details of the popular effective Lagrangians in RHF and RH are summarized in Table 2.3. It is widely recognized that the three effective mesons as well as their meson-nucleon vertex comprise the minimal set necessary for a quantitative description of nuclear properties: σ-S, ω-V, and ρ-V. An improved modeling of nuclei properties requires the development of more complete effective Lagrangian. Different types of effective Lagrangians thus have been considered to date. The RHF Lagrangians with density-dependent meson-nucleon couplings differ by the isovector channels (π-T and ρ-T). The RH Lagrangians with density-dependent meson-nucleon couplings differ by the δ-meson degree of freedom while the versions with nonlinear self-couplings mainly differ by the nonlinear terms involved by σ- and ω-meson. More recently, the RH functional has been developed based on the zero-range point-coupling interaction [50–52].

2.2.1 Isoscalar and isovector properties

The EoS of nuclear matter, i.e., the binding energy per nucleon, can be generally written as

$$E(\rho) = E_0 + \frac{1}{2} K_0 \left(\frac{\rho - \rho_0}{3\rho_0} \right)^2 + \frac{1}{6} Q_0 \left(\frac{\rho - \rho_0}{3\rho_0} \right)^3 + ..., \tag{2.67}$$

for symmetric matter where $\rho = \rho_n + \rho_p$ is the baryon density, with ρ_n and ρ_p denoting the neutron and proton densities. The parameter E_0 is the saturation energy while the density dependence of the binding energy is given by the parameters K_0, Q_0, etc...

Table 2.3: Details of the popular RHF and RH models and their basic nuclear matter properties: ρ_0(fm^{-3}), E_0(MeV), K_0(MeV), E_{sym}(MeV), L_{sym}(MeV), M_D^*(M) and M_{NR}^*(M).

Type	Model	π-PV	ρ-T	ρ_0	E_0	K_0	E_{sym}	L_{sym}	M_D^*	M_{NR}^*
	PKA1	✓	✓	0.160	-15.83	229.98	36.02	103.50	0.59	0.68
	PKO1	✓	–	0.152	-16.00	250.28	34.37	97.71	0.60	0.75
DD-RHF	PKO2	–	–	0.151	-16.03	249.53	32.49	75.92	0.59	0.76
	PKO3	✓	–	0.153	-16.04	262.44	32.99	82.99	0.55	0.75

Type	Model	δ-S	ρ_0	E_0	K_0	E_{sym}	L_{sym}	M_D^*	M_{NR}^*
	DD-ME1	–	0.152	-16.20	244.90	33.07	55.47	0.58	0.66
	DD-ME2	–	0.152	-16.14	251.15	32.31	51.27	0.57	0.65
DD-RH	DD-MEδ	✓	0.152	-16.12	219.08	32.35	52.85	0.61	0.69
	PKDD	–	0.150	-16.27	262.19	36.79	90.21	0.57	0.65

Type	Model	σ-NL	ω-NL	ρ_0	E_0	K_0	E_{sym}	L_{sym}	M_D^*	M_{NR}^*
	NL3	✓	–	0.148	-16.24	270.72	37.35	118.32	0.60	0.67
	NL3*	✓	–	0.150	-16.31	258.56	38.71	122.72	0.59	0.67
NL-RH	PK1	✓	✓	0.148	-16.27	281.96	37.59	115.70	0.61	0.68
	TM1	✓	✓	0.145	-16.26	281.46	36.94	111.01	0.63	0.71

For asymmetric matter, introducing the isospin parameter $\delta = (\rho_n - \rho_p)/\rho$, the binding energy is usually expanded as

$$E(\rho, \delta) = E(\rho) + S(\rho)\delta^2 + ..., \tag{2.68}$$

where the symmetry energy $S(\rho)$ is defined as,

$$S(\rho) = E_{sym} + L_{sym}\left(\frac{\rho - \rho_0}{3\rho_0}\right) + \frac{1}{2}K_{sym}\left(\frac{\rho - \rho_0}{3\rho_0}\right)^2 + \frac{1}{6}Q_{sym}\left(\frac{\rho - \rho_0}{3\rho_0}\right)^3 + ... \tag{2.69}$$

The parameter E_{sym} is related to the symmetry coefficient of the liquid-drop formula. The slope parameter L_{sym}, curvature parameter K_{sym}, and skewness parameter (Q_{sym} characterize the density dependence of the symmetry energy around ρ_0.

It should be noticed that the absence of odd-order δ terms in the binding energy is due to the exchange symmetry between protons and neutrons in nuclear matter since we neglect the Coulomb interaction and assume the charge symmetry of nuclear forces. The higher-order terms in δ are generally negligible for most purposes. For instance, the magnitude of the δ^4 term at ρ_0 is estimated to be less than 1 MeV, compared to the value of the δ^2 term (30 MeV) at the same density [53–56]. Neglecting the contribution from higher-order terms in Eq. (2.70) leads to the well-known parabolic approximation for the EoS of asymmetric nuclear matter, which has been verified by all many-body theories to date, at least for densities up to moderate values. Nevertheless, it should be mentioned that the presence of higher-order terms in δ at supra-normal densities can significantly modify the transition density from non-uniform to β-stable matter in neutron stars, the proton fraction in β-equilibrium neutron star matter, and the critical density for the direct Urca process which can affect significantly the cooling of neutron stars [57–59].

A more general expansion around any reference density $\rho_{\rm ref}$ is given by the following expression,

$$E(\rho, \delta) = \sum_{n=0}^{N}(c_{{\rm IS},n} + c_{{\rm IV},n}\delta^2)\frac{x^n}{n!}, \quad \text{with} \quad \delta = \frac{\rho_n - \rho_p}{\rho}, \quad x = \frac{\rho - \rho_{\rm ref}}{3\rho_{\rm ref}}, \tag{2.70}$$

We introduce in this expression the coefficients $c_{{\rm IS},n}$ and $c_{{\rm IV},n}$, associated respectively with the derivatives of the energy $E(\rho, \delta)|_{\delta=0}$ and of the symmetry energy $S(\rho)$: the index IS (IV) stands for isoscalar

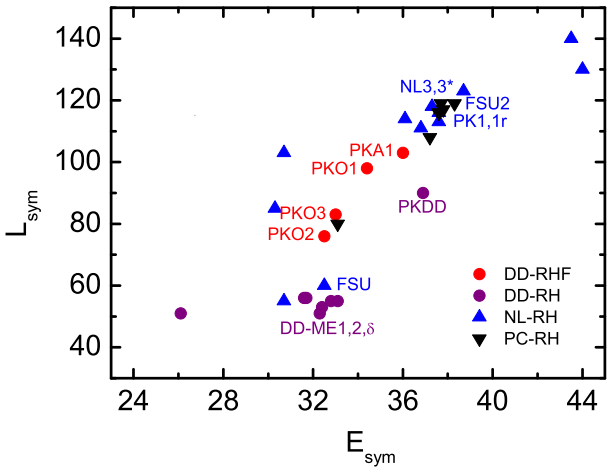

Figure 2.3: The symmetry energy with its slope in symmetric nuclear matter at saturation density.

(isovector). The IS (IV) coefficients are thus expressed as

$$c_{\mathrm{IS},n}(\rho_{\mathrm{ref}}) = (3\rho_{\mathrm{ref}})^n \frac{\partial^n E(\rho,0)}{\partial^n \rho}\Big|_{\rho=\rho_{\mathrm{ref}}}, \tag{2.71a}$$

$$c_{\mathrm{IV},n}(\rho_{\mathrm{ref}}) = (3\rho_{\mathrm{ref}})^n \frac{\partial^n S(\rho,0)}{\partial^n \rho}\Big|_{\rho=\rho_{\mathrm{ref}}}. \tag{2.71b}$$

In the case $\rho_{\mathrm{ref}} = \rho_0$, the lower-order coefficients correspond to the usual nuclear matter empirical parameters, namely the isoscalar properties: $c_{\mathrm{IS},0} = E_0$ (saturation energy), $c_{\mathrm{IS},2} = K_0$ (incompressibility), $c_{\mathrm{IS},3} = Q_0$ (skewness); and the isovector properties: $c_{\mathrm{IS},0} = E_{sym}$ (symmetry energy); $c_{\mathrm{IS},1} = L_{sym}$ (slope of the symmetry energy), $c_{\mathrm{IS},2} = K_{sym}$ (curvature of the symmetry energy), $c_{\mathrm{IS},3} = Q_{sym}$ (skewness of the symmetry energy).

The isoscalar and isovector coefficients in symmetric nuclear matter up to $n = 2$ obtained with selected nuclear models are represented in Table 2.3. More high order coefficients can be found in Appendix C. For the symmetric nuclear matter in Table 2.3, it is clearly seen that DD-RHF models (the 4 first rows) provide a much softer EoS than NL-RH but harder than DD-RH parameterizations. This can be seen more clearly in Fig. 2.3 where the correlation between E_{sym} and its slope L_{sym} is displayed. Extensive independent studies have been performed to constrain the slope L_{sym}, but the uncertainty is still quite large [60–62].

Here, I would like to stress that the properties of nuclear matter such as the saturation point ρ_0, the compression modulus K_0 (or K) and the symmetry energy E_{sym} (or J) are just empirically determined quantities which are known with some uncertainties. Actually, they are always slightly varied to improve the description of finite nuclei. Thus, the quality of the optimized model depends not only on the form of the Lagrangian, but, in addition, on the data used for its calibration. The same is true for non-relativistic models.

2.2.2 Effective mass

The effective mass is a common concept in nuclear physics which is used to characterize the quasiparticle properties of a particle inside a strongly interacting medium. However, many different definitions for the nucleon effective mass can be found in the literature. In the present work, we mainly focus on the following two effective masses: the Dirac mass M_D^* and the non-relativistic effective mass M_{NR}^*.

The Dirac mass is a genuine relativistic quantity without non-relativistic correspondence. It is defined through the scalar part of the nucleon self-energy in the Dirac field equation, i.e.,

$$M_D^* = M + \Sigma_S. \tag{2.72}$$

As we will see later, it is directly related to the spin-orbit potential in finite nuclei. For a realistic description of the spin-orbit splitting in finite nuclei, the constraint $M_D^* \in [0.55, 0.60]$ has been obtained [63, 64].

On the other hand, to discuss the non-relativistic M_{NR}^*, we start from the non-relativistic framework. Here, the most general form of the equation of motion reads

$$i\frac{\partial}{\partial_t}\psi(\boldsymbol{r},t) = -\frac{1}{2M}\nabla^2\psi(\boldsymbol{r},t) + \int d\boldsymbol{r}'dt'U(\boldsymbol{r},\boldsymbol{r}';t-t') \tag{2.73}$$

where $U(\boldsymbol{r},\boldsymbol{r}';t-t')$ represent the most general form of the mean-field.

In the case of stationary states, we have $\psi(\boldsymbol{r},t) = \psi(\boldsymbol{r})\exp(-i\epsilon t)$. In uniform matter, $U(\boldsymbol{r},\boldsymbol{r}';t-t')$ only depends on $|\boldsymbol{r}-\boldsymbol{r}'|$ and ϵ, thus $\psi(\boldsymbol{r})$ is a plane wave $\psi(\boldsymbol{r}) = \exp(-i\boldsymbol{k}\cdot\boldsymbol{r})$. The equation of motion (2.73) therefore yields an energy-momentum relation

$$\epsilon = \frac{k^2}{2M} + U(k,\epsilon). \tag{2.74}$$

The fact that $U(k^\mu)$ depends on k and ϵ reflects the non-locality of the single-particle field in space and in time, respectively.

Inside a uniform medium, the physical velocity of the wave packet associated with the nucleon is the group velocity

$$v_g = \frac{d\epsilon}{dk}. \tag{2.75}$$

Since in free space, the velocity of a nucleon with momentum k is given by $v = k/m$, the group velocity (2.75) leads to the definition of an effective mass m^*,

$$v_g = \frac{k}{m^*}. \tag{2.76}$$

From Eqs. (2.75) and (2.76), the in-medium effective mass is defined as

$$\frac{k}{m^*} \equiv \frac{d\epsilon}{dk}, \tag{2.77}$$

which is a powerful concept used to characterize the quasiparticle properties of a particle inside a strongly interacting medium as the nucleus, or nuclear matter.

Using the relations (2.74) and (2.77), the effective mass can be decomposed into a product of a so-called k-mass and ϵ-mass:

$$m^* = m_k^* \cdot m_\epsilon^*, \tag{2.78}$$

where the k-mass and ϵ-mass read, respectively,

$$m_k^* = \left[1 + \frac{m}{k}\frac{\partial U(k^\mu)}{\partial k}\right]^{-1}, \tag{2.79a}$$

$$m_\epsilon^* = \left[1 - \frac{\partial U(k^\mu)}{\partial \epsilon}\right]. \tag{2.79b}$$

The k-mass comes from the spatial non-locality, or momentum dependence, of the mean field and it is a by-product of the Hartree-Fock approximation, while the ϵ-mass, being related to the time non-locality of the mean field, indicates to which extent the exact wave function is in a single-particle state. The ϵ-mass, therefore, can indeed be related to the inverse of the spectroscopic factor, and its deviation from 1 reveals the fragmentation of the state.

In a relativistic framework the energy-momentum relation is,

$$(\boldsymbol{k} + \hat{\boldsymbol{k}}\Sigma_V)^2 + (M + \Sigma_S)^2 = (E - \Sigma_0)^2. \tag{2.80}$$

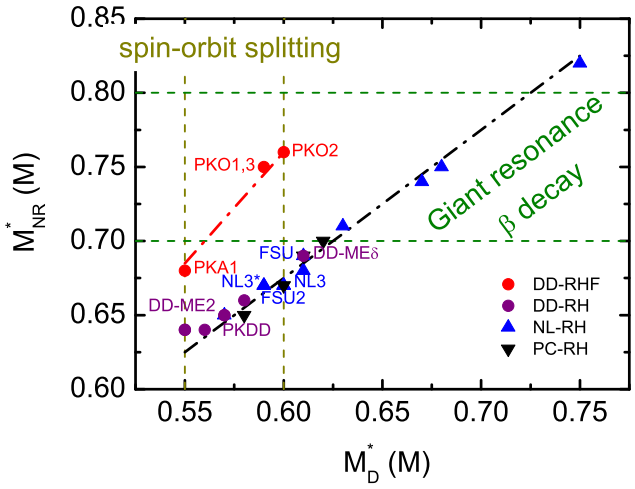

Figure 2.4: The two different nucleon effective masses in symmetric nuclear matter at saturation density.

The effective mass m^* is accordingly obtained from the corresponding Schrödinger equivalent s.p. potential,

$$U(\boldsymbol{k},\epsilon) = \Sigma_S(\boldsymbol{k}) + \frac{1}{M}k^\mu\Sigma_\mu(\boldsymbol{k}) + \frac{\Sigma_S^2(\boldsymbol{k}) - \Sigma_\mu^2(\boldsymbol{k})}{2M}, \tag{2.81}$$

where E is the energy of the quasiparticle, and $\epsilon = E - M$. From the definitions of the k-mass and ϵ-mass (2.79), one can obtain the corresponding expressions in the Dirac approach as

$$m_k^* = \left[1 + \frac{M}{k}\left(\frac{\partial}{\partial k}\Sigma_S + \frac{1}{M}k^\mu\frac{\partial}{\partial k}\Sigma_\mu + \frac{1}{M}\Sigma_V + \frac{1}{M}\left(\Sigma_S\frac{\partial}{\partial k}\Sigma_S + \Sigma_\mu\frac{\partial}{\partial k}\Sigma_\mu\right)\right)\right]^{-1}, \tag{2.82a}$$

$$m_\epsilon^* = 1 - \frac{1}{M}\Sigma_0. \tag{2.82b}$$

Empirically, some calculations of the ground-state properties and the giant resonances of nuclei have shown that a reasonable choice for the effective mass is $M_{NR}^* \in [0.70, 0.90]$ [64, 65]. The smaller M_{NR}^* would lead to a lower level density around the Fermi energy and much spread single-particle levels in finite nuclei. Thus, the M_{NR}^* would be a critical quantity to discuss the formation of new subshell closure in the nuclei far from stability.

For the two different nucleon effective masses in symmetric nuclear matter at saturation density, we show in Table 2.3 the results from the 12 parameter sets in the RHF and RH models, and more data are presented in Fig. 2.4. It is worthwhile to notice that the values of M_{NR}^* predicted by the RHF are much close to the empirical value. Furthermore, Fig. 2.4 shows that there exists an approximately linear correlation between M_{NR}^* and M_D^*, i.e., a larger M_D^* lead to larger M_{NR}^*. It is thus not surprising that some authors took M_D^* as M_{NR}^*, but still given an qualitative result.

2.2.3 Spin-orbit splitting

We now discuss the spin-orbit potential in the RHF approach. The corresponding expressions for the RH case shall be easily obtained by dropping all contributions corresponding to exchange (Fock) terms.

As mentioned in Chap. 1, the solutions of a Dirac equation with large scalar and vector fields yields immediately the spin-orbit splitting

$$\varepsilon_{ls} = \varepsilon_{nlj=l+\frac{1}{2}} - \varepsilon_{nlj=l-\frac{1}{2}}, \tag{2.83}$$

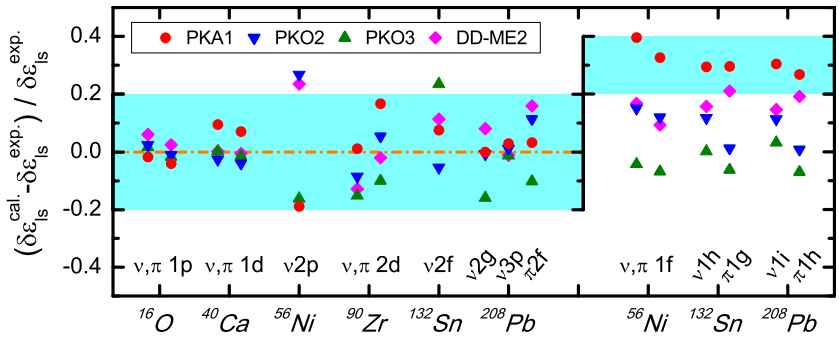

Figure 2.5: Relative differences between the theoretical SO splittings $\delta\epsilon_{ls}^{cal.}$ and the experimental ones $\delta\epsilon_{ls}^{exp.}$ [66] in the (semi)-doubly magic nuclei indicated on the horizontal-axis. Particle and hole SO partners are shown on the left while particle-hole ones are on the right. See the text for details.

which is needed for the understanding of shell structure in finite nuclei. However, it is always helpful to examine the origin of the spin-orbit splitting in the Dirac equation and to discuss its evolution.

From the equation of motion of Dirac nucleon (2.57), it could be decoupled and reduced for the upper and the lower components, respectively,

$$H_G(\kappa, r)G_{n\kappa}(r) = \varepsilon G_{n\kappa}(r), \tag{2.84a}$$
$$H_F(\kappa, r)F_{n\kappa}(r) = \varepsilon F_{n\kappa}(r), \tag{2.84b}$$

with Schrödinger-type Hamiltions $H_{G(F)}$ for the upper (lower) component $G(F)$.

In particularly, by eliminating the lower component of the Dirac spinor in Eq. (2.57), the Schrödinger-type equation for the dominant component reads

$$-M_-^{-1}\left\{\frac{d^2}{dr^2} + V_R\frac{d}{dr} + \big(V_{CB} + V_{SO}\big)\right\}G - V_C G = \varepsilon G, \tag{2.85}$$

with some proper normalization factors

$$M_+ = +V_+^D + Y_G - \varepsilon, \quad M_- = -V_-^D - X_F + \varepsilon, \tag{2.86}$$

and

$$V_\pm^D \equiv \Sigma_0 \pm \Sigma_S \pm M. \tag{2.87}$$

With $2\langle \boldsymbol{l}\cdot\boldsymbol{s}\rangle = \kappa - 1$ in mind, Eq. (2.85) allows us to identify different components of Dirac potential. The V_{CB} corresponds to the centrifugal barrier (CB),

$$V_{CB} \equiv -\frac{\kappa(\kappa+1)}{r^2}. \tag{2.88}$$

The V_{SO} represents spin-orbit potential,

$$V_{SO} \equiv V_{SO}^D + V_{SO}^E = \frac{\kappa}{r}M_-^{-1}\frac{d}{dr}V_-^D + \frac{\kappa}{r}\big(M_-^{-1}\frac{d}{dr}X_F - 2\Sigma_T - X_G - Y_F\big). \tag{2.89}$$

It is clearly seen that the SO splitting is energy dependent, and it depends on the derivative of the local nucleonic potential $\Sigma_S + \Sigma_0$ and the nolocal correlations. Furthermore, the derivative $\frac{d}{dr}$ in equation (2.89) indicates that the SO force is peaked in the surface region and that its strength will thus depend on the surface thickness. The V_C corresponds to the majority of the central potential while V_R appears as relativistic correlation, we don't present the expressions here.

Fig. 2.5 shows the relative differences between calculated and experimental [66] SO splittings for a selection of levels having well controlled spectroscopic factors. The relative differences are typically

$\sim$ 20% when both partners are particle or hole states, but they become larger otherwise. This is not surprising since polarization and correlation effects tend to shift unoccupied and occupied s.p. states into opposite directions [67, 68]. If one compares the results of Fig. 2.5 with those from non-relativistic mean field models such as Skyrme-Hartree-Fock (SHF) [69], it appears that the latter give systematically larger deviations.

2.3 Relativistic Hartree-Fock-Bogoliubov approach

The inclusion of pairing correlations is essential for the correct description of structure phenomena in open-shell and deformed nuclei. The RHF theory, as described in the previous subsection, does not include pairing correlations. The Hamiltonian contains only single-particle field operators with the structure $\psi^\dagger\psi$. Obviously, it is impossible to describe a superfluid behavior of the many fermions systems in such a framework. For this phenomenon, one needs either an additional field of the form $\psi^\dagger\psi^\dagger\psi\psi$ or a generalized single-particle operator of the form $\psi^\dagger\psi^\dagger + \psi\psi$. It is now a general consensus that the Bogoliubov transition can describe the mean field and paring correlations in a self-consistent way. In this subsection, we will briefly present the framework of relativistic Hartree-Fock-Bogoliubov (RHFB) approach.

2.3.1 Derivation of the RHFB equation

The relativistic extension of Hartree-Fock-Bogoliubov (RHFB) theory was introduced in Ref. [70]. In RHF theory the nucleons are quantized while the mesons are treated as classical fields. In order to include pairing correlations in a microscopic way, we have to quantize the meson fields also.

To simplify the following equations in this part, we introduce the Latin index combining the nucleon or meson-indices and the space-time coordinates:

$$a = (\alpha, \boldsymbol{x}, t), \qquad m = (\mu, \boldsymbol{x}, t), \tag{2.90}$$

with the convention to sum or integrate over indices occurring twice in a formula. The interaction (2.11) is then written as

$$\mathcal{H}_{\text{int}} = \bar{\psi}_a \Gamma^m_{ab} \psi_b \phi_m, \tag{2.91}$$

with the local vertices

$$\Gamma^m_{ab} = \Gamma^\mu_{\alpha\beta}(x_a, x_b, x_m) = \Gamma^\mu_{\alpha\beta}\delta(x_a - x_b)\delta(x_a - x_m). \tag{2.92}$$

We define a generalized baryon propagator:

$$S_{ab} = \begin{pmatrix} G_{ab} & F_{ab} \\ \tilde{F}_{ab} & \tilde{G}_{ab} \end{pmatrix} \tag{2.93}$$

with $G(\tilde{G})_{ab}$ the normal and $F(\tilde{F})_{ab}$ the anomalous Green's-functions

$$G_{ab} = -i\langle A|\mathcal{T}(\psi_a\bar{\psi}_b)|A\rangle, \qquad F_{ab} = -i\langle A+2|\mathcal{T}(\bar{\psi}_a\bar{\psi}_b)|A\rangle, \tag{2.94a}$$

$$\tilde{G}_{ab} = -i\langle A|\mathcal{T}(\bar{\psi}_a\psi_b)|A\rangle, \qquad \tilde{F}_{ab} = -i\langle A|\mathcal{T}(\psi_a\psi_b)|A+2\rangle, \tag{2.94b}$$

where $|A\rangle$ is the exact ground state of A-nucleon system, $\mathcal{T}$ represents the time-ordering or chronological operator and, $\bar{\psi}$ ψ now correspond to operators in the Heisenberg picture.

Employing the equation of motion for a Heisenberg operator

$$\partial_t\psi(x) = i[\mathcal{H}, \psi(x)], \tag{2.95}$$

we obtain the time derivatives for the above two-point Green's functions:

$$(\not{p} - M)_{ac}G_{cb} = \delta_{ab} - i\Gamma^m_{ac}\langle A|\mathcal{T}\psi_a\phi_m\bar{\psi}_b|A\rangle, \tag{2.96a}$$

$$(\tilde{\not{p}} - M)_{ca} F_{cb} = -i\Gamma^m_{ca} \langle A+2 | \mathcal{T} \bar{\psi}_c \phi_m \bar{\psi}_b | A \rangle, \tag{2.96b}$$

where $\not{p}$ and $\tilde{\not{p}}$ are defined as

$$\not{p} \equiv \gamma_0 (i\partial_t - \boldsymbol{\alpha} \cdot \boldsymbol{p}), \qquad \tilde{\not{p}} \equiv \gamma_0 (-i\partial_t - \boldsymbol{\alpha} \cdot \boldsymbol{p}). \tag{2.97}$$

In order to eliminate the meson field operator contained in Eq. (2.96), we first derive the meson Klein-Gordon equation (2.12), which can be written in a general form

$$(\partial^\nu \partial_\nu + m_\mu^2) \phi_m = \mp \bar{\psi}_a \Gamma^m_{ab} \psi_b. \tag{2.98}$$

The $+(-)$ sign holds for vector (scalar) fields. This equation can be solved by the meson field operator

$$\phi_m = \mp D_{mm'} \bar{\psi}_a \Gamma^{mm'}_{ab} \psi_b, \tag{2.99}$$

where $D_{mm'}$ represents the propagator:

$$D_{mm'} = -\frac{1}{(2\pi)^4} \int d^4k \frac{e^{ik(x-x')}}{k^2 - m_\mu^2 + i\varepsilon} \delta_{\mu\mu'}, \qquad \text{for scalar meson,} \tag{2.100a}$$

$$D_{mm'} = -\frac{1}{(2\pi)^4} \int d^4k \frac{e^{ik(x-x')}}{k^2 - m_\mu^2 + i\varepsilon} g_{\mu\mu'}, \qquad \text{for vector meson.} \tag{2.100b}$$

Inserting Eq. (2.99) into Eqs. (2.96), we obtain

$$(\not{p} - M)_{ac} G_{cb} = \delta_{ab} \mp i\Gamma^m_{ac} D_{mm'} \Gamma^{m'}_{de} \langle A | \mathcal{T} \psi_e \bar{\psi}_d \psi_c \bar{\psi}_b | A \rangle, \tag{2.101a}$$

$$(\tilde{\not{p}} - M)_{ca} F_{cb} = \mp i\Gamma^m_{ca} D_{mm'} \Gamma^{m'}_{de} \langle A+2 | \mathcal{T} \psi_e \bar{\psi}_d \bar{\psi}_c \bar{\psi}_b | A \rangle. \tag{2.101b}$$

The right hand sides of these equations contain the four-point Green's functions. In general, four-point Green's function can describe the propagation of either two-particle, two-hole or particle-hole excitations depending of the ordering of its time arguments. This set of equations is exact but not closed yet. In order to close this system, we introduce the Gorkov factorization which approximates the four-point Green's function by products of two-point ones:

$$\langle A | \mathcal{T} \psi_e \bar{\psi}_d \psi_c \bar{\psi}_b | A \rangle \approx -G_{ed} G_{cb} + G_{cd} G_{eb} + \tilde{F}_{ec} F_{db}, \tag{2.102a}$$

$$\langle A+2 | \mathcal{T} \psi_e \bar{\psi}_d \bar{\psi}_c \bar{\psi}_b | A \rangle \approx -G_{ed} F_{cb} + G_{ec} F_{db} - G_{eb} F_{dc}. \tag{2.102b}$$

In the second equation we have replaced the normal Green's functions G_{ab} of the $A+2$ system by the one of the A-particle system,

$$-i\langle A+2 | T \psi_a \bar{\psi}_b | A+2 \rangle \approx -i \langle A | T \psi_a \bar{\psi}_b | A \rangle, \tag{2.103}$$

i.e., we neglect the difference in particle number. This leads to the violation of particle number symmetry.

The first and the second terms of the right hand side in Eq. (2.102) are, respectively, the Hartree and the Fock terms. In addition the third term which is commonly called Gorkov term describes correlations between particles. Taking into account all three terms leads to the following system of equations:

$$\begin{aligned} \Big[(\not{p} - M)_{ac} \mp i\Gamma^m_{ac} D_{mm'} \Gamma^{m'}_{de} G_{ed} \pm i\Gamma^m_{ae} D_{mm'} \Gamma^{m'}_{dc} G_{ed} \Big] G_{cb} \\ + \Big[\pm i\Gamma^m_{ad} D_{mm'} \Gamma^{m'}_{ce} \tilde{F}_{ed} \Big] F_{cb} = \delta_{ab}, \end{aligned} \tag{2.104a}$$

$$\begin{aligned} \Big[(\tilde{\not{p}} - M)_{ca} \mp i\Gamma^m_{ca} D_{mm'} \Gamma^{m'}_{de} G_{ed} \pm i\Gamma^m_{da} D_{mm'} \Gamma^{m'}_{ce} G_{ed} \Big] F_{cb} \\ + \Big[\pm i\Gamma^m_{ea} D_{mm'} \Gamma^{m'}_{dc} F_{ed} \Big] G_{cb} = 0. \end{aligned} \tag{2.104b}$$

At the level of the instantaneous approximation, the one-boson exchange (OBE) interaction, which determine the self-energy and pairing field, has the general form

$$V^i_{abcd} = \mp\delta(\boldsymbol{x}_a - \boldsymbol{x}_c)\delta(\boldsymbol{x}_b - \boldsymbol{x}_d)\sum_\mu (\gamma_0\Gamma^\mu)_{\alpha\gamma} D_i (\gamma^0\Gamma_\mu)_{\beta\delta}. \tag{2.105}$$

Introducing the normal and anomalous density matrix

$$\rho_{ab} \equiv \rho_{\alpha\beta}(\boldsymbol{x}_a, \boldsymbol{x}_b) = \langle A|\psi^\dagger_\beta(\boldsymbol{x}_b)\psi_\alpha(\boldsymbol{x}_a)|A\rangle, \tag{2.106a}$$
$$\kappa_{ab} \equiv \kappa_{\alpha\beta}(\boldsymbol{x}_a, \boldsymbol{x}_b) = \langle A|\psi_\beta(\boldsymbol{x}_b)\psi_\alpha(\boldsymbol{x}_a)|A\rangle, \tag{2.106b}$$

we obtain the following self-energy operator Σ in Hartree-Fock approximation and the pairing field Δ,

$$\Sigma_{ac} = M\delta_{ab} + \gamma^0 V_{adce}\rho_{ed} + \gamma^0 V_{adec}\rho_{ed}, \tag{2.107a}$$
$$\Delta_{ac} = V_{adec}\kappa_{de}. \tag{2.107b}$$

The Green's function G_{ab} depends only on the difference in time $t = t_a - t_b$, whereas the anomalous functions $F(\tilde{F})_{ab}$ depend on this difference and an exponential part of t_a. We thus define:

$$\hat{G}_{ab}(t_a - t_b) \equiv \hat{G}_{\alpha\beta}(\boldsymbol{x}_a, \boldsymbol{x}_b; t_a - t_b) = G_{\alpha\beta'}(\boldsymbol{x}_a, t_a; \boldsymbol{x}_b, t_b)\gamma^0_{\beta'\beta}, \tag{2.108a}$$
$$\hat{F}_{ab}(t_a - t_b) \equiv \hat{F}_{\alpha\beta}(\boldsymbol{x}_a, \boldsymbol{x}_b; t_a - t_b) = e^{-i2\lambda t_a}\gamma^0_{\alpha'\alpha}F_{\alpha'\beta'}(\boldsymbol{x}_a, t_a; \boldsymbol{x}_b, t_b)\gamma^0_{\beta'\beta}, \tag{2.108b}$$
$$\hat{\tilde{F}}_{ab}(t_a - t_b) \equiv \hat{\tilde{F}}_{\alpha\beta}(\boldsymbol{x}_a, \boldsymbol{x}_b; t_a - t_b) = e^{i2\lambda t_a}\tilde{F}_{\alpha'\beta'}(\boldsymbol{x}_a, t_a; \boldsymbol{x}_b, t_b), \tag{2.108c}$$

where $2\lambda = E_{A+2} - E_A$, and E_A is the ground state energy of the A-particle system.

Equations (2.104) can thus be written in the following form:

$$\begin{pmatrix} (i\partial_t - \boldsymbol{\alpha}\cdot\boldsymbol{p} - \beta\Sigma)_{ac} & -\Delta_{ac} \\ -\Delta^*_{ca} & (-i\partial_t - \boldsymbol{\alpha}\cdot\boldsymbol{p} - \beta\Sigma + 2\lambda)_{ac} \end{pmatrix} \begin{pmatrix} \hat{G}_{cb}(t) \\ \hat{F}_{cb}(t) \end{pmatrix} = \begin{pmatrix} \delta_{ab} \\ 0 \end{pmatrix}. \tag{2.109}$$

The time dependence is taken into account explicitly by a Fourier transformation:

$$G_{ab}(\omega) \equiv G_{\alpha\beta}(\boldsymbol{x}_a, \boldsymbol{x}_b; \omega) = \int dt \hat{G}_{\alpha\beta}(\boldsymbol{x}_a, \boldsymbol{x}_b; t)e^{i(\omega+\lambda)t}, \tag{2.110a}$$
$$F_{ab}(\omega) \equiv F_{\alpha\beta}(\boldsymbol{x}_a, \boldsymbol{x}_b; \omega) = \int dt \hat{F}_{\alpha\beta}(\boldsymbol{x}_a, \boldsymbol{x}_b; t)e^{i(\omega+\lambda)t}. \tag{2.110b}$$

This transforms Eq. (2.109) into the following matrix equation:

$$(\omega - \mathcal{H}) \begin{pmatrix} G(\omega) \\ F(\omega) \end{pmatrix} = \begin{pmatrix} 1 \\ 0 \end{pmatrix}, \tag{2.111}$$

with the Dirac-Hartree-Fock-Bogoliubov matrix

$$\mathcal{H} = \begin{pmatrix} h - \lambda & \Delta \\ -\Delta^* & -h^* + \lambda \end{pmatrix}. \tag{2.112}$$

Like in non-relativistic physics we obtain the eigenfunctions by a spectral decomposition

$$G_{ab}(\omega) = \sum_\nu \frac{U_{a\nu}U^*_{b\nu}}{\omega - \varepsilon_\nu + i\eta} + \frac{V^*_{a\nu}V_{b\nu}}{\omega + \varepsilon_\nu - i\eta}, \tag{2.113a}$$
$$F_{ab}(\omega) = \sum_\nu \frac{V_{a\nu}U^*_{b\nu}}{\omega - \varepsilon_\nu + i\eta} + \frac{U^*_{a\nu}V_{b\nu}}{\omega + \varepsilon_\nu - i\eta}, \tag{2.113b}$$

where the poles are the quasiparticle energies ε_ν, and the residues are given by the spectroscopic amplitudes

$$U_{a\nu} = \langle A|\psi_a|A+1,\upsilon\rangle, \tag{2.114a}$$

$$V_{a\nu} = \langle A|\psi_a^\dagger|A-1,\upsilon\rangle, \tag{2.114b}$$

containing wave functions and the occupation numbers.

Finally, we obtain the relativistic form of the Hartree-Fock-Bogoliubov equations, which we have called the Dirac-Hartree-Fock-Bogoliubov equations:

$$\begin{pmatrix} h-\lambda & \Delta \\ -\Delta^* & -h^*+\lambda \end{pmatrix} \begin{pmatrix} U \\ V \end{pmatrix}_\nu = \varepsilon_\nu \begin{pmatrix} U \\ V \end{pmatrix}_\nu . \tag{2.115}$$

These equations can be used for a fully self-consistent description of open-shell nuclei, where the mean field h and the pairing field Δ are determined simultaneously.

2.3.2 Covariant density functional theory

In the previous section, the equations of motion for the nucleon and meson fields have been derived explicitly from the Lagrangian density. An alternative approach to the nuclear many-body system is possible within the covariant density functional (CDF) theory, based on the widely used concept of density functional theory (DFT) in atomic, molecular and condensed matter physics.

The ground state of a nucleus is described by a generalized Slater determinant $|\Phi\rangle$ which represents the vacuum with respect to independent quasiparticles,

$$\alpha_k|\Phi\rangle = 0. \tag{2.116}$$

The quasiparticle operators $(\alpha^\dagger, \alpha)$ are defined by the unitary Bogoliubov transformation of the single-nucleon creation and annihilation operators $(c^\dagger, c)$:

$$\alpha_k^\dagger = \sum_l \int d\boldsymbol{r}\big(U_{lk}(\boldsymbol{r})c_l^\dagger + V_{lk}(\boldsymbol{r})c_l\big) \tag{2.117a}$$

where U_{lk}, V_{lk} are the Dirac-Bogoliubov coefficients. The index l denotes an arbitrary basis. In the coordinate space representation $l = (\boldsymbol{r}, s, \tau)$, with the spin index s and the isospin index τ. We require the new operators $(\alpha^\dagger, \alpha)$ to obey the same Fermion commutation relations as the old ones $(c^\dagger, c)$.

The generalized density matrix associated with a quasiparticle vacuum $|\Phi\rangle$ was introduced by Valatin in the following way

$$\mathcal{R} = \begin{pmatrix} \rho & \kappa \\ -\kappa^* & 1-\rho^* \end{pmatrix} \tag{2.118}$$

with the hermitian single-particle density matrix ρ and the antisymmetric pairing tensor κ, defined respectively as

$$\rho_{ll'}(\boldsymbol{r},\boldsymbol{r'}) = \langle\Phi|c_{l'}^\dagger c_l|\Phi\rangle = \sum_k V_{l'k}^*(\boldsymbol{r})V_{lk}^T(\boldsymbol{r'}), \tag{2.119a}$$

$$\kappa_{ll'}(\boldsymbol{r},\boldsymbol{r'}) = \langle\Phi|c_{l'}c_l|\Phi\rangle = \sum_k V_{lk}^*(\boldsymbol{r})U_{kl'}^T(\boldsymbol{r'}). \tag{2.119b}$$

The hermitian $\mathcal{R}$ matrix meets the condition $\mathcal{R}^2 = \mathcal{R}$ for the RHFB ground state (quasiparticle vacuum).

In CDF approach with pairing correlations, the energy functional depends not only on the generalized density matrix $\mathcal{R}$, but also on the meson field ϕ_m. The expectation value $\langle\Phi|H|\Phi\rangle$ can be expressed as

$$E[\mathcal{R},\phi_m] = E_{ph}[\rho,\phi_m] + E_{pp}[\kappa] \tag{2.120}$$

where $E_{ph}[\rho, \phi_m]$ is the RHF energy functional defined in Eq. (2.25), and the pairing energy

$$E_{pp}[\kappa] = \frac{1}{4}\mathrm{Tr}[\kappa^* V^{pp} \kappa] \tag{2.121}$$

is expressed in terms of V^{pp}, an effective particle-particle (pp) interaction in the pairing channel.

The total energy depends on the generalized density matrix, which obeys the time-dependent HFB equations

$$i\partial_t \mathcal{R} = \big[\mathcal{H}(\mathcal{R}), \mathcal{R}\big] \tag{2.122}$$

that are actually an extension of Eq. (2.47) after we have included the pairing correlations. $\mathcal{H}$ is the generalized single-particle Hamiltonian, i.e., the RHFB Hamiltonian, which can be obtained as a functional derivative of the energy with respect to the generalized density,

$$\mathcal{H} \equiv \frac{\delta \mathcal{E}}{\delta \mathcal{R}} = \begin{pmatrix} h - \lambda & \Delta \\ -\Delta^* & -h^* + \lambda \end{pmatrix}. \tag{2.123}$$

It is clear that the RHFB Hamiltonian contains two average potentials: the self-consistent mean field h which encloses all the long range particle-hole (ph) correlations, and the pairing field Δ, which includes the particle-particle (pp) correlations. Later on, the Lagrange multiplier λ will turn out to be the Fermi energy of the system. The single-particle potential results from the variation of the energy functional with respect to the hermitian density matrix,

$$h \equiv \frac{\delta \mathcal{E}}{\delta \rho} = \boldsymbol{\alpha} \cdot \boldsymbol{p} + \Sigma, \tag{2.124}$$

i.e., it is given in terms of the Dirac kinetic energy $\boldsymbol{\alpha} \cdot \boldsymbol{p}$ and the HF field Σ. At the HF level, h is a non-local field

$$h(\boldsymbol{r}, \boldsymbol{r}') = \boldsymbol{\alpha} \cdot \boldsymbol{p} + \Sigma_H(\boldsymbol{r})\delta(\boldsymbol{r} - \boldsymbol{r}') - \Sigma_F(\boldsymbol{r}, \boldsymbol{r}'). \tag{2.125}$$

If the Fock term is neglected, one has

$$h(\boldsymbol{r}) = \boldsymbol{\alpha} \cdot \boldsymbol{p} + \gamma^5 \Sigma_T(\boldsymbol{r}) + \beta\big(M + \Sigma_S(\boldsymbol{r})\big) + \Sigma_V(\boldsymbol{r}). \tag{2.126}$$

The relativistic pairing field is obtained from the variation of the energy functional with respect to the pairing tensor

$$\Delta \equiv \frac{\delta \mathcal{E}}{\delta \kappa} = \begin{pmatrix} \Delta_{++} & \Delta_{+-} \\ \Delta_{-+} & \Delta_{--} \end{pmatrix}. \tag{2.127}$$

The indices $++, \cdots$ characterize the upper and lower components in this 2×2 Dirac field. In general Δ is also a non-local field

$$\Delta_{ab}(\boldsymbol{r}, \boldsymbol{r}') = \frac{1}{2}\sum_{cd} V^{pp}_{abcd}(\boldsymbol{r}, \boldsymbol{r}')\kappa_{cd}(\boldsymbol{r}, \boldsymbol{r}'), \tag{2.128}$$

where a, b, c, d denote quantum numbers that specify the Dirac indices of the spinors, V^{pp} are matrix elements of one-meson exchange interaction. One should note that the exchange part of the potential Σ and Δ usually involve an integral operator.

In the RHFB approach, the ground state of an open-shell nucleus, $|\Phi\rangle$, is obtained in the static limit of Eq. (2.122). The eigenvalue equation for $\mathcal{H}$ can then be written as

$$\int d\boldsymbol{r}' \begin{pmatrix} h(\boldsymbol{r}, \boldsymbol{r}') & \Delta(\boldsymbol{r}, \boldsymbol{r}') \\ -\Delta(\boldsymbol{r}, \boldsymbol{r}') & h(\boldsymbol{r}, \boldsymbol{r}') \end{pmatrix} \begin{pmatrix} U(\boldsymbol{r}') \\ V(\boldsymbol{r}') \end{pmatrix} = \begin{pmatrix} \lambda + E & 0 \\ 0 & \lambda - E \end{pmatrix} \begin{pmatrix} U(\boldsymbol{r}) \\ V(\boldsymbol{r}) \end{pmatrix}. \tag{2.129}$$

The energy scale is selected in such a way that the positive energy continuum starts at zero energy. The chemical potential λ is determined from the condition that the expectation value of the particle number operator in the ground state equals the number of nucleons,

$$N = \mathrm{Tr}\rho = \int d\boldsymbol{r} \sum_i \rho(\boldsymbol{r}). \tag{2.130}$$

The variation of the energy functional $E[\mathcal{R}, \phi_m]$ with respect to the fields ϕ_m yields, as in the case without pairing, the Klein-Gordon equations

$$\big(-\Delta + m_\phi^2 \big)\phi(r) = s_\phi(r) \tag{2.131}$$

where the sources are determined by the various densities

$$\rho_s(\boldsymbol{r}) = \sum_i V_i^\dagger(\boldsymbol{r})\gamma^0 V_i(\boldsymbol{r}), \tag{2.132a}$$

$$\rho_v(\boldsymbol{r}) = \sum_i V_i^\dagger(\boldsymbol{r}) V_i(\boldsymbol{r}), \tag{2.132b}$$

$$\rho_t(\boldsymbol{r}) = \sum_i V_i^\dagger(\boldsymbol{r})\sigma^{0i} V_i(\boldsymbol{r}). \tag{2.132c}$$

According to the no-sea approximation, the summation runs over the quasiparticle states corresponding to single-particle energies in and above the Fermi sea. The RHFB equations are solved self-consistently, with potentials determined in the mean-field approximation from the solutions of the static Klein-Gordon equations.

2.3.3 Canonical basis

The advantage of the general RHFB theory is that the variational method based on the quasiparticle transformation unifies the self-consistent description of the nuclear mean field and pairing field into a single variational theory. It is essential to study the particle shell structure in the canonical basis.

The canonical states are obtained by diagonalizing the vector density matrix

$$\int d\boldsymbol{r}' \rho_v(\boldsymbol{r}, \boldsymbol{r}')\psi_\alpha(\boldsymbol{r}') = v_\alpha^2 \psi_\alpha(\boldsymbol{r}). \tag{2.133}$$

All canonical states have localized wave functions and form a basis. The eigenvalues v_α^2 are thus the occupation probabilities.

The energies of the canonical states are defined as the diagonal matrix elements of the RHF field h in the canonical basis,

$$\varepsilon_\alpha = \langle\psi_\alpha|h|\psi_\alpha\rangle. \tag{2.134}$$

The pairing gaps associated with these states are the diagonal matrix elements of the pairing field,

$$\Delta_\alpha = \langle\psi_\alpha|\Delta|\psi_\alpha\rangle. \tag{2.135}$$

2.3.4 Effective pairing interaction

In the first applications of the relativistic Hartree-Bogoliubov theory to nuclear matter [70], the same meson parameters were used both in the *ph*-channel and in the *pp*-channel. However, it was found that the standard RH effective interactions produce pairing correlations that are much too strong. On the other hand, pairing correlations in nuclei are restricted to an energy window of a few MeV around the Fermi level, and their scale is well separated from the scale of binding energies, that are in the range from several hundred to thousand MeV. There is no empirical evidence for any relativistic effect in the

nuclear pairing field Δ and, therefore, a relativistic model with a non-relativistic pairing interaction is generally accepted.

One thus replaces the one-meson exchange interaction V^{pp} by a phenomenological pairing interaction in the pairing channel just as in the conventional non-relativistic HFB theory. The interaction used for the pairing channel is either a density-dependent contact interaction (DDCI) of the form [71]:

$$V(r,r') = V_0 \frac{1}{2}(1-P_\sigma)\left(1-\frac{\rho(r)}{\rho_0}\right)\delta(r-r'), \tag{2.136}$$

with an adjusted strength V_0; or the finite-range Gogny interaction D1S [72], which is known to have the right pairing content and has a natural energy cut-off due to its finite-range feature:

$$V(\boldsymbol{r},\boldsymbol{r'}) = \sum_{i=1,2} e^{((r-r')/\mu_i)^2}(W_i + B_i P^\sigma - H_i P^\tau - M_i P^\sigma P^\tau), \tag{2.137}$$

with the parameters μ_i, W_i, B_i, H_i and $M_i (i = 1, 2)$. Notice that the DDCI requires a regularisation scheme.

2.3.5 Evaluation of the pairing correlations

For practical evaluation of the pairing correlations, several prescriptions for the average pairing gap have been used in the literature.

(i) The *spectral gap* in quasiparticle basis is defined as the ratio of the pairing energy over the pairing density,

$$\Delta_{uv} = \mathrm{Tr}(\Delta\kappa)/\mathrm{Tr}\kappa. \tag{2.138}$$

This quantity is weighted with κ, a quantity which is concentrated around the Fermi surface. However, since κ diverges for zero-range forces, Δ_{uv} turns out to depend on the pairing window.

(ii) The *effective pairing gap* in the canonical basis is defined as [73]

$$\Delta_{vv} = \sum_\alpha (v_\alpha^2 \Delta_\alpha) / \sum_\alpha v_\alpha^2, \tag{2.139}$$

where the v_α^2 are the canonical occupation probabilities (2.133) and Δ_α are the diagonal matrix element of the pairing field in Eq. (2.135). This definition, however, puts too much weight on deeply bound states where pairing is less active.

(iii) The *lowest canonical state pairing gap*, Δ_{LCS}, is defined as the diagonal pairing matrix element corresponding to the canonical single-particle state [74], whose quasiparticle energy,

$$E_\alpha = \sqrt{(\varepsilon_\alpha - \lambda)^2 + \Delta_\alpha^2} \tag{2.140}$$

is the lowest. Here ε_α stands for the diagonal matrix element of the single-particle field h in Eq. (2.134). Obviously, Δ_{LCS} considers only the canonical state closest to the Fermi level and therefore, it is more connected to the pairing phenomenon. However it depends on a specific orbital and thus it is not really an average.

These quantities are calculated for neutrons (Δ_n) and protons (Δ_p) separately and they are discussed in different chapters of this work. We first compare here the difference between these definitions. The calculated quantities are presented in Fig. 2.6 for the Sn isotopic chain using the Gogny force D1S for the pairing channel and the RHF field provided by the PKO1. From Fig. 2.6 it can be observed that the three definitions of the pairing gap give quite similar tendency for their evolution. In the majority of the cases the Δ_{vv} values are larger than those of Δ_{uv} and Δ_{LCS} ones, which overestimate experimental data.

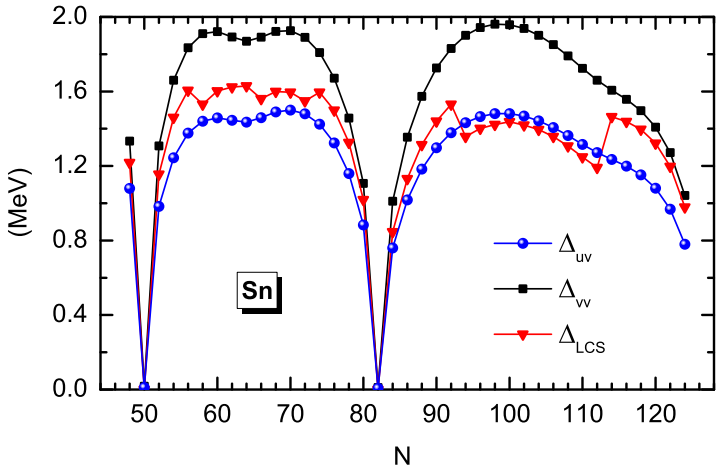

Figure 2.6: The evolution of pairing gaps Δ_{uv}, Δ_{vv} and Δ_{LCS} as functions of the neutron number N in Sn isotopes, obtained from RHFB calculations with the PKO1 and the Gogny force D1S in the pairing channel.

2.3.6 RHFB for spherical nuclei

In spherically symmetric systems the Dirac-Bogoliubov spinor can be written as

$$\psi_{U_\alpha}(\boldsymbol{r}) = \frac{1}{r}\begin{pmatrix} iG_{U_a}(r) \\ F_{U_a}(r)\boldsymbol{\sigma}\cdot\hat{\boldsymbol{r}} \end{pmatrix} \mathscr{Y}^l_{jm}(\hat{\boldsymbol{r}})\chi_{\frac{1}{2}}(\tau), \tag{2.141a}$$

$$\psi_{V_\alpha}(\boldsymbol{r}) = \frac{1}{r}\begin{pmatrix} iG_{V_a}(r) \\ F_{V_a}(r)\boldsymbol{\sigma}\cdot\hat{\boldsymbol{r}} \end{pmatrix} \mathscr{Y}^l_{jm}(\hat{\boldsymbol{r}})\chi_{\frac{1}{2}}(\tau), \tag{2.141b}$$

where G_U and F_U correspond to the radial parts of the upper and lower components, respectively.

The relativistic Hartree-Fock-Bogoliubov equation can be derived as

$$\int d\boldsymbol{r}' \begin{pmatrix} h(\boldsymbol{r},\boldsymbol{r}') & \Delta(\boldsymbol{r},\boldsymbol{r}') \\ -\Delta(\boldsymbol{r},\boldsymbol{r}') & h(\boldsymbol{r},\boldsymbol{r}') \end{pmatrix} \begin{pmatrix} \psi_U(\boldsymbol{r}') \\ \psi_V(\boldsymbol{r}') \end{pmatrix} = \begin{pmatrix} \lambda+E & 0 \\ 0 & \lambda-E \end{pmatrix} \begin{pmatrix} \psi_U(\boldsymbol{r}) \\ \psi_V(\boldsymbol{r}) \end{pmatrix}, \tag{2.142}$$

where $h(\boldsymbol{r},\boldsymbol{r}')$ is the Dirac HF Hamiltonian, which have a form identical to Eq. (2.48), can be deduced by replacing

$$G \to G_V, \qquad F \to F_V, \tag{2.143}$$

for the corresponding terms.

The pairing field $\Delta(\boldsymbol{r},\boldsymbol{r}')$ reads:

$$\Delta(\boldsymbol{r},\boldsymbol{r}') = -\frac{1}{2}\sum_\beta V^{pp}_{\alpha\beta}(\boldsymbol{r},\boldsymbol{r}')\kappa_\alpha(\boldsymbol{r},\boldsymbol{r}'), \tag{2.144}$$

with the pairing interaction V^{pp} and the pairing tensor

$$\kappa_\alpha(\boldsymbol{r},\boldsymbol{r}') = \psi^*_{V_\alpha}(\boldsymbol{r})\psi_{U_\alpha}(\boldsymbol{r}'). \tag{2.145}$$

The chemical potential λ is determined by the particle number subsidiary condition.

The total binding of the system is calculated as

$$E = E_{\text{nucleon}} + E_{\text{meson}} + E_{\text{photon}} + E_{\text{cm}}, \tag{2.146}$$

except for $E_{\rm nucleon}$, the other terms are the same as those in the spherical RHF theory. The energy of nucleons $E_{\rm nucleon}$ is calculated as

$$E_{\rm nucleon} = {\rm Tr}(\rho H) \tag{2.147}$$

$$= \sum_a \int dr(\lambda - \epsilon_a)\Big\{[G^2_{V_a}(r) + F^2_{V_a}(r)]\Big\} - 2E_{\rm pair}, \tag{2.148}$$

and

$$E_{\rm pair} = \frac{1}{2}{\rm Tr}(\Delta\kappa). \tag{2.149}$$

The center of mass (CM) correction is given by

$$E_{\rm cm} = -\frac{1}{2M}\Big[2\sum_k \rho_{kk}\Delta_{kk} + 2\sum_{kl}(\rho_{kk}\rho_{ll} + \kappa_{k\bar{k}}\tilde{\kappa}_{l\bar{l}})(\nabla_{kl}\cdot\nabla^*_{kl} + \nabla_{k\bar{l}}\cdot\nabla^*_{k\bar{l}})\Big], \tag{2.150}$$

where k, l denote the RHFB states.

The above RHFB equations can be reduced to the following integro-differential equations,

$$\Big[\frac{d}{dr} + \frac{\kappa}{r} + \Sigma_T\Big]G_U(r) - (\varepsilon - \Sigma_- + \lambda)F_U(r) + X_U(r) + r\int r'dr'\Delta(r,r')F_V(r') = 0, \tag{2.151a}$$

$$\Big[\frac{d}{dr} - \frac{\kappa}{r} - \Sigma_T\Big]F_U(r) + (\varepsilon - \Sigma_+ + \lambda)G_U(r) - Y_U(r) + r\int r'dr'\Delta(r,r')G_V(r') = 0, \tag{2.151b}$$

$$\Big[\frac{d}{dr} + \frac{\kappa}{r} + \Sigma_T\Big]G_V(r) + (\varepsilon + \Sigma_- - \lambda)F_V(r) + X_V(r) + r\int r'dr'\Delta(r,r')F_U(r') = 0, \tag{2.151c}$$

$$\Big[\frac{d}{dr} - \frac{\kappa}{r} - \Sigma_T\Big]F_V(r) - (\varepsilon + \Sigma_+ - \lambda)G_V(r) - Y_V(r) + r\int r'dr'\Delta(r,r')G_U(r') = 0, \tag{2.151d}$$

where ε are the quasiparticle energies (without the rest mass), and the local self-energies Σ_+ and Σ_- are

$$\Sigma_+ \equiv \Sigma_0 + \Sigma_S, \qquad \Sigma_- \equiv \Sigma_0 - \Sigma_S - 2M. \tag{2.152}$$

X_V, Y_V, X_U and Y_U denote the contributions from the Fock terms, which are of a general form:

$$\begin{pmatrix} Y_V^{(\phi)} \\ X_V^{(\phi)} \end{pmatrix}_r = \int dr' \begin{pmatrix} Y_G^{(\phi)} & Y_F^{(\phi)} \\ X_G^{(\phi)} & X_F^{(\phi)} \end{pmatrix}_{(r,r')} \begin{pmatrix} G_V^{(\phi)} \\ F_V^{(\phi)} \end{pmatrix}_{r'}. \tag{2.153}$$

Then, the Dirac-Bogoliubov equations must be solved self-consistently, with the auxiliary potential terms $X_{V(U)}$ and $Y_{V(U)}$ to be determined iteratively until convergency.

2.3.7 RHFB equation in the Dirac Woods-Saxon basis

In the RHFB theory the radial equations (2.3.6) are fully integro-differential. It is thus difficult to solve such equations in coordinate space. We therefore choose to solve them by an expansion of the Dirac-Bogoliubov spinors in an appropriate basis, namely the Dirac Woods-Saxon (DWS) basis [75], which can provide an appropriate asymptotical behavior for the continuum states.

If one sticks to the Hartree level and neglects tensor terms in Eq. (2.1), the Dirac equation (2.57) is therefore reduced to

$$\varepsilon_a \begin{pmatrix} G_n^\kappa(r) \\ F_n^\kappa(r) \end{pmatrix} = \begin{pmatrix} M + \Sigma_0 + \Sigma_S & -\frac{d}{dr} + \frac{\kappa_a}{r} \\ \frac{d}{dr} + \frac{\kappa_a}{r} & -M + \Sigma_0 - \Sigma_S \end{pmatrix} \begin{pmatrix} G_n^\kappa(r) \\ F_n^\kappa(r) \end{pmatrix}. \tag{2.154}$$

Introducing Woods-Saxon shape potentials

$$V_\pm \equiv (\Sigma_0 \pm \Sigma_S) \sim \begin{cases} V_0(1 + e^{(r-R_0)/a_0})^{-1}, & r < R_{\rm max}, \\ \infty, & r \geq R_{\rm max}, \end{cases} \tag{2.155}$$

the RH equation (2.154) may be solved by the shooting method in coordinate space. We thus can construct a complete Dirac Woods-Saxon (DWS) basis

$$\left\{[\epsilon_{n\kappa m}, \varphi_{n\kappa m}(\boldsymbol{r}, s, \tau)]; \epsilon_{n\kappa m} \gtrless 0\right\}_{\mathrm{DWS}} \tag{2.156}$$

with $n = 0, 1, \cdots, \kappa = \pm 1, \pm 2, \cdots, m = -j_\kappa, \cdots, j_\kappa$. The basis wave function $\varphi_{n\kappa m}$ takes the form

$$\varphi_{n\kappa m}(\boldsymbol{r}, s, \tau) = \frac{1}{r}\begin{pmatrix} iG_n^\kappa(r)\mathcal{Y}_{jm}^l(\hat{\boldsymbol{r}}, s) \\ -F_n^\kappa(r)\mathcal{Y}_{jm}^{l'}(\hat{\boldsymbol{r}}, s)\end{pmatrix}\chi_\tau(\tau). \tag{2.157}$$

Notice that the states both in the Fermi sea (positive energy states) and in the Dirac sea (negative energy states) should be included in the basis for completeness.

The nucleon wave function can thus be expanded on this basis:

$$\psi_{\alpha\kappa m}(\boldsymbol{r}, s, \tau) = \sum_{n=0}^{n_{max}} c_{\alpha n}\varphi_{n\kappa m}(\boldsymbol{r}, s, \tau) \tag{2.158}$$

where $n_{max} = n_{max}^+ + n_{max}^-$ and the summation runs over positive energy levels in the Fermi sea for $0 \le n^+ \le n_{max}^+$ and over negative energy levels in the Dirac sea for $n_{max}^+ + 1 \le n^- \le n_{max}$

The U and V components of the Dirac Bogoliubov spinors can be expanded as

$$\psi_{U_\alpha}(r) = \sum_{n^+=1}^{n_{max}^+} U_{n^+}\varphi_{n^+}(r) + \sum_{n^-=1}^{n_{max}^-} U_{n^-}\varphi_{n^-}(r), \tag{2.159a}$$

$$\psi_{V_\alpha}(r) = \sum_{n^+=1}^{n_{max}^+} V_{n^+}\varphi_{n^+}(r) + \sum_{n^-=1}^{n_{max}^-} V_{n^-}\varphi_{n^-}(r). \tag{2.159b}$$

Obviously, because of the spherical symmetry the quantum number κ is preserved, i.e., the RHFB equations have to be solved for each value of κ and the sums in the expansion (2.159) run only over states with the same κ. For a fixed value of κ, we have the radial basis spinors

$$\varphi_{n^+}(r) = \begin{pmatrix} G_{n^+}(r) \\ F_{n^+}(r)\end{pmatrix}, \tag{2.160a}$$

$$\varphi_{n^-}(r) = \begin{pmatrix} G_{n^-}(r) \\ F_{n^-}(r)\end{pmatrix}. \tag{2.160b}$$

In the DWS basis the radial RHFB equations are transformed to a matrix eigenvalue problem,

$$\begin{pmatrix} H - \lambda & \Delta \\ \Delta & -H + \lambda\end{pmatrix}\begin{pmatrix} U \\ V\end{pmatrix} = \varepsilon\begin{pmatrix} U \\ V\end{pmatrix} \tag{2.161}$$

where H and Δ are $(n_{max}^+ + n_{max}^-) \times (n_{max}^+ + n_{max}^-)$ dimensional matrices, U and V are the column vectors with $(n_{max}^+ + n_{max}^-)$ elements. From the expressions of the single particle Hamiltonian h and pairing potential Δ given in the previous part, we then obtain the matrix elements of H and Δ as

$$\begin{aligned} H_{nn'}^K &= \langle\varphi_n(r)|h^K|\varphi_{n'}(r)\rangle \\ &= \int dr G_n\Big(-\frac{d}{dr} + \frac{\kappa}{r}\Big)F_{n'} + \int dr F_n\Big(-\frac{d}{dr} + \frac{\kappa}{r}\Big)G_{n'}, \end{aligned} \tag{2.162a}$$

$$\begin{aligned} H_{nn'}^D &= \langle\varphi_n(r)|h^D|\varphi_{n'}(r)\rangle \\ &= \int dr(G_n\Sigma_+ G_{n'} + F_n\Sigma_- F_{n'}) + \int dr\Sigma_T(G_n F_{n'} + F_n G_{n'}), \end{aligned} \tag{2.162b}$$

$$H_{nn'}^E = \langle\varphi_n(r)|h^E|\varphi_{n'}(r)\rangle$$

$$= \int dr \int dr' (G_n, F_n)_r \begin{pmatrix} Y_G & Y_F \\ X_G & X_F \end{pmatrix}_{(r,r')} \begin{pmatrix} G_{n'} \\ F_{n'} \end{pmatrix}_{r'}, \tag{2.162c}$$

$$\Delta_{nn'} = \langle \varphi_n(r) | \Delta_\alpha | \varphi_{n'}(r) \rangle$$
$$= \int dr \int dr' \Delta_\kappa(r,r') \big[G_n(r) G_{n'}(r') + F_n(r) F_{n'}(r') \big], \tag{2.162d}$$

where n, n' run over the radial quantum numbers of the DWS basis states with both positive energies $(n, n' = n_+)$ and negative energies $(n, n' = n_-)$.

2.4 Finite-temperature RHFB approach

The finite-temperature RHFB (FT-RHFB) approach is a straightforward extension of the normal RHFB theory that readily incorporates a statistical ensemble of excited states. In this subsection, we briefly recall the general feature of thermodynamics, and present the generalization of RHFB to the finite temperature case.

2.4.1 Thermodynamics and statistical mechanics

The thermodynamical properties of a system are calculated here in the canonical ensemble. For a statistical N-body system at finite temperature T, the equilibrium state is obtained from the variational principle applied to the grand canonical potential Ω [76–78],

$$\Omega(T, \lambda) = F - \lambda N = E - TS - \lambda N, \tag{2.163}$$

where F is the free energy, S the entropy, E the total energy, and λ the associated Lagrange multiplier. The variation

$$\delta\Omega = 0 \tag{2.164}$$

defines the density operator $\mathcal{D}$ with trace equal to 1, and the grand partition function Z, respectively read as:

$$\mathcal{D} = Z^{-1} \exp\{-\beta(\mathcal{H} - \lambda\mathcal{N})\}, \tag{2.165a}$$
$$Z = \mathrm{Tr}[\exp\{-\beta(\mathcal{H} - \lambda\mathcal{N})\}], \tag{2.165b}$$

where $\mathcal{N}$ is the particle number operator, and $\beta = T^{-1}$. As it is conventional, the temperature T is given in energy units. For an arbitrary operator $\mathcal{O}$, the thermal average over the excited states populated at finite temperature is defined as:

$$\langle \mathcal{O} \rangle = \mathrm{Tr}(\mathcal{D}\mathcal{O}), \tag{2.166}$$

where the trace is taken over all possible excited states. At finite temperature, the total energy, entropy and number of particles are therefore expressed as

$$E = \langle \mathcal{H} \rangle = \mathrm{Tr}(\mathcal{D}\mathcal{H}), \tag{2.167a}$$
$$S = -\langle \ln\mathcal{D} \rangle = -\mathrm{Tr}(\mathcal{D}\ln\mathcal{D}), \tag{2.167b}$$
$$N = \langle \mathcal{N} \rangle = \mathrm{Tr}(\mathcal{D}\mathcal{N}). \tag{2.167c}$$

2.4.2 FT-RHF approach

In the simple HF case without pairing correlations at $T = 0$, for instance, the doubly magic nuclei, the statistical Dirac occupation probabilities is

$$\eta_i = \begin{cases} 1 & \text{for the occupied levels,} \\ 0 & \text{for the unoccupied levels.} \end{cases} \tag{2.168}$$

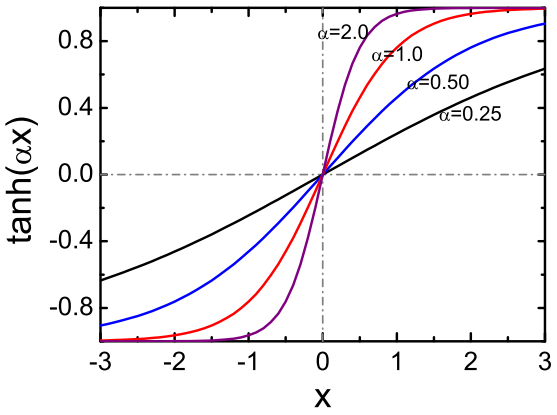

Figure 2.7: The hyperbolic tangent (tanh) function.

At finite temperature, the thermodynamic temperature is introduced through the statistical Fermi-Dirac occupation probabilities:

$$\eta_i = f_i = \left[1 + \exp\Big(\beta(\epsilon_i - \lambda)\Big)\right]^{-1} \tag{2.169}$$

for a s.p. orbital i having energy ϵ_i, where λ denotes the chemical potential.

The minimization of Ω yields the FT-RHF equations which retain the same form as that of the RHF equations.

2.4.3 FT-BCS approach

In a mean field variational approach the temperature-dependent BCS theory is derived by the minimization of the thermodynamical potential Ω, which yields the FT-BCS equation

$$\Delta_i = -\frac{1}{2}\sum_{i'} V^{pp}_{ii'}\frac{\Delta_{i'}}{\varepsilon_{i'}}\tanh\Big(\frac{1}{2}\beta\varepsilon_i\Big), \tag{2.170}$$

with the quasi-particle energies ε_i defined as

$$\varepsilon_i = \sqrt{(\epsilon_i - \lambda)^2 + \Delta_i^2}. \tag{2.171}$$

It is clear that, when $T = 0$, the factor $\tanh\big(\frac{1}{2}\beta\varepsilon_i\big)$ is 1, and Eq. (2.170) reduces to the zero-temperature BCS equation; when $T \to \infty$, the factor $\tanh\big(\frac{1}{2}\beta\varepsilon_i\big)$ becomes 0, and the pairing gap Δ_i vanishes. Therefore, pairing correlations are destroyed by increasing the temperature.

The normal and anomalous occupation probabilities of HF s.p. states are obtained through Eq. (2.170)

$$\begin{cases} \eta_i = (1 - f_i)v_i^2 + f_i u_i^2, \\ \zeta_i = (1 - f_i)v_i u_i, \end{cases} \tag{2.172}$$

where v_i and u_i denote the usual quasiparticle occupation factors and the thermal occupation factors f_i depend on the quasiparticle energy,

$$f_i = \frac{1}{1 + e^{\beta\varepsilon_i}}. \tag{2.173}$$

We present in Fig. 2.7 the evolution of the hyperbolic tangent (tanh) function. It is very useful to understand the interplay between temperature and pairing correlations. In finite nuclei the pairing correlations are active only around the Fermi level, for a typical value of pairing gap $\Delta \sim 2.0$ MeV within a pairing window of ~ 5.0 MeV, the critical temperature T_c for pair correlation quenching could be expressed around 1 MeV.

2.4.4 FT-RHFB approach

The FT-RHFB theory is a straightforward generalization of the RHFB theory that readily incorporates a statistical ensemble of excited states. At the finite-temperature mean field level, the density operator is approximated by [76]:

$$\mathcal{D} = \prod_{\alpha} \left[f_\alpha \mathcal{N}_\alpha + (1 - f_\alpha)(1 - \mathcal{N}_\alpha) \right], \tag{2.174}$$

where f_α is the Fermi-Dirac distribution defined as

$$f_\alpha = \langle \mathcal{N}_\alpha \rangle = \frac{1}{1 + e^{\beta E_\alpha}}. \tag{2.175}$$

Notice that for $T = 0$, we have $f_\alpha = 0$ for all states α. The quasiparticle energy E_α is obtained as the solution of the FT-RHFB equations.

The minimization of Ω with respect to $\mathcal{D}$ leads to the FT-RHFB equations, which are formally identical to the RHFB equations (2.129). The difference in the FT-RHFB theory for $T > 0$ occurs in the definition of the density and pairing tensors:

$$\begin{aligned} \rho_{ll'}(\boldsymbol{r}, \boldsymbol{r}') &= \langle \Phi | c^\dagger_{l'} c_l | \Phi \rangle = \mathrm{Tr}(\mathcal{D} c^\dagger_{l'} c_l) \\ &= \sum_k V^*_{l'k}(\boldsymbol{r})(1 - f_k) V^T_{lk}(\boldsymbol{r}') + \sum_k U_{l'k}(\boldsymbol{r}) f_k U^\dagger_{lk}(\boldsymbol{r}'), \end{aligned} \tag{2.176a}$$

$$\begin{aligned} \kappa_{ll'}(\boldsymbol{r}, \boldsymbol{r}') &= \langle \Phi | c_{l'} c_l | \Phi \rangle = \mathrm{Tr}(\mathcal{D} c_{l'} c_l) \\ &= \sum_k V^*_{lk}(\boldsymbol{r})(1 - f_k) U^T_{kl'}(\boldsymbol{r}') + \sum_k U_{lk}(\boldsymbol{r}) f_k V^\dagger_{kl'}(\boldsymbol{r}'). \end{aligned} \tag{2.176b}$$

In terms of the Fermi-Dirac distribution function (2.175), the entropy S can be evaluated straightforwardly:

$$S(T) = -\sum_\alpha \Big[f_\alpha \ln f_\alpha + (1 - f_\alpha) \ln(1 - f_\alpha) \Big], \tag{2.177}$$

and the specific heat is defined by

$$C_v(T) = T \frac{\partial S(T)}{\partial T}\Big|_N. \tag{2.178}$$

They correspond to the first and second derivative of the free energy F, respectively.

Notice that these equations and the corresponding FT-RHFB equations are derived from a grand canonical ensemble, the energies obtained from solving the eigenvalue problem (2.129) are calculated at a fixed temperature.

Furthermore, we can map the excitation energy of the nucleus E^* to the fixed temperature T via

$$E^*(T) = E(T) - E(0), \tag{2.179}$$

where $E(T)$ is the minimum energy of the nucleus at temperature T. This corresponds well to the excitation energy of a compound nucleus formed through such processes as electron capture, induced fission and heavy-ion fusion.

2.4.5 FT-RHFB for spherical nuclei

Based on the above considerations, we can easily construct the FT-RHFB theory in spherically symmetric systems. The local self-energies Σ_S, Σ_0, and Σ_T in the Dirac Hamiltonian (2.48) contain the contributions from the Hartree (direct) terms and the rearrangement terms, which depend directly on various local quasiparticle densities. They are the vector, scalar and tensor densities, respectively,

$$\rho_v(r) = \frac{1}{4\pi r^2} \sum_a \hat{j}_a^2 \Big\{ \left[G^2_{V_a}(r) + F^2_{V_a}(r) \right](1 - f_a) + \left[G^2_{U_a}(r) + F^2_{U_a}(r) \right] f_a \Big\}, \tag{2.180a}$$

$$\rho_s(r) = \frac{1}{4\pi r^2}\sum_a \hat{j}_a^2\Big\{\big[G_{V_a}^2(r) - F_{V_a}^2(r)\big](1-f_a) + \big[G_{U_a}^2(r) - F_{U_a}^2(r)\big]f_a\Big\}, \tag{2.180b}$$

$$\rho_t(r) = \frac{1}{4\pi r^2}\sum_a \hat{j}_a^2\Big\{2G_{V_a}(r)F_{V_a}(r)(1-f_a) + 2G_{U_a}(r)F_{U_a}(r)f_a\Big\}. \tag{2.180c}$$

The nonlocal self-energies $X_{G(F)}$ and $Y_{G(F)}$, coming from the Fock (exchange) terms, are expressed as

$$\begin{aligned} X_{G_a}^{(\phi)}(r,r') = \sum_b \mathscr{T}_{ab}^{\phi}\hat{j}_b^2\Big[&(g_\phi F_{V_b})_r \mathscr{R}_{ab}^{X_G}(m_\phi;r,r')(g_\phi G_{V_b})_{r'}(1-f_b) \\ &+ (g_\phi F_{U_b})_r \mathscr{R}_{ab}^{X_G}(m_\phi;r,r')(g_\phi G_{U_b})_{r'} f_b\Big], \end{aligned} \tag{2.181a}$$

$$\begin{aligned} X_{F_a}^{(\phi)}(r,r') = \sum_b \mathscr{T}_{ab}^{\phi}\hat{j}_b^2\Big[&(g_\phi F_{V_b})_r \mathscr{R}_{ab}^{X_F}(m_\phi;r,r')(g_\phi F_{V_b})_{r'}(1-f_b) \\ &+ (g_\phi F_{U_b})_r \mathscr{R}_{ab}^{X_F}(m_\phi;r,r')(g_\phi F_{U_b})_{r'} f_b\Big], \end{aligned} \tag{2.181b}$$

$$\begin{aligned} Y_{G_a}^{(\phi)}(r,r') = \sum_b \mathscr{T}_{ab}^{\phi}\hat{j}_b^2\Big[&(g_\phi G_{V_b})_r \mathscr{R}_{ab}^{Y_G}(m_\phi;r,r')(g_\phi G_{V_b})_{r'}(1-f_b) \\ &+ (g_\phi G_{U_b})_r \mathscr{R}_{ab}^{Y_G}(m_\phi;r,r')(g_\phi G_{U_b})_{r'} f_b\Big], \end{aligned} \tag{2.181c}$$

$$\begin{aligned} Y_{F_a}^{(\phi)}(r,r') = \sum_b \mathscr{T}_{ab}^{\phi}\hat{j}_b^2\Big[&(g_\phi G_{V_b})_r \mathscr{R}_{ab}^{Y_F}(m_\phi;r,r')(g_\phi F_{V_b})_{r'}(1-f_b) \\ &+ (g_\phi G_{U_b})_r \mathscr{R}_{ab}^{Y_F}(m_\phi;r,r')(g_\phi F_{U_b})_{r'} f_b\Big]. \end{aligned} \tag{2.181d}$$

In these expressions, $\mathscr{T}_{ab}^{\phi}$ denotes the isospin factors: δ_{ab} for isoscalar channels and $2-\delta_{ab}$ for isovector channels, $\hat{j}_b^2 = 2j_b+1$ is the degeneracy number of the corresponding energy level, g_ϕ represents the coupling constants, and $\mathscr{R}_{ab}$ denote the multipole expansions of meson propagators.

Next, we consider the pairing tensor κ. If we take a finite-range pairing force, it will read as

$$\begin{aligned} \kappa_a(r,r') = \hat{j}_a^2\Big\{&\big[G_{V_a}(r)G_{U_a}(r') + F_{V_a}(r)F_{U_a}(r')\big] \\ &+ \big[G_{U_a}(r)G_{V_a}(r') + F_{U_a}(r)F_{V_a}(r')\big]\Big\}(1-2f_a). \end{aligned} \tag{2.182}$$

Notice that the temperature dependence of the solution $(E_\alpha;\psi_{U_\alpha},\psi_{V_\alpha})$ of the FT-RHFB comes implicitly through the quasiparticle densities $\rho_{v,s,t}$, the nonlocal potentials $X(Y)$ and the pairing tensor κ.

The self-consistent solutions of the FT-RHFB equation allow one to obtain all the quantities of interest (scalar-, vector-, tensor-densities, pairing fields and pairing tensors) from which one can deduce physical properties such as the average pairing gap $\Delta(T)$, the entropy $S(T)$ and the specific heat $C_v(T)$.

2.5 Wigner-Seitz cell approximation

According to the standard model of neutron star, the inner crust is considered as the system of nuclear clusters in a body-centered-cubic lattice stabilized by Coulomb force. Theoretically it can be treated as infinite and pure matter made of only one type of nucleus-like structures at a given density. Since these nuclear clusters exhibit discrete translational symmetry, we utilize the Wigner-Seitz (WS) cell approximation [79] to model and study such a periodic system in the inner crust of neutron stars.

To describe the unbound homogeneous neutron gas in the WS cells, we need to choose appropriate boundary conditions for the s.p. wave functions. In nonrelativistic approaches, the Dirichlet-Neumann boundary conditions are usually imposed:

$$\begin{cases} \varphi_{nlj}(r)\big|_{r_c} = 0, & \text{if } l \text{ is even} \\ \frac{d}{dr}\varphi_{nl'j}(r)\big|_{r_c} = 0, & \text{if } l' \text{ is odd} \end{cases}. \tag{2.183}$$

It means that (i) the even parity wave functions vanish at the edge r_c of the WS cell box; (ii) the first derivative of the odd-parity wave functions vanish at r_c. The purpose of these chosen boundary conditions is to obtain an approximately constant density at large distance from the center of the cell, thus simulating a lattice of nucleus-like systems embedded in a uniform neutron gas. It is clear that with this mixed boundary condition all the s.p. wave function solved to the Schrödinger equation are orthogonal to one another.

It is, therefore, natural to extend such boundary conditions in the relativistic approach,

$$\begin{cases} G_{nlj}(r)\big|_{r_c} = 0, & \text{if } l \text{ is even} \\ \frac{d}{dr}G_{nl'j}(r)\big|_{r_c} = 0, & \text{if } l' \text{ is odd} \end{cases}. \tag{2.184}$$

The orthogonality of the Dirac s.p. wave functions can be expressed as follows,

$$\int d\boldsymbol{r}\psi_n^{\kappa}(\boldsymbol{r})\psi_{n'}^{\kappa'}(\boldsymbol{r}) = \delta_{nn'}\delta_{\kappa\kappa'}. \tag{2.185}$$

Unfortunately it is shown that with the above boundary condition (2.184), the orthogonality of the single particle wave functions solved in the Dirac equation is not fulled. In order to satisfy the orthogonality, two kinds of boundary conditions have been suggested [80]:

$$\begin{cases} G_{nlj}(r)\big|_{r_c} = 0, & \text{if } l \text{ is even} \\ F_{nl'j}(r)\big|_{r_c} = 0, & \text{if } l' \text{ is odd} \end{cases}, \tag{2.186}$$

or

$$\begin{cases} G_{nlj}(r)\big|_{r_c} = 0, & \text{if } \kappa < 0 \\ F_{nl'j}(r)\big|_{r_c} = 0, & \text{if } \kappa > 0 \end{cases}. \tag{2.187}$$

It is clear that single particle wave functions solved in the Dirac equation with the boundary conditions (2.186) and (2.187) are orthogonal to each other. However, it has been checked that the violation of the orthogonality in case (2.184) is not large, which is less than 10^{-3} [80].

The mixed Dirichlet-Neumann boundary conditions have been implemented in the FT-RHFB model. This allows the study of the WS cells configurations which are present in the crust of neutron stars with a state-of-the-art relativistic model. Some limitation were actually found, such as for instance the one related to the memory space. With a 16 Go computer, we could calculate only a $A = 400$ WS cell in a small box (40 fm, step= 0.2 fm). This limitation could be raised by use of more RAM memory computer, and/or by storing partial results during the self-consistent iterations. I had no time during my PhD to investigate further this limitation. The application of the FT-RHFB model to neutron star crust's is my project for the future.

Chapter 3

Nuclear structure of superheavy elements

Prediction is very difficult, especially if it's about the future.

Niels Bohr, 1885-1962

3.1 Introduction

For a fairly long period, it remains a challenging issue in nuclear physics to explore the existence limit of very heavy nuclei, i.e., the superheavy elements (SHE) with $Z \geq 104$ and the so-called stability island of superheavy nuclei (SHN). If at all, the existence of this island in the nuclear chart would come from very subtle contributions to the nuclear binding energy [81]. Experimentally, the discoveries of new elements up to $Z = 118$ have been reported in Refs. [82,83]. The increasing survival probabilities with increasing proton number of SHE from $Z = 114$ to 118 seem to indicate enhanced shell effects with increasing Z and therefore a possible proton magic shell may emerge beyond $Z \geq 120$ [84].

On the other hand, theoretical studies have provided a large amount of valuable information for the exploration of SHN. These studies can be separated into different categories: Microscopic - Macroscopic (Mic-Mac) models [3,85], non-relativistic mean field [69,86,87] and covariant mean field [69,86,88] approaches. The extrapolation towards the superheavy region challenges the predictivity of nuclear models. The Mic-Mac approach, despite its great success in predicting nuclear binding energies for exotic nuclei, can hardly be extrapolated towards very new regions where experimental data are extremely scarce. The stability of nuclei is mostly driven by shell effects and therefore, self-consistent mean field methods are probably the best conceptual tool to explore the superheavy region, although the Mic-Mac models still give a better quantitative description of heavy nuclides.

We are searching for doubly closed-shell systems and we assume spherical symmetry. Then, the shells are essentially determined by the spin-orbit (SO) splittings, and by the effective masses. A comparison of the SO splittings obtained from various relativistic models with the experimental data is shown in Fig. 2.5, Chap. 2. It shows a very stable reproduction of experimental data from light to heavy nuclei, at variance with non-relativistic approaches, e.g., Ref [69]. The effect of increasing the mass from light to heavy nuclei seems to be better taken into account with relativistic models. Fig. 2.5 therefore provides a good motivation for predictions of SHE based on relativistic Lagrangians. Another effect which affects the shell structure is related to the possible occurrence of an almost degeneracy among pseudo-spin (PS) partners [48, 89]. In the non-relativistic self-consistent mean field theory [7, 9], the SO splittings depend directly on an extra SO parameter in the energy density functional. In the superfluid covariant density functional (CDF) theory, like the relativistic Hartree-Bogoliubov (RHB) [8,37] or the relativistic Hartree-Fock-Bogoliubov (RHFB) [90] approaches, the SO

splitting depends directly on the Lorentz scalar and vector mean fields without additional term. The SO splitting is not adjusted and can be considered as a prediction of relativistic Lagrangians, even in ordinary nuclei. This might be an advantage for exploring unknown regions. Furthermore, in the more complete RHFB version of the CDF theory the SO splittings can be affected by meson-nucleon couplings like Lorentz ρ-tensor couplings [48] not present in the simple RHB. This is one of the main motivations for undertaking the present study in the framework of the RHFB approach.

SHE predictions have been carried out using relativistic mean field (RMF) models [86] or RHB models [88]. In such Hartree-type approaches, the contribution of the Fock term is disregarded, at variance with RHF, leading to a renormalization of the coupling constants. It is an approximation which forbids the inclusion of the π and the ρ-tensor mesons. While RMF models are as predictive as RHF ones for medium and heavy nuclei, it is preferable to base extrapolations to SHE on calculations including correctly the contribution of the Fock term. It is also a motivation of the present study.

In this chapter we investigate the superheavy nuclides covering Z = 110-140. Before we start the analysis of our model predictions, we give the general numerical details of the code which are fixed once-for-all in the next sections. In the pairing channel, the finite-range Gogny force D1S [72] renormalized by a strength factor f is adopted as the effective pairing interaction. The strength factor f is introduced to compensate level-density differences among various mean field approaches. It was indeed shown that pairing related quantities, such as odd-even mass differences and moments of inertia, are systematically overestimated in the RHFB calculations of heavy nuclei with the original Gogny pairing force [91]. The strength factor $f = 0.9$ is therefore adjusted to reproduce the odd-even mass differences of odd Pb isotopes. Concerning the relativistic Hartree-Fock (RHF) mean field, the adopted effective Lagrangians are PKA1 [48] and the PKOi series (i=2, 3) [40, 49]. To compare with approaches neglecting the Fock term (RHB), we also use PKDD [92] and DD-ME2 [93] Lagrangians. The integro-differential RHFB equations are solved by using a Dirac Woods-Saxon basis [75] with a radial cutoff R = 28 fm. The numbers of positive and negative energy states in the basis expansion for each single-particle (s.p.) angular momentum (l, j) are chosen to be 44 and 12, respectively.

3.2 Magic numbers in the superheavy region

In this section, the superheavy magic structure are systematically searched for in terms of different observables for more than 800 even-even nuclei. Then, the model deviations are discussed in a macroscopic view.

3.2.1 Superheavy magic numbers

To identify the magic shells, different observables can be chosen, such as nucleon separation energies, pairing gap energy, s.p. spectra, etc. The magic shells in SHN might not be as well-marked as in the ordinary nuclei. Here, we concentrate on two types of observables. One is the so-called two-nucleon gap [δ_{2p} (proton) and δ_{2n} (neutron)], i.e., the difference of two neighboring two-nucleon separation energies $S_{2n(p)}$, which is an efficient way to evaluate the shell effects,

$$\delta_{2p}(N,Z) = S_{2p}(N,Z) - S_{2p}(N,Z+2), \tag{3.1a}$$

$$\delta_{2n}(N,Z) = S_{2n}(N,Z) - S_{2n}(N+2,Z). \tag{3.1b}$$

Obviously, the peak values of the two-nucleon gaps are essentially determined by the sudden jump of the two-nucleon separation energies, which can be taken as the evidence for the magic shell occurrence. The other observable is the pairing gap energy [Δ_π (proton) or Δ_ν (neutron)], whose zero values appear with the emergence of magic shells,

$$\Delta_\nu = \frac{1}{N}\sum_{i=1}^{N}(2j_i+1)v_i^2\Delta_i, \tag{3.2a}$$

$$\Delta_\pi = \frac{1}{Z}\sum_{i=1}^{Z}(2j_i+1)v_i^2\Delta_i. \tag{3.2b}$$

where the sums run over all the neutron (ν) or proton (π) occupied canonical orbits, N (Z) represents the neutron (proton) number, and Δ_i is the pairing gap of orbital i. Notice that Eq. (3.2) is an alternative definition of the pairing gap in Eq. (2.139).

Figure 3.1 presents the two-proton (left panels) and two-neutron (right panels) gaps for the $Z = 110-140$ even-even isotopes calculated with the selected effective Lagrangians. We have adopted the presentation of Ref. [86] so that the similarities and differences in the predictions of the earlier study can be more easily seen. The red-solid lines stand for the two-proton drip lines defined as the change in sign of the two-proton separation energy. Nuclei that are stable with respect to β-decay or fission are represented with filled green stars or filled blue circles, respectively. For a given A (resp. Z), the β-stability (resp. fission-stability) line is located at the maximum of the binding energy per nucleon, and corresponds as well to the minimum of the Q-value for β-decay (resp. fission) [94]. The dashed blue line represents the β-stability line given by the empirical formula $Z = A/(1.98+0.0155A^{2/3})$ [95]. Experimental data taken from the NUBASE2012 evaluation of nuclear properties [96], including the extrapolated SHN, are located below $Z = 118$ and are shown in Fig. 3.1 with empty red squares. It is observed from Fig. 3.1 that these nuclei coincide largely with the nuclei which are stable with respect to fission (filled blue circles), as predicted by our models, especially by PKA1. The effects of deformation are not included in the present study of δ_{2p} and δ_{2n} although they may also play a significant role [97, 98]. On the neutron-poor side, the large Coulomb barrier existing in SHN pushes further down the two-proton drip line. The effect is expected to change by a few units the position of the drip line.

In Fig. 3.1, the squares are filled in proportion of the gap, which varies from 1 to 5 MeV, as shown in the grey-scale index. Structures with large gaps between 3 and 5 MeV appear clearly in Fig. 3.1. From the comparison of the different models shown in Fig. 3.1, it is clear that PKA1 is the Lagrangian which predicts the larger gaps for $Z = 120$, 126, 138 and $N = 184$, 258. These numbers are thus the predicted magic numbers in neutron-rich SHN based on the PKA1-RHFB model. The other effective Lagrangians also present a remarkable proton shell at $Z = 120$. In addition, $Z = 132$ for PKDD-RHB and $Z = 138$ for both RHFB (PKA1 and PKOi) and RHB (PKDD and DD-ME2) approaches are found to be possible proton magic numbers, consistent with the predictions in Ref. [88]. Concerning the neutron shells, besides $N = 184$ and 258, PKA1 also presents a well-marked shell structure at $N = 172$, which is also present in the predictions of the other Lagrangians. Fairly distinct shell effects at $N = 184$ and 258 are also found with the other parameterizations, except with PKO2. Remarkable shell effects are found at $N = 228$, although less pronounced compared to those at $N = 184$ and 258 predicted by PKA1. Furthermore, a neutron shell is predicted at $N = 164$ with PKO2, PKDD and DD-ME2 models, and another is predicted at $N = 198$ with RHB models (PKDD and DD-ME2).

We have checked that the neutron and proton pairing gaps, shown in Fig. 3.2, are also quenched for the same proton and neutron magic numbers as those obtained in Fig. 3.1 for each considered Lagrangian. Combined with the two-nucleon gaps, it is found that the proton shell $Z = 120$ is predicted by PKA1 as well as by the other Lagrangians used in Fig. 3.1. It is also predicted by some SHF models such as SLy6, SkI1, SkI3 and SkI4 [86], but it must be stressed that the SHF models can give different predictions for $Z = 114$ and $Z = 126$, see for instance Ref. [86]. $Z = 120$ can however be considered as a fairly good candidate for proton magic number. In Ref. [86] SHF forces such as SkM* or SkP predict $Z = 126$ as a magic number for neutron-poor isotopes. $Z = 126$ is also predicted as a magic number by PKA1 model, but not by the other Lagrangians used in Fig. 3.1, which predict a weak SO splitting for high-j states.

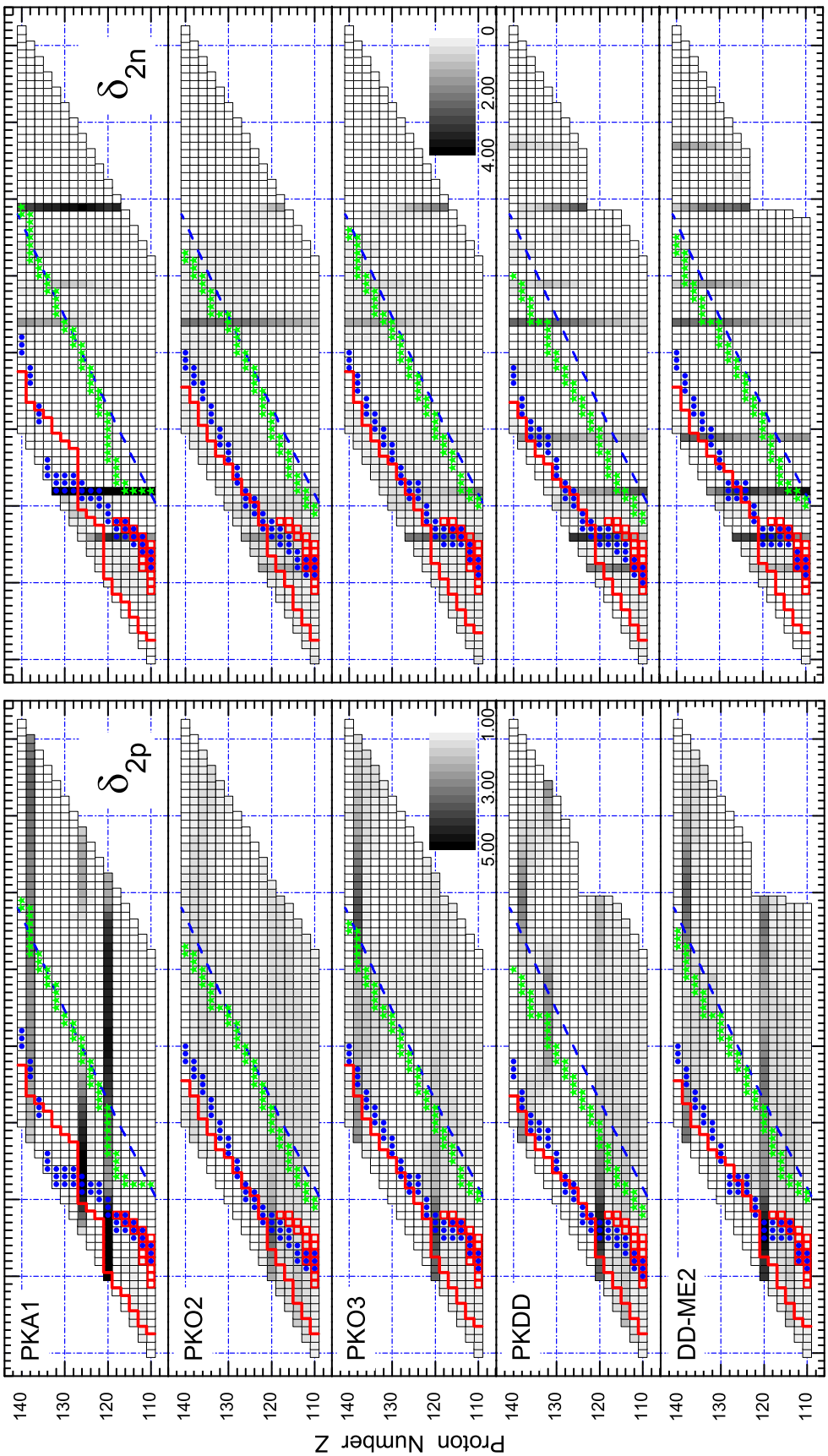

Figure 3.1: Contour plots (in MeV) for the two-proton gaps δ_{2p} (left panels) and the two-neutron gaps δ_{2n} (right panel) as functions of N and Z. The two-nucleon gaps are obtained with PKA1, PKO2 and PKO3 parametrizations for RHFB, and PKDD and DD-ME2 parametrizations for RHB. The red-solid lines represent the two-proton drip lines. Nuclei stable with respect to β-decay and fission are marked with green filled stars and blue circles, respectively. The blue long-dashed lines represent the empirical β-stability line [95]. The red empty squares indicate the experimental SHN from NUSEBASE2012 [96]. See text for more details.

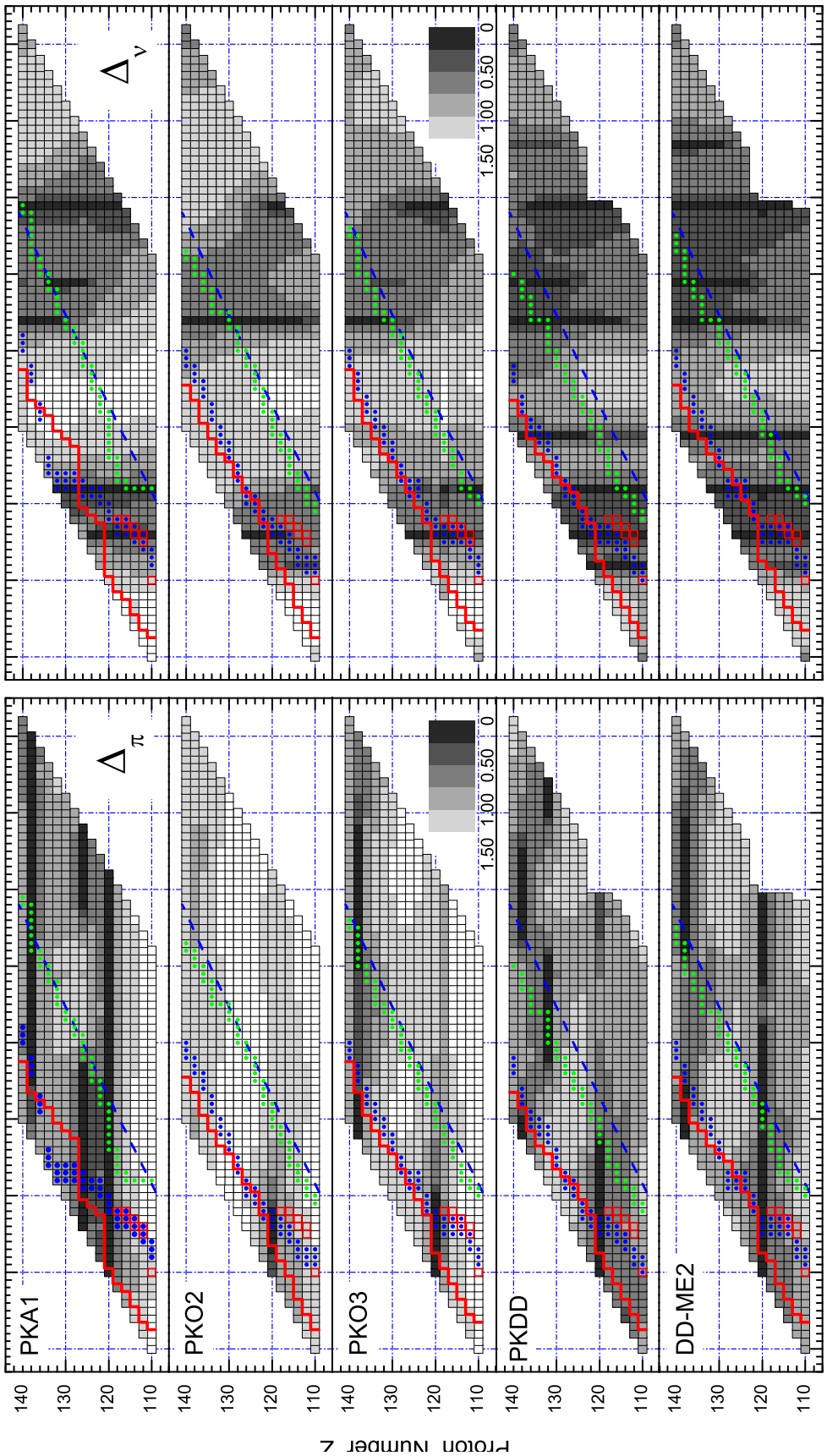

Figure 3.2: Similar as in Fig. 3.1 but for the proton (left panels) and neutron (right panels) effective pairing gaps Δ_π and Δ_ν.

Table 3.1: Bulk properties of symmetric nuclear matter calculated with the effective interactions PKA1, PKOi series, PKDD and DD-ME2: saturation density ρ_0 (fm^{-3}), binding energy per particle E_B/A (MeV), incompressibility K (MeV), asymmetry energy coefficient J (MeV), scalar mass M_S^* and non-relativistic effective mass M_{NR}^* in units of nucleon mass M.

Force	ρ_0	E_B/A	K	J	M_S^*	M_{NR}^*
PKA1	0.160	−15.83	229.96	36.02	0.547	0.681
PKO1	0.152	−16.00	250.28	34.37	0.590	0.746
PKO2	0.151	−16.03	249.53	32.49	0.603	0.764
PKO3	0.153	−16.04	262.44	32.98	0.586	0.742
PKDD	0.150	−16.27	262.18	36.79	0.571	0.651
DD-ME2	0.152	−16.14	250.97	32.31	0.572	0.652

On the other hand, the situation for the neutrons is more complex. Although $N = 172$ and 228 magic numbers seem to be generally predicted by the selected effective Lagrangians, the corresponding shell effects are rather weak. Except for PKO2, $N = 184$ and 258 are also generally predicted as candidates for neutron magic numbers. Let us notice that a large number of SHF models considered in Ref. [86] as well as Gogny forces [87] have also a large gap for these neutron numbers. Specifically, PKA1 can provide a better description of the nuclear shell structure than the others [48] and a better agreement on the fission stability of observed SHN (see Fig. 3.1), and it leads to pronounced shell effects. In fact, as indicated by SHF investigations [99] $N = 184$ is also favored evidently to be a spherical neutron magic number and the $N = 184$ isotones are expected to have spherical shapes. By comparing the predictions between the various models discussed here, we conclude that $^{304}120_{184}$ is a most probable doubly magic system in the SHN region, and $^{292}120_{172}$ might be another candidate with less stability.

3.2.2 Model deviation

Nevertheless, from Figs. 3.1 and 3.2 one can find distinct deviations among the models in predicting the magic numbers. $Z = 120$ can be considered as a reliable prediction of proton magic number and $Z = 138$ could be another candidate with more model dependence. The neutron shells $N = 172$, 184, 228 and 258 are common to several models. Other shells, e.g., $N = 198$, appear essentially model dependent. Among the present results, one may notice that RHB calculations (PKDD and DD-ME2) predict more shell closures than RHFB, and PKO2-RHFB predicts fewest candidates. To interpret such distinct deviations, Table 3.1 shows the bulk properties of symmetric nuclear matter determined by the present sets of Lagrangians. In general the occurrence of superheavy magic shells is closely related with both the scalar mass M_S^* and effective mass M_{NR}^* [40], which essentially determine the strength of SO couplings and level densities, respectively. Among the present models, the effective Lagrangian PKO2 predicts the largest values of both masses, leading to relatively weak SO couplings and high level density on the average. As a result there remains little space in the spectra for the occurrence of magic shells. On the other hand, the RHB models (PKDD and DD-ME2) predict more magic shells due to the relatively small masses. In fact, as seen from Figs. 3.1 and 3.2, PKO2 also presents weaker shell effects than the others. For PKA1 the situation is different. Although it has a larger effective mass M_{NR}^* than PKDD or DD-ME2, PKA1 gives a smaller scalar mass M_S^* and shows stronger shell effects than the others. These may partially explain why PKA1 does not suffer from the common drawback of the CDF calculations — the so-called artificial shell closures induced by low M_S^* and M_{NR}^* [100] — and why it leads to more degenerate PS partners [48, 101, 102].

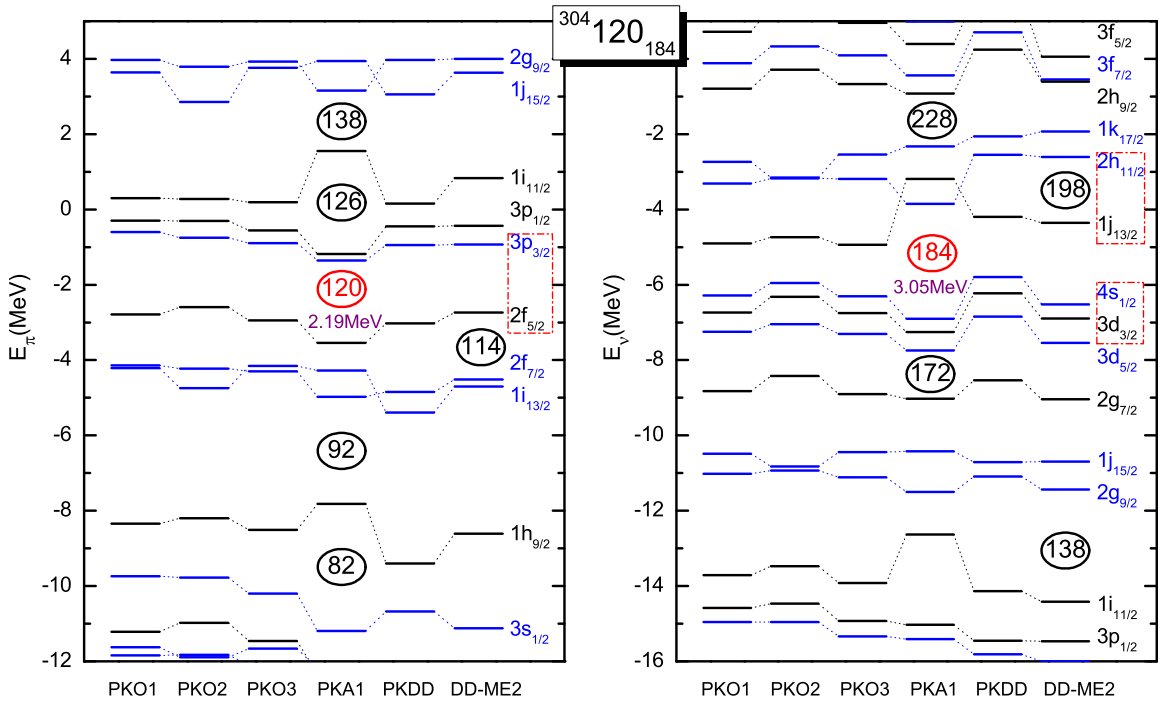

Figure 3.3: Proton (left panel) and neutron (right panel) canonical s.p. spectra of superheavy nuclide $^{304}120$. The results are extracted from the RHFB calculations with PKOi series and PKA1, and compared to the RHB ones with PKDD and DD-ME2. In all cases the pairing force is derived from the finite range Gogny force D1S with the strength factor $f = 0.9$. See the text for details.

3.3 Single-particle spectra of doubly magic nuclei

The presence of the island of stability of SHN is due to large gaps in the s.p. spectra which prevent the nuclear fission. As mentioned before, there is no consensus on the location of the superheavy magic number, and it is important to understand the sources of the differences and uncertainties in the prediction of the shell structure of SHN from a microscopic point of view. We thus compare the s.p. spectra of two doubly magic SHN obtained with different effective Lagrangians.

3.3.1 Shell structure of $^{304}120$

We first take the doubly magic SHN $^{304}120_{184}$ as an example. Fig. 3.3 shows the proton (left panel) and neutron (right panel) canonical s.p. spectra provided by selected models. It is found that PKA1 provides the most evident magicity at $Z = 120$ and $N = 184$, respectively, although these shell closures are much weaker than in ordinary nuclei. For the neutron shell $N = 184$, it is essentially determined by the degeneracy of two PS partners $\{2h_{11/2}, 1j_{13/2}\}$ and $\{4s_{1/2}, 3d_{3/2}\}$, respectively above and below the shell. For the latter, the PS partners are predicted to be almost degenerate by all the models considered, while for the former, the PS partners have high angular momentum and some differences among models are observed: PKA1 predicts a weak PS splitting, at variance with the predictions of the other Lagrangians.

It is interesting to discuss the structure of the s.p. levels for the proton shell closure $Z = 120$. As shown in the left panel of Fig. 3.3 the proton shell closure coincides with a large PS splitting, $\{3p_{3/2}, 2f_{5/2}\}$, whereas the SO doublet $\{3p_{1/2}, 3p_{3/2}\}$ above the shell is almost degenerate. The shell gap at $Z = 120$ can therefore be interpreted as a manifestation of a large PS splitting and a weak SO splitting. Below the shell $Z = 120$, the protons filling in the high-j states will be driven towards the surface of the nucleus due to the strong centrifugal potential and large repulsive Coulomb field in SHN. Both effects lead to an interior depression of the proton distributions and consequently

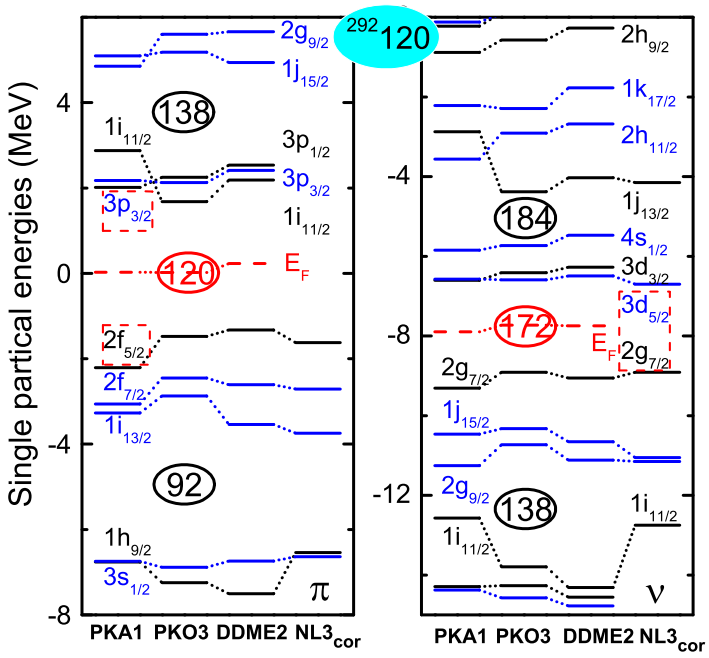

Figure 3.4: Proton (left panel) and neutron (right panel) canonical single-particle spectra of $^{292}120$. The results were calculated by RHFB with PKA1 and PKO3, as compared to those by RHB with DD-ME2. The column NL3$_{\rm cor}$ shows the spectra obtained with NL3 but modified by some empirical shifts, see Ref. [105]. for more details.

the interior region of the mean potential is not flat any more [87]. As a result the SO splitting is reduced, particularly for the low-l states $3p$ and $2f$ which have more overlap with the interior depression. Consequently the splitting between neighboring PS partners (i.e., $3p_{3/2}$ and $2f_{5/2}$) is somewhat enlarged [103]. In Ref. [104] it is also pointed out that the pronounced central depressions in the densities lead to the spherical shell gaps at $Z = 120$ and $N = 172$ as a direct consequence of a large PS splitting, whereas a flatter density profile favors the shell occurrence at $N = 184$ and $Z = 126$.

3.3.2 Shell structure of $^{292}120$

The proton shell closure at $Z = 120$ coupled to at least another subshell closure at $N = 172$ which shows the character of doubly magic nucleus. One may see that in Figs. 3.1 and 3.2 the $Z = 120$ and $N = 172$ shell gaps are especially pronounced in the $^{292}120$ nucleus. It is therefore worth to take a detailed look at the s.p. spectra of $^{292}120$ which are shown in Fig. 3.4, though it is very close to be unbound.

The left panel shows the proton levels, and the right one shows the neutron levels. As already discussed, the occurrence of the shell closure at $Z = 120$ depends on the amplitude of the SO splitting of the $3p$ states above the Fermi level and the $2f$ levels below it. It appears only when the level density at the Fermi energy is small and the SO splitting is weak. A strong $Z = 120$ shell appears for all forces under investigation. There is no gap in the s.p. spectrum large enough to interpret $Z = 114$ as a subshell closure due to SO splitting.

Similar to the $Z = 120$ isotopes, the $N = 172$ is the consequence of central depression in the density distribution. We shall discuss it later. The $N = 172$ shell can be understood as a large energy splitting between the PS partner states $\{2g_{7/2}, 3d_{5/2}\}$, and it is general smaller than the $Z = 120$ shell gap. It has to be noted that for almost all forces this nucleus has a positive Fermi energy, therefore the possibility that these nuclei exist is very small. This is somewhat surprising, since two-proton

separation energies S_{2p} is positive. Therefore it appears that there are cases in the SHN region for which the definition of the two-particle separation energy $S_{2p(n)}$ does not correspond to the physical interpretation of the chemical potential.

Up to now, there have been no direct data of the s.p. energies of SHN, while the empirical shift is obtained by extracting available deformed s.p. levels in the $A{\sim}250$ region which emerge from spherical subshells in SHN [105, 106]. The theoretical discrepancies are fairly large for the high-j states, e.g., $\pi 1h_{9/2}$, $\nu 1i_{11/2}$, $\nu 1j_{15/2}$ and $\nu 2g_{9/2}$ spherical subshells, in the range of 0.6-1.0 MeV. As a common feature, all theses states are high-j states and related to PS symmetry (PSS). Thus, the s.p. energies of these states will be strongly affected by the tensor force, e.g., ρ-tensor couplings, which was not included in RH parametrizations. The appropriate description of empirical shifts can provide support for the predictions of properties of SHN, especially the nuclear magicity. When compared with the NL3 spectra corrected by empirical shifts (columns $\mathrm{NL3_{cor}}$ in Fig. 3.4), one can see that the PKO3 parametrization provides a better description of the proton $\pi 1h_{9/2}$ state and the neutron $\nu 1i_{11/2}$ state as compared with DD-ME2 (the s.p. spectra of the $^{292}120$ nucleus obtained with DD-ME2 are similar to the those of NL3) thus giving an improved description of nuclear matter and nuclei far from stability, but does not remove the problems. An encouraging sign is that with the inclusion of the ρ-tensor coupling, the empirical shift between $\pi 1h_{9/2}$ and $\pi 3s_{1/2}$ can be well reproduced by PKA1, and it tends to shift the relative position between $\pi 1i_{11/2}$ and $\pi 3p$ orbitals, and the formation of the $Z = 126$ shell closure does not appear. On the other hand, the empirical shift for $\nu 1i_{11/2}$ in the single-neutron spectrum is also reproduced with PKA1. In the light of the present results, the parametrization PKA1 may be considered as more reliable.

There are some systematic overestimates of the SO splittings of some high-j states, e.g., $\pi 1i$ and $\nu 1j$. For these spin-partner states, one of the partner is not occupied, and one may expect sizable corrections from particle-vibration coupling (PVC). As an important alternative for the description of correlations beyond the mean field, its effects generally tend to shift the occupied and unoccupied states to the Fermi surface. Therefore, the systematic overestimation of the SO splittings may leave some space for this effect, in particular in SHN which are very soft objects [107]. A study addressing proton rich $Z = 120$ isotopes in the RH framework [108] have confirmed this view.

The question whether $^{292}120$ has a spherical or a deformed ground state, however, is very sensitive to details of the effective interaction. The Gogny force and most Skyrme interactions [109] give similar results as an oblate minimum, whereas some other Skyrme interactions [110] and most RMF models [88] give a spherical minimum.

3.3.3 The role of Coulomb interaction

In spite of an impressive agreement with available experimental data for the medium-heavy and heavy elements, theoretical uncertainties are large when extrapolating to unknown nuclei with larger atomic numbers. With increasing A, the s.p. spectrum becomes more compressed, and the binding energy increases due to the increased range of the average potential. An interesting and novel feature of SHN is that the Coulomb interaction can no longer be treated as a small perturbation on top of the nuclear mean field, its feedback on the nuclear potential is significant. As discussed in previous theoretical work [111], the main factors that influence the single-proton shell structure of SHN are the Coulomb potential and the SO splitting. Thus, the self-consistent treatment of the Coulomb potential is a key factor.

Some of the systematic changes in the s.p. spectra are illustrated in Fig. 3.5 which display the spherical canonical s.p. energies in $^{304}120$. In order not to expand the energy scale too much, the single-proton levels in $e = 0$ cases are shifted from the $e = 1$ cases by $\Delta e = E_A(s_{1/2})$. When including the Coulomb interaction, the high-j orbits with $n = 1$ such as $1h_{9/2}$, $1i_{11/2}$, $1j_{13/2}$, etc., are considerably shifted down with respect to low-j orbits due to a weakened SO splitting at large values of

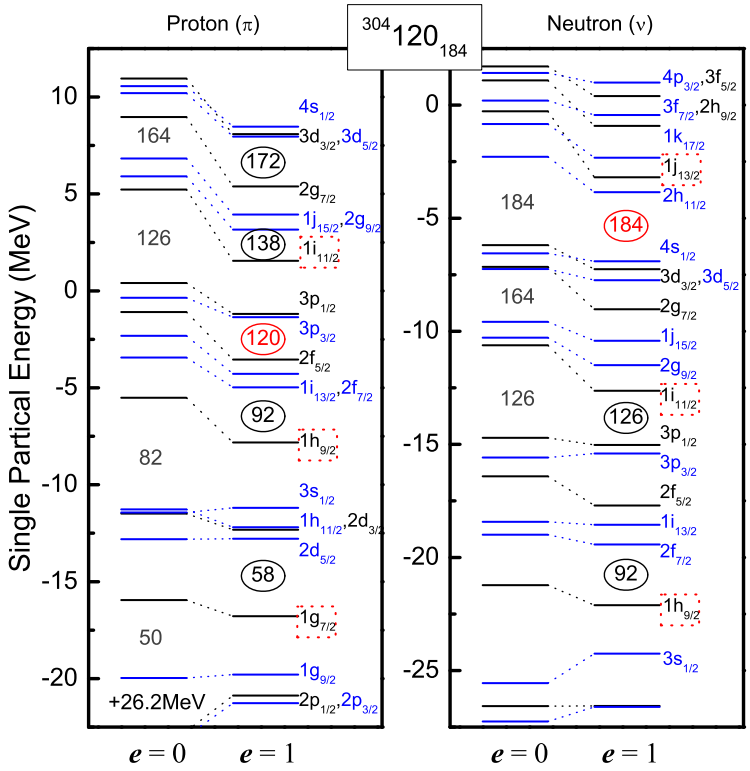

Figure 3.5: Proton and neutron canonical s.p. spectra for $^{304}120$. The results ($e = 1$) are extracted from the self-consistent calculations of RHFB with PKA1, in comparison to those without Coulomb interactions ($e = 0$). In order not to expand the energy scale too much, the s.p. levels in $e = 0$ case are shifted by the coulomb energy of $\pi 1s_{1/2}$ state in $e = 1$ case which has identified in the figure. See the text for details.

A. This is consistent with the classical [112], where the one-body coupling constant of the SO term decreases faster than expected from the usual radial $A^{-1/3}$-scaling law. The weakly bound states with small angular momentum spend a considerable amount of time outside the nucleus and thus benefit less from an increase in the size of the average potential than do the orbits with high-j. This shift, however, does not lead to any significant change in the spherical shell structure of ^{208}Pb. That is, the Coulomb term does not change the position of magic gaps 50, 82, and 126. The situation is different in the SHN $^{304}120$. Here, the Coulomb energy acting together with the energy shifts due to the increased radius and the changes in the SO splitting, induces significant changes in the shell structure. Consequently, the Coulomb potential gives rise to a lowering of the unique-parity shell ($l = n$) with respect to the normal-parity orbitals with $n' = n - 1$. In particular, the lowering of the $1g_{7/2}$, $1h_{9/2}$ and $1i_{11/2}$ orbitals gives rise to the closing of the spherical gaps at 50, 82, 126, and 164, and the appearance of the subshell closure at $Z = 120$ and $N = 172$.

Table 3.2 shows the SO splittings of the proton (π) and neutron (ν) orbits close to the Fermi surfaces in $^{184}120$ and ^{208}Pb. The full results ($e = 1$) are extracted from the self-consistent calculations of RHFB with PKA1, compared to those without Coulomb interaction ($e = 0$). In the fourth and last columns are given the ratios between these two cases. As can be seen, the SO splitting decrease is consistent in heavy nuclei due to the contributions of the Coulomb interaction, but reflect significantly difference for SHN, even proves quenching of SO effect for low-j orbit.

3.3.4 Self-consistency polarization

Next, we try to demonstrate why the SO splittings of low-j states are more sensitive to the Coulomb terms than the high-j states. we have investigated the mean-field potential which is closely related

Table 3.2: Spin-orbit splittings of the proton (π) and neutron (ν) orbits close to the Fermi surfaces in $^{304}120$ and ^{208}Pb. The results ($e = 1$) are extracted from the self-consistent calculations of RHFB with PKA1, compared to those without Coulomb interaction ($e = 0$). In the fourth and last columns are given the ratios between the two cases $e = 1$ and $e = 0$.

State	$^{304}120$			State	^{208}Pb		
	$e = 1$	$e = 0$	Ratio		$e = 1$	$e = 0$	Ratio
$\pi 1i$	5.83	7.55	0.77	$\pi 1h$	6.38	7.79	0.82
$\pi 2f$	1.43	2.34	0.61	$\pi 2d$	1.51	2.07	0.75
$\pi 3p$	0.17	0.77	0.22	$\pi 3p$	0.78	1.10	0.71
$\nu 1j$	7.23	9.22	0.78	$\nu 1i$	7.94	9.71	0.82
$\nu 2g$	2.47	3.14	0.79	$\nu 2f$	2.34	2.76	0.84
$\nu 3d$	0.49	1.06	0.46	$\nu 3p$	0.93	1.10	0.85

to the shell structure and level crossing. The RHFB proton and neutron density distributions, local potential $\Sigma_S + \Sigma_0$ (with and without Coulomb interactions), for $^{304}120$ from RHFB are given in Fig. 3.6, where Σ_S represents the scalar self-energy from the scalar coupling Hartree terms, whereas Σ_0 contains the contributions of the Hartree terms from vector couplings and the rearrangement terms Σ_R. With increasing proton numbers in SHN, strong Coulomb repulsive forces push the protons as far apart from each other as possible leading to a significant depression in the central density. Reflecting the density change, the local potentials become concave in the central part of the nucleus by about the same factor as the density. In other words, there are an inner and an outer surface, and the sign of the potential gradient is opposite for the two. Another consequence is an increase of the surface diffuseness both in the densities and in the potentials. The changes in proton density are reflected on the neutron density, because the isovector $T = 0$ interaction tries to keep them alike. As a consequence, the neutron density and potential distribution also become concave. The reduction in the central density and the resulting increase of the rms radius are the consequences of the large repulsive Coulomb energy in these nuclei. It is clear that the Coulomb interaction is at the origin of this systematic polarization effect. The lowest Coulomb energy would be reached if all the protons were located in a thin layer at the nuclear surface. For ^{208}Pb, the density distributions and potential do not change much, and they keep a flat bottom.

The large dip at the nuclear center, where the density is reduced to 2/3 of its nuclear matter value, leads to a region around $r \approx 3$ fm, where the (P)SO potential has the opposite sign, see the middle row of Fig. 3.6. Thus the total (P)SO splitting turns out to be smaller (larger) than in the case of a normal nucleus. In addition, for states with large occupation probability in this region, the amplitude of the (P)SO splitting is dramatically reduced (enhanced) or even has the opposite sign. As one can see in the bottom panel of Fig. 3.6, the proton $\pi 3p$ ($\pi 2\tilde{d}$) states and neutron $\nu 3d$ ($\nu 2\tilde{f}$) states with more nodes but small angular momentum have large overlaps with both the attractive and repulsive part of the (P)SO potential, leading to vanishing (enhanced) (P)SO effects, while the proton $\pi 1i$ ($\pi 12\tilde{h}$) states and neutron $\nu 1j$ ($\nu 1\tilde{i}$) with less nodes and large angular momenta feel only the (P)SO potential at the nuclear surface, showing the usual (P)SO splitting. Consequently, the splittings of the low-j orbitals with one or several nodes are strongly modified by the Coulomb terms, but those of the nodeless high-j orbitals are quite insensitive.

In our RHFB calculations we find a central depression in the nuclear density distribution, which generates a wine-bottle shaped local nuclear potential. This is in agreement with the various self-consistent microscopic calculations [69, 104, 109, 113]. Thus, the predictions of the magic numbers for SHN within the Mic-Mac method should be considered with caution. As compared to a flat bottom potential, the high-j orbitals are more, and the low-j ones are less bound in an attractive wine-bottle potential (see Fig. 3.5). Its magic numbers differ from those of the phenomenological flat-bottom

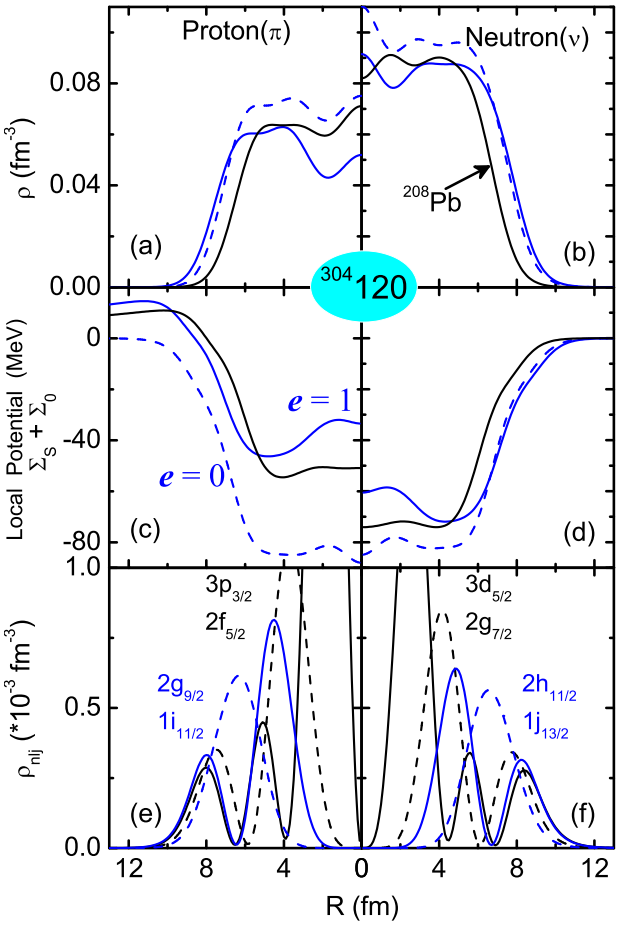

Figure 3.6: Proton (left) and neutron (right) density distributions (upper panels) and local nucleonic potentials (middle panels) in $^{304}120$ with (without) Coulomb interactions, i.e, $e = 1(e = 0)$, as well as the occupation densities (bottom panels) of the PS doublets $\pi 2\tilde{d}, \pi 1\tilde{g}$ and $\nu 2\tilde{f}, \nu 1\tilde{i}$, calculated with PKA1. The density and potentials of ^{208}Pb are shown for comparison. See the text for details.

nucleonic potentials. Furthermore, a new symmetry feature raises, which is dictated by the nodal structure of the wave functions in a leptodermic potential. This generic result differs from the common perception [114–116] that quasi-degenerate PS doublets do exist near the Fermi surface, PSS may be restored better as one increases the radial quantum number and moves closer to the continuum limit.

3.4 Evolution of superheavy shell structures

All the heaviest elements found recently are believed to be well deformed. However, spherical doubly magic SHN are still expected. When looking at shell gaps from spherical calculations we have to keep in mind that a spherical shape can only be guaranteed for doubly magic nuclei. Singly magic nuclei have a large chance to stay spherical, but can be deformed occasionally. Only a deformed calculation [117] — a very time-consuming task — can definitely decide in such cases of the appropriate ground-state shape. Nonetheless, the spherical assumption gives a reliable first orientation in the landscape of SHN.

3.4.1 Single-particle spectra of $Z = 120$ isotopes

The s.p. spectra help to provide a clue as to whether a particular particle number has a magic character or not. The shell gaps also can be modified with changing N or Z. We have therefore

examined the s.p. spectra to study the detailed shell evolution of the isotopes. The proton (left panel) and neutron (right panel) s.p. energies along the $Z = 120$ isotopic chain are shown in Fig. 3.7. First of all it is to be noted that the s.p. spectrum is relatively dense, the amplitude of shell effects changes with increasing size of the nucleus, small relative shifts in positions of s.p. levels can influence the strength of s.p. gaps and are crucial for determining the shell stability of a nucleus.

As far as the protons are concerned, it is shown that $Z = 120$ remains a rather stable proton shell structure along the whole isotopic chain. The occurrence of the shell closure at $Z = 120$ depends on the degeneracies of spin partners $\pi 3p$ and $\pi 2f$ above and below the shell, while the detailed structure of the proton levels shows some rearrangements induced by the neutron addition. Even minimal relative changes of the proton levels produce an effect of higher level density at the proton Fermi surface around $N = 184$, the neutron number where the proton shell gap is lower. The relative changes of the levels are due to modification in the amplitude of the SO splitting. This phenomenon related to the $T = 0$ NN interaction and the shape evolution of the density distribution of these nucleus, the details are discussed later. This example also illustrates that the shell closures in SHN are an extremely sensitive property. It is not surprise that this question imposes severe constraints on models and forces.

The "traditional" prediction of shell closure at $Z = 114$ is located between two SO partner states, the $\nu 2f_{5/2}$ and $\nu 2f_{7/2}$ levels. Additionally, the $\nu 1i_{13/2}$ state which has a similar energy as the $2f$ states is pushed down. Therefore, it is immediately clear that $Z = 114$ is only magic in the case of a large SO splitting.

For the neutron closure, since the beginning of the isotopic chain $N = 184$ represents a stable neutron structure within a fairly wide range. $N = 184$ is essentially related with the SO splitting of the high-j states $\nu 1j_{13,15/2}$. On the other hand, $N = 184$ can be also treated as the result of well-conserved PSS of the pseudo-spin partners $\nu 1\tilde{i} = \{\nu 1j_{13/2}, \nu 2h_{11/2}\}$ and $\nu 3\tilde{p} = \{\nu 3d_{3/2}, \nu 4s_{1/2}\}$. Besides $N = 184$, the $N = 172$ shell results from the large energy splitting between the PS partner states $\nu 2\tilde{f} = \{\nu 2g_{7/2}, \nu 3d_{5/2}\}$, and it seems to be a remarkable neutron structure at the beginning of the isotopic chain of $Z = 120$, while the positive proton Fermi energy at $N = 172$ means that it couples to the continuum. We also see a major shell gap at $N = 258$, but it is of little practical importance in synthesis of SHN due to the large number of neutrons involved.

In addition, a proton shell is also found in the calculations with PKA1 at the proton-rich side of the $Z = 126$ isotopic chain related with enhanced binding of the low-j states $\pi 3p_{1,3/2}$. However, the proton states below the $Z = 126$ gap have a slightly positive energy suggesting the nuclei to be unstable against proton emission [111], although the high Coulomb barrier would make other decay channels more probable [118,119]. A decrease in splitting between PS partners $\nu 1\tilde{h} = \{\nu 1i_{11/2}, \nu 2g_{9/2}\}$ also opens a possible shell gap at $Z = 138$ beyond $N = 210$ in the neutron-rich isotopes, which is far beyond current experimental limits. This was also reflected in the s.p. spectra across the $Z = 126$ isotopes, although the $Z = 126$ shell gap was significantly decreased in comparison to the $Z = 120$ gap, indicating a clear dependence on neutron number.

We reminded here that the presence of pronounced magic gaps at $Z = 120$ and $N = 172$ in CDF models is a direct manifestation of the PSS breaking. In non-relativistic models, these pairs are very close in energy, and this degeneracy is related to the PSS. Considering the fact that the idea of PS has relativistic roots [89, 114–116], it is surprising to see that this symmetry is so dramatically violated.

3.4.2 Density distributions of superheavy nuclei

Proton and neutron density distributions together with the neutron-skin thickness provide fundamental information on nuclear structure. For example, halo nuclei are characterized by long tails in density distributions [120–122]. The density is a direct probe of the size of an atomic nucleus and

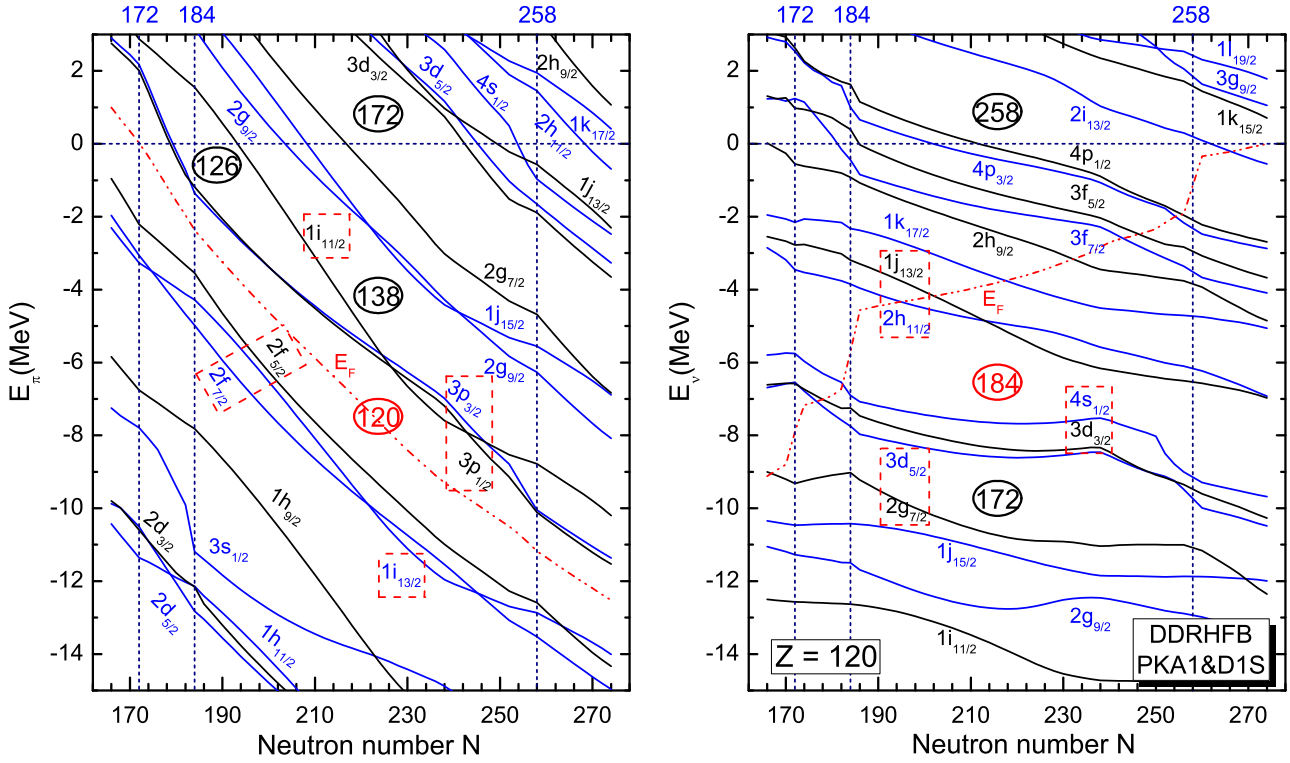

Figure 3.7: Proton (left panel) and neutron (right panel) canonical single-particle spectra of the $Z = 120$ isotopes. The results are extracted from the calculations of RHFB with PKA1, where the pairing effects are treated by Gongy force D1S with a scaling parameter $f = 0.9$. The Fermi energies E_F are presented in red dash-dotted lines. See the text for details.

plays an important role in the cross sections of nuclear reactions. Although charge densities can be measured from the elastic scattering of electrons, neutron densities are largely unknown. In the future, the neutron densities of more nuclei can be expected to be measured.

We start with ^{208}Pb, where the RHFB theory provides a good description of the experimental charge density distribution [48]. With increasing neutron and proton numbers the corresponding densities are modified in the way shown in Fig. 3.8. The calculations with PKA1 and PKO3 give similar density distributions but they differ in detail. The central depression exists generally in the spherical SHN. In the region $Z = 82 \sim 92$ the protons fill the high-j state $\pi 1h_{9/2}$, between $Z = 92 \sim 120$ they fill the high-j state $\pi 1i_{13/2}$ and the medium-j group $\pi 2f_{5,7/2}$, and between $Z = 120 \sim 138$ they fill the high-j state $\pi 1i_{11/2}$ and the low-j group $\pi 3p_{1,3/2}$. The variation of the proton density is seen most clearly in the $N = 172$ or 184 isotones. The filling of the high-j group $\pi 1h_{9/2}, \pi 1i_{13/2}$ increases the density at the surface (compare $Z = 82$ and $Z = 120$ in Fig. 3.8). The filling of medium-j group $\pi 2f_{5,7/2}$ increases the density between central and surface areas (see $Z = 120$ isotopes), This is consistent with the classical picture in which orbits with large angular momentum are located at the surface. Finally, the filling of the low-j group $\pi 3p_{1,3/2}$ increases the density in the central region of the nucleus (see $Z = 126$ isotopes). Furthermore, strong Coulomb repulsion should reduce the proton density in the interior producing a more or less deep dip as indicated in Fig. 3.8 beyond $Z = 82$.

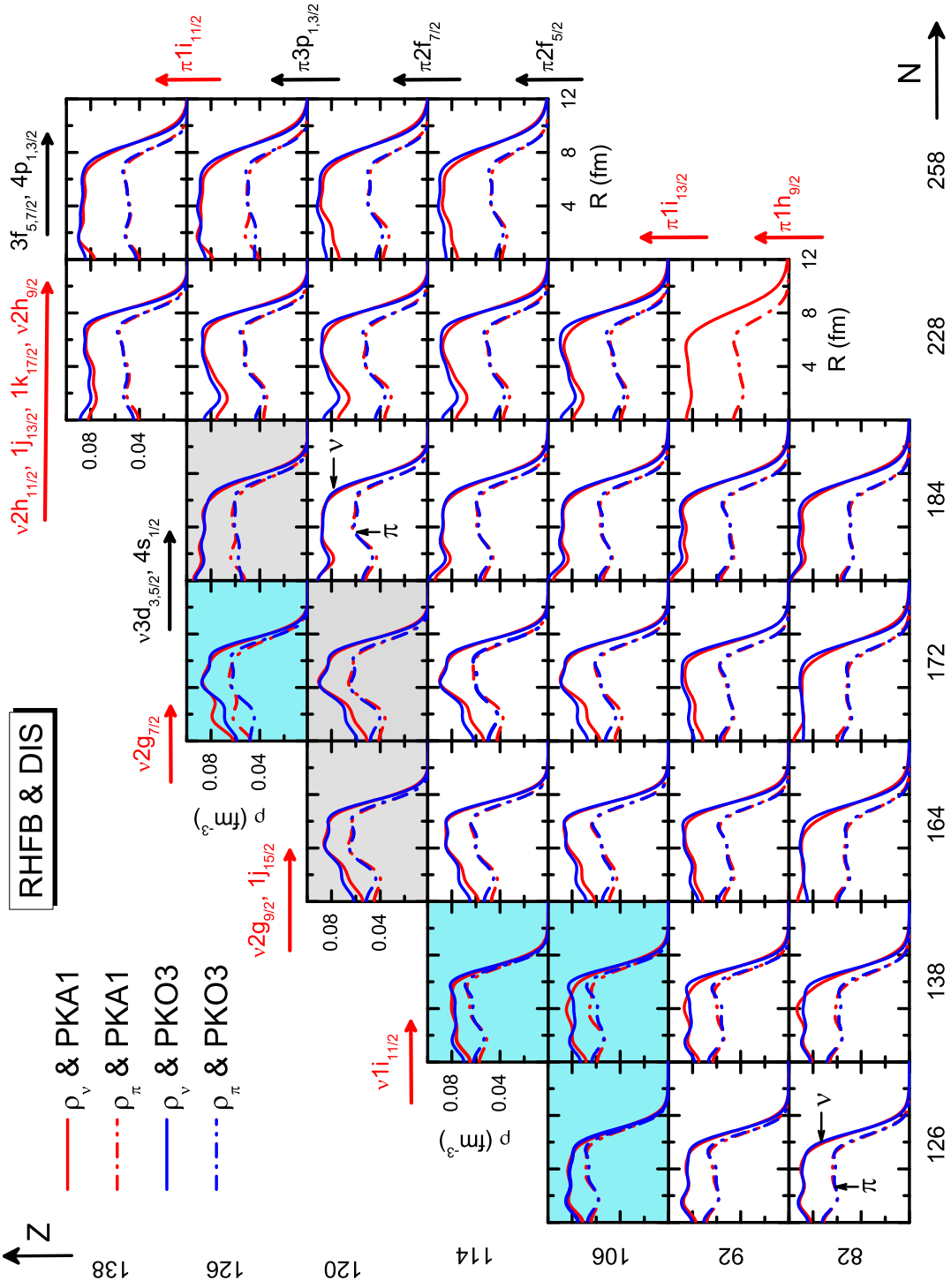

Figure 3.8: The evolution of proton and neutron densities with the changes of proton and neutron numbers. Arrows indicate the group of single-particle subshells which become occupied with the change of the nucleon number. The figure shows the results of spherical RHFB calculations with the PKA1 and PKO3 parametrizations. The blue background is used for nuclei located beyond the two proton-drip line identified by two-proton separation energies, whereas the shaded background represent the nuclei with negative proton chemical potentials but may be stable against nucleon emission due to the large Coulomb barriers. See the text for details.

The analogous polarization effects caused by the groups of low-j and high-j subshells in the neutron subsystem are illustrated in Fig. 3.8. The variation of the neutron density generated by filling these groups is seen most clearly in the $Z = 106$, 120 isotopes. Filling the high-j group $\nu 1i_{11/2}, \nu 1j_{15/2}$ and the medium-j group $\nu 2g_{7,9/2}$ increases the density near the surface. Filling the low-j group $\nu 3d_{3,5/2}, \nu 4s_{1/2}$ increases the central density, and filling the high-j group $\nu 1j_{13/2}, \nu 2h_{11/2}$ and $\nu 1k_{17/2}$ adds matter to the surface region. Analyzing the published results, the neutron levels have the same ordering for nearly all models/parametrizations. With increasing neutron richness, protons are drifted more and more towards the surface region of the nucleus, and the central depression of the density distribution is enlarged.

As seen in Fig. 3.8, the combined occupation of the high-j neutron subshells and proton subshells leads to a central depression in the nuclear density between $Z = 92 \sim 120$ and $N = 164 \sim 172$, which is especially pronounced in the $Z = 120$, $N = 172$ system. As seen from the density variations in Fig. 3.8, the proton and neutron subsystem play the same role in the creation of the central depression and the high-j proton and neutron orbits will modify the radial profile in a comparable way. However, the high-j proton orbits should be more efficient, because the enhanced Coulomb interaction pushes them to larger radii and therefore density distributions are changed significantly. As a result the SO splitting is reduced remarkably for the low-l states $3p$ which have more overlap with the interior depression, and it is reduced less for $2f$ states. Consistently the splitting between neighboring PS partners (i.e., $3p_{3/2}$ and $2f_{5/2}$) is somewhat enlarged, which corresponds to the emergence of a proton magic shell $Z = 120$. In Ref. [104] it is also pointed out that the pronounced central depressions in the densities lead to the spherical shell gaps at $Z = 120$ and $N = 172$ as a direct consequence of a large PS splitting, whereas a flatter density profile favors the shell occurrence at $N = 184$ and $Z = 126$. In fact, from $N = 172$ to 184 the valence neutrons start to fill the low-l states $\nu 4s$ and $\nu 3d$, which leads to fairly flat neutron density profiles in the interior region for $N = 184$ isotones. Due to the enhanced proton-neutron correlations by the PKA1 functional [102], the proton density profile for the nuclide $^{304}120_{184}$ is affected consistently and becomes less depressed in the interior region. As a result, the shell gap $Z = 120$ is somewhat reduced at $N = 184$ as well as $N = 258$ due to a similar mechanism.

With increasing mass number, the neutron excess becomes larger in general and it is natural to think that SHN provide the largest neutron excesses. This phenomenon is especially significant in the neutron-rich side.

In addition, as we found that beyond $Z = 82$, results from the PKA1, the proton density in the interior is smaller than in the other models and has a longer tail. Therefore, it has a larger charge radius and lower binding energies per nucleon as it can be seen in Table 3.3. This phenomenon is due to the isovector coupling channel and its dependency on density. The isovector coupling channel is represented by the isovector-vector meson ρ whose density dependence enlarged due to the introduction of tensor correlations. The coupling strength increases with decreasing density, leading to a stronger proton-neutron coupling in the surface and central regions of the nucleus than in its internal region. Furthermore, the results are concordant with previous work showing that the magnitude of the central depression increases with the decrease of the compression modulus [104].

3.4.3 Isospin dependence and structure evolution

As a consequence of including the tensor component, an improved isospin dependence of the shell structure is found [49, 123, 124]. The strong A-dependence of the shell structure in this region is a consequence of the high level density in the SHN. As shown in Fig. 3.7, the shell structure evolution $\pi 2\tilde{d}$ in $Z = 120$indeed shows an isospin dependence consistent with the neutron shell evolution in $N = 172, 184$.

To clarify this consistency between shell evolution and PSS conservation we present in Fig. 3.9 the two-body interaction matrix elements $V_{\pi\nu}$ calculated with PKA1 and responsible for the coupling

Table 3.3: The binding energies per nucleon (in MeV) and charge radii (in fm) for the various RHFB and RHB models.

Force	$^{292}120$		$^{304}120$		$^{378}120$	
	ρ_c	E/A	ρ_c	E/A	ρ_c	E/A
PKA1	6.293	7.011	6.327	7.008	6.792	6.311
PKO2	6.266	7.049	6.314	7.023	6.713	6.299
PKO3	6.261	7.044	6.305	7.028	6.709	6.329
PKDD	6.256	7.058	6.288	7.021	6.681	6.229
DD-ME2	6.275	7.041	6.305	7.027	6.683	6.292

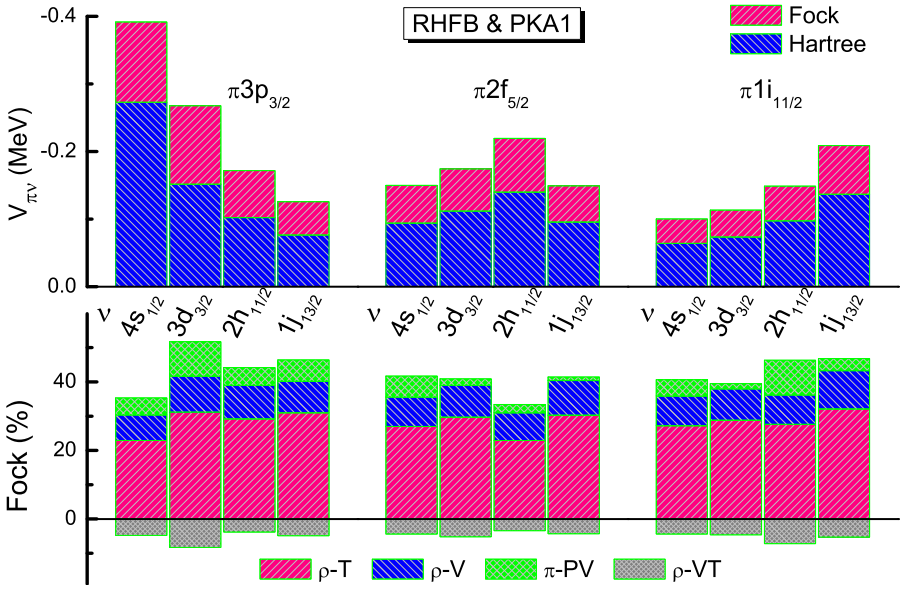

Figure 3.9: Upper panel: Two-body interaction matrix elements $V_{\pi\upsilon}$ (MeV) between proton (π) and neutron (ν) valence orbits in $^{304}120$. Lower panel: The detailed Fock contributions, i.e., the ratio of the ρ- and π-meson contributions. See the text for details.

between the proton and the neutron valence orbits of $^{304}120$. It is shown that there exist distinct nodal effects concerning the shell structure evolutions.

Starting from the proton rich side at $N = 172$, the valence neutron orbits with nodes are gradually occupied, i.e., $\nu 4s_{1/2}$ and $\nu 3d$. Due to the nodal effects, such states have stronger coupling with the proton nodal states $\pi 3p$ than with $\pi 2f$ and $\pi 1i_{13/2}$. As a direct result, the proton structure $Z = 120$ is quenched and another proton structure $Z = 126$ emerges. While beyond $N = 184$, the neutrons start to occupy the high-j states $\nu 1j_{12/2}$ and $\nu 2h_{11/2}$ with less nodes, which have stronger couplings with $\pi 2f$ and $\pi 1i$ than with nodal states $\pi 3p$. Thus, the proton shell structure $Z = 120$ is enhanced, $Z = 126$ is strongly compressed and the detailed structure of the proton levels shows some rearrangements. When approaching the neutron-rich side, the neutron nodal states are continuously occupied, mainly the $\nu 3f$ and $\nu 4p$ states, which induce the proton shell structure $Z = 120$ is slightly quenched.

For the evolution of the neutron shell structure in $N = 184$, one can also find distinct nodal effects. Beyond $N = 184$, the valence neutrons occupy the states with less nodes in a fairly wide range. These states have stronger couplings with the neutron orbits with less nodes above $N = 184$ than with nodal states below $N = 184$, which leads to the quenching of $N = 184$ from $N = 210$ to $N = 238$. When the neutron nodal states $\nu 3f$ and $\nu 4p$ are gradually occupied, the neutron structure $N = 184$ is enhanced also due to the nodal effects.

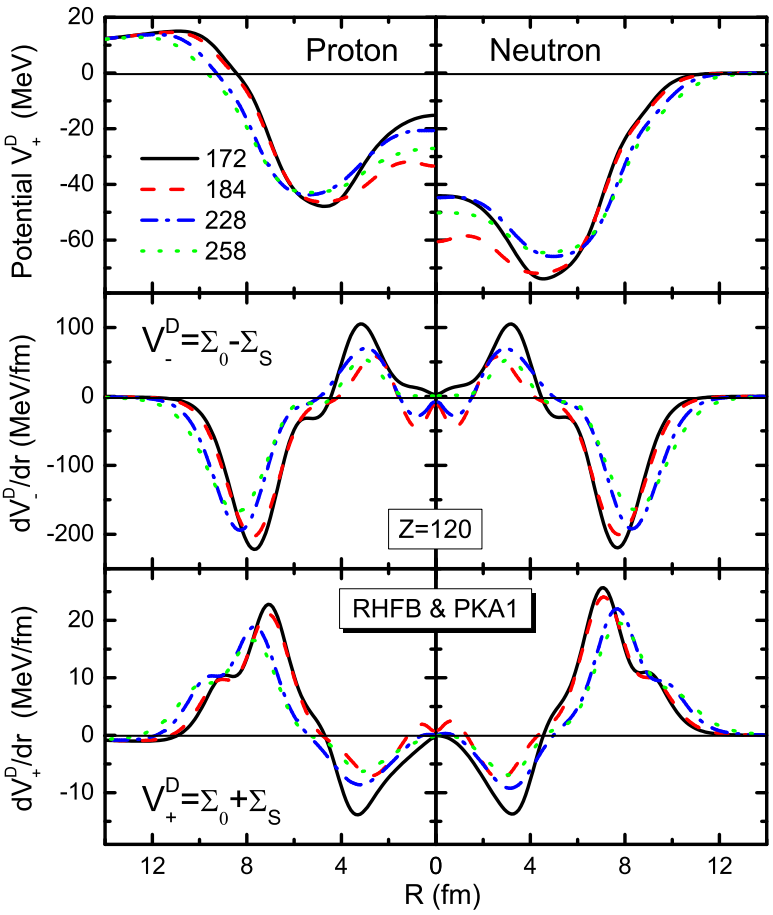

Figure 3.10: Local nucleonic potentials $\Sigma_S(r) + \Sigma_0(r)$ (upper panel), the Hartree contributions of spin-orbit potential (middle panel) and pseudospin-orbit potential (lower panel) of protons (right) and neutrons (left) in the nuclei $120_{172,184,228,258}$, calculated with PKA1. See the text for details.

From Fig. 3.9 it also seen that Fock terms present significant contributions to the $T = 0$ NN interaction, more than 30% of the total in most cases. In the $T = 0$ channel, Fock terms come from isovector mesons, mainly (about two-thirds) from the tensor ρ, which cannot be efficiently taken into account in the Hartree approach. One can see that the nodal structure shows substantial effects in determining the NN interaction strength and it plays an essential role in the structure evolution. On the other hand, The PSS on $\nu 1\tilde{i}$ is still well preserved as shown in Fig. 3.7, especially the presence of pronounced magic 198 gap predicted by the RMF or PKO series calculations is a direct manifestation of the PSS breaking. In fact we also found similar nodal effects from the calculations with PKO series and RMF models, while the questionable large gap between $\nu 1j_{13/2}$ and $\nu 2h_{11/2}$ breaks the consistency because the valence protons can only occupy the $\nu 1j_{13/2}$ orbit. In contrast, the PSS is properly conserved by PKA1 such that the PS partner states are simultaneously occupied and the occupations are changed consistently. From Fig. 3.9 one can see that the tensor ρ plays a significant role in conserving PSS.

To have a further understanding, we investigate the mean-field potential which is closely related to the shell structure evolution. Figure 3.10 shows the local nucleonic potentials $\Sigma_S(r) + \Sigma_0(r)$ and the Hartree contributions of (P)SO potential for protons and neutrons in nuclei $120_{172,184,228,258}$. See Fig. 3.8, for the neutrons at spherical case, the high-j orbits of $1i_{11/2}$, $2g_{7,9/2}$, and $1j_{15/2}$ appear in the region of $N = 126 \sim 172$, and $1j_{13/2}$, $2h_{9,11/2}$, and $1k_{17/2}$ appear in the region of $N = 186 \sim 238$. The low-j orbits of $4s_{1/2}$ and $3d_{3/2,5/2}$ are at $N = 174 \sim 184$, and $3f_{5,7/2}$ and $4p_{1,3/2}$ are at $N = 238 \sim 258$. Filling the low-j group increases the central density, and occupying the high-j group increases the

density near the surface region. Reflect the density change, the shapes of local potential and the (P)SO potential changes consistently. So there is a mutual changes of the $Z = 120$ and $N = 172$ gaps.

3.4.4 Pseudospin symmetry and ρ-tensor correlations

As a matter of fact, the $Z = 120$ and $N = 172$ magic gaps predicted in our RHFB calculations as well as various RMF models appear as a direct consequence of PSS breaking of low-j partners which have a more central localization. However, according to this point of view, the occurrence of a neutron shell closure $N = 198$ from the large gap between the PS partners $\nu 1\tilde{i} = \{\nu 1j_{13/2}, \nu 2h_{11/2}\}$ in various RH models [88, 125] becomes very questionable.

As with the discussion of the s.p. spectra of $^{304}120$ in the previous section, one can find significant improvements with the inclusion of ρ-tensor correlations in RHFB calculations.
From the Dirac equation, one can express the s.p. energy of state α as

$$E_\alpha = E_{k,\alpha} + E_{\sigma,\alpha} + E_{\omega,\alpha} + E_{\rho,\alpha} + E_{\pi,\alpha} + E_{A,\alpha} + E_{R,\alpha} \tag{3.3}$$

where $E_{k,\alpha}$ denotes the kinetic contribution, $E_{i,\alpha}(i = \sigma, \omega, \rho, \pi, A)$ represent the contributions from the mesons and photon coupling channels including the direct and exchange parts, and $E_{R,\alpha}$ accounts for the rearrangement terms. From Eq. (3.3), one can also obtain the contributions to the pseudospin-orbit (PSO) splittings from different channels.

To understand the improvement due to the ρ-tensor correlations, we have studied the contributions from different terms in Eq. (3.3) to the PSO splittings. In Table 3.4.4 are shown the results calculated by RHFB with PKA1 (upper panels), PKO1 (middle panels) and RHB with DD-ME2 (lower panels), respectively, for $^{304}120$ particle orbits. One can see that PKA1 conserves PSS better than PKO1 and RMF for the states near the Fermi levels, especially for the high-j doublets $\pi 1\tilde{g}$ and $\nu 1\tilde{i}$. This result is consistent with the rule of thumb in Skyrme case: the tensor terms mainly affect nodeless intruder states [126].

For the PSO splittings, PKA1 and PKO1 provide similar contributions in magnitude to the kinetic part (ΔE_k), the rearrangement term (ΔE_R), and the π-coupling (ΔE_π) except for a few cases. For the contributions from σ, ω mesons ($\Delta E_{\sigma+\omega}$) and ρ-meson (ΔE_ρ) couplings, there exist a distinct difference between PKA1 and PKO1, especially for the states near the Fermi surfaces. From Table 3.4.4, one can see that the ρ-meson couplings in PKA1 give larger contributions to the PSO splittings than those in PKO1 and RMF, and the ρ-tensor couplings increase the splittings. For the states near the Fermi surface, PKA1 provides negative values of ($\Delta E_{\sigma+\omega}$), which cancel largely with (ΔE_k) and (ΔE_ρ). In the PKO1 results, the ($\Delta E_{\sigma+\omega}$) is always positive, and only the rearrangement term (ΔE_R) partially cancels the contributions from the other channels.

As a relativistic symmetry, the conservation of the PSS is mainly determined by the balance of the nuclear attractions and repulsions, which is also well demonstrated in this table. Compared to the PKO1 results, this balance is much changed by PKA1 because of the extra binding induced by the ρ-tensor couplings, which indicates the physical reason for the improvement of the nuclear shell structure.

Comparing PKA1, PKO1 to DD-ME2, one finds that the Fock terms of the Coulomb interaction increase the proton shell effects significantly. On the other hand, because of the serious violation of PSS on $\nu 1\tilde{i}$ by PKO1 and DD-ME2, particularly beyond $N = 200$, the valence protons occupy only the $\nu 1j_{13/2}$ state and this greatly increases the neutron $N = 198$ shell and reduces $N = 184$ shell effects. In contrast, the PSS is properly conserved by PKA1 such that the PS doublets are simultaneously occupied and the occupations are changed consistently.

Table 3.4: Contributions (in MeV) from different terms in Eq. (3.3) to the pseudospin orbital splittings ΔE for proton (π) neutron (ν) orbits in $^{304}120$, calculated by RHFB with PKA1 (upper panel) and PKO1 (middle panel)and RHB with DDME2 (lower panel). The average binding energy $\bar{E}$ for the pseudospin partner states j_1 and j_2 is $[E_1(2j_1+1)+E_2(2j_2+1)]/(2j_1+2j_2+2)$.

Force	State	$\bar{E}$	ΔE	$\Delta E_{\sigma+\omega}$	ΔE_R	ΔE_k	ΔE_ρ	ΔE_π	ΔE_A	ΔE_A^D	ΔE_A^E
PKA1	$\pi 1\tilde{g}$	−6.551	2.843	−0.301	−0.831	2.608	0.780	0.498	0.089	0.045	0.044
	$\pi 2\tilde{d}$	−2.670	2.188	−0.130	−0.280	1.294	0.246	0.284	0.774	0.517	0.258
	$\pi 1\tilde{h}$	2.283	1.605	−3.173	−1.241	3.559	1.031	0.803	0.622	0.589	0.032
	$\nu 2\tilde{f}$	−8.473	1.279	−0.145	−0.732	0.416	1.168	0.486	–	–	–
	$\nu 3\tilde{p}$	−7.133	0.351	−0.232	−0.157	0.400	0.141	0.168	–	–	–
	$\nu 1\tilde{i}$	−3.513	−0.663	−3.159	−1.784	1.622	1.641	0.911	–	–	–
PKO1	$\pi 1\tilde{g}$	−6.475	4.201	1.328	−1.060	2.449	0.559	0.378	0.546	0.500	0.046
	$\pi 2\tilde{d}$	−1.958	2.186	0.301	−0.368	1.157	0.105	0.203	0.788	0.541	0.247
	$\pi 1\tilde{h}$	1.969	3.673	−0.984	−0.765	3.596	0.318	0.590	0.916	0.874	0.043
	$\nu 2\tilde{f}$	−8.147	1.575	1.337	−0.776	0.172	0.417	0.426	–	–	–
	$\nu 3\tilde{p}$	−6.583	0.376	0.298	−0.089	−0.015	0.025	0.157	–	–	–
	$\nu 1\tilde{i}$	−4.169	1.595	0.124	−1.581	1.774	0.583	0.702	–	–	–
DD-ME2	$\pi 1\tilde{g}$	−6.789	4.097	2.284	−0.767	2.415	−0.139	–	0.303	0.303	–
	$\pi 2\tilde{d}$	−2.016	1.806	1.171	−0.329	1.070	−0.492	–	0.386	0.386	–
	$\pi 1\tilde{h}$	2.271	3.164	0.050	−0.794	3.286	−0.091	–	0.709	0.709	–
	$\nu 2\tilde{f}$	−8.394	1.496	2.576	−0.674	−0.281	−0.125	–	–	–	–
	$\nu 3\tilde{p}$	−6.767	0.377	0.892	−0.172	−0.210	−0.134	–	–	–	–
	$\nu 1\tilde{i}$	−3.790	1.216	2.614	−1.373	0.417	−0.443	–	–	–	–

3.5 Summary and conclusions

In this chapter, the occurrence of spherical shell closures for SHN and the physics therein have been investigated using the RHFB theory with density-dependent meson-nucleon couplings, in comparison with the predictions of some RHB models. The shell effects are quantified in terms of two-nucleon gaps $\delta_{2n(p)}$ and pairing gaps $\delta_{n(p)}$. The results indicate that the nuclide $^{304}120_{184}$ could be the next spherically doubly magic nuclide beyond ^{208}Pb. It is also found that the shell effects in SHN are sensitive to the values of both scalar mass and effective mass, which essentially determine the spin-orbit effects and level density, respectively. Additionally the analysis of the shell evolution as well as of the density profile indicate that the emergence or disappearance of shell closure is tied up with the evolution of the central and spin-orbit mean fields, a feature that covariant mean field models may describe in a more unified way as compared to non-relativistic EDF approaches. A further advantage of the RHFB framework is that exchange (Fock) terms are explicitly treated rather than approximately included by readjusted direct (Hartree) contributions as it is done in RHB (this is particularly true for the Coulomb exchange energy which is basically absent in RHB).

Strong Coulomb repulsion and large isospin variations in SHN are found to modify the nuclear mean-field picture and also the long-range and short-range correlations. The (P)SO interaction reduces (reinforces) as the nuclear interior polarizes when going towards superheavy region. The role of isovector interactions is enhanced with proton-neutron asymmetry, in particular the tensor correlations. The combination of these effects mean that new shell gaps and magic numbers appear as unusual features. The emergence of magic shells is essentially related with the restoration of relativistic symmetry. The proton magic shell $Z = 120$ and $N = 172$ are tied to the quenching of spin-orbit effects with the increasing of proton number. The Coulomb potential plays an important role in forming a central depression in the nuclear density and potential distribution, which leads to the quenching of SO effects and strongly violated PSS, particularly for low-j doublets. In fact, the emergence of new shell closures $Z/N = 16$ and $N = 32$ [127, 128] can be also related with the violation of PSS in light exotic nuclei. In contrast, the neutron shell gap $N = 184$ remains robust due to the degeneracy of PS doublets above and below the shell.

Concerning the shell structure evolutions, there exist distinct nodal effects, which induce systematical quenching and enhancement of the magic shell structure $Z = 120$ and $N = 184$. In contrast, significant improvement in the single-particle spectra is also found due to the inclusion of ρ-tensor couplings, the PS degeneracy holds in most cases for high-j doublets. Our RHFB results qualitatively agree with the current experimental status [129], which suggests that a shell closure is more probable around $Z = 120 - 126$, particularly in neutron-deficient nuclei.

In the future, experimental investigation through fission time measurements of compound nuclei [130] are expected to bring new results. Indeed, if our prediction locating the new superheavy doubly magic nucleus at $^{304}120$ is correct, then the present experimental investigation (located at $Z = 118$) is not too far. From a view point, our study being based on spherical symmetry shall be extended to account deformation effects. Present limitations of deformed RHF approach makes calculation beyond $Z = 20$ very different. It is therefore a challenging issue to calculated deformed SHN.

Chapter 4

Magicity of neutron rich isotopes

I am frequently astonished that it so often results in correct predictions of experimental results.

Murray Gell-Mann, 1929-

4.1 Introduction

In recent years the role of the tensor interaction in nuclei has gained renewed interest [131]. Essentially induced by the Lorentz pseudo-vector (PV) pion and the Lorentz tensor (T) rho meson-nucleon couplings, the tensor interaction is known to play an important role in the binding of light nuclei, such as the deuteron. At this point, we must make clear the terminology employed throughout this paper. The name "tensor interaction" will be used for the part of the non-relativistic nucleon-nucleon NN interaction which behaves as an irreducible second-rank tensor [132]. Such a "tensor interaction" can originate from a non-relativistic reduction of PV or T meson-nucleon couplings. Note, however, that the PV and T couplings contribute only to the exchange part of the nucleon-nucleon interaction, not to its direct part. Therefore, relativistic approaches such as the relativistic mean field (RMF) where Fock terms are dropped will not lead to any tensor interaction. It was however difficult to assign a clear effect of the tensor interaction in medium-heavy and heavy nuclei. As a consequence, many-body approaches going from the non-relativistic Skyrme and Gogny effective interactions to the RMF approach, see e.g. Ref. [7] and references therein, have simply ignored the presence of the tensor interaction, without loss of precision with respect to global properties of nuclei, e.g., masses or charge radii. The situation has recently changed when it was shown that the nuclear tensor force could play a very important role in the isotopic evolution of some single-particle (s.p.) states [34, 49, 124, 126, 133–140], causing the disappearance of the usual magic numbers and the emergence of new ones in some extreme cases of very neutron-rich nuclei [141–144]. It is now clear that the modelling of exotic nuclei requires the development of more complete nuclear effective interactions that include the nuclear tensor force.

Employing the non-relativistic approaches based on Skyrme interactions, the improvement of the isotopic evolution of s.p. energies by introducing the tensor force was found to be systematically correlated to a degradation of the binding energy [126]. The tensor interaction considered in Refs. [126, 136, 137, 143, 144] is a non-relativistic contact interaction. The effects of a finite-range form of the tensor interaction were also explored in the case of the finite-range Gogny force [124, 134]. It was shown that the finite-range tensor force has a large impact on s.p. energies along isotopic and isotonic chains but its effect on binding energies was not discussed. Finally, we must mention the finite-range M3Y interactions which contain the tensor interaction and are satisfactory for binding energies and s.p. spectra [34, 142]. In this approach the in-medium tensor interaction is not much modified and resembles to a large extent that of the original one in the bare NN interaction. Shell model calculations with $V_{low\,k}$ low-momentum interactions have also been performed, including systematic comparisons

with and without tensor interactions, illustrating the important role of the tensor terms [139].

In all the previously mentioned studies, the tensor interaction at work was mostly explored in a non-relativistic framework. In a relativistic framework, it however contributes only to the Fock diagrams, where not only the π-N and Lorentz tensor ρ-N couplings play an important role but the other meson-nucleon couplings also carry considerable tensor force components [145]. Since in the RMF approaches [8, 37] the Fock diagrams are simply dropped, the relativistic Hartree-Fock (RHF) approach [38, 40, 138] becomes the only relativistic model which generates a tensor force. In this work, we compare the predictions based on relativistic Hartree-Fock-Bogoliubov (RHFB) [90] and relativistic Hartree-Bogoliubov (RHB) [8, 37] approaches, which can both reproduce satisfactorily global properties such as binding energies and radii of finite nuclei. In the RHFB approach, the π-pseudo-vector (π-PV) and ρ-tensor (ρ-T) couplings can be taken into account while they do not contribute in the RHB models. Considering the Foldy-Wouthuysen (FW) transformation [146], the relation between the Lorentz PV and T and, the rank-2 tensor forces could be analyzed, as well as their respective contributions to s.p. energies and shell evolutions. We investigate the shell evolution of Ca isotopes, $N = 16$, 32 and 34 isotones and analyse the appearance of a large shell gap in ^{24}O and ^{52,54}Ca making $N = 16$, 32 and 34 candidates for being new magic numbers in neutron-rich nuclei.

4.2 Lorentz pseudo-vector and tensor interactions

Within the relativistic framework, PV π-N coupling and T ρ-N coupling can be introduced into the effective Lagrangian. The corresponding interaction vertices are:

$$\Gamma_{\pi}^{PV}(1,2) \equiv -\frac{1}{m_{\pi}^2}\left(f_{\pi}\vec{\tau}\gamma_5\gamma_{\mu}\partial^{\mu}\right)_1 \cdot \left(f_{\pi}\vec{\tau}\gamma_5\gamma_{\nu}\partial^{\nu}\right)_2, \tag{4.1}$$

$$\Gamma_{\rho}^{T}(1,2) \equiv +\frac{1}{4M^2}\left(f_{\rho}\vec{\tau}\sigma_{\lambda\mu}\partial^{\mu}\right)_1 \cdot \left(f_{\rho}\vec{\tau}\sigma^{\lambda\nu}\partial_{\nu}\right)_2, \tag{4.2}$$

where m_{π} and M denote the mass of the π meson and of the nucleon, respectively, f_{π} and f_{ρ} are the coupling constants of the π-PV and ρ-T meson-nucleon vertices. The other coupling channels, namely the isoscalar scalar σ (σ-S) and vector ω (ω-V), the isovector vector ρ (ρ-V), and the vector photon A (A-V) couplings are identical to those presented in Refs. [38, 48].

In the non-relativistic limit, using the FW transformation [146], the finite-range part of the one-π exchange potential V_{π} can be divided into two terms: the tensor and the central potentials, V_{π}^{T} and V_{π}^{C},

$$V_{\pi}^{T}(\boldsymbol{r}) = \frac{1}{3}f_{\pi}^2\,\boldsymbol{\tau}_1\cdot\boldsymbol{\tau}_2\,S_{12}\left(1+\frac{3}{m_{\pi}r}+\frac{3}{(m_{\pi}r)^2}\right)\frac{e^{-m_{\pi}r}}{r}, \tag{4.3}$$

$$V_{\pi}^{C}(\boldsymbol{r}) = \frac{1}{3}f_{\pi}^2\,\boldsymbol{\tau}_1\cdot\boldsymbol{\tau}_2\;\boldsymbol{\sigma}_1\cdot\boldsymbol{\sigma}_2\,\frac{e^{-m_{\pi}r}}{r}, \tag{4.4}$$

where S_{12} is a standard rank-2 tensor operator,

$$S_{12}(\boldsymbol{r}) \equiv 3(\boldsymbol{\sigma}_1\cdot\boldsymbol{e}_r)(\boldsymbol{\sigma}_2\cdot\boldsymbol{e}_r) - \boldsymbol{\sigma}_1\cdot\boldsymbol{\sigma}_2. \tag{4.5}$$

The FW transformation [146] could similarly be applied to the V_{ρ} potential originating from the T ρ-N coupling. One must notice that, in the non-relativistic formalism, the central and rank-2 tensor forces generally appear independently from each other, while here they originate from the same interaction vertices. The central term $V_{\pi(\rho)}^{C}$ plays an important role in determining the shell structure, which is different but as important as the rank-2 tensor term $V_{\pi(\rho)}^{T}$ [34, 147].

In our relativistic approaches the Lorentz PV and T couplings, when present, cannot be switched off without degrading the accuracy of the model. We instead compare various Lagrangians having,

or not, the Lorentz PV and T terms as explained below. For the RHFB approach, we consider the effective interactions PKA1 [48] and PKO3 [49]. The former is the most complete relativistic model to date, taking both π-PV and ρ-T into account, while the latter does not contain the ρ-T coupling. All meson-nucleon couplings are density-dependent and their values have been adjusted in previous studies. Two density-dependent RHB models are also used throughout this work: DD-ME2 [93] and DD-MEδ [148]. The DD-MEδ differs from DD-ME2 by the inclusion of the δ-meson, which leads to different proton (π) and neutron (ν) Dirac masses. Since all these modelings do not contain originally a term describing the pairing effects, the Gogny force D1S [72] is employed in the pairing channel. DD-ME2 and DD-MEδ do not have tensor terms (neither of Lorentz type, or of rank-2 type). Since these four effective Lagrangians reproduce equally well the energies and radii of finite nuclei, we could compare in the following the impact of the tensor force on more detailed quantities such as s.p. energies, within a spherical model which was described in Refs. [90, 149].

4.3 Lorentz pseudo-vector and tensor effects on Ca isotopes

The analysis of the oxygen isotopes has revealed the very important role of the spin-isospin properties of the nuclear interaction and their impact on the magicity of ^{24}O [34, 147]. The origin of this strong spin-isospin interaction is directly related, in a one boson-exchange picture, to the contribution of π and tensor-ρ mesons. In a similar way, it is interesting to explore the role of these mesons along the next semi-magic $Z = 20$ (resp. $N = 20$) isotopic (resp. isotonic) chains with respect to the neutron (resp. proton) shell evolution. Therefore, it is expected that, since there exist a large number of measured properties, the analysis of the theoretical predictions could shed light on the role of these meson fields, and more precisely, of the tensor force. Notice that ^{40}Ca is spin-saturated in the proton and neutron shells, and the tensor interaction that contributes in calcium isotopes above ^{40}Ca is mostly active between a few neutron states: mostly $\nu 2p$ and $\nu 1f$ states. Calcium isotopes therefore provide an ideal isotopic chain for the theoretical and experimental analysis of the neutron-neutron tensor interaction and for studying its role in the formation and evolution of neutron shells in medium mass nuclei.

4.3.1 Proton channel

We first analyze the question of the possible proton level inversion in ^{48}Ca. The normal level sequence being $\{\pi 2s_{1/2}, \pi 1d_{3/2}\}$, it has been suggested that the inversion of this sequence if well marked, could induce the formation of a proton depletion, a kind of bubble structure, in the neighbouring ^{46}Ar, reducing the spin-orbit (SO) splitting [154]. The energy difference $\Delta E^{\pi}_{sd} = \varepsilon_{\pi 2s_{1/2}} - \varepsilon_{\pi 1d_{3/2}}$ along the

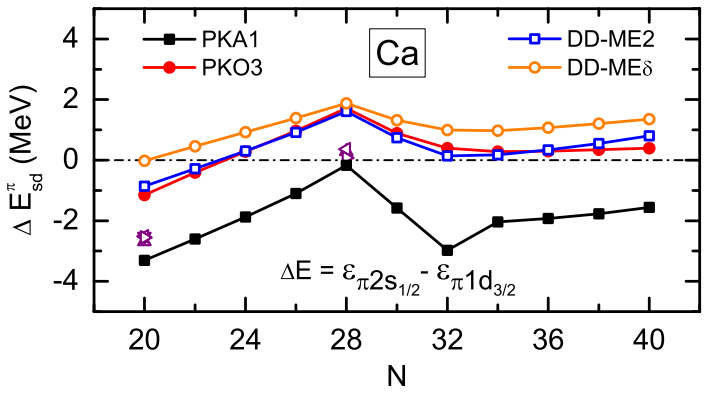

Figure 4.1: Energy difference $\Delta E^{\pi}_{sd} = \varepsilon_{\pi 2s_{1/2}} - \varepsilon_{\pi 1d_{3/2}}$ of Ca isotopes. The experimental values of ^{40}Ca and ^{48}Ca are taken from Ref. [150] (up-triangle), Ref. [151] (down-triangle), Ref. [152] (left-triangle), and Ref. [153] (right-triangle), respectively.

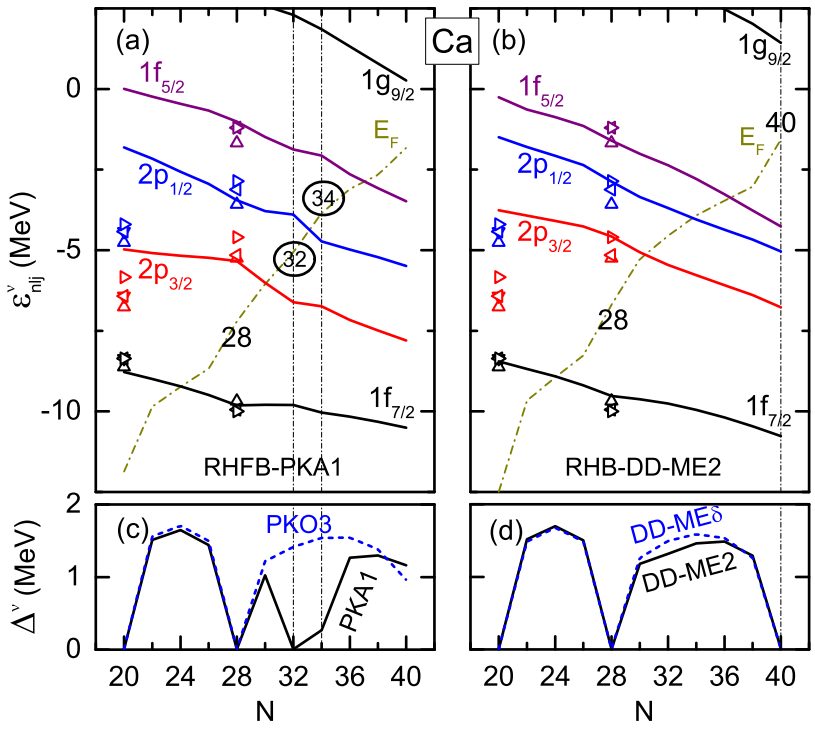

Figure 4.2: Upper panels: Neutron s.p. spectra of Ca isotopes, extracted from the RHFB calculations with PKA1 (plot a) and the RHB ones with DD-ME2 (plot b). Lower panels: Neutron pairing gaps determined by the RHFB (plot c) and RHB (plot d) calculations. The experimental data (in various triangles) are taken from Refs. [150–153], see Fig. 4.1 for the convention of symbols.

calcium isotopic chain is shown in Fig. 4.1 for the selected effective Lagrangians: PKA1, PKO3, DD-ME2 and DD-MEδ. The experimental data of the relevant s.p. energies in both ^{40}Ca and ^{48}Ca are also reported in Refs. [150–153]. Experimentally, s.p. energies are difficult to determine due to the strength fragmentation caused by the particle-vibration coupling [107, 155, 156]. Among these effective Lagrangians, it appears that only the RHFB-PKA1 model gives a satisfactory agreement with the experimental results and predicts an almost perfect degeneracy between the $\pi 2s_{1/2}$ and $\pi 1d_{3/2}$ states, consistent with the data (see Fig. 4.1). The other effective Lagrangians, which do not contain the Lorentz PV and T couplings or only partially (such as PKO3 which has the PV coupling), fail to reproduce the experimental points, and a level inversion is even predicted around ^{48}Ca, in contradiction with the data. From the comparison shown in Fig. 4.1, we deduce that the tensor-ρ meson-nucleon coupling, which can be treated as a mixture of central and tensor forces, is an important ingredient in order to reproduce the s.p. spectra in Ca isotopes. The importance of the tensor force in this context has also been stressed by non-relativistic approaches [140, 157, 158]. It is worthwhile to notice that the two proton states $\pi 2s_{1/2}$ and $\pi 1d_{3/2}$ are pseudo-spin (PS) partners [89, 159]. The energy difference ΔE^{π}_{sd} could therefore be interpreted as a measure of the PS degeneracy. In this case, the Lorentz tensor ρ-field is also an important ingredient for discussing the occurrence of PS degeneracy in ^{48}Ca.

4.3.2 Neutron channel

The role of the different components of the nuclear interaction can be analyzed from various perspectives. The mean-field in non-relativistic Skyrme approaches allows to analyse the respective roles of the central, SO and effective mass terms [157]; the tensor force in M3Y-type models was found to be important in reproducing the experimental trends [142]; the comparison between the relativistic and non-relativistic approaches show that N or $Z = 8$, 20 are suitable for fitting the tensor parameters [123], and finally, calcium isotopes have been used as benchmark nuclei to illustrate the role of the three-body (TB) force [21, 24, 160]. Concerning the last study, it is worth noticing a recent

work showing that a properly optimized chiral two-body interaction can also describe many aspects of nuclear structure in oxygen and calcium isotopes without explicitly invoking TB force [161]. Just after the measurements of neutron-rich calcium isotopes [162, 163], it was argued from a Skyrme Hartree-Fock (SHF) approach that the magicity of ^{52}Ca and ^{54}Ca might be reproduced selecting fitted tensor parameters [143]. Pairing correlations have however not been considered and the magicity has been inferred only from the size of the s.p. gaps. It is known that relatively large s.p. gaps could still be overcome by pairing correlations leading to fractional occupations above the expected s.p. shell gap. As proposed in a non-relativistic approach based on the Skyrme force [144], a criterium for the magicity should thus also refer to the occupation number above the s.p. gap which, in case of magicity, should be found to be zero.

Fig. 4.2 shows the isotopic evolution of the canonical s.p. energies (upper panels) and average pairing gaps (lower panels) from ^{40}Ca to ^{60}Ca, going over the possible new magic numbers at $N = 32$ and 34, and using RH(F)B approach with the selected effective Lagrangians. In Figs. 4.2 (a) and (b) are shown the evolutions of the neutron s.p. energies around the Fermi energy determined by RH(F)B calculations with PKA1 and DD-ME2, respectively. We remind that the RHB-DD-ME2 model does not contain either the Lorentz tensor or non-relativistic rank-2 tensor force components. In Fig. 4.2, the experimental values taken from Refs. [150–153] are also shown. It should be noticed that we only take the experimental data as a reference due to the limit of mean-field approach. In the present calculations, the correlations beyond mean field [107, 155, 156, 164, 165], such as the particle-vibration couplings, are not taken into account. Another fact is that among the selected s.p. states some states such as the $\nu 2p_{1/2}$ in ^{40}Ca or $\nu 1f_{5/2}$ in ^{48}Ca are highly fragmented.

The general feature reflected in Fig. 4.2 is that, as the number of neutrons increases, the s.p. energies decrease due to the enhanced mean-field potential. This trend is smooth for the RHB-DD-ME2, as well as for the other non-presented models RHFB-PKO3 and RHB-DD-MEδ, while we observe abrupt changes in the RHFB-PKA1 results when the s.p. energies cross the Fermi energy. Notice moreover that ^{40}Ca is spin-saturated, while the spin asymmetry reaches a maximum at ^{52}Ca. We have analysed the isotopic evolution of the two-body interaction matrix elements $V_{ii'}$ between neutron valence orbits and we found that the couplings are quite constant for the RHB-DD-ME2 while for the RHFB-PKA1 they are slightly more dependent on the number of neutrons. In particular, it is observed a reduction of the coupling between $\nu 2p_{1/2}$ and $\nu 2p_{3/2}$ states at $N = 32$ by about 40% as compared to the values at $N = 30$ and 34. This reduction is associated with the emergence of a shell gap at $N = 32$. We also observe that the coupling between $\nu 2p_{1/2}$ and $\nu 2p_{3/2}$ states is reduced by a factor 2 with the RHFB-PKA1 as compared to the RHB-DD-ME2, which explains why the gap at $N = 32$ is not so distinct for the RHB-DD-ME2. In contrast, although both Lagrangians give almost identical coupling strengths between the $\nu 2p_{1/2}$ and $\nu 1f_{5/2}$ states, only the RHFB-PKA1 shows a gap at $N = 34$. The gaps at $N = 32$ and 34 are therefore related to different parts of the nuclear interaction, and we will analyse it with respect to the Lorentz PV and T interactions in the following.

4.3.3 Magicity of ^{52,54}Ca

As discussed before, the magicity is not solely related to an increase of the shell gap, but also to a quenching of the pairing correlations at magic numbers. As seen from Figs. 4.2(c) and 4.2(d), the suppression of the neutron pairing gaps at traditional magic numbers $N = 20$ and $N = 28$ is confirmed by all the models considered here. In the RHFB-PKA1 results, there is an additional suppression of the neutron pairing gap at $N = 32$ which is not predicted by the other Lagrangians. This large quenching for $N = 32$ is an additional hint which suggests that the $N = 32$ magic number should be analyzed in the light of the Lorentz PV and T interactions. A weaker, but still distinct and important, quenching is also predicted by the RHFB-PKA1 at $N = 34$, which may suggest as well $N = 34$ to be a submagic number. It is also interesting to notice the predictions at $N = 40$: the RHB models indicate a quenching of the pairing correlations at $N = 40$, while the RHFB ones predict a small decrease but not a quenching. The origin of these discrepancies is related to the Fock term and to the effect of the

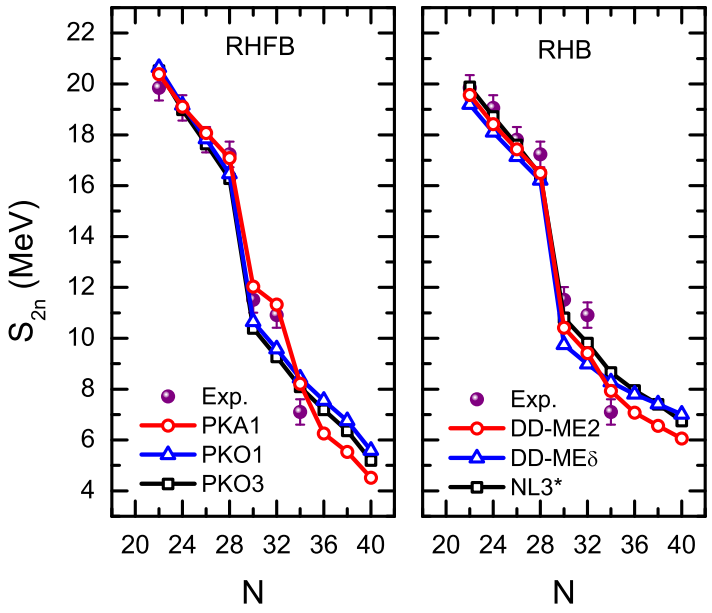

Figure 4.3: Two-neutron separation energies S_{2n} of the Ca isotopes for the (a) RHFB and (b) RHB Lagrangians. Experimental values are taken from [162, 166].

Lorentz PV and T interactions. The most advanced Lagrangians presented here (PKA1 and PKO3) therefore do not predict $N = 40$ as a magic number for ^{60}Ca.

We now consider two-neutron separation energy S_{2n} which is a preferred probe of the evolution of nuclear structure, and can be used to challenge model predictions. As shown in Fig. 4.3, the PKA1 calculations predict the $N = 32$ and 34 sub-structure very close to the measurements. While the other calculations predict an almost linear progression beyond $N = 28$.

In order to further understander the mechanism in formation of $N = 32$ and 34 shell gaps. We show in Fig. 4.4, the neutron s.p. spectra of ^{52,54}Ca. The neutron $N = 32$ shell closure coincides with a large SO splitting of $\nu 2p$. It can be, only, recognized by PKA1 due to a more bound (~ 1.0 MeV) $\nu 2p_{3/2}$ state. For ^{54}Ca, the filled low-j $\nu 2p_{1/2}$ state is pushed downwards, whereas the tiny occupied high-j state $\nu 1f_{5/2}$ are pushed upwards. The gap arises this time. One should note, however, even if we disregard the tensor effects in modeling the gap evolution, a strong pure SO effect would also prefer a magic nuclei ^{52}Ca [167].

4.4 Evolution along $N = 32, 34$ down to the drip line

It is important to understand the evolution of the above new magic shells, especially, the region below $Z = 20$ was not well explored until now.

4.4.1 Evolution of $N = 32$ gaps

We now analyze the contribution of the neutron-proton interaction to the SO splittings of $\nu 2p$ states. To do so, we fix the neutron number as $N = 32$ and vary the proton number from ^{60}Ni down to ^{52}Ca, and along the isotonic line the valence protons are gradually removed from the $\pi 1f_{7/2}$ state (which is a $j_>$ state). The energy differences associated to the $N = 32$ and 34 shell gaps are given in Table 4.1 for a set of selected isotones going from the stability line down to the drip line: ^{60,62}Ni, ^{52,54}Ca and ^{46,48}Si. Comparing the $\nu 2p$ SO splittings ($N = 32$) given by different effective Lagrangians, it is interesting to notice that the values are almost the same for ^{60}Ni (1.4 ± 0.2 MeV)

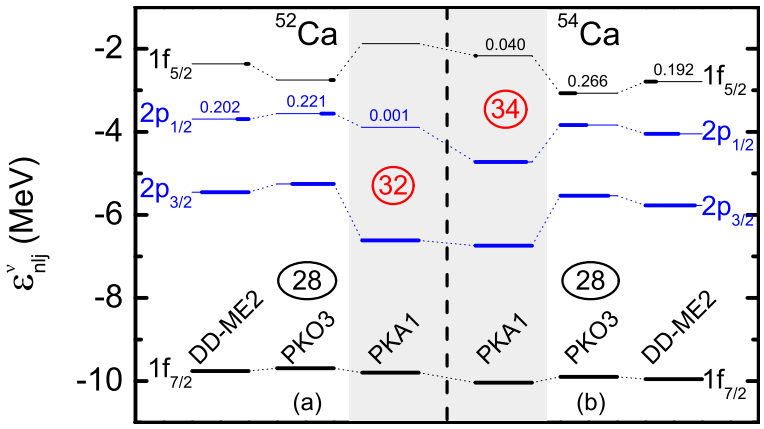

Figure 4.4: Neutron canonical single-particle spectra of ^{52}Ca (a) and ^{54}Ca (b). The results are extracted from the RHFB calculations with PKA1 and PKO3, and compared to the RHB one with DD-ME2. The lengths of thick bars correspond with the occupation probabilities of neutron states.

Table 4.1: Energy difference $\Delta E(i,i') \equiv \varepsilon_i - \varepsilon_{i'}$ (in MeV) in Ni, Ca and Si at $N = 32$ and 34. The results correspond to RHFB-PKA1, PKO3 and RHB-DD-ME2 Lagrangians. See text for details.

Force	$\Delta E(i,i')$	N	Ni	Ca	Si
PKA1	$(\nu 2p_{1/2}, \nu 2p_{3/2})$	32	1.51	**2.72**	0.81
	$(\nu 1f_{5/2}, \nu 2p_{1/2})$	34	1.04	**2.45**	**4.05**
PKO3	$(\nu 2p_{1/2}, \nu 2p_{3/2})$	32	1.22	1.69	0.68
	$(\nu 1f_{5/2}, \nu 2p_{1/2})$	34	−1.72	0.77	2.72
DD-ME2	$(\nu 2p_{1/2}, \nu 2p_{3/2})$	32	1.58	1.76	0.92
	$(\nu 1f_{5/2}, \nu 2p_{1/2})$	34	−1.23	1.21	3.18

and for ^{46}Si (0.8 ± 0.1 MeV), while they are quite different for ^{52}Ca. A more systematic calculation along the $N = 32$ isotonic line is shown in Fig. 4.5 where Fig. 4.5(a) shows the comparison of the SO splittings between the models (PKA1, PKO3, DD-ME2 and DD-MEδ) and Fig. 4.5(b) presents the detailed contributions of PKA1. To better analyze the isotonic evolution, we present the results with respect to the values calculated in ^{52}Ca.

As shown in Fig. 4.5(a), the RHFB-PKA1 results show a distinct enhancement of the SO splitting from Ni to Ca (∼1.2 MeV), while it is less pronounced for RHFB-PKO3 (∼0.5 MeV) and much less for RHB-DD-ME2 and RHB-DD-ME2δ (∼0.2 MeV). On the other side, from S to Ca the situation is changed. Towards Ca, the RHFB-PKO3 results present a 0.8 MeV enhancement of the $\nu 2p$ SO splitting (∼0.5 and 0.4 MeV respectively for RHB and RHFB-PKA1). Here, we truncate at S to make the figures more readable, but the conclusions extend beyond. To further analyse the origin of this behaviour and the role of the Lorentz PV and T interactions, we have plotted in Fig. 4.5(b) the contribution from the Lorentz PV and T couplings in RHFB-PKA1, which are decomposed into the rank-2 tensor term V^T and the central term V^C, as compared to the other terms (Rest) associated with the kinetic energy term, σ-S, ω-V and ρ-V couplings. We find that the Lorentz PV and T couplings, namely the π-PV and ρ-T ones in PKA1, play a dominant role in determining the enhancement of the $\nu 2p$ SO splitting from Ni to Ca, while from Ca to S, the contributions of the Lorentz PV and T couplings are close to zero. Such difference is due to the fact that the contributions of the central and rank-2 tensor terms, namely V^C and V^T, add up between Ni and Ca, while they mutually compensate between Ca and S. In addition, it is worth noticing the large contribution of the central term to the SO splitting between Ni and Ca (70% of the increase), while the rank-2 tensor accounts for only 30% of the increase. In conclusion, it is illustrated in the case of the $N = 32$ isotones that the effects of the Lorentz PV and T on the s.p. energy gaps is certainly not reducible to the contribution of the rank-2

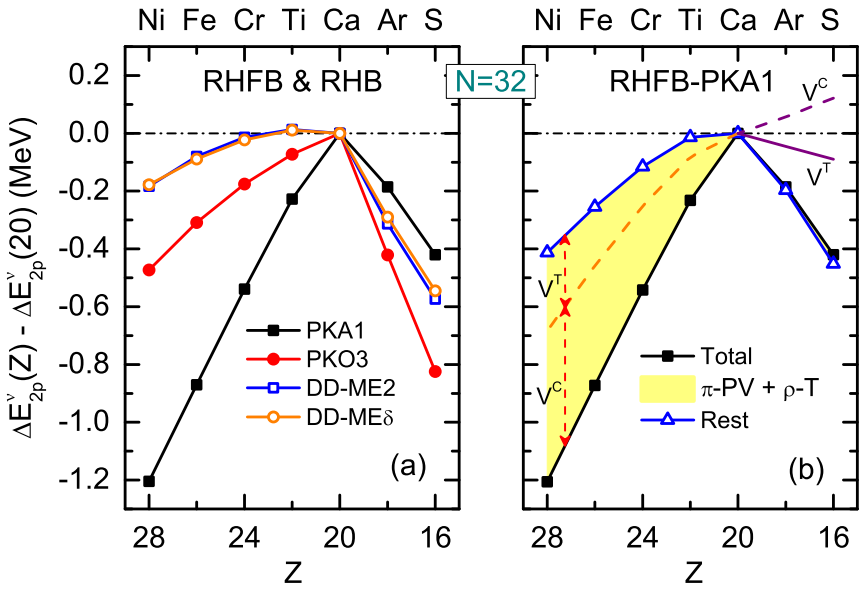

Figure 4.5: (a) The SO splitting ΔE_{2p} of $\nu 2p$ along the $N = 32$ isotonic chain, calculated with the RHFB (full symbols) and RHB (open symbols). (b) Detailed contributions to the SO splitting from the Lorentz PV and T components (π-PV + ρ-T), in comparison with those from the other components.

tensor because the central term plays a more important role.

4.4.2 Evolution of $N = 34$ gaps

We now turn to the $N = 34$ gap which is appearing between the $\nu 2p_{1/2}$ and $\nu 1f_{5/2}$ states. Similarly to the $N = 32$ case, we first refer to Table 4.1 where the energy differences responsible for the $N = 34$ shell gap, $\Delta E^{\nu}_{fp_<} = \varepsilon_{\nu 1f_{5/2}} - \varepsilon_{\nu 2p_{1/2}}$, are given for Ni, Ca and Si. Only the RHFB-PKA1 model presents fairly distinct shell gap at $N = 34$ for ^{54}Ca and all the models predict much enhanced gap for ^{48}Si. For ^{62}Ni, the order of the states is even changed in the RHFB-PKO3 and RHB-DD-ME2 results. In order to clarify the role of the Lorentz PV and T in the $N = 34$ case, we represent in Fig. 4.6(a) the evolution of the energy difference $\Delta E^{\nu}_{fp_<}$ shifted by that in ^{54}Ca, while the energy difference involving the SO partner of the occupied state, $\Delta E^{\nu}_{fp_>} = \varepsilon_{\nu 1f_{5/2}} - \varepsilon_{\nu 2p_{3/2}}$, is represented in Fig. 4.6(b). The role of the Lorentz PV and T is not so straightforward since the states are not SO partners. It is found, for PKA1, that the Lorentz PV and T forces present tiny contributions to the splitting between the $\nu 2p_{1/2}$ and $\nu 1f_{5/2}$ states. As shown in Fig. 4.6(a) the origin of this weakening is due to the near cancellation between the central and the rank-2 tensor components of the Lorentz PV and T couplings. This cancellation occurs for all isotones considered here, from Ni to S.

It is interesting to notice that the states $\{\nu 2p_{3/2}, \nu 1f_{5/2}\}$, involving the SO partner of the occupied state of the $N = 34$ gap, are PS partners and usually named $\nu 1\tilde{d}$, cf Fig. 4.2. The contribution to the PS splitting of Lorentz PV and T terms (π-PV and ρ-T) as well as that coming from the other terms (Rest) calculated with the RHFB-PKA1 model are represented in Fig. 4.6(b). It is observed that the other terms (Rest) largely contribute to the energy difference $\Delta E^{\nu}_{fp_>}$, while the Lorentz PV and T contribute only to about 30% of the splitting. For the $N = 34$ isotones, we observe that the $\nu 2p$ SO splitting is changing rather weakly from $Z = 28$ to 20, and therefore the opening of the $N = 34$ gap for $Z = 20$ can be understood, to a large extent, from the evolution of the PS splitting. The shell gap at $N = 34$ can therefore be interpreted as a manifestation of a strong isospin-dependent PS splitting in which the Lorentz PV and T terms have only a weak impact.

It is worth comparing our results to very recent experimental analyses of shell gaps in ^{50}Ar, ^{52,54}Ca, ^{54}Ti [168]. Using RHFB-PKA1, we observe as well that the $N = 32$ subshell gaps in ^{50}Ar, ^{52}Ca, ^{54}Ti

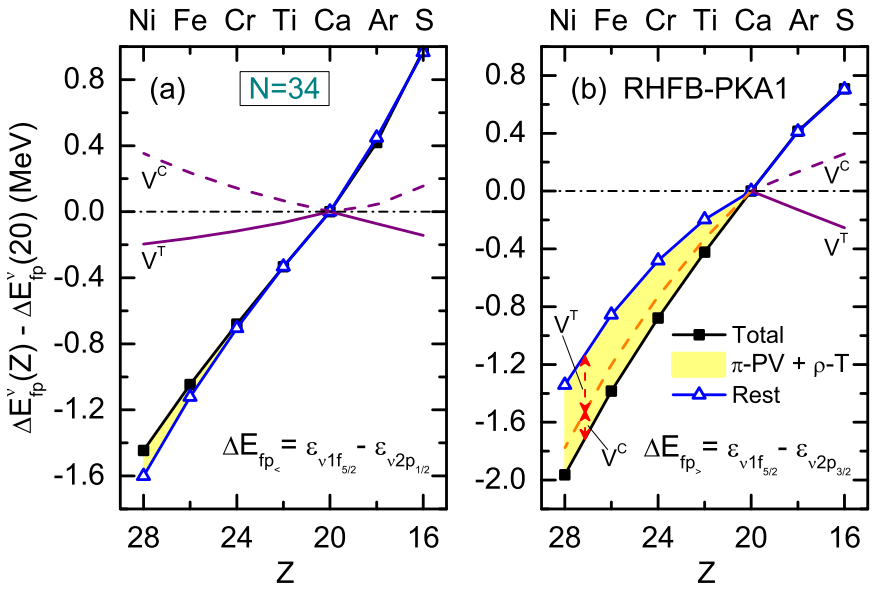

Figure 4.6: (a) Detailed contributions from the π-PV and ρ-T couplings to the energy difference $\Delta E^{\nu}_{fp_<}$ (in MeV) between the neutron $\nu 2p_{1/2}$ and $\nu 1f_{5/2}$ states and (b) the energy difference $\Delta E^{\nu}_{fp_>}$ (in MeV) between the states $\nu 2p_{3/2}$ and $\nu 1f_{5/2}$ along the isotonic chain of $N = 34$. The results correspond to the RHFB-PKA1 Lagrangian.

are similar in magnitude, see Fig. 4.5(a), and that the $N = 34$ subshell closure in ^{52}Ar is larger than in ^{54}Ca, see Fig. 4.6(a). In addition, the shell gaps continue to increase between ^{52}Ar and ^{50}S, see Fig. 4.6(a), and this tendency is confirmed for the next $N = 34$ nucleus which is ^{48}Si. RHFB-PKA1 predicts a large gap for the drip line nucleus ^{48}Si (∼4.0 MeV) and a small pairing gap, while the other Lagrangian predict a small gap, see Table 4.1.

In conclusion of this part, the effect of the Lorentz PV and T couplings (π-PV and ρ-T) on the $N = 32$ shell gap is shown to be dominant at variance with the $N = 34$ one. The origin of these shell gaps are indeed different: the $N = 32$ shell gap is related to the $\nu 2p$ SO splitting while the $N = 34$ shell gap can be related to the $\nu 1\tilde{d}$ PS splitting. The prediction of two successive magic numbers in Ca isotopes (^{52,54}Ca) is not related to the same origin.

4.5 Magicity of $N = 16$ in neutron rich isotopes

Based on the evolution of neutron separation energies and cross sections in light nuclei, it was originally proposed $N = 16$ to be a new magic number lying between the usual $N = 8$ and 20 for N, O and F nuclei [127]. In these nuclei, the s.p. gap at $N = 16$ is occurring between the $\nu 1d_{3/2}$ and $\nu 2s_{1/2}$ states. Several experimental analyses have concluded as well that $N = 16$ could be a magic number. For instance, from proton knockout reactions using ^{26}F beam, the s.p. gap between these states was deduced to be 4.86(13) MeV [169]. Another confirmation came also from the measurement of a relatively high excitation energy and a small β_2 value in ^{24}O [170]. These results also indicate that ^{24}O has a spherical character.

4.5.1 Magicity of ^{24}O

We show in Fig. 4.7 the neutron s.p. spectra of ^{24}O. The neutron $N = 16$ shell closure coincides with a large PS splitting of $\nu 1\tilde{p}$. Here, we have used as pairing interaction the original D1S Gogny force modified by an adjusted strength factor $f = 1.10$, so as to reproduce the odd-even mass differences of Oxygen isotopes [91]. In particular, we notice that RHFB-PKA1 gives more bound s state and

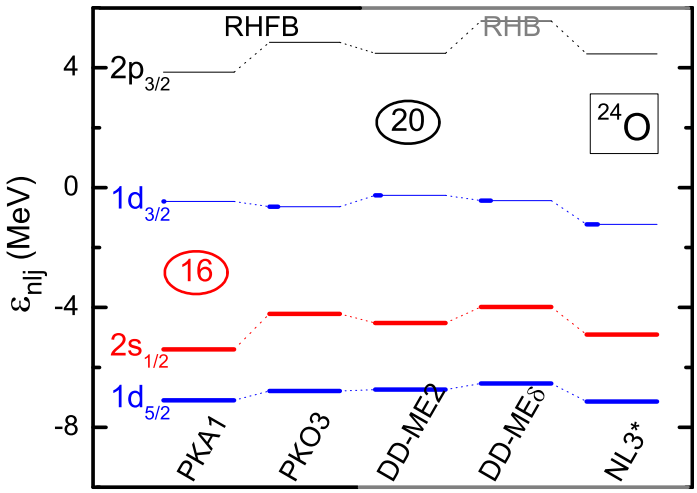

Figure 4.7: Neutron canonical single-particle spectra of ^{24}O. The results are extracted from the RHFB calculations with PKA1 and PKO3, and compared to the RHB one with DD-ME2, DD-MEδ and NL3. The lengths of thick bars correspond with the occupation probabilities of neutron states.

slightly large SO splitting of $\nu 1d$ than other the other interactions. However, as a critical requirement for the drip line in Oxygen to be found at ^{24}O, the neutron $\nu 1d_{3/2}$ orbital should become unbound.

4.5.2 Evolution along $N = 16$ down to the drip line

Our predictions are shown in Fig. 4.8 where we represent the energy difference between the $\nu 1d_{3/2}$ and $\nu 2s_{1/2}$ states, namely $\Delta E^{\nu}_{ds} = \varepsilon_{\nu 1d_{3/2}} - \varepsilon_{\nu 2s_{1/2}}$, along the $N = 16$ isotonic chain from $Z = 20$ down to 8. Here, we have used as pairing interaction the original Gogny force D1S modified by an adjusted strength factor $f = 1.10$, so as to reproduce the odd-even mass differences of oxygen isotopes [91]. In Fig. 4.8(a) we compare the predictions of different effective Lagrangians, PKA1, PKO3, DD-ME2 and DD-MEδ, with the experimental data in ^{24}O [169]. The effective Lagrangian PKA1 predicts a large s.p. gap from $Z = 8$ up to 20, as well as a s.p. gap in ^{24}O close to the experimental value. At variance with this prediction, the three other effective Lagrangians (PKO3, DD-ME2, and DD-MEδ) predict a strong reduction of the s.p. gap when going from $Z = 8$ to 20, and the s.p. gap predicted for ^{24}O is well below the data.

In order to analyse the role played by the Lorentz PV and T couplings on the s.p. gap evolution, we present in Fig. 4.8(b) the contributions from the central and rank-2 tensor terms of the Lorentz PV and T couplings, as well as the other terms (Rest) for the RHFB-PKA1 model. For $Z = 20$ down to 8, the Lorentz PV and T couplings contribute about 30-50% of the s.p. gap, and it is interesting to note that the contribution from the central terms of the Lorentz PV and T couplings are dominant and the effect of the rank-2 tensor coupling is quite weak. The latter observation contradicts previous studies based on non-relativistic approaches using Skyrme and Gogny forces where a stronger rank-2 tensor force is necessary to reproduce s.p. evolutions [124]. The contribution of the Lorentz PV and T tensor couplings (yellow region in Fig. 4.8) for $N = 16$ is rather constant along the isotonic chain, and the observed Z-evolution is mostly related to the "Rest" terms and seems to be quite impacted by shell effects. A general feature observed with our relativistic models is that the shell gap is decreasing from O to Si, despite an increase around $Z = 14$.

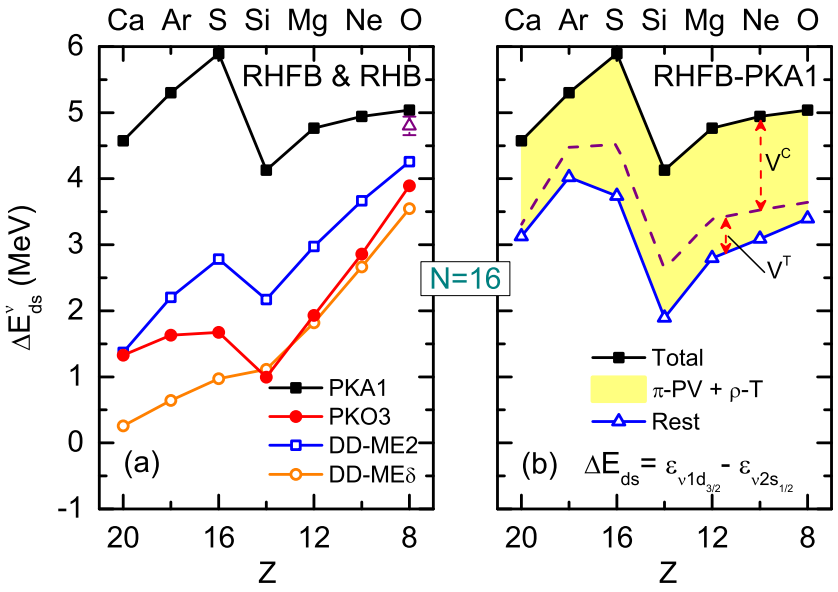

Figure 4.8: (a) Energy difference $\Delta E_{ds} = \varepsilon_{\nu 1d_{3/2}} - \varepsilon_{\nu 2s_{1/2}}$ along the isotonic chain of $N = 16$. The experimental value of ^{24}O [169] is also displayed as a reference. (b) Detailed contributions to ΔE_{ds} from the π-PV and ρ-T terms, in comparison with those from the other channels. The results are obtained with the RHFB-PKA1 effective Lagrangian.

4.6 Summary and conclusions

In summary, the formation of new shell gaps in neutron-rich nuclei is investigated within the RHFB theory and the role of the Lorentz PV and T interactions is studied in detail by comparing different Lagrangians with or without such terms. Based on the most complete RHFB-PKA1 effective Lagrangian, we confirm and predict that ^{48}Si, ^{52,54}Ca and ^{24}O are the magic neutron-rich nuclei. In the case of ^{52}Ca, the role of the Lorentz PV and T components is determinant, while it is less important for ^{24}O, and negligible for ^{54}Ca and ^{48}Si. Analyzing shell evolutions along the $N = 32$, 34 and $N = 16$ isotonic chains, we observe that the global variation of the s.p. energies is due to the isoscalar component of the effective Lagrangian, while the more specific evolution of SO and PS partners is related to the Lorentz PV and T couplings (π-PV and ρ-T). Based on the FW transformation, we analyze the role played by the central and rank-2 tensor terms of the Lorentz PV and T couplings in the formation of the $N = 16, 32$ and 34 shell gaps. It is shown that those terms drive the distinct enhancement of the $N = 32$ gap along isotonic chains going from ^{60}Ni to ^{52}Ca, while the increase of the $N = 34$ gap from ^{62}Ni to ^{54}Ca, and ^{48}Si, is mainly due to the other channels. The shell gap at $N = 34$ can be also interpreted as a manifestation of a strong isospin-dependent PS splitting. Finally, we also observe that the Lorentz PV and T couplings are not likely to support the appearance of $N = 40$ magicity in ^{60}Ca.

In this study, we have illustrated in intermediate mass nuclei the very important role played by the Lorentz PV and T interactions which cannot be simply reduced to their rank-2 irreducible tensor contribution. We have indeed observed a strong interplay between the rank-2 tensor and the central terms originating from the Lorentz PV and T interactions. While these two terms generally appear separately in non-relativistic nuclear models, they originate from the same interaction vertex in the relativistic ones. In the intermediate mass nuclei that we have explored, the s.p. energies are shown to be very much impacted by the Lorentz PV and T interactions which impose some very specific behaviour along isotonic chains. Even their weak influence results from the cancellation of two of their constituent terms. The effect of the Lorentz PV and T couplings — which are purely relativistic terms — in s.p. energies is therefore very different from the rank-2 tensor force. We conclude from this study that, while both relativistic and non-relativistic models for the nuclear interaction could equally well

reproduce global properties of finite nuclei, such as binding energies and radii, the detailed evolution of s.p. energies could potentially sign relativistic effects such as the Lorentz PV and T interactions. This statement requires however further analysis based on other modelings of the nuclear interaction, but we propose here a clear relation between Lorentz PV and T relativistic vertices and s.p. evolution.

Chapter 5

Pairing phase transition

Non-realized idea is not an idea yet.

Andrei Sakharov, 1921-1989

5.1 Introduction

Over the past several decades, the thermodynamical properties of excited nuclei have drawn renewed attention due to the advanced accurate measurements of level densities at low excitation energies [171–175]. Pairing correlations play an essential role in many Fermion systems and have thus a strong influence on nuclear structure at low excitation energies [176–180]. Pairing correlations in finite systems such as nuclei or Wigner-Seitz cells, and in infinite ones such as in neutron star matter, may exhibit different behaviors reflected in the specific heat and the level density [181–185]. Moreover, the phase transition is a complex and rich phenomenon, where pairing re-entrance in asymmetric matter, in odd-nuclei, rotating nuclei, and even in doubly magic nuclei close to the drip line may occur [176, 184, 186–188]. The interplay between temperature and shell effects in superfluid systems, giving rise to re-entrance or its opposite phenomenon — suppression, still remains to be studied.

The competition between temperature and pairing correlations in nuclei at low excitation energies has been studied for several decades, with the pioneering works based on finite-temperature BCS (FT-BCS) theory [189] and finite-temperature Hartree-Fock-Bogoliubov (FT-HFB) theory [76]. It was predicted that the critical temperature T_c for pair correlation quenching could be expressed, as in uniform matter, as a function of the average pairing gap at zero temperature $\Delta(0)$ following the relations $T_c = 0.57\Delta(0)$ for a constant pairing force [189]. The more evolved Bogoliubov approach later has been applied to finite nuclei confirming the existence of such relations between T_c and $\Delta(0)$. For the simplified degenerate model, the relation was found to be $T_c = 0.50\Delta(0)$ [76], while in rare-earth transition nuclei the interplay with deformation induces shape transitions in the superfluid phase, leading to the ratio $T_c/\Delta(0) = 0.57$ for protons and 0.63 for neutrons [190]. In addition, pairing correlations are expected to play an important role in the decay of compound nuclei formed in heavy-ion collisions, as illustrated in the seminal work presented in Ref. [78]. More recently, the BCS and HFB approaches have been extended to self-consistent mean-field models in order to improve the description of the pairing transition in spherical nuclei [191–193], as well as in deformed nuclei where shape transitions have been predicted [194–198]. In summary, the ratio $T_c/\Delta(0)$ lies in the interval $0.50 - 0.60$, where the uncertainty originates mainly from the detailed level structure of spherical and deformed nuclei which depends itself on models.

It is worth noticing that in most of the quoted studies, the calculations were performed either on the harmonic oscillator basis, or within the non-relativistic framework. Due to the limitation of the harmonic oscillator basis in giving an appropriate asymptotic behavior of the single particle (s.p.) wave functions, the nucleon densities at large distance converge very slowly with respect to the size

Table 5.1: Bulk properties of symmetric nuclear matter at the saturation point: density ρ_0 (fm^{-3}), binding energy E_B/A (MeV), compression modulus K (MeV), symmetry energy J (MeV) and non-relativistic effective masses M^*_{NR} (M) predicted by selected RHF and RH models. The non-relativistic effective masses in neutron matter are also listed.

Model	Interaction	Ref.	symmetric matter					neutron matter	
			ρ_0	E_B/A	K	J	M^*_{NR}	$M^*_{NR}(\nu)$	$M^*_{NR}(\pi)$
RHF	PKA1	[48]	0.160	−15.83	229.96	36.02	0.68	0.68	0.70
	PKO1	[49]	0.152	−16.00	250.28	**34.37**	0.75	0.73	0.76
	PKO2	[49]	0.151	−16.03	249.53	**32.49**	**0.76**	0.75	0.77
RH	DD-ME2	[93]	0.152	−16.14	250.97	32.31	**0.65**	0.64	0.70
	PK1r	[92]	0.148	−16.27	**283.68**	37.83	0.68	0.64	0.72
	NL3*	[138]	0.150	−16.30	**258.56**	38.70	0.67	0.63	0.72

of the basis. The situation becomes even more serious in the weakly bound nuclei close to the drip line [199, 200]. Nowadays a realistic framework is to perform the calculations in an appropriate basis that can provide a reasonable description of both the overall and asymptotic behaviors of the density profiles, for instance the Woods-Saxon (WS) basis [75, 201]. In some applications, the small component of the Dirac spinors were usually neglected in determining the relativistic Hartree-Bogoliubov (RHB) and finite-temperature RHB (FT-RHB) pairing tensor [193, 202]. We therefore present, in this work, the first fully RHFB calculations at finite temperature (FT-RHFB): both the large and small components of the Dirac spinors contribute to the pairing channel, and the contributions of the Fock terms are naturally included. In addition, the Dirac WS (DWS) basis [75] is employed to better describe weakly bound nuclei.

In this chapter, we compare the predictions based on several effective Lagrangians. In practice, the integro-differential FT-RHFB equations are solved by using a DWS basis with a radial cut off $R = 26$ fm. The numbers of positive and negative energy states in the basis expansion for each s.p. angular momentum (l, j) are chosen to be 36 and 12, respectively. We have verified that this truncation scheme provides sufficient numerical accuracy for the description of weakly bound nuclei (Pb and Sn isotopes). The pairing interaction is either a finite-range Gogny D1S interaction [72] or a density-dependent contact interaction (DDCI). Notice that the DDCI requires a regularization scheme. We have considered in this study a simple cut-off scheme, defined to be 100 MeV in quasiparticle space, and the strength V_0 is adjusted to reproduce the same average pairing gap as that obtained with the Gogny D1S interaction. These values of V_0 will be given with the results hereafter. The D1S pairing interaction depends slightly on the mass: A general factor g is therefore introduced for its strength, as in Refs. [91, 203]. We consider 6 different model Lagrangians which are given in Table 5.1. Some of the bulk properties of nuclear matter determined by these Lagrangians are also shown. They are generally compatible with the expected gross properties of finite nuclei, e.g., the binding energy $E/A \simeq 16$ MeV, the saturation density $\rho_0 \simeq 0.15$ fm^{-3}, the incompressibility modulus $K \in [220, 280]$ MeV, and the symmetry energy $J \in [32, 39]$ MeV.

5.2 Critical temperature

In this section, we evaluate the influence of the model on the pairing properties in hot finite nuclei, taking ^{124}Sn as an example for testing pairing correlations. The ratio of the critical temperature over the average pairing gap at zero temperature $T_c/\Delta_n(0)$ is also studied as a function of the model, varying either the Lagrangian or the type of pairing interaction.

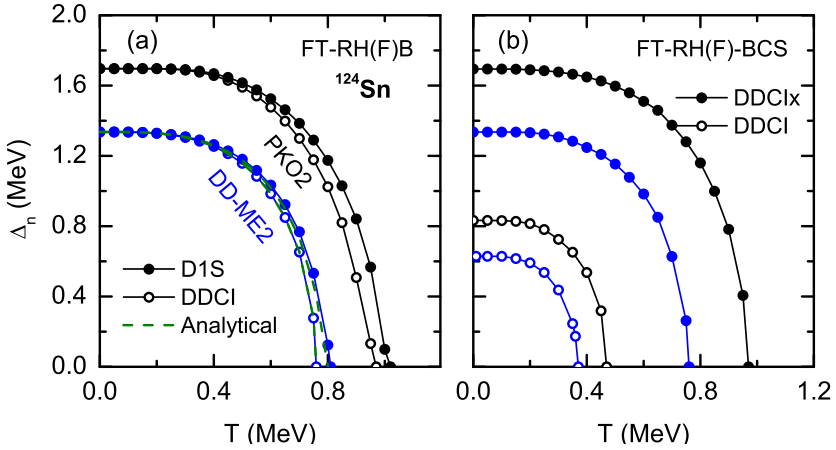

Figure 5.1: The neutron pairing gaps in ^{124}Sn as a function of temperature, calculated with PKO2 (black) and DD-ME2 (blue) corresponding to different M^*_{NR}. In the pairing channel, we compare finite-range D1S (filled circles) and contact DDCI (empty circles) forces. The analytical results (dashed lines) are also shown. Notice that here, we took the factor $g = 1$ for the Gogny D1S force, and for the DDCI pairing, we have taken the following values for V_0 (in MeV.fm^{-3}): 335 (PKO2), and 342 (DD-ME2) for the RH(F)B and BCS calculations. For the DDCIx force used in BCS, we took for V_0 (in MeV.fm^{-3}): 526 (PKO2) and 539 (DD-ME2).

5.2.1 Influence of the pairing force

Since pairing correlations are active only around the Fermi level, the ratio $T_c/\Delta_n(0)$ is expected to be modified by the effective mass which influences the s.p. level spacing to a large extent. Notice that here, the effective mass corresponds to the non-relativistic one M^*_{NR} instead of the quantity $M^*_S = M + \Sigma_S$ that is named as the Dirac mass [40, 65]. It can indeed be shown that, in the weak coupling limit of the BCS approximation, the average pairing gap at the Fermi surface Δ_F can be expressed as [204]

$$\Delta_F \approx 2\epsilon_F \exp\left[2/(N_F v_{\text{pair}})\right], \tag{5.1}$$

where ϵ_F is the Fermi energy, $N_F = m^*_F k_F/\pi^2$ is the average density of state in uniform matter at the Fermi energy, and k_F denotes the Fermi momentum, and v_{pair} is a constant pairing interaction. It is clear from Eq. (5.1) that the pairing gap Δ_F is quite sensitive to the effective mass at the Fermi energy ϵ_F. Equation (5.1) is obtained in infinite matter and it provides only a qualitative understanding of the relation between the pairing force strength and the effective mass. In the following, we present a quantitatively precise analysis of the correlation between the critical temperature and the non-relativistic effective mass in finite nuclei.

Figure 5.1(a) displays the evolution of the neutron pairing gap as a function of temperature for ^{124}Sn, a good candidate for studying pairing correlations. We compare two Lagrangians, PKO2 and DD-ME2 (see Table 5.1) both with two kinds of pairing interactions: the finite-range Gogny D1S force [72] and the contact force DDCI [71]. The two Lagrangians PKO2 and DD-ME2 mostly differ by their non-relativistic effective mass M^*_{NR} (see Table 5.1), and it is observed that the average pairing gap at zero temperature Δ_n scales with M^*_{NR}, as expected from the weak coupling expression (5.1). Comparing the different types of pairing interaction (finite- or zero-range) for the same Lagrangian, it is observed in Fig. 5.1 that the vanishing of pairing correlations at finite temperature slightly depends on the type of pairing force, namely, with the zero-range pairing interaction, the critical temperature T_c is slightly lower than with the finite-range interaction. From Fig. 5.1, the ratio $T_c/\Delta_n(0)$ is obtained as 0.60 for D1S, and 0.57 for DDCI. In Ref. [73], it was shown that the dependence of the pairing gap on the state around the Fermi energy is qualitatively different for contact and finite-range interactions. In addition, with a finite-range interaction, the pairing gap and the pairing tensor have non-local components which cannot be simply absorbed in the DDCI. The slight increase of the

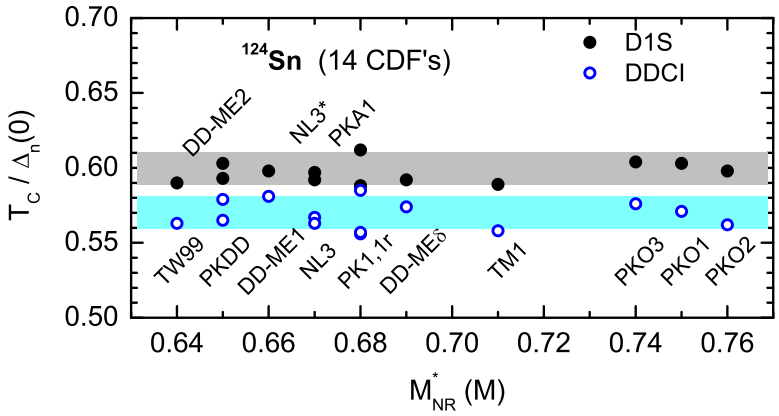

Figure 5.2: The ratios $T_c/\Delta_n(0)$ in ^{124}Sn as a function of the non-relativistic effective mass M^*_{NR}, calculated using the FT-RH(F)B theory with 14 parameter sets. In the pairing channel the finite-range D1S and the contact force DDCI are employed.

critical temperature with the D1S interaction is therefore an effect of the finite-range nature of the interaction, dispersing the pairing effects among more s.p. states. For comparison, and taking $T_c = 0.60\Delta_n(0)$ (finite-range pairing force) and $T_c = 0.57\Delta_n(0)$ (zero-range pairing forces), the analytical relation [205],

$$\Delta_n(T) = \Delta_n(0)\left[1 - \left(\frac{T}{T_c}\right)^m\right]^{1/2} \Theta(T - T_c) \tag{5.2}$$

where $m = 3.32$, is plotted for the DD-ME2 model [dashed lines in Fig. 5.1(a)]. There is almost no difference between the analytical model, i.e., Eq. (5.2), and the numerical calculations for stable nuclei like ^{124}Sn.

Figure 5.1(b) shows the neutron pairing gap calculated with the RHF theory plus BCS pairing at finite temperature (FT-RHF-BCS), using the same DDCI interaction as in the FT-RHFB calculations shown in Fig. 5.1(a) and the modified one (DDCIx) with enhanced pairing strength parameter V_0 (see caption for more details). It is found that, with the same DDCI pairing interaction, the neutron pairing gaps determined by the BCS method are reduced to about half of the Bogoliubov results. Such a distinct difference is due to the fact that the off-diagonal couplings, which account for about half of the pairing correlations, are absent in the BCS pairing. As a result, the strength parameter V_0 in BCS calculations is usually larger than in HFB, see for instance Ref. [206]. We have therefore readjusted V_0 in the RHF-BCS calculation at zero temperature to obtain the same pairing gap as the RHFB prediction, leading to the DDCIx interaction in Fig. 5.1(b). Applying such a simple modification of the parameter V_0 in ^{124}Sn, the temperature dependence of the pairing gap predicted by the FT-RHFB and FT-RHF-BCS frameworks are almost undistinguishable. However, this is not always true and as we will see that the above simple renormalization of the pairing strength will not work towards the drip line where the coupling to continuum states becomes more and more important.

5.2.2 Influence of the effective mass

The critical temperatures is also expected to depend on the non-relativistic effective mass, see for instance Refs. [144, 191, 194]. The dependence of the ratio $T_c/\Delta_n(0)$ on the effective mass is, however, not very well known. In Fig. 5.2, we plot the ratio $T_c/\Delta_n(0)$ as a function of M^*_{NR} in ^{124}Sn, and we compare the predictions of two pairing interactions (finite versus zero range). The effective mass M^*_{NR} is obtained with 14 CDFs (the 6 CDFs given in Table 5.1 completed with 8 other CDFs: PKO3 [49], PKDD [92], DD-ME1 [207], DD-MEδ [148], TW99 [208], PK1 [92], NL3 [209] and TM1 [210]). It is found that the ratio $T_c/\Delta_n(0)$ does not depend much on M^*_{NR}.

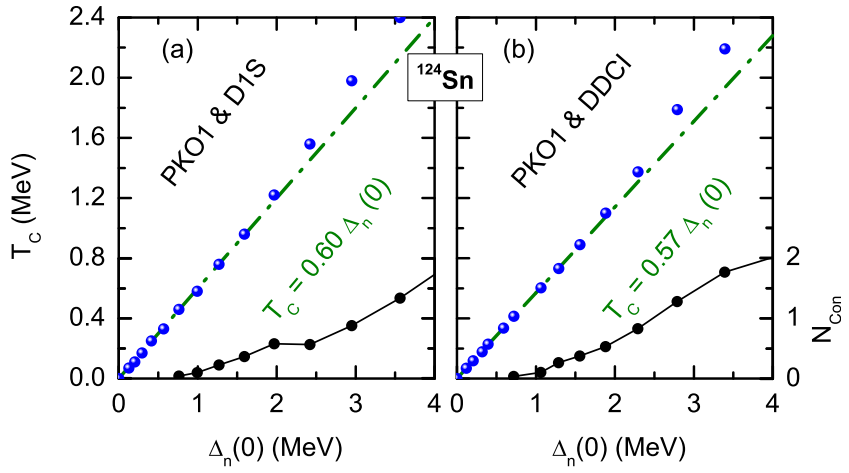

Figure 5.3: The critical temperature T_c (left axes, blue circles) and the occupation number of continuum states N_{con} (right axes, black squares) at zero temperature in ^{124}Sn as a function of the neutron pairing gap calculated from PKO1 FT-RHFB with Gogny D1S (a) and DDCI (b) pairing forces. The dashed lines correspond to the relation $T_c = 0.60(0.57)\Delta_n(0)$. The strength parameter of the pairing interaction is varied to obtain different values of the pairing gap at zero temperature.

Similar analyses were also carried out to check the relations with the incompressibility modulus K and the symmetry energy J, but no evidence of correlation is found. The small fluctuations observed in Fig. 5.2 are therefore mostly shell effects. In conclusion, the critical temperature in stable nuclei scales very well with the average pairing gap at zero temperature, the shell effects contributing to a dispersion of less than 4%.

5.2.3 Influence of the pairing strength

In order to check whether the ratio $T_c/\Delta_n(0)$ is still constant for larger pairing strength, we have artificially varied the pairing interaction strength and correlated the critical temperature T_c with the neutron pairing gap $\Delta_n(0)$ at zero temperature. Figures 5.3(a) and 5.3(b) respectively show the results calculated with the pairing interactions D1S and DDCI using the PKO1 Lagrangian, where the average pairing gap $\Delta_n(0)$ goes from 100 keV up to about 3.5 MeV. At the low pairing gap, the ratios $T_c/\Delta_n(0)$ are consistent with the analytic ones (dashed lines) as expected, until small deviations emerge beyond $\Delta_n(0) \sim 2.5$ MeV, where the continuum contributions become sizable (filled squares). These results are consistent with previous findings [193] based on a separable version of the Gogny D1S pairing force [211] and RH Lagrangian with PC-PK1 point coupling [52]. A simple calculation in infinite matter with a contact pairing interaction gives a correction to the ratio [212]

$$\frac{T_c}{\Delta(0)} \approx 0.57\Big[1 - \frac{1}{4\omega_D^2}\Delta(0)^2\Big], \tag{5.3}$$

where ω_D represents the pairing window. According to Eq. (5.3), the next-to-leading order correction has a negative sign, at variance with our results in ^{124}Sn, see Fig. 5.3. Notice that for the DDCI pairing interaction, the pairing window is about 100 MeV. The correction to the linear approximation of Eq. (5.3) is therefore very small: for the maximal pairing gap considered in this work ($\Delta(0) \approx 4.0$ MeV), the correction represents no more than a few percentages of the linear leading term.

In Fig. 5.3, the increase of the critical temperature for $\Delta_n(0) > 2.0$ MeV reveals an enhancement of the thermal pairing correlations, as well as an the important role played by the continuum states. We remind that the next-to-the-leading order correction appearing in the simple expression in uniform matter (5.3) is negative. However Fig. 5.3 shows a continuous enhanced continuum effect with respect to the pairing gap $\Delta_n(0)$. To better stress the increasing contribution of the continuum states and

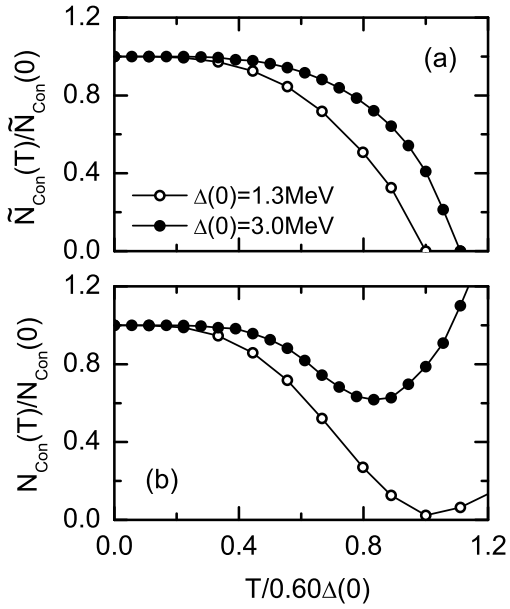

Figure 5.4: Contributions, in ^{124}Sn, of the continuum states to the pairing number $\tilde{N}_{con}$ (a) and to the neutron number N_{con} (b), normalized to their value at zero temperature, as a function of the temperature $T/0.6\Delta(0)$. The results correspond to PKO1 Lagrangian and D1S pairing interaction.

their role in the pairing correlations, we have introduced the following two quantities: the cumulative occupation number of the neutron continuum states N_{con},

$$N_{con} = \sum_{a,\epsilon_a \geq 0} \int 4\pi r^2 \rho_a(r) dr, \tag{5.4}$$

and the cumulative pairing-occupation number of the neutron continuum states $\tilde{N}_{con}$,

$$\tilde{N}_{con} = \sum_{a,\epsilon_a \geq 0} \int 4\pi r^2 \kappa_a(r) dr. \tag{5.5}$$

Here the continuum states a are determined in the $T = 0$ canonical basis, for simplicity [77,194], with s.p. energy ϵ_a above the continuum threshold. The increasing role of the continuum states at finite temperature is illustrated in Fig. 5.4 where the contributions to the pairing number $\tilde{N}_{con}$ [plot (a)] and to the neutron number N_{con} [plot (b)] from the continuum states in ^{124}Sn, normalized to their values at zero temperature, are shown. Results with a weak pairing ($\Delta_n(0) = 1.3$ MeV) and with a stronger pairing ($\Delta_n(0) = 3.0$ MeV) are compared. Even if in the latter case the pairing is slightly larger than the expected value in finite nuclei, its inclusion in our analysis helps to understand the role of the continuum states. For the weak pairing case, the continuum effects are very small, see Fig. 5.3, and both N_{con} and $\tilde{N}_{con}$ drop to zero at the expected value $T_c = 0.6\Delta(0)$, see Fig. 5.4. For the strong pairing case, a clear correlation is observed in Fig. 5.4 between the increase of the occupation of the continuum states at finite temperature N_{con} [see plot (b)] and the persistence of the pairing numbers $\tilde{N}_{con}$ [see plot (a)]. The persistence of pairing correlations below the critical temperature modifies also the critical temperature, and it is observed in Fig. 5.4(a) a larger value of the quantity $T/0.6\Delta(0)$ where pairing correlations in the continuum space drops to zero in the case of strong pairing compared to the weak one. Coming back to Fig. 5.3, we now understand better the correlation between the slight deviations of T_c from the analytical behaviors and enhanced continuum effects for $\Delta(0) \gtrsim 2.5$ MeV. Since the presence of resonance states in the continuum is a typical feature of finite systems, the increase observed in Fig. 5.3, which differs from the prediction of Eq. (5.3), is then expected only in finite systems. Anticipating the results shown in the next figures, a similar enhancement of pairing correlations in other nuclei will also be observed, revealing here also the role of the resonant states.

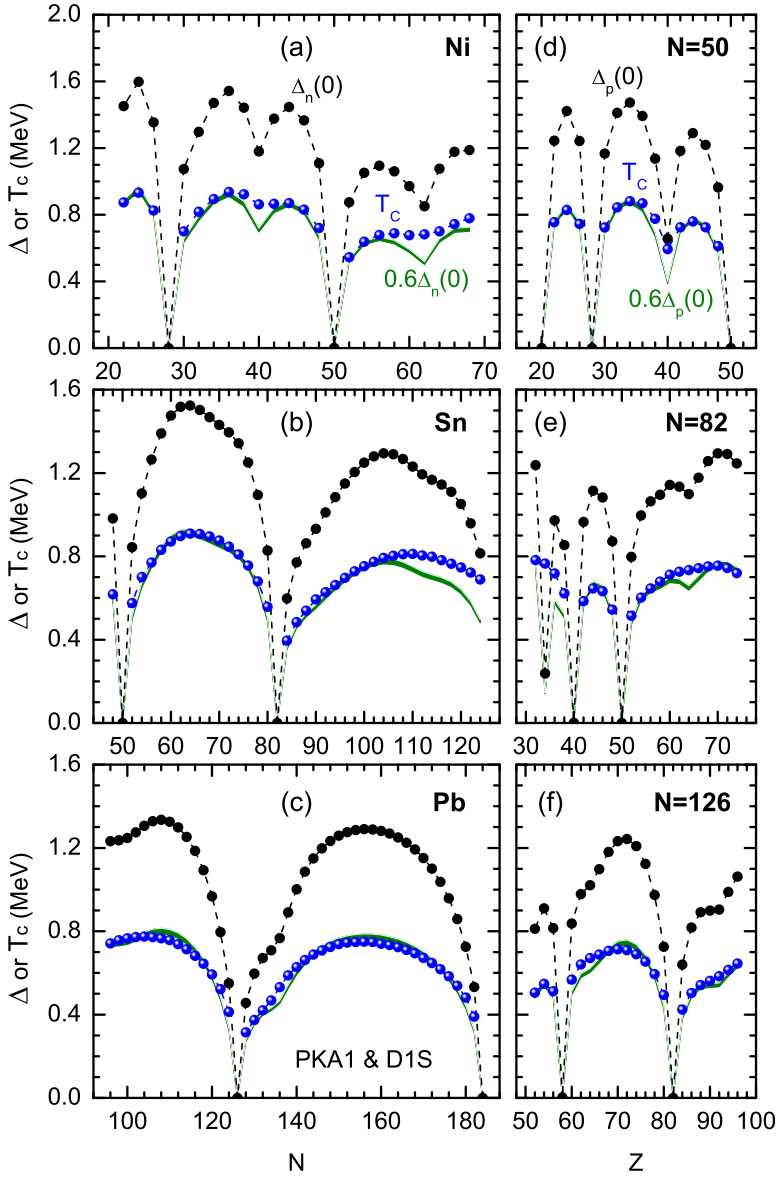

Figure 5.5: Comparison of $\Delta(0)$ (black circles), $0.60\Delta(0)$ (green curves) and T_c (blue circles) in the even-even Ni, Sn, Pb isotopes (left panels) and $N = 50$, 82, 126 isotones (right panels), calculated in FT-RHFB with PKA1 and the Gogny pairing interaction D1S.

5.3 Pairing persistence and re-entrance

In this section, we perform a systematic analysis of the evolution of the pairing gaps and critical temperature along isotopic and isotonic chains of semi-magic nuclei. Through this extensive analysis, we have access to various s.p. configurations going from stable nuclei towards weakly bound drip line nuclei, and we probe the pairing correlations inside various major shells. We consider three models, PKA1 and PKO1 (RHF) and DD-ME2 (RH) which have different symmetry energies and non-relativistic effective masses, see Table 5.1. Anticipating our results, we will see that these models lead to rather different predictions for the pairing gap Δ.

Then, the persistence and re-entrance of the pairing phenomenon will be discussed and analyzed. Let us briefly recall the unifying mechanism which is at play in these various phenomena, recently discussed in Ref. [184]. Due to thermal excitations, s.p. states above the Fermi energy can be slightly populated while states below the Fermi energy can be partially depleted. This occurs if the involved new states are not too far in energy from the last occupied state, but it should also be not too close,

otherwise, these states would already participate to pairing correlations at zero temperature. The typical shell gap should be around 2 MeV. The participation of these states at finite temperature gives rise either to the persistence of pairing correlations slightly above the usual critical temperature for nuclei which are already superfluid at zero temperature, or to pairing re-entrance at finite temperature for nuclei which have weak or no pairing at zero temperature. The best nuclei, in which such a phenomenon is expected, are those close to the drip line, as well as those located at a subshell closure as shown in this section.

5.3.1 Evolution of the critical temperature

Our results are shown for PKA1 (Fig. 5.5), PKO1 (Fig. 5.6) and DD-ME2 (Fig. 5.7) models, with the pairing channel described by the D1S interaction. In Figs. 5.5-5.7, we have represented isotopic (Ni, Sn and Pb) and isotonic ($N = 50$, 82, and 126) average pairing gap evolution as a function of N (for isotopes) and Z (for isotones). The isotopic and isotonic chains are bounded by the drip lines predicted by each of the considered models and determined by the two-nucleon separation energy. These drip lines are consistent, within a few units of uncertainty, with predictions given by other models obtained with Skyrme forces [213,214], Gogny forces [215,216] and RH Lagrangians [203,217]. We have calculated the average pairing gap at zero temperature (filled black circles) defined from Eq. (2.138), and compared the calculated critical temperature (filled blue circles) with the approximate relation, i.e., $0.6\Delta(0)$ (green curves). The arch structure of the results shown in Figs. 5.5-5.7 reflect the presence of magic numbers where pairing correlations completely vanish.

The PKA1 model (Fig. 5.5) is the most complete RHF version of the CDF theory. It contains the ρ-N Lorentz tensor coupling which is known to enhance the spin-orbit splitting [48,101,149]: in many cases the subshell structure is found to be closer to the experimental data than those predicted by other models without the ρ-N Lorentz tensor coupling, such as the RH approaches shown in Fig. 5.7. These subshell structures are clearly visible in Figs. 5.5-5.7 since they induce a partial quenching of the pairing gap for the associated submagic numbers. Going towards the drip lines, a reduction of the pairing gaps is often observed, revealing the presence of closed-shell nuclei at or near the drip lines. For the neutron drip line, it is the case of Sn and Pb isotopes, and for the proton drip line, it is observed for $N = 50$.

We first discuss the pairing properties of finite nuclei at zero temperature, which are influenced by the underlying s.p. structure around the Fermi energy. For the Ni isotopes, a subshell closure at $N = 40$ is predicted with PKA1 and PKO1 Lagrangians, as expected from experiments [218], while DD-ME2 shows a more pronounced shell closure. For neutron rich Ni isotopes, PKA1 indicates another subshell closure at $N = 62$ which is not seen with PKO1 or DD-ME2. It is, however, beyond the present experimental limits. For the Sn isotopes, a decrease of the pairing gap induced by subshell closure is observed at $N = 64$ with PKO1 and DD-ME2 Lagrangians, but not with PKA1. For Pb, a small decrease of the pairing gap is observed at $N = 138$ with PKA1 and at $N = 146$ with PKO1 and DD-ME2. On the isotonic side, we observe a subshell closure at $Z = 40$ for $N = 50$ with PKA1 Lagrangian, but not with PKO1 or DD-ME2. For $N = 82$ isotones, PKA1 predicts a well marked shell closure at $Z = 40$ and a subshell closure at $Z = 34$ and $Z = 64$, while at $Z = 58$ PKO1 predicts a shell closure and DD-ME2 only a subshell closure. Finally, for $N = 126$, PKO1 and DD-ME2 indicate a reduction of the pairing gap at $Z = 92$, which is not confirmed by experimental data [100] and is not present with PKA1 Lagrangian. We will see below that these structures can have an impact on the thermal properties.

Turning now to the thermal properties of these isotopes and isotones, the comparison of the calculated critical temperature T_c and the approximate relation $0.60\Delta(0)$ shown in Figs. 5.5-5.7 exhibits some interesting features. The critical temperature T_c and the approximate relation $0.60\Delta(0)$ are identical in most cases with some exceptions. In heavy nuclei (Pb and $N = 126$), there are no strong deviations between these two quantities, but they are however more marked in lighter nuclei. More-

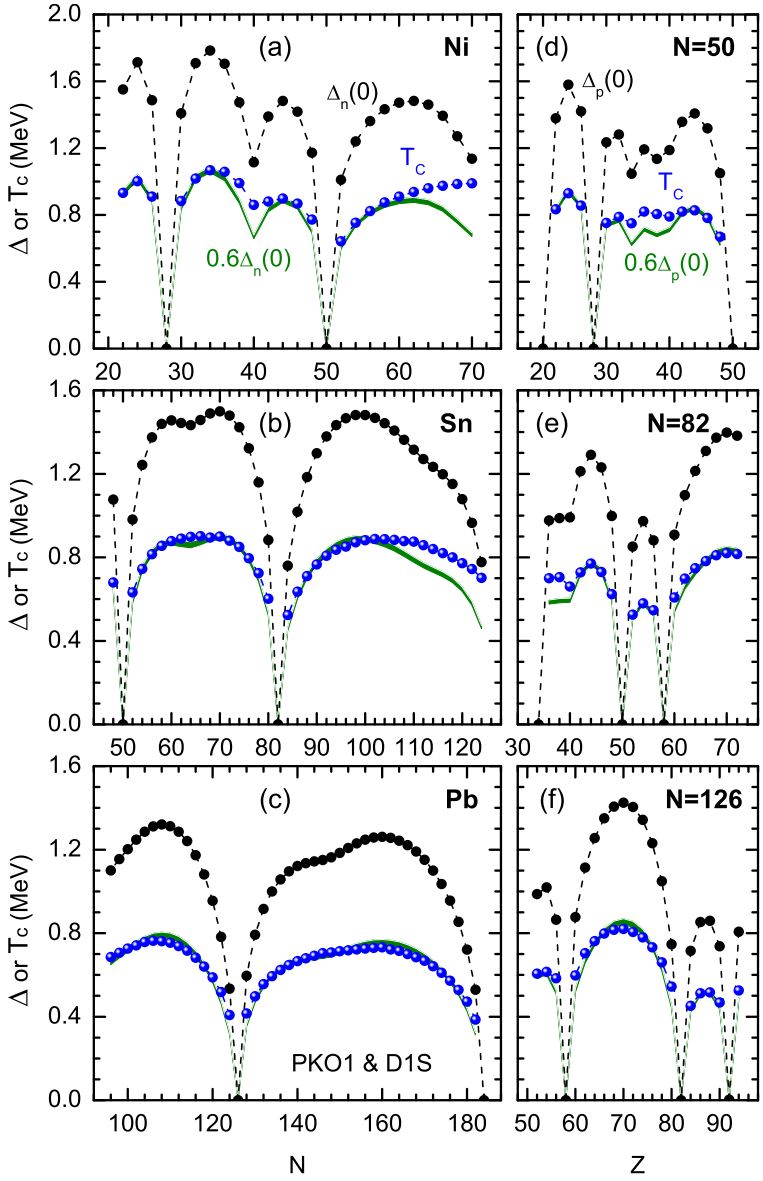

Figure 5.6: The same as in Fig. 5.5, but calculated in the FT-RHFB theory with the effective interaction PKO1.

over, the cases where the exact and the approximate values of T_c differ are correlated with either the presence of a subshell closure, or with the proximity of the drip lines. In the case of subshell closure, the effect of the temperature is to "wash out" the decrease of the pairing correlations. This can be understood as the consequence of the thermal occupation probabilities which overcome small shell gaps. Close to the neutron drip lines, the more pronounced effects are observed in Ni and Sn isotopes. This is also due to the thermal occupation of close-by resonant states as discussed in Refs. [184, 219]. In the non-relativistic Skyrme Hartree-Fock plus BCS (SHF-BCS) approach, an enhancement of the critical temperature was found in ^{140}Sn using SkT6 [191]. We do not confirm this enhancement in ^{140}Sn with the models used in this work. However, it is interesting to notice that the origin of such an enhancement found in Ref. [191] is also related to the existence of a subshell closure.

Let us finish this subsection with some general remarks concerning the nuclei which do not manifest any enhancement of the critical temperature. For the Pb isotopes, as shown in Figs. 5.5-5.7, we have not observed any marked enhancement of the critical temperature near the drip line as in the case of Sn isotopes. Comparing Pb and Sn, since the pairing gap for these isotopes is decreasing near the drip line, one could have expected to observe an enhancement of the critical temperature in Pb as

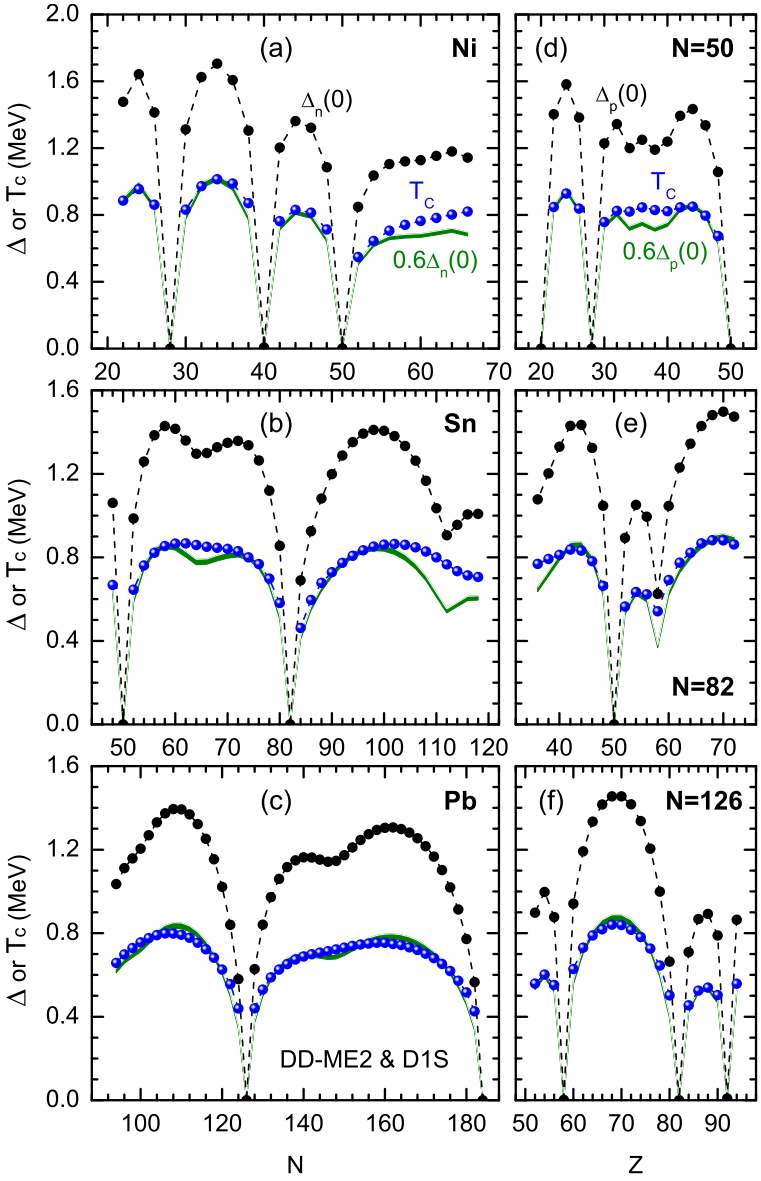

Figure 5.7: The same as in Fig. 5.5, but calculated in the FT-RHB theory with the effective interaction DD-ME2.

it is observed in Sn. For instance, the last occupied state in the drip line nucleus ^{266}Pb is indeed found to be well bound ($\epsilon_{3d_{3/2}} < -2.0$ MeV), and the lowest s.p. resonance $\epsilon_{2h_{1/2}}$ is found to be above 1.5 MeV. There is therefore a rather strong gap in the neutron rich Pb isotopes ($N = 184$) which prevents the large coupling to the continuum. For the isotonic chains, we do not find any pairing persistence phenomenon around the drip line. This can be related to the well developed shell closures at $Z = 50, 82$ and 92 for proton-rich nuclei, which quench the coupling to continuum states, as it would have been expected in such exotic nuclei. In addition, the coupling to the continuum is weaker for protons since the Coulomb barrier tends to localize the proton density in the nuclear interior [220]. For these reasons, the persistence phenomenon is strongly quenched in the proton channel.

5.3.2 Pairing persistence in ^{68}Ni

In this subsection, we analyze in more details the temperature dependence of the pairing gap for two representative nuclei, ^{68}Ni and ^{174}Sn. On the one hand, ^{68}Ni is an isotope which is slightly more neutron rich than the five stable isotopes $^{58-64}$Ni. As shown in the previous subsection, ^{68}Ni is considered as a subshell isotope [203, 221, 222], and as a consequence, the pairing gap at zero temperature

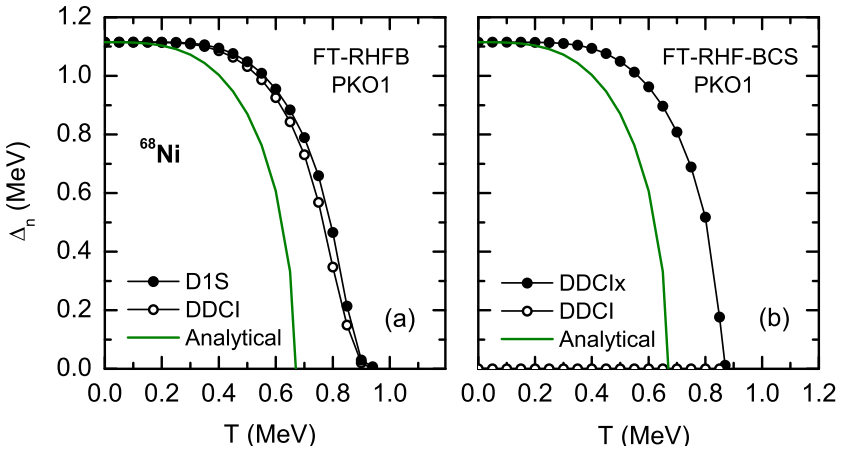

Figure 5.8: The neutron pairing gaps in ^{68}Ni as a function of temperature, calculated by FT-RHFB with Gogny D1S and DDCI pairing forces, and by FT-RHF-BCS with DDCI pairing force. To evaluate the persistence provoked by the subshell, the analytical results are also shown. The pairing strength V_0 (in MeV.fm^{-3}) is fixed to be 326 (DDCI) and 537 (DDCIx).

is either reduced or strongly quenched depending on the model, see Figs. 5.5-5.7. On the other hand, ^{174}Sn is a very neutron-rich isotope at or close to the neutron drip line, where the continuum effects are expected to be remarkable [73,184,185,223]. However, since ^{174}Sn is close to the potentially doubly magic ^{176}Sn (Z=50, N=126), a gap is expected to be present in the s.p. structure between bound and resonant states. These two nuclei are therefore representative of quantum systems for which pairing at zero temperature is weakened by the presence of a gap above the Fermi energy and where a finite amount of temperature allows to overcome the gap and provokes an enhancement of pairing correlations, giving rise to pairing persistence.

We first show the temperature dependence of the pairing gap for ^{68}Ni in Fig. 5.8(a), calculated with the FT-RHFB model where we consider the PKO1 Lagrangian in the mean field channel and either Gogny D1S or DDCI interaction in the pairing channel. The analytical model is also shown for reference. It is found that the predictions for $\Delta_n(T)$ do not practically depend on the pairing force. The critical temperature predicted by the FT-RHFB approach is increased with respect to the reference analytical model: the FT-RHFB pairing gaps vanish around $T = 0.90$ MeV, which is 0.25 MeV higher than the expected value (0.65 MeV). The pairing gap predicted by FT-RHF-BCS is shown in Fig. 5.8(b). Surprisingly, the pairing gap is zero if the same DDCI pairing interaction is used. An increase of the pairing strength V_0 is therefore necessary. It is also interesting to observe that the DDCIx pairing interaction, where V_0 is increased to match with the zero temperature pairing gap obtained with FT-RHFB case, reproduces almost exactly the temperature dependence of the FT-RHFB case and predicts as well an increase of the critical temperature with respect to the analytical model. The nucleus ^{68}Ni is a typical example of pairing persistence at finite temperature in closed subshell ($N = 40$) nuclei. We hereafter name this phenomenon type I pairing persistence. Other examples of similar behavior are: ^{90}Ni (PKA1), ^{114}Sn (PKO1, DD-ME2), ^{220}Pb (PKA1), ^{230}Pb (DD-ME2) for the neutron pairing gap, and ^{90}Zr (PKA1, PKO1 and DD-ME2), ^{140}Ce (DD-ME2), ^{146,190}Gd (PKA1) for the proton pairing gap.

5.3.3 Pairing persistence in ^{174}Sn

We turn now to the analysis of the results in ^{174}Sn. As stated above, this is a nucleus where pairing correlations are slightly weakened due to the proximity of shell closure. A small amount of temperature is expected to reorganize the level occupancy around the Fermi energy, opening more space below the Fermi energy, and producing a non-zero occupancy of the first levels above the Fermi energy which are in the continuum. Most of the occupied states in the continuum are resonance

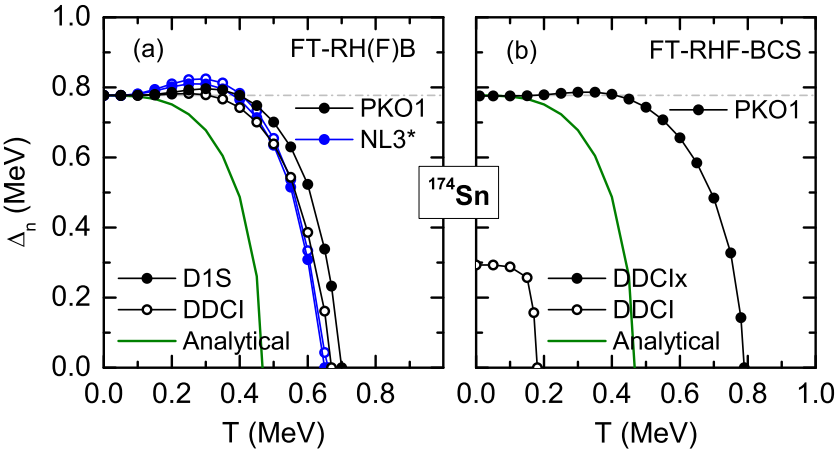

Figure 5.9: The neutron pairing gaps in ^{174}Sn as a function of temperature, calculated with PKO1 and NL3*, using Gogny D1S and DDCI pairing forces. The results of the analytical model are also shown. The pairing strength V_0 (in MeV.fm^{-3}) is: 333 (DDCI with PKO1), 317 (DDCI with NL3*) and 596 (DDCIx with PKO1 and BCS framework).

states, but it is interesting to notice that a small number of them are also non-resonant states [224]. Without the participation of these non-resonant states, the asymptotic behavior of the density would be ill-defined and present an unexpected gas component, as it is also observed in the BCS theory [73]. The Bogoliubov transformation couples all states in a sub-(l, j) space and a truncation among these states breaks the unitarity of this transformation. To avoid the presence of non-physical gas component in the density profile, it is therefore important to couple all states in the continuum within the Bogoliubov transformation.

Figure 5.9(a) displays the evolution of the neutron pairing gap as a function of temperature in ^{174}Sn with different Lagrangians and pairing forces. The results are very weakly affected by the choice of the pairing interaction. The effect induced by the choice of Lagrangian is also very small. We find a systematic increase of the critical temperature ($T_c \approx 0.65 - 0.70$ MeV) with respect to that expected from the analytical relation ($T_c \approx 0.47$ MeV), independently of the considered model. In addition, for temperature $T > 0.2$ MeV, an increase of the pairing gap is observed, which can also be related to the thermally induced contribution of the continuum states. We compare these results to the ones obtained with the FT-RHF-BCS framework shown in Fig. 5.9(b). As already discussed, the DDCI interaction predicts a reduced pairing gap in BCS compared to RHFB. On the other side, the DDCIx interaction where the pairing strength is increased to match the $T = 0$ predictions of RHFB leads to an overestimation of the critical temperature compared to the FT-RHFB case. It shows that, in this case of dripline nucleus, the RHFB calculation cannot be simply reproduced by a BCS calculation where the pairing strength is just increased. Since the coupling to the continuum plays a dominant role in the persistence phenomenon in ^{174}Sn, we hereafter call it type II phenomenon. From our results, it is also expected to occur in Ni and Sn neutron-rich nuclei, Ni ($N > 54 \sim 60$) and Sn ($N > 100$).

5.4 Entropy and specific heat

We now focus on the entropy S and specific heat C_v which are the first and second derivatives of the free energy F with respect to the temperature, and thus sensitive to thermal changes of the ground state, see for instance Ref. [225] and Refs. therein. To test the sensitivity of these quantities to the choice of different models, we select two Sn isotopes, ^{120}Sn and ^{160}Sn. The former is a good example of a stable well-paired nucleus, while the latter is yet far from actual nuclear experiments but represents an extreme case with large isospin asymmetry.

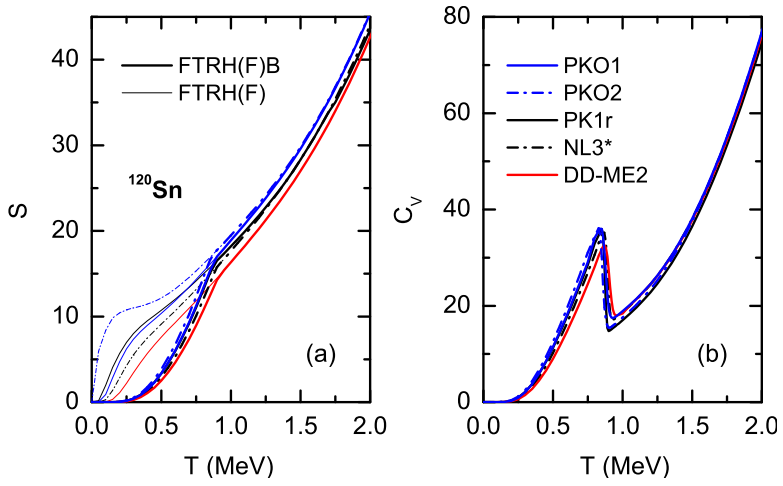

Figure 5.10: Entropy and specific heat in ^{120}Sn as a function of temperature, calculated using the FT-RH(F)B and FT-RH(F) theories.

In Fig. 5.10 are shown the entropy S and the specific heat C_v as functions of the temperature calculated by the RHF functionals PKO1 and PKO2, the RH ones with the non-linear self-couplings PK1r and NL3*, and the RH one with density-dependent meson-nucleon couplings DD-ME2. In the pairing channel, the value of the scaling factor g, is slightly modified to give identical pairing gaps at zero temperature for the different models. In Fig. 5.10(a), the entropy calculated with the pairing correlations [labeled FT-RH(F)B] is compared to that neglecting the pairing correlations [labeled FT-RH(F)]. At low temperature, if the pairing effects are ignored, the entropy is found to be largely model-dependent, i.e., the model with smaller non-relativistic effective mass (see Table 5.1), which leads to larger s.p. level spacing on the average, presents smaller entropy. As the temperature increases, and also as the pairing correlations are switched on, the entropy becomes less model-dependent.

In fact, at low temperature or without pairing correlations, the entropy is largely determined by the few states around the Fermi energy, and the number of the involved states is essentially determined by the detailed s.p. spectrum which depends on the models, therefore leading to model-dependent entropy. Both temperature and pairing correlations can disperse the particle over the states beyond the Fermi level. As the temperature increases, and/or as the pairing correlations are enhanced, more s.p. states will get involved to contribute to the entropy, and the average properties such as the density of states will become dominant, instead of a few states as in the FT-RH(F) cases. Compared to distinctly different s.p. spectra around the Fermi surface, the dispersions of the non-relativistic effective masses (see Table 5.1) between the models are less remarkable. Even though, in Fig. 5.10(a) it is clearly shown that the FT-RH(F)B results are grouped by the values of the effective masses when $T \gtrsim 1$ MeV which correspond to different average densities of states. As expected, the effect of the pairing correlations is clearly visible below the critical temperature ($T_c \approx 0.8$ MeV), inducing a strong reduction of the entropy [see Fig. 5.10(a)] and singular behaviors of the specific heat around the critical temperature as shown in Fig. 5.10(b). Just above the critical temperature, we can notice that the specific heat is not linear in T, as expected from the Fermi gas model [226, 227], and the linear dependence seems to be found at slightly larger temperature ($T > 1.5$ MeV). The non-linearity of the specific heat around T_c might be related to shell effects.

The results thus clearly show that the pairing correlations contribute to the s-shaped behavior of the specific heat, as it has already been inferred from the analysis of thermal excited nuclei in laboratory experiments [178,180,227]. A realistic description of the smooth s-shaped behavior in finite nuclei requires a more elaborated modeling, including for instance particle number projection [177,228–230]. It is however shown in Ref. [198] that the smooth s-shaped behavior may be even washed out in some rare earth nuclei. The results presented in Fig. 5.10 should not be compared directly to the

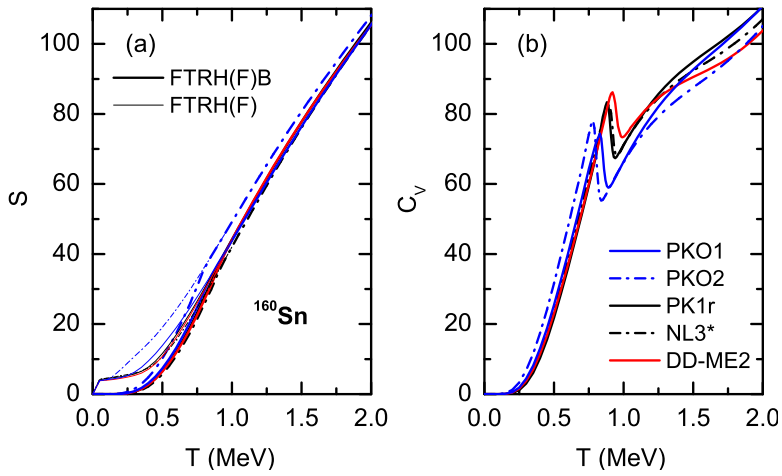

Figure 5.11: The same as in Fig. 5.10, but for ^{160}Sn.

semi-experimental data.

The situation for the neutron-rich nucleus ^{160}Sn is more complex as shown in Fig. 5.11. The model dependence of entropy at low temperature is reduced compared to the case of ^{120}Sn. Only PKO2 predictions differ from the other models. The predictions for the critical temperature, associated to the discontinuity in the specific heat of Fig. 5.11, vary among the modelings to a much larger extent than what was found in ^{120}Sn. ^{160}Sn is located in the region where pairing persistence is expected to appear, see Figs. 5.5-5.7. Since this phenomenon is strongly related to the position of resonance states in the continuum, we expect to observe deviations among models predicting different positions of these states. This model dependence therefore reveals our lack of knowledge in extrapolating Lagrangians which have been adjusted for less exotic nuclei.

5.5 Summary and conclusions

In this work, we have developed the first FT-RHFB theory for spherical nuclei. The self-consistent FT-RHFB equations are solved by using a DWS basis which provides an appropriate asymptotic behavior for the continuum states. We have performed systematic FT-RHFB calculations for both stable and weakly bound nuclei and discussed their thermal properties. The influence of the pairing interaction on the pairing phase transition is evaluated. It is found that the critical temperature for a pairing transition generally follows the rule $T_c = 0.60\Delta(0)$ with a finite-range pairing force and $T_c = 0.57\Delta(0)$ with a contact pairing force. The finite- or zero-range nature of the pairing force, while generating different state-dependence pairing gaps, causes only small differences in our results. We have described the pairing persistence in two kinds of situations: nuclei at subshell closure (type I), and nuclei strongly coupled to continuum states which are close to the drip line (type II). We have observed that, while a refitting of the pairing strength could match the FT-RHF-BCS with the FT-RHFB predictions for the pairing gap in the case I, it is no longer the true in the case II. This is due to the participation of the continuum states in the second case which involve coupling of a different nature.

We have also analyzed the influence of the interaction on the thermal response. The results show clearly that the pairing correlations contribute to the *s*-shaped behavior of the specific heat curve, and help to wash out the model dependence. For stable nuclei the model deviations, to some extent, can be traced back to the effective mass, since the level structure only weakly depends on the choice of the CDF. The situation for exotic nuclei is more complex since it is related to our lack of knowledge in very exotic nuclei, and the pairing persistence would have large effects on their thermal property.

In conclusion, we have illustrated the richness and complexity of pairing correlations at finite

temperature and in finite systems within the first FT-RHFB calculation. The discussion of correlations beyond mean-field, induced for instance by particle number projection, is not addressed in this work. It is however expected that the particle number projection will contribute to increase the pairing correlations in the case where they are weak [198], like in the pairing persistence phenomenon discussed in this paper. In future work, a more quantitative calculation will be necessary to estimate the strength these additional correlations and how they modify the results presented in this work. Another interesting perspective which is suggested by this work is the possibility that similar phenomena can be observed in other domains of physics. For instance, it was studied whether cold atoms in a double potential could demonstrate pairing persistence as well [231]. Finally, the application of this formalism for the prediction of temperature evolution of pairing properties in the crust of neutron stars [181, 232, 233] will be performed in the near future. There, the thermal modification of pairing correlations could have a large impact on the thermal relaxation of the crust [182], and could be observed during the quiescent period of low mass X-ray transients.

Chapter 6

Conclusions and perspectives

An expert is a persion who has made all the mistakes that can be made in a very narrow field.

Niels Bohr, 1885-1962

This work was undertaken to give a global survey of properties of exotic and superheavy elements using the CDF method and its extension to finite temperature case. This survey serves on the one hand to confirm recent experimental achievements and to make predictions in the regime of exotic and superheavy elements. On the other hand these large scale calculations, especially in the very neutron rich region, will provide necessary nuclear information in order to constrain RHF model itself. The CDF model is also able to describe extreme systems such as Wigner-Seitz cells in the crust of neutron stars.

After giving a short review of the CDF theory and its generalization to the finite temperature case, we journeyed to extreme conditions of mass, isospin and temperature.

In the first part of this work, the occurrence of spherical shell closures in SHN and the physics therein have been investigated using the RHFB theory with density-dependent meson-nucleon couplings, in comparison with the predictions of some RHB models. The shell effects are quantified in terms of two-nucleon gaps $\delta_{2n(p)}$ and pairing gaps $\Delta_{2n(p)}$. The results indicate that the nuclide $^{304}120$ could be the next spherically doubly magic nuclide beyond ^{208}Pb. It is also found that the shell effects in SHN are sensitive to the values of both scalar mass and effective masses, which essentially determine the spin-orbit (SO) effects and level density, respectively. The splittings between pseudospin (PS) partners are found to be tightly related with the emergence of superheavy magic shells. Additionally the analysis of shell evolution as well as the density profile indicate that the emergence or the disappearance of shell closure is tied up with the evolution of the central and SO mean fields, a feature that covariant mean field models may describe in a more unified way as compared to non-relativistic density functional approaches.

In the second part of the work, the formation of new shell gaps in neutron-rich nuclei is investigated within the RHFB theory and the role of the Lorentz pseudo-vector and tensor interactions is studied in detail. Since both relativistic and non-relativistic models could equally well reproduce global properties of finite nuclei, such as binding energies and radii, we here concentrate on predictions for s.p. evolution. We have illustrated in intermediate mass nuclei the very important role played by the Lorentz pseudo-vector and tensor interactions which cannot be simply reduced to their rank-2 irreducible tensor contribution. While these two terms generally appear separately in non-relativistic nuclear models, they originate from the same interaction vertex in the relativistic ones, which impose some very specific behavior. We confirm new magic nuclei such as ^{24}O, ^{52,54}Ca. We conclude from this study that the detailed evolution of s.p. energies could potentially sign relativistic effects such as

the Lorentz pseudo-vector and tensor interactions.

In the third part of the work, we have implemented the first FT-RHFB calculation for studying the thermal excitations and phase transitions of both stable and weakly-bound nuclei. The predictions of various relativistic Lagrangians and different pairing interactions are discussed. The critical temperature of the pairing transition is found to depend linearly on the zero-temperature pairing gap, and this dependence is similar for a zero-range or a finite-range pairing interaction. The present calculations show interesting features of the pairing correlations at finite temperature, such as the pairing persistence and pairing re-entrance phenomena. Two types of pairing persistence are analyzed: type I pairing persistence occurs in closed subshell nuclei while type II pairing persistence can occur in loosely bound nuclei strongly coupled to the continuum states.

We would also like to give a brief outlook of future extensions and improvements, planned or already under development, which show the direction and possibilities that such a framework offers. These include:

- I. Improving parameter sets. The limitation of the RHF model is related to the fact that, although the nuclear effective interaction used nowadays is based on meson-exchange theory with relativistic covariance, it is not exactly derived from the basic theory of the strong interaction. In fact, within the RHF framework, some attempts were already devoted to evaluate the nuclear in-medium effects under the constraints of the microscopic calculations. I have already initiated a work in this direction which is presented in the appendix of the document. The idea is to complement the Lagrangian to get realistic nuclei.

- II. Applications to astrophysics. A direct and natural application of this work is the better determination of the crust of neutron stars from a fully self-consistent RHFB approach and the investigation of the effects of temperature therein. Then, one could study the impact of WS cells on neutron pairing gap, and further extract the contribution of neutron superfluidity to specific heat, from which the correlation between neutron superfluidity and pulsar glitches shall be explored, in comparison with the observational data. I have already implemented the mixed Dirichlet-Neumann boundary condition to this direction. Present limitation is given by the number of states involved which cannot exceed about 400 nucleons, due to the memory space. The numerical limitation shall be overcome taking advantage of a new algorithm — for matrix orthogonalization.

- III. Toward hyperonic matter. Extend the RHF approach of nucleonic matter to RHF approach of hyperonic matter, for both a uniform system and a non-uniform system. As a further project, we aim at extending RHF to the hypernuclear sector within the SU(3) symmetry. Then apply systematically this new approach to known properties of hypernuclei. Finally, one can deduce the consequence of these constraints to the physics of neutron stars.

Appendix A

Dirac self-energies and Hartree-Fock potentials

In this appendix the basic ideas of how to derive the Dirac self-energy and their detailed expressions are presented.

A.1 Dirac Hartree-Fock equations

The variational procedure with respect to the single-particle wave functions $G(r)$ and $F(r)$ leads to the radial integro-differential Dirac HF equations,

$$E_a \begin{pmatrix} G_a(r) \\ F_a(r) \end{pmatrix} = \begin{pmatrix} M + \Sigma_S(r) + \Sigma_0(r) & -\frac{d}{dr} + \frac{\kappa_a}{r} + \Sigma_T(r) \\ \frac{d}{dr} + \frac{\kappa_a}{r} + \Sigma_T(r) & -[M + \Sigma_S(r) - \Sigma_0(r)] \end{pmatrix} \begin{pmatrix} G_a(r) \\ F_a(r) \end{pmatrix} + \begin{pmatrix} Y_a(r) \\ X_a(r) \end{pmatrix}. \tag{A.1}$$

In these equations, Σ_S and Σ_0 represent the contributions from the direct (Hartree) terms and the rearrangement term, X and Y denote the contributions from the exchange (Fock) terms. The explicit expressions are listed in the following.

A.2 Dirac Hartree-Fock potentials

From the variational principle (2.26), one obtains the local self-energies

$$\Sigma_H \begin{pmatrix} G_a \\ F_a \end{pmatrix} = \begin{pmatrix} \dfrac{\delta}{\delta G_a} \\ \dfrac{\delta}{\delta F_a} \end{pmatrix} E \tag{A.2}$$

with E being potential energy. While, the non-local self-energies $(X, Y)^T$ terms are introduced by

$$\Sigma_F = \begin{pmatrix} X_\alpha \\ Y_\alpha \end{pmatrix} = \frac{1}{2\hat{j}_a^2} \begin{pmatrix} \dfrac{\delta}{\delta F_a} \\ \dfrac{\delta}{\delta G_a} \end{pmatrix} E, \tag{A.3}$$

they are in fact integrals involving the unknown functions $\{G_a, F_a\}$.

In RHF calculation, extensive use will be made of the reduced matrix elements of the tensorial operators $Y_L^m(\hat{\boldsymbol{r}})$ and $\mathcal{T}_{\mathcal{J}L}^{\mathcal{M}}(\hat{\boldsymbol{r}})$, the last one being defined as

$$\mathcal{T}_{\mathcal{J}L}^{\mathcal{M}} = \sum_{mk} \langle L1mk \| \mathcal{J}\mathcal{M} \rangle Y_L^m \sigma^k \tag{A.4}$$

with

$$\sigma^{\pm 1} = \sigma_{\pm 1} = \mp\frac{1}{2}\sqrt{2}(\sigma_1 \pm i\sigma_2), \quad \text{and} \quad \sigma^0 = \sigma_3. \tag{A.5}$$

Introducing $|a\rangle = |\alpha\mathcal{J}\rangle$, we obtain their reduced matrix elements

$$\langle a\|Y_L\|b\rangle, \qquad \langle a\|\mathcal{T}_{\mathcal{J}L}\|b\rangle, \tag{A.6}$$

which are defined via the Wigner-Eckart theorem, see Remark 1.

A.2.1 Scalar coupling: $\Gamma = 1$

We take here the σ-meson as an example. The contributions from σ-meson in Hamiltonian (2.17) can be expressed as

$$E_\sigma = -\frac{1}{2}\sum_{\alpha\beta}\iint d\boldsymbol{r}d\boldsymbol{r}'\bar{f}_\alpha(\boldsymbol{r})\bar{f}_\beta(\boldsymbol{r}')\big[g_\sigma(\boldsymbol{r})g_\sigma(\boldsymbol{r}')D_\sigma(\boldsymbol{r},\boldsymbol{r}')\big]f_\beta(\boldsymbol{r}')f_\alpha(\boldsymbol{r}) \tag{A.7}$$

with $D_\sigma(\boldsymbol{r},\boldsymbol{r}')$ is a Yukawa propagator. At the HF level, the contributions to potential energy can be separated into two parts: direct and exchange parts.

Hartree term

Using

$$\int d\hat{\boldsymbol{r}}Y_L(\hat{\boldsymbol{r}}) = \sqrt{4\pi}\delta_{L0}, \tag{A.8}$$

the evaluation of Hartree terms becomes a simple task. There is only a contribution from $L = 0$ in the multipole expansion of Yukawa propagator in Remark 2.

$$E_\sigma^D = -\frac{1}{2}4\pi\int dr\, r^2 g_\sigma(r)\int dr'\, r'^2 g_\sigma(r')\rho_s(r)\mathcal{R}_{00}(m_\sigma;r,r')\rho_s(r') \tag{A.9}$$

where the expression of the propagator $\mathcal{R}_{00}$ is

$$\mathcal{R}_{00}(m_\sigma;r,r') = -m_\sigma\frac{e^{-m_\sigma r_<} - e^{m_\sigma r_<}}{2m_\sigma r_<}\cdot\frac{e^{-m_\sigma r_>}}{m_\sigma r_>}. \tag{A.10}$$

and $r_>$ ($r_<$) denotes the larger (smaller) of r and r'. The scalar density ρ_s is defined in Eq. (2.60a). With the relation (A.2), we obtain the Hartree components of self-energy as

$$\Sigma_{S,\sigma}(r) = -g_\sigma\int dr'\, r'^2 g_\sigma(r')\rho_s(r')\mathcal{R}_{00}(m_\sigma;r,r'). \tag{A.11}$$

Fock term

The Fock contributions are more complicated. With the expansion of $D_\sigma(m_\sigma;r,r')$ given in Remark 2, it can be expressed in terms of reduced matrix elements defined in Remark 6,

$$\begin{aligned} E_\sigma^E = \frac{1}{2}\iint dr dr'\sum_{ab}\delta_{\tau_a\tau_b}\hat{j}_a^2\sum_L\Big[g_\sigma\big(G_aG_b\langle a\|Y_L\|b\rangle - F_aF_b\langle a'\|Y_L\|b'\rangle\big)\Big]_r \\ \times R_{LL}(m_\sigma;r,r')\Big[g_\sigma\big(G_bG_a\langle a\|Y_L\|b\rangle - F_bF_a\langle a'\|Y_L\|b'\rangle\big)\Big]_{r'}. \end{aligned} \tag{A.12}$$

The relation (A.3) leads to the Fock components of the self-energy

$$\begin{pmatrix} X^{(\sigma)} \\ Y^{(\sigma)} \end{pmatrix}_r = g_\sigma\hat{j}_a^{-2}\sum_b\delta_{\tau_a\tau_b}\begin{pmatrix} -F_b \\ G_b \end{pmatrix}_r\sum_L|\langle a\|Y_L\|b\rangle|^2$$

$$\times \int dr' R_{LL}(m_\sigma; r, r') \big[g_\sigma (G_a G_b - F_a F_b) \big]_{r'}. \tag{A.13}$$

For the reduced matrix element, it is convenient to use expression (B.27) in Remark 7. Equation (A.13) thus can be rewritten as,

$$\begin{pmatrix} X^{(\sigma)} \\ Y^{(\sigma)} \end{pmatrix}_r = g_\sigma \sum_b \delta_{\tau_a \tau_b} \frac{\hat{j}_b^2}{4\pi} \begin{pmatrix} -F_b \\ G_b \end{pmatrix}_r \sum_L{}' \left(C^{L0}_{j_a \frac{1}{2} j_b -\frac{1}{2}} \right)^2 \times \int dr' R_{LL}(m_\sigma; r, r') \big[g_\sigma (G_a G_b - F_a F_b) \big]_{r'}, \tag{A.14}$$

the summation over b is carried out over all occupied states. Here and after, the notation $\sum_L{}'$ ($\sum_L{}''$) means that $L + l_a + l_b$ must be even (odd).

The contribution to the rearrangement term from the density-dependent meson-nucleon coupling is

$$\Sigma_R^{(\sigma)} = \frac{\partial g_\sigma}{\partial \rho_v} \frac{1}{g_\sigma} \Big[\rho_s \Sigma_{S,\sigma} + \sum_\alpha \frac{\hat{j}_a^2}{4\pi r^2} \big(G_a Y_\alpha^{(\sigma)} + F_a X_\alpha^{(\sigma)} \big) \Big]. \tag{A.15}$$

The contributions of the δ meson is deduced from the σ meson, making the following replacements:

$$m_\sigma, g_\sigma \to m_\delta, g_\delta, \qquad \rho_s \to \rho_s^{(3)}, \qquad \sum_{ab} \delta_{\tau_a \tau_b} \to \sum_{ab} (2 - \delta_{\tau_a \tau_b}). \tag{A.16}$$

A.2.2 Vector coupling: $\Gamma = \gamma^\mu$

We take the ω-meson as an example. The contributions from ω-N vector coupling can be expressed as

$$E_\omega = -\frac{1}{2} \sum_{\alpha\beta} \iint d\boldsymbol{r} d\boldsymbol{r}' \bar{f}_\alpha(\boldsymbol{r}) \bar{f}_\beta(\boldsymbol{r}') \big[g_\omega(\boldsymbol{r}) \gamma_\mu(1) g_\omega(\boldsymbol{r}') \gamma^\mu(2) D_\omega(\boldsymbol{r}, \boldsymbol{r}') \big] f_\beta(\boldsymbol{r}') f_\alpha(\boldsymbol{r}) \tag{A.17}$$

with propagator $D_\omega(\boldsymbol{r}, \boldsymbol{r}')$.

Hartree term

Since the baryon current is conserved, $\partial_\nu j^\nu = 0$, the spatial part of the ω-field vanishes. Thus, as we have done for the σ-meson, the direct contributions reads,

$$E_\omega^D = \frac{1}{2} 4\pi \int dr\, r^2 g_\omega(r) \int dr'\, r'^2 g_\omega(r') \rho_v(r) \mathcal{R}_{00}(m_\omega; r, r') \rho_v(r'), \tag{A.18}$$

where the vector density ρ_v is defined in Eq. (2.60b). The corresponding contributions to self-energy is

$$\Sigma_{0,\omega}(r) = +g_\omega \int dr'\, r'^2 g_\omega(r') \rho_v(r') \mathcal{R}_{00}(m_\omega; r, r'). \tag{A.19}$$

Fock term

The expressions for the ω meson are to be split into time-like ($\mu = 0$) and space-like ($\mu \neq 0$) components, due to the respective γ^0 and $\boldsymbol{\gamma}$ coupling. Here and after, we denote $\mu = 0$ component as $\bar{O}$ and $\mu \neq 0$ component as $\bar{\bar{O}}$. For the γ^0 component, it can be treated in analogy with the derivation of σ-meson. It contributions to energy

$$\bar{E}_\omega^E = \frac{1}{2} \iint dr dr' \sum_{ab} \delta_{\tau_a \tau_b} \hat{j}_a^2 \sum_L \Big[g_\sigma \big(G_a G_b \langle a \| Y_L \| b \rangle + F_a F_b \langle a' \| Y_L \| b' \rangle \big) \Big]_r$$

$$\times R_{LL}(m_\omega;r,r')\Big[g_\sigma\big(G_bG_a\langle a\|Y_L\|b\rangle+F_bF_a\langle a'\|Y_L\|b'\rangle\big)\Big]_{r'}, \tag{A.20}$$

and self-energy

$$\begin{aligned}\begin{pmatrix}\bar{X}^{(\omega)}\\ \bar{Y}^{(\omega)}\end{pmatrix}_r &= -g_\omega\hat{j}_a^{-2}\sum_b\delta_{\tau_a\tau_b}\begin{pmatrix}F_b\\ G_b\end{pmatrix}_r\sum_L|\langle a\|Y_L\|b\rangle|^2\\ &\quad\times\int dr' R_{LL}(m_\omega;r,r')\big[g_\omega(G_aG_b+F_aF_b)\big]_{r'}.\end{aligned} \tag{A.21}$$

In term of CG coefficients, Eq. (A.21) can be transformed into

$$\begin{aligned}\begin{pmatrix}\bar{X}^{(\omega)}\\ \bar{Y}^{(\omega)}\end{pmatrix}_r &= -g_\omega\sum_b\delta_{\tau_a\tau_b}\frac{\hat{j}_b^2}{4\pi}\begin{pmatrix}F_b\\ G_b\end{pmatrix}_r{\sum_L}'\Big(C^{L0}_{j_a\frac{1}{2}j_b-\frac{1}{2}}\Big)^2\\ &\quad\times\int dr' R_{LL}(m_\omega;r,r')\big[g_\omega(G_aG_b+F_aF_b)\big]_{r'}.\end{aligned} \tag{A.22}$$

The space component becomes a little bit complicated. Considering the expansion of Yukawa propagator in Remark 2 and the definition of $\boldsymbol{\gamma}$ matrix in Remark 8, It is convenient to introduce a vector spherical harmonic operator

$$\sigma_\nu Y_{LM}=\sum_{\mathcal{J}\mathcal{M}}C^{\mathcal{J}\mathcal{M}}_{LM1\nu}\mathcal{T}^L_{\mathcal{J}\mathcal{M}}. \tag{A.23}$$

Then, the exchange contributions for $\mu\neq 0$ component reads

$$\begin{aligned}\bar{\bar{E}}^E_\omega &= +\frac{1}{2}\sum_{ab}\delta_{\tau_a\tau_b}\hat{j}_a^2\int drdr'\sum_{\mathcal{J}L}\Big[g_\omega\big(G_aF_b\langle a\|\mathcal{T}_{\mathcal{J}L}\|b'\rangle-F_aG_b\langle a'\|\mathcal{T}_{\mathcal{J}L}\|b\rangle\big)\Big]_r\\ &\quad\times R_{LL}(m_\omega;r,r')\Big[g_\omega\big(G_aF_b\langle a\|\mathcal{T}_{\mathcal{J}L}\|b'\rangle-F_aG_b\langle a'\|\mathcal{T}_{\mathcal{J}L}\|b\rangle\big)\Big]_{r'},\end{aligned} \tag{A.24}$$

and

$$\begin{aligned}\begin{pmatrix}\bar{\bar{X}}^{(\omega)}\\ \bar{\bar{Y}}^{(\omega)}\end{pmatrix}_r &= g_\omega\hat{j}_a^{-2}\sum_b\delta_{\tau_a\tau_b}\sum_{\mathcal{J}L}\begin{pmatrix}G_b\langle a'\|\mathcal{T}_{\mathcal{J}L}\|b\rangle\\ -F_b\langle a\|\mathcal{T}_{\mathcal{J}L}\|b'\rangle\end{pmatrix}_r\\ &\quad\times\int dr' R_{LL}(m_\omega;r,r')\Big[g_\omega\big(F_aG_b\langle a'\|\mathcal{T}_{\mathcal{J}L}\|b\rangle-G_aF_b\langle a\|\mathcal{T}_{\mathcal{J}L}\|b'\rangle\big)\Big]_{r'},\end{aligned} \tag{A.25}$$

where $|a\rangle$ and $|a'\rangle$ only differ in their orbital angular momentum: $l'=2j-l$, i.e., $a'\equiv(\tau_a,n_a,l'_a,j_a)$.

For the reduced matrix elements, we can use the relations in Remark 8. Equation (A.25) thus reduces to

$$\begin{aligned}\begin{pmatrix}\bar{\bar{X}}^{(\omega)}\\ \bar{\bar{Y}}^{(\omega)}\end{pmatrix}_r &= g_\omega\sum_b\delta_{\tau_a\tau_b}\frac{\hat{j}_b^2}{4\pi}\begin{pmatrix}G_b\\ F_b\end{pmatrix}_r{\sum_L}''\int dr' R_{LL}(m_\omega;r,r')\\ &\quad\times\left\{g_\omega\Big(C^{L0}_{j_a\frac{1}{2}j_b-\frac{1}{2}}\Big)^2\begin{pmatrix}G_aF_b-G_bF_a\\ G_bF_a-G_aF_b\end{pmatrix}+2g_\omega\Big(C^{L0}_{l'_a0l_b0}\Big)^2\begin{pmatrix}F_aG_b\\ G_aF_b\end{pmatrix}\right\}_{r'}.\end{aligned} \tag{A.26}$$

The rearrangement contribution is

$$\Sigma_R^{(\omega)}=\frac{\partial g_\omega}{\partial\rho_v}\frac{1}{g_\omega}\Big[\rho_v\Sigma_{0,\omega}+\sum_\alpha\frac{\hat{j}_a^2}{4\pi r^2}\big(G_aY_\alpha^{(\omega)}+F_aX_\alpha^{(\omega)}\big)\Big]. \tag{A.27}$$

The ρ-N vector coupling can be deduced by replacing

$$m_\omega,g_\omega\to m_\rho,g_\rho,\qquad \rho_v\to\rho_v^{(3)},\qquad \sum_{ab}\delta_{\tau_a\tau_b}\to\sum_{ab}(2-\delta_{\tau_a\tau_b}), \tag{A.28}$$

for the corresponding terms.

A.2.3 Pseudovector coupling: $\Gamma = \gamma^5\gamma^\mu$

The potential energy of the pion meson can be written as

$$E_\pi^E = \frac{1}{2}\frac{1}{m_\pi^2}\sum_{\alpha\beta}(2-\delta_{\tau_\alpha\tau_\beta})\iint d\boldsymbol{r}d\boldsymbol{r}'\bar{f}_\alpha(\boldsymbol{r})\bar{f}_\beta(\boldsymbol{r}')\big(f_\pi\gamma_5\gamma^k\big)_1 \times\big(f_\pi\gamma_5\gamma^l\big)_2\partial_k(1)\partial_l(2)D_\pi(m_\pi;r,r')f_\beta(\boldsymbol{r}')f_\alpha(\boldsymbol{r}). \tag{A.29}$$

Hartree term

Due to the parity conservation in spherical and axially deformed nuclei, the Hartree (direct) contributions of π are zero, and only the exchange contribution remains.

Fock term

The calculation of the π contribution is more elaborate as a consequence of the pseudovector character of the interaction. Here, the gradient of the Yukawa propagator (B.13) in Remark 2 are needed. Introducing

$$\mathcal{T}_{LM}^{L_1} \equiv \boldsymbol{\sigma}\cdot Y_{LM}^{L_1}(\hat{\boldsymbol{r}}) = \sum_{\mu k} C_{L_1\mu 1k}^{LM}Y_{L_1\mu}\sigma_k, \tag{A.30}$$

and considering the condition $L_1 = L\pm 1$, we obtain

$$\langle a\|\mathcal{T}_{LL_1}\|b\rangle = (-1)^{j_a+L-\frac{1}{2}}\frac{1}{\sqrt{4\pi}}\hat{j}_a\hat{j}_b\hat{L}^{-1}\frac{\kappa_{ab}+\beta_{LL_1}}{\sqrt{|\beta_{LL_1}|}}C^{L0}_{j_a\frac{1}{2}j_b-\frac{1}{2}}, \tag{A.31}$$

with κ_{ab} and β_{LL_1} defined in Remark 9.

Then, the potential energy from π-meson can be written as

$$E_\pi^E = \frac{1}{2}\sum_{ab}(2-\delta_{\tau_a\tau_b})\hat{j}_a^2\sum_L\hat{L}^{-4}|\langle a|Y_L|b'\rangle|^2\sum_{L_1L_2}i^{L_2-L_1}\int drdr'\Big\{f_\pi\big[(\kappa_{ab}+\beta_{LL_1})G_aG_b - (\kappa_{ab}-\beta_{LL_1})F_aF_b\big]\Big\}_r\mathcal{V}_L^{L_1L_2}(m_\pi;r,r')\Big\{f_\pi\big[(\kappa_{ab}+\beta_{LL_2})G_bG_a-(\kappa_{ab}-\beta_{LL_2})F_bF_a\big]\Big\}_{r'} \tag{A.32}$$

which contains two parts corresponding to the zero range and finite range term of $V_L^{L_1L_2}(m_\pi;r,r')$ in Remark 2. The zero range term can be further reduced to

$$\frac{1}{2}\frac{1}{m_\pi^2}\sum_{\alpha\beta}(2-\delta_{\tau_a\tau_b})\frac{\hat{j}_b^2\hat{j}_a^2}{4\pi}\int dr\frac{1}{2}\frac{1}{r^2}\big[f_\pi(G_aG_b+F_aF_b)\big]\big[f_\pi(G_bG_a+F_bF_a)\big]. \tag{A.33}$$

In the end, the exchange part of the potential energy for π-meson with the pseudo-vector coupling can be expressed as,

$$E_\pi^E = \frac{1}{2}\sum_{ab}(2-\delta_{\tau_\alpha\tau_\beta})\frac{\hat{j}_a^2\hat{j}_b^2}{4\pi}\Bigg\{\int dr\frac{f_\pi^2(G_aG_b+F_aF_b)^2}{2m_\pi^2r^2} - \sum_L\hat{L}^{-4}|\langle a|Y_L|b'\rangle|^2\times\sum_{L_1L_2}^{L\pm1}i^{L_2-L_1}\int dr'\big[f_\pi\mathcal{G}_{ab}^{LL_1}\big]_r R_{L_1L_2}(m_\pi;r,r')\Big[f_\pi\mathcal{G}_{ab}^{LL_2}\Big]_{r'}\Bigg\} \tag{A.34}$$

where

$$\mathcal{G}_{ab}^{LL_1}(r) \equiv (\kappa_{ab}+\beta_{LL_1})G_aG_b+(\kappa_{ab}-\beta_{LL_1})F_aF_b, \tag{A.35}$$

and the values of L_1 and L_2 can only be $L\pm1$.

From the definition (A.3), one obtains the contributions to self-energy from π-meson. The results read as follows,

$$\begin{aligned}\begin{pmatrix} X^{(\pi)} \\ Y^{(\pi)} \end{pmatrix}_r = f_\pi \hat{j}_a^{-2} \sum_b (2-\delta_{\tau_a\tau_b}) \Bigg\{ \frac{\hat{j}_a^2 \hat{j}_b^2}{8\pi} \frac{\big[f_\pi (G_a G_b + F_a F_b)\big]_r}{m_\pi^2 r^2} \begin{pmatrix} F_b \\ G_b \end{pmatrix}_r \\ - \sum_L \hat{L}^{-4} |\langle a \| Y_L \| b' \rangle|^2 \sum_{L_1,L_2} i^{L_2-L_1} \begin{pmatrix} F_b[\beta_{LL_1} - \kappa_{ab}] \\ G_b[\beta_{LL_1} + \kappa_{ab}] \end{pmatrix}_r \int dr' R_{L_1L_2}(m_\pi; r, r') [f_\pi \mathcal{G}_{ab}^{LL_2}]_{r'} \Bigg\},\end{aligned} \tag{A.36}$$

or in term of CG coefficients,

$$\begin{aligned}\begin{pmatrix} X^{(\pi)} \\ Y^{(\pi)} \end{pmatrix}_r = f_\pi \sum_b (2-\delta_{\tau_a\tau_b}) \frac{\hat{j}_b^2}{4\pi} \Bigg\{ \frac{\big[f_\pi (G_a G_b + F_a F_b)\big]_r}{2m_\pi^2 r^2} \begin{pmatrix} F_b \\ G_b \end{pmatrix}_r \\ - {\sum_L}'' \hat{L}^{-4} \Big(C^{L0}_{j_a \frac{1}{2} j_b -\frac{1}{2}} \Big)^2 \sum_{L_1 L_2}^{L\pm 1} i^{L_2-L_1} \begin{pmatrix} F_b(\beta_{LL_1} - \kappa_{ab}) \\ G_b(\beta_{LL_1} + \kappa_{ab}) \end{pmatrix}_r \int dr' R_{L_1L_2}(m_\pi; r, r') \big[f_\pi \mathcal{G}_{ab}^{LL_2}\big]_{r'} \Bigg\}.\end{aligned} \tag{A.37}$$

Contact term

The zero range δ term (A.33) which arises in pseudo-vector coupling can be removed by adding

$$\begin{aligned}E_\pi^\delta = -\frac{1}{2}\frac{1}{m_\pi^2} \sum_{\alpha\beta} (2-\delta_{\tau_\alpha\tau_\beta}) \frac{1}{3} \iint d\boldsymbol{r} d\boldsymbol{r}' \bar{f}_\alpha(\boldsymbol{r}) \bar{f}_\beta(\boldsymbol{r}') \big(f_\pi \gamma_5 \gamma^k\big)_1 \\ \times \big(f_\pi \gamma_5 \gamma_k\big)_2 \delta(\boldsymbol{r}-\boldsymbol{r}') f_\alpha(\boldsymbol{r}') f_\beta(\boldsymbol{r}).\end{aligned} \tag{A.38}$$

Using the expression of δ function in Remark 4 and vector spherical harmonic $\mathcal{T}_{\mathcal{J}\mathcal{M}}$ defined in Eq. (A.23), Such zero range δ term contributes to the potential energy as

$$\begin{aligned}E_\pi^\delta = -\frac{1}{3}\hat{j}_a^2 \sum_b (2-\delta_{\tau_a\tau_b}) \frac{f_\pi^2}{m_\pi^2 r^2} \sum_{\mathcal{J}L} \Big[G_a F_b \langle a' \| \mathcal{T}_{\mathcal{J}L} \| b' \rangle + F_a G_b \langle a \| \mathcal{T}_{\mathcal{J}L} \| b \rangle \Big]_r \\ \times \Big[G_a G_b \langle a \| \mathcal{T}_{\mathcal{J}L} \| b \rangle + F_a F_b \langle a' \| \mathcal{T}_{\mathcal{J}L} \| b' \rangle \Big]_r,\end{aligned} \tag{A.39}$$

and to the self-energy as

$$\begin{aligned}\begin{pmatrix} \delta X^\pi \\ \delta Y^\pi \end{pmatrix}_r = -\frac{1}{3}\hat{j}_a^{-2} \sum_b (2-\delta_{\tau_a\tau_b}) \frac{f_\pi^2}{m_\pi^2 r^2} \begin{pmatrix} F_b \langle a' \| \mathcal{T}_{\mathcal{J}L} \| b' \rangle \\ G_b \langle a \| \mathcal{T}_{\mathcal{J}L} \| b \rangle \end{pmatrix}_r \\ \times \Big[\langle a \| \mathcal{T}_{\mathcal{J}L} \| b \rangle G_a G_b + \langle a' \| \mathcal{T}_{\mathcal{J}L} \| b' \rangle F_a F_b \Big]_r.\end{aligned} \tag{A.40}$$

Using the expressions in Remark 8, the above expressions become quite concise,

$$\delta X^\pi = -\sum_b (2-\delta_{\tau_a\tau_b}) \frac{\hat{j}_b^2}{4\pi} \frac{f_\pi^2}{2m_\pi^2 r^2} F_b(r) \Big[F_a F_b - \frac{1}{3} G_a G_b \Big]_r \tag{A.41a}$$

$$\delta Y^\pi = -\sum_b (2-\delta_{\tau_a\tau_b}) \frac{\hat{j}_b^2}{4\pi} \frac{f_\pi^2}{2m_\pi^2 r^2} G_b(r) \Big[G_a G_b - \frac{1}{3} F_a F_b \Big]_r. \tag{A.41b}$$

The η-N pseudo-vector coupling can be deduced by replacing

$$m_\pi, f_\pi \to m_\eta, f_\eta, \qquad \sum_{ab} (2-\delta_{\tau_a\tau_b}) \to \sum_{ab} \delta_{\tau_a\tau_b}, \tag{A.42}$$

for the corresponding terms.

A.2.4 Tensor coupling: $\Gamma = \sigma^{\mu\nu}\partial_\nu$

Again, we take the ω-N tensor coupling as an example.

$$E_\omega = \frac{1}{2}\sum_{\alpha\beta}\frac{1}{4M^2}\int d\boldsymbol{r}d\boldsymbol{r}' \times \bar{f}_\alpha(\boldsymbol{r})\bar{f}_\beta(\boldsymbol{r}')\Big[f_\omega(1)\sigma_{\nu k}(1)f_\omega(2)\sigma^{\nu l}(2)\partial^k(1)\partial_l(2)D(m_\omega;\boldsymbol{r},\boldsymbol{r}')\Big]f_\beta(\boldsymbol{r}')f_\alpha(\boldsymbol{r}). \tag{A.43}$$

It is convenient to separate in the tensor coupling $\sigma^{\nu k}\partial_k$ contributions coming either from $\nu = 0$ or from $\nu = 1, 2, 3$.

Hartree term

We first present the direct contribution. For $\nu = 0$ component, by introducing

$$\mathcal{T}^{L_1}_{LM} \equiv \boldsymbol{\sigma}\cdot Y^{L_1}_{LM}(\hat{\boldsymbol{r}}), \tag{A.44}$$

one finds that only the $L_1 = L_2 = 1$ components of the gradient of propagator (B.13) in Remark 2 remain,

$$\begin{aligned}\bar{E}^D_\omega =& -\frac{1}{2}4\pi m_\omega^2\iint dr\, r^2 dr'\, r'^2\frac{f_\omega(r)}{2M}\rho_t(r)\mathcal{R}_{11}(m_\omega;r,r')\frac{f_\omega(r')}{2M}\rho_t(r') \\ &+\frac{1}{2}4\pi\int dr\, r^2\Big[\frac{f_\omega}{2M}\rho_t(r)\Big]^2,\end{aligned} \tag{A.45}$$

where the tensor density ρ_t is defined in Eq. (2.60c).

For $\nu = 1, 2, 3$ components, there is no contribution. The reason for the vanishing of these components is that after summation over the angular momentum projection quantum numbers m_a or m_b the matrix element

$$\langle a|[\sigma_\mu,\boldsymbol{\sigma}]\cdot\boldsymbol{Y}^{L_1}_{LM}|a\rangle \tag{A.46}$$

arising from (A.43) is zero.

Therefore the local self-energy comes only from the time-component,

$$\Sigma^T_\omega(r) = -m_\omega^2\frac{f_\omega}{2M}\int r'^2dr'\frac{f_\omega(r')}{2M}\rho_t(r')\mathcal{R}_{11}(m_\omega;r,r') + \frac{f_\omega^2}{4M^2}\rho_t. \tag{A.47}$$

Fock term

The exchange contributions are also divided into two parts. For $\nu = 0$, using the definition in (A.44) and the results listed in Remark 5 and 7, we find

$$\begin{aligned}\bar{E}^E_\omega = -\frac{1}{2}\frac{m_\rho^2}{4M^2}\sum_{ab}\frac{1}{4\pi}\Bigg\{&\frac{1}{2}\hat{j}_a^2\hat{j}_b^2\int dr\frac{f_\omega^2[G_aF_b+F_aG_b]^2}{m_\omega^2r^2} - \hat{j}_a^2{\sum_L}'\hat{L}^{-4}|\langle a\|Y_L\|b\rangle|^2 \\ &\sum_{L_1L_2}^{L\pm1}i^{L_2-L_1}\int drdr'\Big[f_\omega\mathcal{G}^{LL_1}_{ab}\Big]_r R_{L_1L_2}(m_\omega;r,r')\Big[f_\omega\mathcal{G}^{LL_2}_{ab}\Big]_{r'}\Bigg\}\end{aligned} \tag{A.48}$$

where

$$\mathcal{G}^{LL_1}_{ab}(r) \equiv (\beta_{LL_1}+\tilde{\kappa}_{ab})G_aF_b + (\beta_{LL_1}-\tilde{\kappa}_{ab})F_aG_b, \tag{A.49}$$

with $\tilde{\kappa}_{ab}$ and β_{LL_1} defined in Remark 9. Notice that the first piece on the right hand side appears as a zero range term.

Furthermore, we obtain for the $\nu = 1, 2, 3$ components

$$\bar{\bar{E}}^E_\omega = 3\frac{m_\omega^2}{4M^2}\sum_{ab}\delta_{\tau_a\tau_b}\frac{1}{4\pi}\hat{j}_a^2\sum_L\sum_{\mathcal{J}}\hat{\mathcal{J}}^{-2}|\langle a\|Y_L\|b\rangle|^2\sum_{L_1L_2}f_{L\mathcal{J}}(L_1)f_{L\mathcal{J}}(L_2)$$
$$\int dr_1dr_2\Big[f_\omega\big(B^{ab}_{\mathcal{J}L_1}G_aG_b+B^{a'b'}_{\mathcal{J}L_1}F_aF_b\big)\Big]_r\mathcal{V}_L^{L_1L_2}\Big[f_\omega\big(B^{ab}_{\mathcal{J}L_2}G_aG_b+B^{a'b'}_{\mathcal{J}L_2}F_aF_b\big)\Big]_{r'} \quad (A.50)$$

where we have introduced

$$f_{L\mathcal{J}}(L_1)\equiv\hat{L}\hat{L}_1\begin{pmatrix}L_1 & L & 1\\ 0 & 0 & 0\end{pmatrix}\begin{Bmatrix}L_1 & L & 1\\ 1 & 1 & \mathcal{J}\end{Bmatrix}=(-)^{L_1}\hat{L}_1C^{L_10}_{L010}\begin{Bmatrix}L_1 & L & 1\\ 1 & 1 & \mathcal{J}\end{Bmatrix} \quad (A.51)$$

and $B^{ab}_{\mathcal{J}L}$ is defined in Remark 8.

From the above results, one can obtain the contributions to the $(X,Y)^T$ components. The time component reads as

$$\begin{pmatrix}\bar{X}^{(\omega)}\\ \bar{Y}^{(\omega)}\end{pmatrix}_r=-\Big(\frac{m_\omega}{2M}\Big)^2f_\omega\hat{j}_a^{-2}\sum_b\delta_{\tau_a\tau_b}\Bigg\{\frac{\hat{j}_a^2\hat{j}_b^2}{8\pi}\frac{\big[f_\omega(G_aF_b+F_aG_b)\big]_r}{m_\omega^2r^2}\begin{pmatrix}G_b\\ F_b\end{pmatrix}_r \quad (A.52)$$
$$-\sum_L\hat{L}^{-4}|\langle a\|Y_L\|b\rangle|^2\sum_{L_1L_2}i^{L_2-L_1}\begin{pmatrix}G_b[\beta_{LL_1}-\tilde{\kappa}_{ab}]\\ F_b[\beta_{LL_1}+\tilde{\kappa}_{ab}]\end{pmatrix}_r\int dr'\big[f_\omega\mathcal{G}^{LL_2}_{ab}\big]_{r'}R_{L_1L_2}(m_\omega;r,r')\Bigg\},$$

or in terms of CG coefficients,

$$\begin{pmatrix}\bar{X}^{(\omega)}\\ \bar{Y}^{(\omega)}\end{pmatrix}_r=-\Big(\frac{m_\omega}{2M}\Big)^2f_\omega\hat{j}_a^{-2}\sum_b\delta_{\tau_a\tau_b}\Bigg\{\frac{\hat{j}_a^2\hat{j}_b^2}{8\pi}\frac{\big[f_\omega(G_aF_b+F_aG_b)\big]_r}{m_\omega^2r^2}\begin{pmatrix}G_b\\ F_b\end{pmatrix}_r \quad (A.53)$$
$$-{\sum_L}'\hat{L}^{-4}\Big(C^{L0}_{j_a\frac{1}{2}j_b-\frac{1}{2}}\Big)^2\sum_{L_1L_2}i^{L_2-L_1}\begin{pmatrix}G_b[\beta_{LL_1}-\tilde{\kappa}_{ab}]\\ F_b[\beta_{LL_1}+\tilde{\kappa}_{ab}]\end{pmatrix}_r\int dr'\big[f_\omega\mathcal{G}^{LL_2}_{ab}\big]_{r'}R_{L_1L_2}(m_\omega;r,r')\Bigg\}.$$

The space components read as

$$\begin{pmatrix}\bar{\bar{X}}^{(\omega)}\\ \bar{\bar{Y}}^{(\omega)}\end{pmatrix}_r=6\Big(\frac{m_\omega}{2M}\Big)^2f_\omega\hat{j}_a^{-2}\sum_b\delta_{\tau_a\tau_b}\sum_{L\mathcal{J}}\sum_{L_1L_2}f_{L\mathcal{J}}(L_1)f_{L\mathcal{J}}(L_2)\begin{pmatrix}F_b\langle a'\|\mathcal{T}_{\mathcal{J}L_1}\|b'\rangle\\ -G_b\langle a\|\mathcal{T}_{\mathcal{J}L_1}\|b\rangle\end{pmatrix}_r \quad (A.54)$$
$$\times\int dr'f_\omega(r')\big[\langle a\|\mathcal{T}_{\mathcal{J}L_2}\|b\rangle G_aG_b-\langle a'\|\mathcal{T}_{\mathcal{J}L_2}\|b'\rangle F_aF_b\big]_{r'}\Big[R_{L_1L_2}(m_\omega;r,r')-\frac{\delta(r-r')}{m_\omega^2r'^2}\Big],$$

or more explicitly,

$$\begin{pmatrix}\bar{\bar{X}}^{(\omega)}\\ \bar{\bar{Y}}^{(\omega)}\end{pmatrix}_r=6\Big(\frac{m_\omega}{2M}\Big)^2f_\omega\hat{j}_a^{-2}\sum_b\delta_{\tau_a\tau_b}{\sum_L}''\sum_{\mathcal{J}}\hat{\mathcal{J}}^2\sum_{L_1L_2}^{L\pm1}f_{L\mathcal{J}}(L_1)f_{L\mathcal{J}}(L_2)\begin{pmatrix}F_bB^{a'b'}_{\mathcal{J}L_1}\\ -G_bB^{ab}_{\mathcal{J}L_1}\end{pmatrix}_r \quad (A.55)$$
$$\times\int dr'f_\omega(r')\big[B^{ab}_{\mathcal{J}L_2}G_aG_b-B^{a'b'}_{\mathcal{J}L_2}F_aF_b\big]_{r'}\Big[R_{L_1L_2}(m_\omega;r,r')-\frac{\delta(r-r')}{m_\omega^2r'^2}\Big].$$

Contact term

To remove the contribution of the $\delta(\boldsymbol{r}_1-\boldsymbol{r}_2)$ term, one needs to consider the contact part of the ω-N tensor coupling,

$$\delta E_\omega=\frac{1}{6}\frac{1}{4M^2}\sum_{\alpha\beta}\int d\boldsymbol{r}d\boldsymbol{r}'f_\omega\bar{f}_\alpha(\boldsymbol{r})\sigma^{\mu i}f_\beta(\boldsymbol{r}')\delta(\boldsymbol{r}-\boldsymbol{r}')f_\omega\bar{f}_\beta(\boldsymbol{r}')\sigma_{\mu i}f_\alpha(\boldsymbol{r}). \quad (A.56)$$

For the direct contribution of contact term, there is only the $\mu=0$ component left,

$$\delta\bar{E}_\omega=-\frac{1}{6}4\pi\int dr\,r^2\big(\frac{f_\omega}{2M}\big)^2\rho_t\rho_t \quad (A.57)$$

and the contribution to the self-energy is

$$\delta\Sigma_{T,\omega} = -\frac{1}{3}\big(\frac{f_\rho}{2M}\big)^2\rho_t. \tag{A.58}$$

For the exchange contribution of contact term, we need the expansion of Delta function in Remark 4. Introducing the vector spherical harmonic operator

$$\sigma_\nu Y_{LM} = \sum_{\mathcal{J}\mathcal{M}} C^{\mathcal{J}\mathcal{M}}_{LM1\nu}\mathcal{T}^L_{\mathcal{J}\mathcal{M}}, \tag{A.59}$$

one has subsequently,

$$\delta\bar{E}^E_\rho = \frac{1}{6}\sum_{ab}\delta_{\tau_a\tau_b}\hat{j}_a^2\sum_{\mathcal{J}L}\int\frac{f_\omega^2}{4M^2r^2}\big[\langle a\|\mathcal{T}_{\mathcal{J}L}\|b'\rangle G_aF_b + \langle a'\|\mathcal{T}_{\mathcal{J}L}\|b\rangle F_aG_b\big]^2dr, \tag{A.60}$$

$$\delta\bar{\bar{E}}^E_\rho = \frac{1}{6}\sum_{ab}\delta_{\tau_a\tau_b}\hat{j}_a^2\sum_{\mathcal{J}L}\int\frac{f_\omega^2}{4M^2r^2}\big[\langle a\|\mathcal{T}_{\mathcal{J}L}\|b\rangle G_aF_b + \langle a'\|\mathcal{T}_{\mathcal{J}L}\|b'\rangle F_aG_b\big]^2dr, \tag{A.61}$$

and

$$\begin{aligned}\begin{pmatrix}\delta\bar{X}^{(\omega)}\\ \delta\bar{Y}^{(\omega)}\end{pmatrix}_r =& \frac{1}{3}\Big(\frac{f_\omega}{2M}\Big)^2\hat{j}_a^{-2}\sum_b\delta_{\tau_a\tau_b}\frac{1}{r^2}\sum_{\mathcal{J}L}\begin{pmatrix}G_b\langle a'\|\mathcal{T}_{\mathcal{J}L}\|b\rangle\\ F_b\langle a\|\mathcal{T}_{\mathcal{J}L}\|b'\rangle\end{pmatrix}_r \\ &\times\Big[\langle a\|\mathcal{T}_{\mathcal{J}L}\|b'\rangle G_aF_b + \langle a'\|\mathcal{T}_{\mathcal{J}L}\|b\rangle F_aG_b\Big]_r,\end{aligned} \tag{A.62}$$

$$\begin{aligned}\begin{pmatrix}\delta\bar{\bar{X}}^{(\omega)}\\ \delta\bar{\bar{Y}}^{(\omega)}\end{pmatrix}_r =& \frac{2}{3}\Big(\frac{f_\omega}{2M}\Big)^2\hat{j}_a^{-2}\sum_b\delta_{\tau_a\tau_b}\frac{1}{r^2}\sum_{\mathcal{J}L}\begin{pmatrix}F_b\langle a'\|\mathcal{T}_{\mathcal{J}L}\|b'\rangle\\ -G_b\langle a\|\mathcal{T}_{\mathcal{J}L}\|b\rangle\end{pmatrix}_r \\ &\times\Big[\langle a\|\mathcal{T}_{\mathcal{J}L}\|b\rangle G_aG_b - \langle a'\|\mathcal{T}_{\mathcal{J}L}\|b'\rangle F_aF_b\Big]_r.\end{aligned} \tag{A.63}$$

Further processing the reduced matrix elements, the self-energy can be deduced as

$$\delta\bar{X}^{(\omega)} = \frac{1}{3}\Big(\frac{f_\omega}{2M}\Big)^2\sum_b\delta_{\tau_a\tau_b}\frac{\hat{j}_b^2}{4\pi}\frac{1}{r^2}G_b(r)\Big[\frac{3}{2}G_bF_a - \frac{1}{2}G_aF_b\Big]_r, \tag{A.64a}$$

$$\delta\bar{Y}^{(\omega)} = \frac{1}{3}\Big(\frac{f_\omega}{2M}\Big)^2\sum_b\delta_{\tau_a\tau_b}\frac{\hat{j}_b^2}{4\pi}\frac{1}{r^2}F_b(r)\Big[\frac{3}{2}G_aF_b - \frac{1}{2}G_bF_a\Big]_r, \tag{A.64b}$$

and

$$\delta\bar{\bar{X}}^{(\omega)} = -\frac{1}{3}\Big(\frac{f_\omega}{2M}\Big)^2\sum_b\delta_{\tau_a\tau_b}\frac{\hat{j}_b^2}{4\pi}\frac{1}{r^2}F_b(r)\Big[3F_aF_b + G_aG_b\Big]_r, \tag{A.65a}$$

$$\delta\bar{\bar{Y}}^{(\omega)} = -\frac{1}{3}\Big(\frac{f_\omega}{2M}\Big)^2\sum_b\delta_{\tau_a\tau_b}\frac{\hat{j}_b^2}{4\pi}\frac{1}{r^2}G_b(r)\Big[3G_aG_b + F_aF_b\Big]_r. \tag{A.65b}$$

The contributions of the ρ-N tensor coupling is practically identical to those of the ω meson which can be obtained by making the following replacements:

$$m_\omega, f_\omega \to m_\rho, f_\rho, \qquad \rho_t \to \rho_t^{(3)}, \qquad \sum_{ab}\delta_{\tau_a\tau_b} \to \sum_{ab}(2-\delta_{\tau_a\tau_b}). \tag{A.66}$$

A.2.5 Vector-Tensor coupling: $\Gamma = \gamma_\mu\sigma^{\mu\nu}\partial_\nu$

The contributions to the energy functional from ω-N vector-tensor couplings read as

$$H_\omega^{(VT)} = -\frac{1}{2}\sum_{\alpha\beta\gamma\delta}c_\alpha^\dagger c_\beta^\dagger c_\gamma c_\delta\langle\tau_\alpha|\vec{\tau}_1|\tau_\delta\rangle\cdot\langle\tau_\beta|\vec{\tau}_2|\tau_\gamma\rangle$$

$$\times \int d\boldsymbol{r}_1 d\boldsymbol{r}_2 \bar{f}_\alpha(\boldsymbol{r}_1)\bar{f}_\beta(\boldsymbol{r}_2)\Gamma_{12}v(m_\omega;1,2)f_\gamma(\boldsymbol{r}_2)f_\delta(\boldsymbol{r}_1), \tag{A.67}$$

where

$$\Gamma_{12} = g_\omega(1)\gamma_\nu(1)\frac{f_\rho(2)}{2M}\sigma^{\nu l}(2)\partial_l(2) + \frac{f_\rho(1)}{2M}\sigma^{\nu l}(1)\partial_l(1)g_\omega(2)\gamma_\nu(2), \tag{A.68}$$

and

$$\sigma^{\mu\nu} = -\sigma^{\nu\mu}. \tag{A.69}$$

The gradients of the propagator are

$$\boldsymbol{\nabla}_1 v(m_\omega;\boldsymbol{r}_1,\boldsymbol{r}_2) = -m_\omega \sum_{LM}\sum_{L_1} C^{L_1 0}_{L010}\mathcal{S}_{LL_1}(m_\omega;r_1,r_2)\boldsymbol{Y}^{L_1}_{LM}(\hat{\boldsymbol{r}}_1)Y^*_{LM}(\hat{\boldsymbol{r}}_2) \tag{A.70a}$$

$$\boldsymbol{\nabla}_2 v(m_\omega;\boldsymbol{r}_1,\boldsymbol{r}_2) = +m_\omega \sum_{LM}\sum_{L_1} C^{L_1 0}_{L010}\mathcal{S}_{L_1 L}(m_\omega;r_1,r_2)Y_{LM}(\hat{\boldsymbol{r}}_1)\boldsymbol{Y}^{L_1 *}_{LM}(\hat{\boldsymbol{r}}_2). \tag{A.70b}$$

Hartree term

Similarly to the tensor coupling, only the $\nu = 0$ component remains in the Hartree term,

$$E^{(VT),D}_\omega = -m_\omega \int r_1^2 dr_1 r_2^2 dr_2 \frac{1}{2M}\big[f_\omega\rho_t\big]_1 S_{01}(m_\omega;r_1,r_2)\big[g_\omega\rho_b\big]_2 \tag{A.71}$$

where

$$m_\omega \mathcal{S}_{01}(m_\omega;r_1,r_2) = \frac{d}{dr_1}\mathcal{R}_{00}(m_\omega;r_1,r_2). \tag{A.72}$$

Its contributions to local self-energies are

$$\Sigma^{VT}_{0,\omega}(r) = -g_\omega \int r'^2 dr' \frac{1}{2M} f_\omega(r')\rho_t(r')m_\omega\mathcal{S}_{01}(m_\omega;r,r'), \tag{A.73}$$

$$\Sigma^{VT}_{T,\omega}(r) = -\frac{f_\omega}{2M}\int r'^2 dr' g_\omega(r')\rho_v(r')m_\omega\mathcal{S}_{01}(m_\omega;r,r'). \tag{A.74}$$

Fock term

For the $\nu = 0$ component, one has

$$\begin{aligned}\bar{E}^{(VT),E}_\omega = {} & m_\omega \sum_{\alpha\beta}\delta_{\tau_a\tau_b} j_a^2 \sum_L\sum_{L_1} C^{L_1 0}_{L010} \\ & \times \int dr_1 dr_2 \Big[\frac{f_\omega}{2M}(G_a F_b\langle a\|\mathcal{T}_{LL_1}\|b'\rangle + F_a G_b\langle a'\|\mathcal{T}_{LL_1}\|b\rangle)\Big]_1 \\ & \times\mathcal{S}_{LL_1}(m_\rho;r_1,r_2)\big[g_\omega(G_a G_b\langle a\|Y_L\|b\rangle + F_a F_b\langle a'\|Y_L\|b'\rangle)\big]_2,\end{aligned} \tag{A.75}$$

or

$$\begin{aligned}\bar{E}^{(VT),E}_\omega = {} & m_\omega \sum_{\alpha\beta}\delta_{\tau_a\tau_b}\frac{j_a^2 j_b^2}{4\pi}{\sum_L}'\sum_{L_1} i^{L_1-L-1}\hat{L}^{-2}C^{L0}_{j_a\frac{1}{2}j_b-\frac{1}{2}}C^{L0}_{j_a\frac{1}{2}j_b-\frac{1}{2}} \\ & \times \int dr_1 dr_2 \Big\{\frac{f_\omega(r')}{2M}\big[(\tilde{\kappa}_{ab}+\beta_{LL_1})G_a F_b - (\tilde{\kappa}_{ab}-\beta_{LL_1})F_a G_b\big]\Big\}_1 \\ & \times\mathcal{S}_{LL_1}(m_\rho;r_1 r_2)\big\{g_\rho[G_a G_b + F_a F_b]\big\}_2.\end{aligned} \tag{A.76}$$

The corresponding contributions to local self-energies are

$$\begin{aligned}\begin{pmatrix}\bar{X}^{(\omega)}\\ \bar{Y}^{(\omega)}\end{pmatrix}_r &= \Big(\frac{f_\omega g_\omega}{2M}\Big) m_\omega \hat{j}_a^{-2} \sum_b \delta_{\tau_a\tau_b} \sum_{LL_1} (-)^{L_1} \hat{L}_1 \begin{pmatrix} L_1 & L & 1\\ 0 & 0 & 0\end{pmatrix} \\ &\times \Bigg\{ \begin{pmatrix} G_b\langle a'\|\mathcal{T}_{LL_1}\|b\rangle \\ F_b\langle a\|\mathcal{T}_{LL_1}\|b'\rangle\end{pmatrix}_r \int dr' \big[\langle a\|Y_L\|b\rangle G_a G_b + \langle a'\|Y_L\|b'\rangle F_a F_b\big]_{r'} \mathcal{S}_{LL_1}(m_\omega; r, r') \\ &+ \begin{pmatrix} F_b\langle a'\|Y_L\|b'\rangle \\ G_b\langle a\|Y_L\|b\rangle\end{pmatrix}_r \int dr' \big[\langle a\|\mathcal{T}_{LL_1}\|b'\rangle G_a F_b + \langle a'\|\mathcal{T}_{LL_1}\|b\rangle F_a G_b\big]_{r'} \mathcal{S}_{LL_1}(m_\omega; r, r') \Bigg\},\end{aligned} \tag{A.77}$$

or in terms of CG coefficients,

$$\begin{aligned}\begin{pmatrix}\bar{X}^{(\omega)}\\ \bar{Y}^{(\omega)}\end{pmatrix}_r &= m_\omega \sum_b \delta_{\tau_a\tau_b} \frac{j_b^2}{4\pi} \sum_L{}' \sum_{L_1}^{L\pm1} i^{L_1-L-1} \hat{L}^{-2} \Big(C^{L0}_{j_a\frac{1}{2}j_b-\frac{1}{2}}\Big)^2 \\ &\times \Bigg\{ g_\omega \begin{pmatrix} F_b \\ G_b\end{pmatrix}_r \int dr' \frac{f_\omega(r')}{2M} \big[(\tilde{\kappa}_{ab}+\beta_{LL_1}) G_a F_b + (\beta_{LL_1}-\tilde{\kappa}_{ab}) F_a G_b\big]_{r'} \mathcal{S}_{LL_1}(m_\omega; r, r') \\ &+ \frac{f_\omega}{2M} \begin{pmatrix} G_b \\ F_b\end{pmatrix}_r (\beta_{LL_1}-\tilde{\kappa}_{ab}) \int dr' g_\omega(r') \big[G_a G_b + F_a F_b\big]_{r'} \mathcal{S}_{LL_1}(m_\omega; r, r') \Bigg\}.\end{aligned} \tag{A.78}$$

For $\nu \neq 0$ components, one has

$$\begin{aligned}\bar{\bar{E}}^{(VT,E)_\omega} &= \sqrt{6} \sum_{\alpha\beta} \delta_{\tau_a\tau_b} \frac{\hat{j}_a^2 \hat{j}_b^2}{4\pi} \sum_{\mathcal{J}L} \sum_{L_1}^{L\pm1} (-)^{\mathcal{J}} \hat{\mathcal{J}}^{-2} f_{L\mathcal{J}}(L_1) \Big(C^{\mathcal{J}0}_{j_a\frac{1}{2}j_b-\frac{1}{2}}\Big)^2 \\ &\times \int dr dr' \Big[\frac{f_\omega}{2M} B^{ab}_{\mathcal{J}L_1} \big(G_a G_b + B^{a'b'}_{\mathcal{J}L_1} F_a F_b\big)\Big]_r \mathcal{S}_{LL_1}(m_\omega; r, r') \Big[g_\omega \big(B^{ab'}_{\mathcal{J}L} G_a F_b + B^{a'b}_{\mathcal{J}L} F_a G_b\big)\Big]_{r'}.\end{aligned} \tag{A.79}$$

The corresponding contributions to $(X, Y)^T$ read as follows,

$$\begin{aligned}\begin{pmatrix}\bar{\bar{X}}^{(\omega)}\\ \bar{\bar{Y}}^{(\omega)}\end{pmatrix}_r &= \sqrt{6}\Big(\frac{f_\omega g_\omega}{2M}\Big) m_\omega \hat{j}_a^{-2} \sum_b \delta_{\tau_a\tau_b} \sum_{\mathcal{J}LL_1} (-)^{\mathcal{J}} f_{L\mathcal{J}}(L_1) \\ &\times \Bigg\{ \begin{pmatrix} F_b\langle a'\|\mathcal{T}_{\mathcal{J}L_1}\|b'\rangle \\ -G_b\langle a\|\mathcal{T}_{\mathcal{J}L_1}\|b\rangle\end{pmatrix}_r \int dr' \big[\langle a\|\mathcal{T}_{\mathcal{J}L}\|b'\rangle G_a F_b - \langle a'\|\mathcal{T}_{\mathcal{J}L}\|b\rangle F_a G_b\big]_{r'} \mathcal{S}_{LL_1}(m_\omega; r, r') \\ &+ \begin{pmatrix} G_b\langle a'\|\mathcal{T}_{\mathcal{J}L}\|b\rangle \\ -F_b\langle a\|\mathcal{T}_{\mathcal{J}L}\|b'\rangle\end{pmatrix}_r \int dr' \big[\langle a\|\mathcal{T}_{\mathcal{J}L_1}\|b\rangle G_a G_b - \langle a'\|\mathcal{T}_{\mathcal{J}L_1}\|b'\rangle F_a F_b\big]_{r'} \mathcal{S}_{LL_1}(m_\omega; r, r') \Bigg\},\end{aligned} \tag{A.80}$$

or in terms of CG coefficients,

$$\begin{aligned}\begin{pmatrix}\bar{\bar{X}}^{(\omega)}\\ \bar{\bar{Y}}^{(\omega)}\end{pmatrix}_r &= \sqrt{6} m_\omega \sum_b \delta_{\tau_a\tau_b} \frac{\hat{j}_a^2}{4\pi} \sum_{\mathcal{J}L} \sum_{L_1}^{L\pm1} (-)^{\mathcal{J}} \hat{\mathcal{J}}^{-2} f_{L\mathcal{J}}(L_1) \Big(C^{\mathcal{J}0}_{j_a\frac{1}{2}j_b-\frac{1}{2}}\Big)^2 \\ &\times \Bigg\{ \frac{f_\omega}{2M} \begin{pmatrix} F_b B^{a'b'}_{\mathcal{J}L_1} \\ -G_b B^{ab}_{\mathcal{J}L_1}\end{pmatrix}_r \int dr' g_\omega(r') \big[B^{ab'}_{\mathcal{J}L} G_a F_b + B^{a'b}_{\mathcal{J}L} F_a G_b\big]_{r'} \mathcal{S}_{LL_1}(m_\omega; r, r') \\ &+ g_\omega \begin{pmatrix} G_b B^{a'b}_{\mathcal{J}L} \\ -F_b B^{ab'}_{\mathcal{J}L}\end{pmatrix}_r \int dr' \frac{f_\omega(r')}{2M} \big[B^{ab}_{\mathcal{J}L_1} G_a G_b + B^{a'b'}_{\mathcal{J}L_1} F_a F_b\big]_{r'} \mathcal{S}_{LL_1}(m_\omega; r, r') \Bigg\}.\end{aligned} \tag{A.81}$$

The contributions of the ρ meson is practically identical to those of the ω meson which can be obtained by making the following replacements:

$$m_\omega, g_\omega, f_\omega \to m_\rho, g_\rho, f_\rho, \qquad \rho_t \to \rho_t^{(3)}, \qquad \rho_v \to \rho_v^{(3)}, \qquad \sum_{ab} \delta_{\tau_a\tau_b} \to \sum_{ab} (2 - \delta_{\tau_a\tau_b}). \tag{A.82}$$

A.2.6 Electro-magnetic interaction

The derivation of the electro-magnetic field is similar to that of the ω-field, with different propagators. The Hamiltonian for the electro-magnetic field reads as

$$E_{e.m} = -\frac{1}{2}e^2 \sum_{\alpha\beta}^{\pi} \int d\boldsymbol{r} \int d\boldsymbol{r}' \bar{f}_\alpha(\boldsymbol{r})\gamma^\mu f_\beta(\boldsymbol{r}')D_{e.m}(\boldsymbol{r},\boldsymbol{r}')\bar{f}_\beta(\boldsymbol{r}')\gamma_\mu f_\alpha(\boldsymbol{r}), \tag{A.83}$$

where the propagator of the electro-magnetic field and its expansion can be found in Remark 3.

Hartree term

For the direct term, only the $L = 0$ term contributes:

$$E^D_{e.m} = \frac{1}{2}4\pi e \iint dr\, r^2 dr'\, r'^2 e\rho_c(r)\frac{1}{r_>}\rho_c(r'), \tag{A.84}$$

where the charge density ρ_c is defined in Eq. (2.60b). It leads to the local self-energy

$$\Sigma_{0,A}(r) = e\int dr'\, r'^2 \rho_c(r')\frac{1}{r_>}, \tag{A.85}$$

where $r_>$ ($r_<$) denotes the larger (smaller) of r and r'.

Fock term

For the exchange part, there are also two types of contributions. The time-like component $\mu = 0$ reads

$$\begin{aligned}\bar{E}^E_{e.m} =& -\frac{1}{2}e^2 \sum_{ab}^{\pi} \hat{j}_a^2 \sum_L \hat{L}^{-2}|\langle a\|Y_L\|b\rangle|^2 \\ &\times \int dr dr' \big[G_a G_b + F_a F_b\big]_{r'} \frac{r_<^L}{r_>^{L+1}} \big[G_b G_a + F_b F_a\big]_r.\end{aligned} \tag{A.86}$$

The space-like component $\mu = i$ gives

$$\begin{aligned}\bar{\bar{E}}^E_{e.m} =& +e^2 \sum_{ab}^{\pi} \frac{\hat{j}_a^2\hat{j}_b^2}{4\pi} \sum_L{}'' \hat{L}^{-2} \int dr dr' \big[F_a G_a\big]_{r'} \frac{r_<^L}{r_>^{L+1}} \\ &\times \Big[C^{L0}_{j_a\frac{1}{2}j_b-\frac{1}{2}} C^{L0}_{j_a\frac{1}{2}j_b-\frac{1}{2}} (F_b G_a - G_b F_a) + 2C^{L0}_{l'_a 0 l_b 0} C^{L0}_{l'_a 0 l_b 0} G_b F_a\Big]_r.\end{aligned} \tag{A.87}$$

The contributions to the $(X, Y)^T$ components in the Dirac equation read as

$$\begin{pmatrix}\bar{X}^{(e.m)}\\ \bar{Y}^{(e.m)}\end{pmatrix}_r = -e^2\hat{j}_a^{-2} \sum_b^{\pi} \begin{pmatrix}F_b\\ G_b\end{pmatrix}_r \sum_L \hat{L}^{-2}|\langle a\|Y_L\|b\rangle|^2 \int dr' \frac{r_<^{L+1}}{r_>^L}\Big[G_a G_b + F_a F_b\Big]_{r'}, \tag{A.88}$$

$$\begin{aligned}\begin{pmatrix}\bar{\bar{X}}^{(c.m.)}\\ \bar{\bar{Y}}^{(c.m.)}\end{pmatrix}_r =& +e^2\hat{j}_a^{-2} \sum_{b;\mathcal{J},L} \begin{pmatrix}G_b\langle a'\|\mathcal{T}_{\mathcal{J}L}\|b\rangle\\ -F_b\langle a\|\mathcal{T}_{\mathcal{J}L}\|b'\rangle\end{pmatrix}_r \\ &\times \int dr' \frac{r_<^{L+1}}{r_>^L}\Big[F_a G_b\langle a'\|\mathcal{T}_{\mathcal{J}L}\|b\rangle - G_a F_b\langle a\|\mathcal{T}_{\mathcal{J}L}\|b'\rangle\Big]_{r'},\end{aligned} \tag{A.89}$$

or in terms of CG coefficients,

$$\begin{pmatrix}\bar{X}^{(e.m)}\\ \bar{Y}^{(e.m)}\end{pmatrix}_r = -e^2 \sum_b^Z \frac{\hat{j}_b^2}{4\pi} \begin{pmatrix}F_b\\ G_b\end{pmatrix}_r \sum_L{}' \hat{L}^{-2}\Big(C^{L0}_{j_a\frac{1}{2}j_b-\frac{1}{2}}\Big)^2 \int dr' \frac{r_<^{L+1}}{r_>^L}\Big[G_a G_b + F_a F_b\Big]_{r'}, \tag{A.90}$$

$$\begin{pmatrix} \bar{\bar{X}}^{(c.m.)} \\ \bar{\bar{Y}}^{(c.m.)} \end{pmatrix}_r = +\,e^2 \sum_b \frac{\hat{j}_b^2}{4\pi} \begin{pmatrix} G_b \\ F_b \end{pmatrix}_r \sum_L{}'' \int dr' \frac{r_<^{L+1}}{r_>^L} \times \left\{ \left(C^{L0}_{j_a \frac{1}{2} j_b -\frac{1}{2}} \right)^2 \begin{pmatrix} G_a F_b - G_b F_a \\ G_b F_a - G_a F_b \end{pmatrix} + 2 \left(C^{L0}_{l'_a 0 l_b 0} \right)^2 \begin{pmatrix} F_a G_b \\ G_a F_b \end{pmatrix} \right\}_{r'} . \tag{A.91}$$

A.3 Numerical recipe

The system of coupled integro-differential equations is rather cumbersome to solve in r space. It is advantageous to rewrite the Fock potentials in a completely equivalent form as proposed in Ref. [38].

Introducing the effective local potentials X_G, X_F , Y_G and Y_F that facilitate the inclusion of the exchange terms by the definitions

$$X_\alpha(r) = \frac{G_a(r) X_\alpha(r)}{G_a^2(r) + F_a^2(r)} G_a(r) + \frac{F_a(r) X_\alpha(r)}{G_a^2(r) + F_a^2(r)} F_a(r) \equiv X_{\alpha,G_a}(r) G_a(r) + X_{\alpha,G_a}(r) F_a(r), \tag{A.92a}$$

$$Y_\alpha(r) = \frac{G_a(r) Y_\alpha(r)}{G_a^2(r) + F_a^2(r)} G_a(r) + \frac{F_a(r) Y_\alpha(r)}{G_a^2(r) + F_a^2(r)} F_a(r) \equiv Y_{\alpha,G_a}(r) G_a(r) + Y_{\alpha,G_a}(r) F_a(r), \tag{A.92b}$$

or in a matrix form

$$\begin{pmatrix} Y_\alpha \\ X_\alpha \end{pmatrix}_r = \int dr' \begin{pmatrix} Y_{G_\alpha} & Y_{F_\alpha} \\ X_{G_\alpha} & X_{F_\alpha} \end{pmatrix}_{(r,r')} \begin{pmatrix} G_\alpha \\ F_\alpha \end{pmatrix}_{r'} , \tag{A.93}$$

all fields are now functions of r. The integro-differential equations are formally transformed into homogeneous differential ones,

$$E_a G_a(r) = -\Big[\frac{d}{dr} - \frac{\kappa_a}{r} - Y_{\alpha,G_a}(r) \Big] F_a(r) + [M + \Sigma_S(r) + \Sigma_0(r) + Y_{\alpha,G_a}(r)] G_a(r), \tag{A.94a}$$

$$E_a F_a(r) = +\Big[\frac{d}{dr} + \frac{\kappa_a}{r} + X_{\alpha,G_a}(r) \Big] G_a(r) - [M + \Sigma_S(r) - \Sigma_0(r) - X_{\alpha,G_a}(r)] F_a(r), \tag{A.94b}$$

which can be solved iteratively by the standard techniques used in the Hartree approach, with the auxiliary potential terms $(X, Y)^T$ to be determined iteratively until convergency.

Appendix B

Mathematical formulae

Remark 1 *Wigner-Eckart theorem*

The Wigner-Eckart theorem is a theorem of representation theory and quantum mechanics a link between the symmetry transformation groups of space and the laws of conservation of energy, momentum, and angular momentum It states that matrix elements of an irreducible tensor operators $\mathcal{T}_{kq}$ on the basis $|jm\rangle$ of angular momentum eigenstates $|\hat{J}^2, \hat{J}_z\rangle$ can be expressed as the product of two factors, one of which is independent of angular momentum orientation, the reduced matrix element $\langle j||T_k||j'\rangle$, and the other a Clebsch-Gordan (CG) coefficient (or a Wigner 3-j symbol) [132],

$$\langle jm|\mathcal{T}_{kq}|j'm'\rangle = (-2)^k \hat{j}^{-1} C^{jm}_{j'm'kq} \langle j||\mathcal{T}_k||j'\rangle = (-)^{j-m} \begin{pmatrix} j & k & j' \\ -m & q & m' \end{pmatrix} \langle j||\mathcal{T}_k||j'\rangle \tag{B.1}$$

The reduced matrix of the composite tensor

$$\mathcal{T}_{KQ}(k_1k_2) = \sum_q C^{KQ}_{k_1qk_2Q-q} R_{k_1q} S_{k_2Q-q} \tag{B.2}$$

may be evaluated in terms of the reduced matrix elements of the R and S,

$$\langle J||\mathcal{T}_K||J'\rangle = (-)^{K+J+J'} \hat{K} \sum_{J''} \begin{pmatrix} J & J' & K \\ k_2 & k_1 & J'' \end{pmatrix} \langle J||R_{k_1}||J''\rangle \langle J''||S_{k_2}||J'\rangle. \tag{B.3}$$

In a two-component system the tensor $R_{k_1}(1)$ acts only on the first part and $S_{k_2}(2)$ only on the second part. Then, the reduced matrix of the composite tensor

$$\mathcal{T}_{KQ}(k_1k_2) = \sum_{q_1q_2} C^{KQ}_{k_1q_1k_2q_2} R_{k_1q_1} S_{k_2q_2} \tag{B.4}$$

may be evaluated as

$$\langle j_1j_2J||\mathcal{T}_K(k_1k_2)||j_1'j_2'J'\rangle = (-)^{K+J+J'} \hat{K}\hat{J}\hat{J}' \begin{Bmatrix} J & J' & K \\ j_1 & j_1' & k_1 \\ j_2 & j_2' & k_2 \end{Bmatrix} \langle j_1||R_{k_1}||j\prime_1\rangle \langle j_2||S_{k_2}||j\prime_2\rangle. \tag{B.5}$$

Remark 2 *Gradient of Yukawa propagator*

As it is conventional, in the meson exchange model, the meson propagators are Yukawa functions

$$v(\mu; \boldsymbol{r}_1, \boldsymbol{r}_2) = \frac{1}{4\pi} \frac{e^{-\mu|\boldsymbol{r}_1 - \boldsymbol{r}_2|}}{|\boldsymbol{r}_1 - \boldsymbol{r}_2|} \tag{B.6}$$

which can be expanded in terms of spherical modified Bessel functions combined with the spherical harmonics,

$$v(\mu;\boldsymbol{r}_1,\boldsymbol{r}_2)=\sum_{L=0}^{\infty}R_{LL}(\mu;r_1,r_2)\boldsymbol{Y}_L(\hat{\boldsymbol{r}}_1)\cdot\boldsymbol{Y}_L(\hat{\boldsymbol{r}}_2) \tag{B.7}$$

where

$$R_{L_1L_2}(\mu;r_1,r_2)=\sqrt{\frac{1}{r_1r_2}}\Big[I_{L_1+\frac{1}{2}}(z_1)K_{L_2+\frac{1}{2}}(z_2)\theta(z_2-z_1)+K_{L_1+\frac{1}{2}}(z_1)I_{L_2+\frac{1}{2}}(z_2)\theta(z_1-z_2)\Big]. \tag{B.8}$$

with $z=\mu r$, $\theta(z)=1$ for $z\geq 0$, and $\theta(z)=0$ for $z<0$.

The first gradient on the propagator with respect to $\boldsymbol{r}_1$ or $\boldsymbol{r}_2$ read

$$\boldsymbol{\nabla}_1 v(\mu;\boldsymbol{r}_1,\boldsymbol{r}_2)=-\mu\sum_{LM}\sum_{L_1}C_{L010}^{L_10}S_{LL_1}(\mu;r_1,r_2)Y_{LM}^{L_1}(\hat{\boldsymbol{r}}_1)Y_{LM}^{*}(\hat{\boldsymbol{r}}_2), \tag{B.9a}$$

$$\boldsymbol{\nabla}_2 v(\mu;\boldsymbol{r}_1,\boldsymbol{r}_2)=+\mu\sum_{LM}\sum_{L_1}C_{L010}^{L_10}S_{LL_1}(\mu;r_1,r_2)Y_{LM}(\hat{\boldsymbol{r}}_1)Y_{LM}^{L_1*}(\hat{\boldsymbol{r}}_2), \tag{B.9b}$$

where

$$\begin{aligned}S_{LL_1}(\mu;r_1,r_2)&\equiv\Big(\frac{d}{dz_1}+\frac{\alpha_{LL_1}}{z_1}\Big)R_{LL}(\mu;r_1,r_2)\\&=\mu\sqrt{\frac{1}{z_1z_2}}\Big[I_{L_1+\frac{1}{2}}(z_1)K_{L+\frac{1}{2}}(z_2)\theta(z_2-z_1)-K_{L_1+\frac{1}{2}}(z_1)I_{L+\frac{1}{2}}(z_2)\theta(z_1-z_2)\Big]\end{aligned} \tag{B.10}$$

and α_{LL_1} is defined in Remark 9. Obviously, one has $S_{LL_1}(\mu;r_1,r_2)=-S_{L_1L}(\mu;r_2,r_1)$.

The second gradient with respect to $\boldsymbol{r}_2$ reads as,

$$\begin{aligned}\boldsymbol{\nabla}_2\boldsymbol{\nabla}_1 v(\mu;\boldsymbol{r}_1,\boldsymbol{r}_2)&=\mu^2\sum_{LM}\sum_{L_1L_2}C_{L010}^{L_10}C_{L010}^{L_20}\Big(\frac{d}{dz_2}+\frac{\alpha_{LL_2}}{z_2}\Big)S_{LL_1}(\mu;r_1,r_2)(-1)^M Y_{LM}^{L_1}(\hat{\boldsymbol{r}}_1)Y_{L-M}^{L_2}(\hat{\boldsymbol{r}}_2)\\&=\mu^2\sum_{L}\sum_{L_1L_2}C_{L010}^{L_10}C_{L010}^{L_20}\big[-R_{L_1L_2}+D_{LL_1}\delta(z_1-z_2)\big]\boldsymbol{Y}_{LL_1}(\hat{\boldsymbol{r}}_1)\cdot\boldsymbol{Y}_{LL_2}(\hat{\boldsymbol{r}}_2)\end{aligned} \tag{B.11}$$

where

$$D_{LL_1}(\mu;r_1,r_2)=\mu\sqrt{\frac{1}{z_1z_2}}\Big[I_{L_1+\frac{1}{2}}(z_1)K_{L+\frac{1}{2}}(z_2)\delta(z_2-z_1)+K_{L_1+\frac{1}{2}}(z_1)L_{L+\frac{1}{2}}(z_2)\delta(z_1-z_2)\Big] \tag{B.12}$$

For simplicity, one can write the second gradient into a more compact form

$$\boldsymbol{\nabla}_2\boldsymbol{\nabla}_1 v(\mu;\boldsymbol{r}_1,\boldsymbol{r}_2)=\mu^2\sum_{L}\sum_{L_1L_2}^{L\pm1}C_{L010}^{L_10}C_{L010}^{L_20}\mathcal{V}_L^{L_1L_2}(\mu;r_1,r_2)\boldsymbol{Y}_{LL_1}(\hat{\boldsymbol{r}}_1)\cdot\boldsymbol{Y}_{LL_2}(\hat{\boldsymbol{r}}_2) \tag{B.13}$$

with

$$\mathcal{V}_L^{L_1L_2}(\mu;r_1,r_2)\equiv-R_{L_1L_2}(\mu;r_1,r_2)+D_{LL_1}\delta(z_1-z_2), \tag{B.14}$$

or

$$\mathcal{V}_L^{L_1L_2}(\mu;r_1,r_2)\equiv-R_{L_1L_2}(\mu;r_1,r_2)+\mu\frac{1}{z_1^2}\delta(z_1-z_2). \tag{B.15}$$

Remark 3 *Expansion of electro-magnetic propagator*

The propagator of the electro-magnetic fields

$$v(\boldsymbol{r}_1, \boldsymbol{r}_2) = \frac{1}{4\pi} \frac{1}{|\boldsymbol{r}_1 - \boldsymbol{r}_2|} \tag{B.16}$$

can be expanded in terms of spherical harmonics,

$$v(\boldsymbol{r}_1, \boldsymbol{r}_2) = \sum_{L=0}^{\infty} \hat{L}^2 \frac{r_<^L}{r_>^{L+1}} \boldsymbol{Y}_L(\hat{\boldsymbol{r}}_1) \cdot \boldsymbol{Y}_L(\hat{\boldsymbol{r}}_2) \tag{B.17}$$

where $r_>$ ($r_<$) denotes the larger (small) of r_1 and r_2.

Remark 4 *Expansion of Delta function*

The delta function $\delta(\boldsymbol{r}_1 - \boldsymbol{r}_2)$ can be expanded in terms of spherical harmonics,

$$\delta(\boldsymbol{r}_1 - \boldsymbol{r}_2) = \frac{\delta(r_1 - r_2)}{r_1^2} \sum_{L=0}^{\infty} \boldsymbol{Y}_L(\hat{\boldsymbol{r}}_1) \cdot \boldsymbol{Y}_L(\hat{\boldsymbol{r}}_2). \tag{B.18}$$

Remark 5 *Gradient of function containing spherical harmonics*

The gradient of $f(r)Y_{lm}(\hat{\boldsymbol{r}})$, with $f(r)$ an arbitrary function of $r \equiv |r|$, can be expanded in terms of vector spherical harmonics $\boldsymbol{Y}_{lm}^{l'}$ (where $l' = l \pm 1$),

$$\boldsymbol{\nabla} f(r) Y_{lm}(\hat{\boldsymbol{r}}) = -\sum_{l_1} C_{l010}^{l_1 0} \Big(\frac{d}{dr} + \frac{\alpha_{ll_1}}{r} \Big) f(r) Y_{lm}^{l_1}(\hat{\boldsymbol{r}}) \tag{B.19}$$

with $\alpha_{ll_1} = -l$ if $l_1 = l + 1$, and $\alpha_{ll_1} = l + 1$ if $l_1 = l - 1$.

For C-G coefficients, we have

$$C_{L010}^{L_1 0} = \begin{cases} -\frac{\sqrt{L}}{\sqrt{2L+1}}, & \text{if } L_1 = L - 1; \\ +\frac{\sqrt{L+1}}{\sqrt{2L+1}}, & \text{if } L_1 = L + 1. \end{cases} \tag{B.20}$$

thus

$$C_{L010}^{L_1 0} C_{L010}^{L_2 0} = i^{L_2 - L_1} \sqrt{|\beta_{LL_1} \beta_{LL_2}|} \hat{L}^{-2} \tag{B.21}$$

with

$$\beta_{LL_1} = \begin{cases} -L, & \text{if} \quad L_1 = L - 1; \\ L + 1, & \text{if} \quad L_1 = L + 1. \end{cases} \tag{B.22}$$

Remark 6 *Modified spherical Bessel function*

For the Modified Spherical Bessel functions,

$$f_n(z) = \sqrt{\frac{1}{2}\pi/z} I_{n+\frac{1}{2}}(z), \quad (-1)^{n+1} \sqrt{\frac{1}{2}\pi/z} K_{n+\frac{1}{2}}(z); \qquad (n = 0, \pm 1, \pm 2 \cdots). \tag{B.23}$$

we have the following derivative relationship,

$$\Big(\frac{d}{dz} + \frac{\alpha_{nn_1}}{z} \Big) f_n(z) = f_{n_1}(z) \tag{B.24}$$

with $\alpha_{nn_1} = -n$ if $n_1 = n + 1$, and $\alpha_{nn_1} = n + 1$ if $n_1 = n - 1$. From this derivative relation, one can easily obtain

$$f_{n-1}(z) - f_{n+1}(z) = (2n + 1) z^{-1} f_n(z) \tag{B.25a}$$

$$nf_{n-1}(z) + (n+1)f_{n+1}(z) = (2n+1)\frac{d}{dz}f_n(z) \tag{B.25b}$$

Then because of the different phase between I and K, there is a sign phase for K functions. E.g.,

$$K_{n-1+\frac{1}{2}} - K_{n+1+\frac{1}{2}} = -(2n+1)z^{-1}K_{n\frac{1}{2}}(z) \tag{B.26a}$$

$$\left[\frac{d}{dz} + \frac{\alpha_{nn_1}}{z}\right]\tilde{K}_n(z) = -\tilde{K}_{n_1}(z) \tag{B.26b}$$

with $\tilde{K}_n(z) \equiv z^{-\frac{1}{2}}K_{n+\frac{1}{2}}(z)$

Remark 7 *Some Useful reduced matrix elements*

The reduced matrix element of the spherical harmonic operator reads [234]

$$\langle a\|Y_L\|b\rangle = \begin{cases} \frac{1}{\sqrt{4\pi}}\hat{j}_a\hat{j}_b\hat{L}(-)^{j_b-L-\frac{1}{2}}\begin{pmatrix} j_a & j_b & L \\ \frac{1}{2} & -\frac{1}{2} & 0\end{pmatrix} & \text{if } l_a+l_b+L \text{ is even;} \\ 0, & \text{if } l_a+l_b+L \text{ is odd.}\end{cases} \tag{B.27}$$

or

$$\langle a\|Y_L\|b\rangle \quad = \quad (-1)^{j_a+L-\frac{1}{2}}\frac{1}{\sqrt{4\pi}}\hat{j}_b C^{L0}_{j_a\frac{1}{2}j_b-\frac{1}{2}}. \tag{B.28}$$

It obeys the symmetry property

$$\langle a\|Y_L\|b\rangle = (-)^{j_a-j_b}\langle b\|Y_L\|a\rangle. \tag{B.29}$$

The reduced matrix element of the vector spherical harmonic operator [234]

$$\sigma_\nu Y_{LM} = \sum_{\mathcal{J}\mathcal{M}} C^{\mathcal{J}\mathcal{M}}_{LM1\nu}\mathcal{T}^L_{\mathcal{J}\mathcal{M}}, \tag{B.30}$$

reads

$$\langle a\|\mathcal{T}_{\mathcal{J}L}\|b\rangle = \left[\frac{6}{4\pi}\right]^{\frac{1}{2}}(-)^{l_a}\hat{j}_a\hat{j}_b\hat{l}_a\hat{l}_b\hat{\mathcal{J}}\hat{L}\begin{pmatrix} l_a & L & l_b \\ 0 & 0 & 0\end{pmatrix}\begin{Bmatrix} j_a & j_b & \mathcal{J} \\ l_a & l_b & L \\ \frac{1}{2} & \frac{1}{2} & 1\end{Bmatrix} \tag{B.31}$$

where

$$\mathcal{T}_{JM} = \sum_{\nu k}(-)^{L-1+M}\hat{J}\begin{pmatrix} L & 1 & J \\ \nu & k & -M\end{pmatrix}Y_{L\nu}\sigma_k. \tag{B.32}$$

It can be simplified as

$$\langle a\|\mathcal{T}_{\mathcal{J}L}\|b\rangle = (-1)^{l_a}\frac{1}{\sqrt{4\pi}}\hat{j}_a\hat{j}_b B^{ab}_{\mathcal{J}L}\begin{pmatrix} j_a & j_b & \mathcal{J} \\ \frac{1}{2} & -\frac{1}{2} & 0\end{pmatrix} = (-1)^{l_a}\frac{1}{\sqrt{4\pi}}\hat{j}_a\hat{j}_b\hat{\mathcal{J}}^{-1}B^{ab}_{\mathcal{J}L}C^{\mathcal{J}0}_{j_a\frac{1}{2}j_b-\frac{1}{2}} \tag{B.33}$$

where

$$B^{ab}_{\mathcal{J}L} \quad = \quad \begin{cases} (-1)^{j_b+l_b+\frac{1}{2}}\frac{\kappa_{ab}+\mathcal{J}+1}{\sqrt{(\mathcal{J}+1)}}, & \text{if} \quad L=\mathcal{J}+1, \\ -\frac{1}{2}\hat{\mathcal{J}}\frac{\hat{j}_b^2+(-1)^{j_a+j_b+\mathcal{J}}\hat{j}_a^2}{\sqrt{\mathcal{J}(\mathcal{J}+1)}}, & \text{if} \quad L=\mathcal{J}, \\ (-1)^{j_b+l_b+\frac{1}{2}}\frac{\kappa_{ab}-\mathcal{J}}{\sqrt{\mathcal{J}}}, & \text{if} \quad L=\mathcal{J}-1, \end{cases} \tag{B.34}$$

with κ_{ab} defined in Remark 8. Notice that $B^{ab}_{\mathcal{J}L} \neq B^{ba}_{\mathcal{J}L}$ but $B^{ab}_{\mathcal{J}L} C^{\mathcal{J}0}_{j_a\frac{1}{2}j_b-\frac{1}{2}} = B^{ba}_{\mathcal{J}L} C^{\mathcal{J}0}_{j_b\frac{1}{2}j_a-\frac{1}{2}}$.

Using the orthogonality of $9j$-symbols we obtain

$$\sum_{\mathcal{J}} \langle a||\mathcal{T}_{\mathcal{J}L}||b\rangle\langle a||\mathcal{T}_{\mathcal{J}L}||b\rangle = \frac{\hat{j}_b^2}{4\pi}\left[2C^{L0}_{l_a0l_b0}C^{L0}_{l_a0l_b0} - C^{L0}_{j_a\frac{1}{2}j_b-\frac{1}{2}}C^{L0}_{j_a\frac{1}{2}j_b-\frac{1}{2}}\right], \tag{B.35a}$$

$$\sum_{\mathcal{J}} \langle a\|\mathcal{T}_{\mathcal{J}L}\|b'\rangle\langle a\|\mathcal{T}_{\mathcal{J}L}\|b'\rangle = \frac{\hat{j}_b^2}{4\pi}\left[2C^{L0}_{l_a0l'_b0}C^{L0}_{l_a0l'_b0} - C^{L0}_{j_a\frac{1}{2}j_b-\frac{1}{2}}C^{L0}_{j_a\frac{1}{2}j_b-\frac{1}{2}}\right], \tag{B.35b}$$

$$\sum_{\mathcal{J}} \langle a\|\mathcal{T}_{\mathcal{J}L}\|b'\rangle\langle a'\|\mathcal{T}_{\mathcal{J}L}\|b\rangle = -\frac{\hat{j}_b^2}{4\pi}C^{L0}_{j_a\frac{1}{2}j_b-\frac{1}{2}}C^{L0}_{j_a\frac{1}{2}j_b-\frac{1}{2}}, \tag{B.35c}$$

$$\sum_{\mathcal{J}} \langle a||\mathcal{T}_{\mathcal{J}L}||b\rangle\langle a'||\mathcal{T}_{\mathcal{J}L}||b'\rangle = -\frac{\hat{j}_b^2}{4\pi}C^{L0}_{j_a\frac{1}{2}j_b-\frac{1}{2}}C^{L0}_{j_a\frac{1}{2}j_b-\frac{1}{2}} \tag{B.35d}$$

$$\sum_{L} C^{L0}_{l_a0l_b0}C^{L0}_{l_a0l_b0} = 1 \tag{B.36a}$$

$$\sum_{L=even} C^{L0}_{j_a\frac{1}{2}j_b-\frac{1}{2}}C^{L0}_{j_a\frac{1}{2}j_b-\frac{1}{2}} = \sum_{L=odd} C^{L0}_{j_a\frac{1}{2}j_b-\frac{1}{2}}C^{L0}_{j_a\frac{1}{2}j_b-\frac{1}{2}} = \frac{1}{2} \tag{B.36b}$$

$$\langle a\|\mathcal{T}_{LL_1}\|b'\rangle = (-1)^{j_a+L-\frac{1}{2}}\frac{\kappa_{ab}+\beta_{LL_1}}{\sqrt{|\beta_{LL_1}|}}\frac{\hat{j}_b}{\sqrt{4\pi}\hat{L}}C^{L0}_{j_a\frac{1}{2}j_b-\frac{1}{2}} \tag{B.37}$$

Remark 8 *Dirac matrices*

The γ matrices in the Dirac equation satisfy the anti-commutation relations,

$$\gamma^\mu\gamma^\nu + \gamma^\nu\gamma^\mu = 2g^{\mu\nu} \tag{B.38}$$

and are related to the $\boldsymbol{\alpha}$ and β matrices by

$$\boldsymbol{\gamma} = \beta\boldsymbol{\alpha}, \qquad \beta = \gamma^0. \tag{B.39}$$

A familiar representation of the Dirac matrices is

$$\gamma^0 = \begin{pmatrix} 1 & 0 \\ 0 & 1 \end{pmatrix}, \qquad \boldsymbol{\gamma} = \begin{pmatrix} 0 & \boldsymbol{\sigma} \\ \boldsymbol{\sigma} & 0 \end{pmatrix}, \tag{B.40}$$

where

$$\sigma^1 = \begin{pmatrix} 0 & 1 \\ 1 & 0 \end{pmatrix}, \qquad \sigma^2 = \begin{pmatrix} 0 & -i \\ i & 0 \end{pmatrix}, \qquad \sigma^3 = \begin{pmatrix} 1 & 0 \\ 0 & -1 \end{pmatrix}. \tag{B.41}$$

Frequently appearing combinations are

$$\gamma^5 = i\gamma^0\gamma^1\gamma^2\gamma^3, \qquad \sigma^{\mu\nu} = \frac{i}{2}[\gamma^\mu, \gamma^\nu]. \tag{B.42}$$

In this representation the components of $\sigma^{\mu\nu}$ are

$$\sigma^{0i} = i\begin{pmatrix} 0 & \sigma^i \\ \sigma^i & 0 \end{pmatrix}, \qquad \sigma^{ij} = \begin{pmatrix} \sigma^k & 0 \\ 0 & \sigma^k \end{pmatrix}. \tag{B.43}$$

with $i, j, k = 1, 2, 3$ in cyclic order, and

$$\gamma^5 = \gamma_5 = \begin{pmatrix} 0 & 1 \\ 1 & 0 \end{pmatrix}. \tag{B.44}$$

Remark 9 *Some useful short-hand notations*

Some short-hand notation are often used in the derivations. Here we list them as follows,

$$\hat{j}^2 = 2j + 1, \tag{B.45}$$

$$\kappa_a = \hat{j}_a^2(l_a - j_a), \tag{B.46}$$

$$\kappa_{ab} = \kappa_a + \kappa_b, \tag{B.47}$$

$$\tilde{\kappa}_{ab} = \kappa_a - \kappa_b, \tag{B.48}$$

$$\alpha_{ll_1} = \begin{cases} -l & \text{if } l_1 = l + 1, \\ l + 1 & \text{if } l_1 = l - 1. \end{cases} \tag{B.49}$$

$$\beta_{ll_1} = \begin{cases} -l & \text{if } l_1 = l - 1, \\ l + 1 & \text{if } l_1 = l + 1. \end{cases} \tag{B.50}$$

Appendix C

Links between CDF and nuclear matter properties

In this appendix, we discuss the link between the CDF and the properties on nuclear matter. We first discuss and compare the empirical parameters defined at saturation density between various CDF models. In a second part of this appendix, we show a fit of Dirac-Bruckner-Hartree-Fock (DBHF) binding energies and effective masses as function of the density and isospin asymmetries for various kinds of CDF models. Finally, we compare the predictions of the newly fitted CDF models for closed shell nuclei and compare them to experimental values and other theoretical calculations provided by the PKA1 CDF model.

C.1 Empirical parameters

The empirical parameters in uniform matter have been defined in Chap. 2, as well as the Dirac and non-relativistic effective masses, which are given in Table 2.3 for a set of CDF models widely used in the literature. We now give in Table C.1 a more complete table presenting the empirical parameter up to the skewness parameter in the isoscalar and isovector channels (Q_0 and Q_{sym}).

Table C.1: Nuclear matter properties for different CDF models used in literature: ρ_0(fm^{-3}), $E_0(MeV)$, K_0(MeV), Q_0(MeV), E_{sym}(MeV), L_{sym}(MeV), K_{sym}(MeV) and Q_{sym}(MeV).

Model	ρ_0	E_0	K_0	Q_0	E_{sym}	L_{sym}	K_{sym}	Q_{sym}
PKA1	0.1600	-15.83	229.98	949.85	36.02	103.50	213.17	291.52
PKO1	0.1520	-16.00	250.28	262.15	34.37	97.71	105.59	290.48
PKO2	0.1510	-16.03	249.53	-10.30	32.49	75.92	77.42	820.67
PKO3	0.1530	-16.04	262.44	354.99	32.99	82.99	116.47	690.47
DD-ME1	0.152	-16.20	244.90	317.00	33.07	55.47	-101.08	705.47
DD-ME2	0.152	-16.14	251.15	479.22	32.31	51.27	-87.23	776.76
DD-MEδ	0.152	-16.12	219.08	-748.00	32.35	52.85	-118.08	846.33
PKDD	0.150	-16.27	261.49	-118.84	31.19	79.51	-49.96	-28.45
TW99	0.153	-16.25	240.25	-539.76	32.77	55.31	-124.70	538.52
NL3	0.148	-16.24	270.72	198.02	37.35	118.32	100.53	182.34
NL3*	0.150	-16.31	258.56	124.19	38.71	122.72	105.73	223.58
NL-SH	0.146	-16.35	355.43	602.08	36.12	113.66	79.80	-23.47
PK1	0.148	-16.27	281.96	-29.44	37.59	115.70	55.19	-86.23
TM1	0.145	-16.26	281.46	-284.93	36.94	111.01	33.65	-67.48

It can be remarked that some empirical parameters are rather well defined, such as ρ_0, E_0, K_0 and E_{sym}, while others are much less constrained like Q_0, L_{sym}, K_{sym}, and Q_{sym}. The quantities which

are not well defined correspond to high order in the derivative. The iso-vector parameters are much less known than the isoscalar ones.

C.2 Links with DBHF predictions in uniform matter

In this section, we fit the binding energies and Dirac masses as a function of the density and the isospin asymmetry. These data are provided by the Dirac-Brueckner-Hartree-Fock (DBHF) calculation provided by the Tuebingen group, see Ref. [41] and references therein. It is worth mentioning a previous attempt to fit DBHF data [235]. In this work, it is the DBHF self-energies which are fitted while in our study, we directly fit the DBHF binding energy. In practice, we propose several parameter sets for RH and RHF with density-dependent meson-nucleon couplings by fitting the EoS and Dirac mass calculated by DBHF [41],

$$\Big\{E/\rho_b; M_D\Big\} \qquad \text{where} \qquad \rho_b = 0.05 \sim 0.40, \quad \beta = 0.0, 0.4, 1.0. \tag{C.1}$$

C.2.1 Adjustment of DBHF nuclear matter predictions

The DBHF binding energies and Dirac masses are fitted using a minimisation protocol of the standard deviation between the DBHF binding energy and Dirac mass and the ones provided by RH and RHF models where we have varied the number of mesons. Among the fits that we have selected here, we show a RH model with (σ, ω, ρ, δ) mesons (RH-4), the equivalent RHF model (RHF-4), a RHF model with 5 mesons (σ, ω, ρ, δ, π-PV) (RHF-5) and finally a RHF model with 6 mesons (σ, ω, ρ, ρ-T, δ, π-PV) (RHF-6).

The energy per nucleon E_b and the Dirac mass M_D for symmetric nuclear matter and pure neutron matter are displayed in Figs. C.1 and C.2, respectively. The various RHF models reproduce the DBHF results for symmetric matter reasonably well at saturation density and the largest deviations among the models are observed at lower and higher densities. In symmetric matter, it is also observed that at densities below $\rho \sim 1.0$ fm^{-3} all parameterizations tend to underestimate the binding energy per nucleon calculated in the DBHF approach. It is interesting to notice that only the RHF-6 including ρ-T and π-PV mesons is able to fit the low and high density DBHF binding energies in symmetric matter. For pure neutron matter shown in Fig. C.1, the RHF-6 including ρ-T and π-PV mesons is also the only model which can fit the DBHF data with the best accuracy.

We show in Table C.2 the saturation density ρ_0, saturation binding energy E_0, saturation energy density $E_V = E_0\rho_0$, incompressibility K_0, symmetry energy E_{sym} and Dirac mass $M^*{}_D$ for the DBHF model, for the various fits presented here (RHF-6, RHF-5, RHF-4 and RH-4) as well as for

Table C.2: The bulk properties of symmetric nuclear matter calculated in RHF with fitted parameterizations. The results predicted by the RHF theory with PKA1 and PKO3, and with the RH approach with DD-ME2 and DD-MEδ are also given for comparison.

	ρ_0(fm^{-3})	E_0(MeV)	E_V(MeV.fm^{-3})	K_0(MeV)	E_{sym}(MeV)	$M*_D$(M)
DBHF	0.181	-16.15	-2.923	230	34.6	0.680
RHF-6	0.181	-16.12	-2.917	226	34.0	0.671
RHF-5	0.182	-16.08	-2.926	301	34.5	0.667
RHF-4	0.178	-16.05	-2.857	277	32.8	0.655
RH-4	0.179	-16.01	-2.866	267	33.4	0.663
PKA1	0.160	-15.83	-2.532	230	36.0	0.547
PKO3	0.153	-16.04	-2.454	262	33.0	0.586
DD-ME2	0.152	-16.14	-2.453	251	32.3	0.572
DD-MEδ	0.152	-16.12	-2.450	219	32.4	0.609

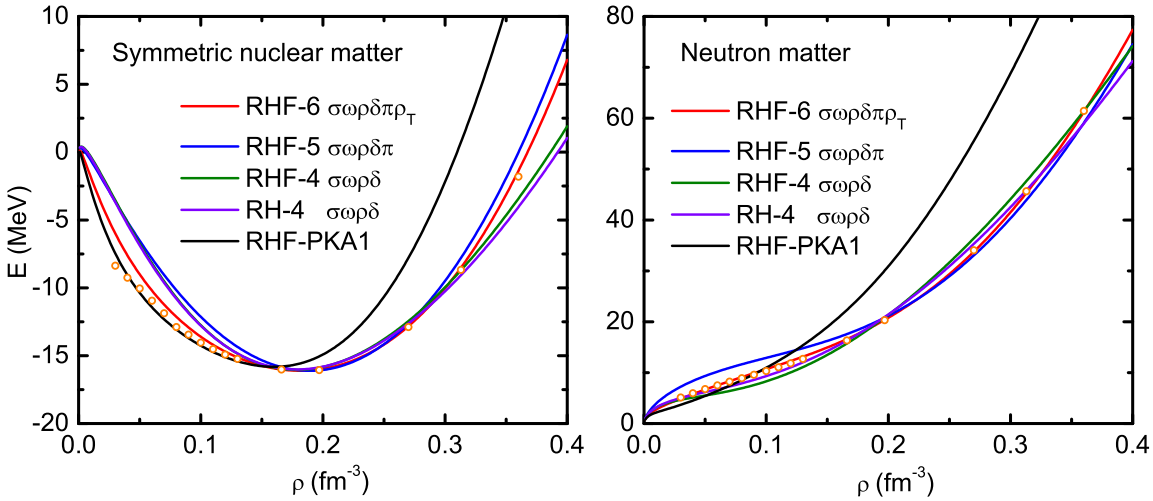

Figure C.1: The binding energy per particle for symmetric matter and neutron matter. Comparison between the RHF adjustments (lines) and the DBHF approach (circles).

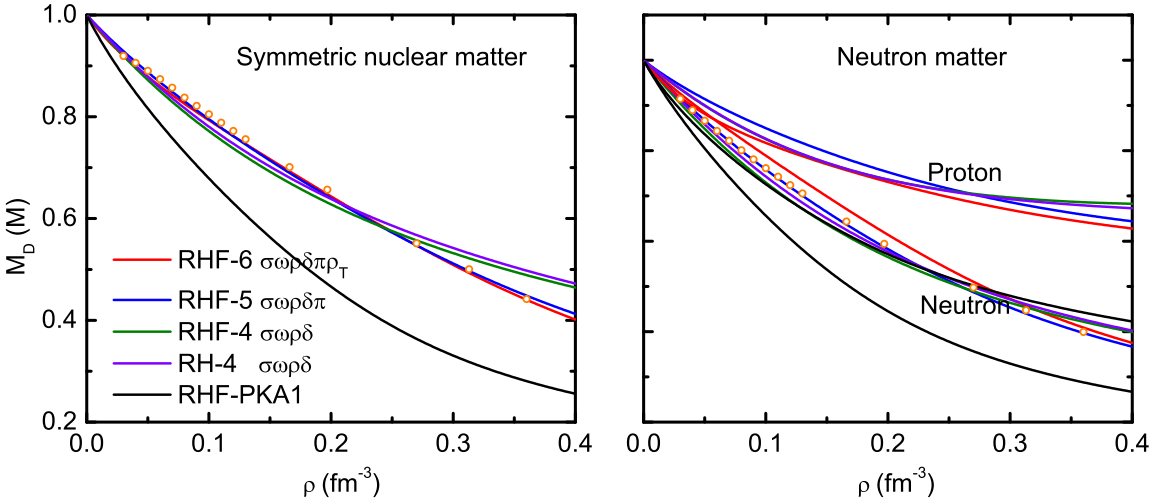

Figure C.2: The Dirac mass for symmetric matter and neutron matter. Comparison between the RHF adjustments (lines) and the DBHF approach (circles).

widely used CDF models (PKA1, PKO3, DD-ME2, DD-MEδ). It can be remarked that the best reproduction of the DBHF empirical parameters shown in Table C.2 is obtained by the RHF-6 fit. The other fits have an incompressibility which is larger than the original DBHF model. A second remark is that the DBHF saturation density is larger than the one expected from usual CDF models, see PKA1 and others for instance. We therefore expect that the nuclear radii of the RHF-i models will be smaller than the experimental ones, see next section. While the binding energy E_0 predicted by the RHF-i models is comparable to the one of the other CDF models, it shall be remarked that the energy density E_V predicted by the RHF-i models are larger (in absolute value) than the one given by the other CDF models. It is again an effect of the saturation density which is too large for the RHF-i models. Since this is the energy density which is integrated through the nuclear densities to calculate the total energy, we can also anticipate from this remark that the RHF-i models will predict, for finite nuclei, too large binding energies (in absolute value). In the next section, we will therefore calculate the predictions of the RHF-i models for a set of double-magic nuclei.

Table C.3: Binding energies (MeV) and the charge radii (fm^{-3}) for closed-shell nuclei, where $\delta_{fit} = (exp. - cal.)/exp.$

Elem.	E_b				r_c			
	EXP.	PKA1	RHF-6	δ_{fit}	EXP.	PKA1	RHF-6	δ_{fit}
^{40}Ca	- 342.05	-342.72	-398.70	-0.16	3.476	3.485	3.274	-0.060
^{90}Zr	- 783.89	-784.35	-864.81	-0.10	4.272	4.279	4.057	-0.050
^{132}Sn	-1102.85	-1103.25	-1180.06	-0.07	-	4.699	4.522	-
^{208}Pb	-1636.43	-1636.96	-1743.66	-0.06	5.501	5.510	5.527	+0.005

C.2.2 Finite nuclei properties

Since the saturation density and the energy-density is slightly to high for the DBHF model and our fits, it is interesting to compare the predictions of these fits for finite nuclei. We have tested some closed-shell nuclei with our "best" model RHF-6. The results obtained for the binding energy and charge radius are presented in Table C.3. As anticipated in the previous section, the RHF-6 model predicts an over-binding for all nuclei considered here as well as the charge radii, except for ^{208}Pb for which the charge radius is slightly larger than the experimental one. The charge radii for ^{90}Zn and ^{208}Pb are represented in Fig. C.3 for PKA1 and RHF-6 models. It is clear that the bulk density is overestimated for the RHF-6 model, and this lead to a faster decrease of the density near the surface of nuclei. In general, we remark that the effect of fitting DBHF data with too large saturation density leads to an over-binding of finite nuclei and a shrink of their size.

In the future, we plan to complete this study and improve the predictions of our fits for finite nuclei by introducing three-body forces. The DBHF calculation is indeed only based on relativistic two-body interactions and not three-body interaction is implemented [41]. This work being not yet finalized, it is not presented in this manuscript.

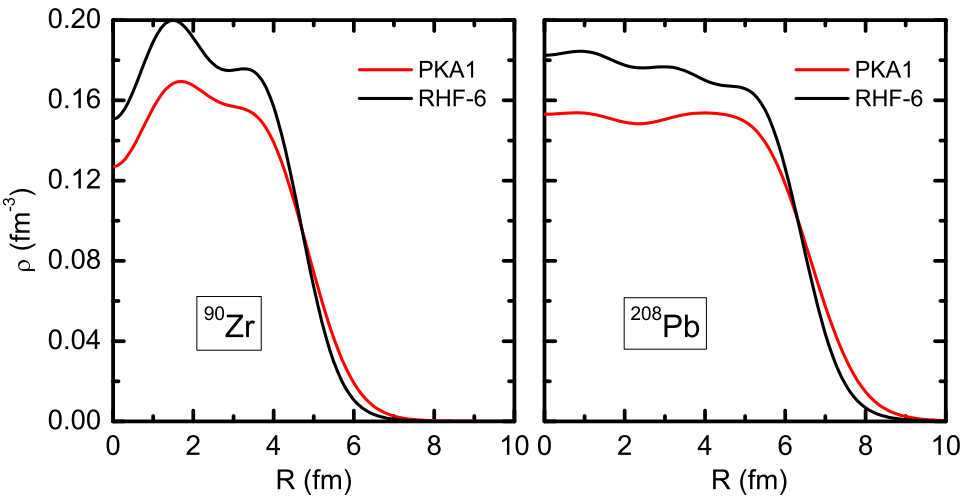

Figure C.3: Density distributions in closed-shell nuclei, RHF-6 vs PKA1.

Bibliography

[1] M. Brack, J. Damgaard, A. S. Jensen, H. C. Pauli, V. M. Strutinsky, C. Y. Wong, Funny hills: The shell-correction approach to nuclear shell effects and its applications to the fission process, Rev. Mod. Phys. 44 (1972) 320–405.

[2] A. Sobiczewski, A. Gyurkovich, M. Brack, An asymptotic form of the smooth part of the total single-particle energy, Nucl. Phys. A 289 (1977) 346–364.

[3] P. Möller, J. R. Nix, W. D. Myers, W. J. Swiatecki, Nuclear ground-state masses and deformations, At. Data Nucl. Data Tables 59 (1995) 185–381.

[4] S. E. Koonin, D. J. Dean, K. Langanke, Shell model monte carlo methods, Phys. Rep. 278 (1997) 1–77.

[5] D. J. Dean, T. Engeland, M. Hjorth-Jensen, M. P. Kartamyshev, E. Osnes, Effective interactions and the nuclear shell-model, Prog. Part. Nucl. Phys. 53 (2004) 419–500.

[6] E. Caurier, G. Martínez-Pinedo, F. Nowacki, A. Poves, A. P. Zuker, The shell model as a unified view of nuclear structure, Rev. Mod. Phys. 77 (2005) 427–488.

[7] M. Bender, P.-H. Heenen, P.-G. Reinhard, Self-consistent mean-field models for nuclear structure, Rev. Mod. Phys. 75 (2003) 121–180.

[8] J. Meng, H. Toki, S. G. Zhou, S. Q. Zhang, W. H. Long, L. S. Geng, Relativistic continuum Hartree Bogoliubov theory for ground-state properties of exotic nuclei, Prog. Part. Nucl. Phys 57 (2006) 470–563.

[9] J. R. Stone, P.-G. Reinhard, The skyrme interaction in finite nuclei and nuclear matter, Prog. Part. Nucl. Phys. 58 (2007) 587–657.

[10] H. Kümmel, K. H. Lührmann, J. G. Zabolitzky, Many-fermion theory in exps-(or coupled cluster) form, Phys. Rep. 36 (1978) 1–63.

[11] H. Feldmeier, T. Neff, R. Roth, J. Schnack, A unitary correlation operator method, Nucl. Phys. A 632 (1998) 61–95.

[12] W. Dickhoff, C. Barbieri, Self-consistent Green's function method for nuclei and nuclear matter, Prog. Part. Nucl. Phys. 52 (2004) 377–496.

[13] P. Möller, A. J. Sierk, A. Iwamoto, Five-dimensional fission-barrier calculations from ^{70}Se to ^{252}Cf, Phys. Rev. Lett. 92 (2004) 072501.

[14] M. Kowal, P. Jachimowicz, A. Sobiczewski, Fission barriers for even-even superheavy nuclei, Phys. Rev. C 82 (2010) 014303.

[15] P. Möller, W. D. Myers, H. Sagawa, S. Yoshida, New finite-range droplet mass model and equation-of-state parameters, Phys. Rev. Lett. 108 (2012) 052501.

[16] B. S. Pudliner, V. R. Pandharipande, J. Carlson, S. C. Pieper, R. B. Wiringa, Quantum monte carlo calculations of nuclei with A$\leq$ 7, Phys. Rev. C 56 (1997) 1720–1750.

[17] R. B. Wiringa, S. C. Pieper, Evolution of nuclear spectra with nuclear forces, Phys. Rev. Lett. 89 (2002) 182501.

[18] K. Kowalski, D. J. Dean, M. Hjorth-Jensen, T. Papenbrock, P. Piecuch, Coupled cluster calculations of ground and excited states of nuclei, Phys. Rev. Lett. 92 (2004) 132501.

[19] G. Hagen, T. Papenbrock, D. J. Dean, A. Schwenk, A. Nogga, M. Włoch, P. Piecuch, Coupled-cluster theory for three-body hamiltonians, Phys. Rev. C 76 (2007) 034302.

[20] R. Roth, S. Binder, K. Vobig, A. Calci, J. Langhammer, P. Navrátil, Medium-mass nuclei with normal-ordered chiral NN+3N interactions, Phys. Rev. Lett. 109 (2012) 052501.

[21] G. Hagen, M. Hjorth-Jensen, G. R. Jansen, R. Machleidt, T. Papenbrock, Evolution of shell structure in neutron-rich calcium isotopes, Phys. Rev. Lett. 109 (2012) 032502.

[22] V. Somà, T. Duguet, C. Barbieri, *Ab initio* self-consistent Gorkov-Green's function calculations of semimagic nuclei: Formalism at second order with a two-nucleon interaction, Phys. Rev. C 84 (2011) 064317.

[23] V. Somà, C. Barbieri, T. Duguet, *Ab initio* Gorkov-Green's function calculations of open-shell nuclei, Phys. Rev. C 87 (2013) 011303.

[24] V. Somà, A. Cipollone, C. Barbieri, P. Navrátil, T. Duguet, Chiral two- and three-nucleon forces along medium-mass isotope chains, Phys. Rev. C 89 (2014) 061301.

[25] W. Kohn, L. J. Sham, Self-consistent equations including exchange and correlation effects, Phys. Rev. 140 (1965) A1133–A1138.

[26] W. Kohn, Nobel lecture: Electronic structure of matter — wave functions and density functionals, Rev. Mod. Phys. 71 (1999) 1253–1266.

[27] M. Beiner, H. Flocard, N. Van Giai, P. Quentin, Nuclear ground-state properties and self-consistent calculations with the skyrme interaction: (i). spherical description, Nucl. Phys. A 238 (1995) 29–69.

[28] E. Chabanat, P. Bonche, P. Hansel, J. Meyer, R. Schaeffer, A skyrme parametrization from subnuclear to neutron star densities, Nucl. Phys. A 627 (1997) 710–746.

[29] J. Dechargé, D. Gogny, Hartree-Fock-Bogolyubov calculations with the D1 effective interaction on spherical nuclei, Phys. Rev. C 21 (1980) 1568–1593.

[30] F. Chappert, N. Pillet, M. Girod, J.-F. Berger, Gogny force with a finite-range density dependence, Phys. Rev. C 91 (2015) 034312.

[31] M. Baldo, P. Schuck, X. Viñas, Kohn–Sham density functional inspired approach to nuclear binding, Phys. Lett. B 663 (2008) 390–394.

[32] M. Baldo, L. M. Robledo, P. Schuck, X. Viñas, New Kohn-Sham density functional based on microscopic nuclear and neutron matter equations of state, Phys. Rev. C 87 (2013) 064305.

[33] F. Hofmann, H. Lenske, Hartree-Fock calculations in the density matrix expansion approach, Phys. Rev. C 57 (1998) 2281–2293.

[34] H. Nakada, Mean-field approach to nuclear structure with semi-realistic nucleon-nucleon interactions, Phys. Rev. C 78 (2008) 054301.

[35] B. D. Serot, J. D. Walecka, The relativistic nuclear many-body problem, Adv. nucl. phys 16.

[36] P. Ring, Relativistic mean field theory in finite nuclei, Prog. Part. Nucl. Phys. 37 (1996) 193–263.

[37] D. Vretenar, A. V. Afanasjev, G. A. Lalazissis, P. Ring, Relativistic Hartree Bogoliubov theory: static and dynamic aspects of exotic nuclear structure, Phys. Rep. 409 (2005) 101–259.

[38] A. Bouyssy, J.-F. Mathiot, N. Van Giai, S. Marcos, Relativistic description of nuclear systems in the Hartree-Fock approximation, Phys. Rev. C 36 (1987) 380–401.

[39] L. N. Savushkin, S. Marcos, M. L. Quelle, P. Bernardos, V. N. Fomenko, R. Niembro, Effective interaction for relativistic theory of nuclear structure, Phys. Rev. C 55 (1997) 167–178.

[40] W. H. Long, N. Van Giai, J. Meng, Density-dependent relativistic Hartree-Fock approach, Phys. Lett. B 640 (2006) 150.

[41] E. Van Dalen, C. Fuchs, C. Fuchs, Dirac-Brueckner-Hartree-Fock calculations for isospin asymmetric nuclear matter based on improved approximation schemes, Eur. Phys. J. A 31 (2007) 29–42.

[42] A. Bouyssy, S. Marcos, J. F. Mathiot, N. Van Giai, Isovector-meson contributions in the Dirac-Hartree-Fock approach to nuclear matter, Phys. Rev. Lett. 55 (1985) 1731–1733.

[43] P. Bernardos, V. N. Fomenko, N. V. Giai, M. L. Quelle, S. Marcos, R. Niembro, L. N. Savushkin, Relativistic Hartree-Fock approximation in a nonlinear model for nuclear matter and finite nuclei, Phys. Rev. C 48 (1993) 2665–2672.

[44] S. Marcos, L. N. Savushkin, V. N. Fomenko, M. L. Quelle, R. Niembro, Description of nuclear systems within the relativistic HartreeFock method with zero-range self-interactions of the scalar field, J. Phys G: Nucl. Part. Phys. 30 (2004) 703–721.

[45] Z. Ma, H. Shi, B. Chen, Isovector meson contribution in the relativistic Hartree-Fock approach for finite nuclei, Phys. Rev. C 50 (1994) 3170–3173.

[46] H.-l. Shi, B.-q. Chen, Z.-y. Ma, Relativistic density-dependent Hartree-Fock approach for finite nuclei, Phys. Rev. C 52 (1995) 144–156.

[47] C. Fuchs, H. Lenske, H. H. Wolter, Density dependent hadron field theory, Phys. Rev. C 52 (1995) 3043–3060.

[48] W. H. Long, H. Sagawa, N. Van Giai, J. Meng, Shell structure and ρ-tensor correlations in density dependent relativistic Hartree-Fock theory, Phys. Rev. C 76 (2007) 034314.

[49] W. H. Long, H. Sagawa, J. Meng, N. Van Giai, Evolution of nuclear shell structure due to the pion exchange potential, Europhys. Lett. 82 (2008) 12001.

[50] B. A. Nikolaus, T. Hoch, D. G. Madland, Nuclear ground state properties in a relativistic point coupling model, Phys. Rev. C 46 (1992) 1757–1781.

[51] T. Bürvenich, D. G. Madland, J. A. Maruhn, P.-G. Reinhard, Nuclear ground state observables and qcd scaling in a refined relativistic point coupling model, Phys. Rev. C 65 (2002) 044308.

[52] P. W. Zhao, Z. P. Li, J. M. Yao, J. Meng, New parametrization for the nuclear covariant energy density functional with a point-coupling interaction, Phys. Rev. C 82 (2010) 054319.

[53] O. Sjöberg, Binding energy of asymmetric nuclear matter, Nucl. Phys. A 222 (1974) 161–167.

[54] I. E. Lagaris, V. R. Pandharipande, Variational calculations of asymmetric nuclear matter, Nucl. Phys. A 369 (1981) 470–482.

[55] I. Bombaci, U. Lombardo, Asymmetric nuclear matter equation of state, Phys. Rev. C 44 (1991) 1892–1900.

[56] C.-H. Lee, T. T. S. Kuo, G. Q. Li, G. E. Brown, Nuclear symmetry energy, Phys. Rev. C 57 (1998) 3488–3491.

[57] A. W. Steiner, High-density symmetry energy and direct Urca process, Phys. Rev. C 74 (2006) 045808.

[58] I. Vidaña, C. Providência, A. Polls, A. Rios, Density dependence of the nuclear symmetry energy: A microscopic perspective, Phys. Rev. C 80 (2009) 045806.

[59] C. Ducoin, J. Margueron, C. Providência, I. Vidaña, Core-crust transition in neutron stars: Predictivity of density developments, Phys. Rev. C 83 (2011) 045810.

[60] M. B. Tsang, J. R. Stone, F. Camera, et al., Constraints on the symmetry energy and neutron skins from experiments and theory, Phys. Rev. C 86 (2012) 015803.

[61] X. Vinas, M. Centelles, X. Roca-Maza, M. Warda, Density dependence of the symmetry energy from neutron skin thickness in finite nuclei, Eur. Phys. J. A 50 (2012) 1–16.

[62] B. M. Santos, M. Dutra, O. Lourenço, A. Delfino, Correlations between the nuclear matter symmetry energy, its slope, and curvature from a nonrelativistic solvable approach and beyond, Phys. Rev. C 90 (2014) 035203.

[63] S. Typel, Relativistic model for nuclear matter and atomic nuclei with momentum-dependent self-energies, Phys. Rev. C 71 (2005) 064301.

[64] T. Marketin, D. Vretenar, P. Ring, Calculation of β-decay rates in a relativistic model with momentum-dependent self-energies, Phys. Rev. C 75 (2007) 024304.

[65] M. Jaminon, C. Mahaux, Effective masses in relativistic approaches to the nucleon-nucleus mean field, Phys. Rev. C 40 (1989) 354–367.

[66] NuDat Databases, National Nuclear Data Center, http://www.nndc.bnl.gov/nudat2/.

[67] K. Rutz, M. Bender, P.-G. Reinhard, J. A. Maruhn, W. Greiner, Odd nuclei and single-particle spectra in the relativistic mean-field model, Nucl. phys. A 634 (1998) 67–88.

[68] E. Litvinova, P. Ring, Covariant theory of particle-vibrational coupling and its effect on the single-particle spectrum, Phys. Rev. C 73 (2006) 044328.

[69] M. Bender, K. Rutz, P.-G. Reinhard, J. Maruhn, W. Greiner, Shell structure of superheavy nuclei in self-consistent mean-field models, Phys. Rev. C 60 (1999) 034304.

[70] H. Kucharek, P. Ring, Relativistic field theory of superfluidity in nuclei, Z. Phys. A 339 (1991) 23–35.

[71] N. Tajima, P. Bonche, H. Flocard, P.-H. Heenen, M. S. Weiss, Self-consistent calculation of charge radii of Pb isotopes, Nucl. Phys. A 551 (1993) 434–450.

[72] J. F. Berger, M. Girod, D. Gogny, Microscopic analysis of collective dynamics in low energy fission, Nucl. Phys. A 428 (1984) 23–36.

[73] J. Dobaczewski, W. Nazarewicz, T. R. Werner, J. F. Berger, C. R. Chinn, J. Dechargé, Mean-field description of ground-state properties of drip-line nuclei: Pairing and continuum effects, Phys. Rev. C 53 (1996) 2809–2840.

[74] T. Duguet, P. Bonche, P.-H. Heenen, J. Meyer, Pairing correlations. II. microscopic analysis of odd-even mass staggering in nuclei, Phys. Rev. C 65 (2001) 014311.

[75] S.-G. Zhou, J. Meng, P. Ring, Spherical relativistic Hartree theory in a Woods-Saxon basis, Phys. Rev. C 68 (2003) 034323.

[76] A. L. Goodman, Finite-temperature HFB theory, Nucl. Phys. A 352 (1981) 30–44.

[77] P. Bonche, S. Levit, D. Vautherin, Properties of highly excited nuclei, Nucl. Phys. A 427 (1984) 278–296.

[78] J. L. Egido, P. Ring, The decay of hot nuclei, J. Phys G: Nucl. Part. Phys. 19 (1993) 1–54.

[79] J. W. Negele, D. Vautherin, Neutron star matter at sub-nuclear densities, Nucl. Phys. A 270 (1973) 298–320.

[80] J.-G. Cao, D. Yang, Z.-Y. Ma, N. Van Giai, Boundary conditions of Wigner-Seitz cell in inner crust of neutron stars with relativistic mean field approach, Chin. Phys. Lett. 25 (2008) 73–76.

[81] M. Block, D. Ackermann, K. Blaum, C. Droese, M. Dworschak, S. Eliseev, T. Fleckenstein, E. Haettner, F. Herfurth, F. P. Heßberger, et al., Direct mass measurements above uranium bridge the gap to the island of stability, Nature 463 (2010) 785–788.

[82] Y. T. Oganessian, V. K. Utyonkov, Y. V. Lobanov, et al., Synthesis of the isotopes of elements 118 and 116 in the ^{249}Cf and ^{245}Cm + ^{48}Ca fusion reactions, Phys. Rev. C 74 (2006) 044602.

[83] Y. T. Oganessian, F. S. Abdullin, P. D. Bailey, D. E. Benker, M. E. Bennett, S. N. Dmitriev, J. G. Ezold, J. H. Hamilton, R. A. Henderson, M. G. Itkis, et al., Synthesis of a new element with atomic number Z= 117, Phys. Rev. Lett 104 (2010) 142502.

[84] G. G. Adamian, N. V. Antonenko, V. V. Sargsyan, Stability of superheavy nuclei produced in actinide-based complete fusion reactions: Evidence for the next magic proton number at $Z \geq 120$, Phys. Rev. C 79 (2009) 054608.

[85] A. Baran, Z. Łojewski, K. Sieja, M. Kowal, Global properties of even-even superheavy nuclei in macroscopic-microscopic models, Phys. Rev. C 72 (2005) 044310.

[86] K. Rutz, M. Bender, T. Bürvenich, T. Schilling, P. Reinhard, J. Maruhn, W. Greiner, Superheavy nuclei in self-consistent nuclear calculations, Phys. Rev. C 56 (1997) 238.

[87] J. Dechargé, J.-F. Berger, M. Girod, K. Dietrich, Bubbles and semi-bubbles as a new kind of superheavy nuclei, Nucl. Phys. A 716 (2003) 55.

[88] W. Zhang, J. Meng, S. Q. Zhang, L. S. Geng, H. Toki, Magic numbers for superheavy nuclei in relativistic continuum Hartree-Bogoliubov theory, Nucl. Phys. A 753 (2005) 106–135.

[89] J. N. Ginocchio, A relativistic symmetry in nuclei, Phys. Rep. 414 (2005) 165–261.

[90] W. H. Long, P. Ring, N. Van Giai, J. Meng, Relativistic Hartree-Fock-Bogoliubov theory with density dependent meson-nucleon couplings, Phys. Rev. C 81 (2010) 024308.

[91] L. J. Wang, B. Y. Sun, J. M. Dong, W. H. Long, Odd-even staggering of the nuclear binding energy described by covariant density functional theory with calculations for spherical nuclei, Phys. Rev. C 87 (2013) 054331.

[92] W. Long, J. Meng, N. Van Giai, S. Zhou, New effective interactions in relativistic mean field theory with nonlinear terms and density-dependent meson-nucleon coupling, Phys. Rev. C 69 (2004) 034319.

[93] G. A. Lalazissis, T. Nikšić, D. Vretenar, P. Ring, New relativistic mean-field interaction with density-dependent meson-nucleon couplings, Phys. Rev. C 71 (2005) 024312.

[94] C.-L. Wu, M. Guidry, D. H. Feng, $Z = 110 - 111$ elements and the stability of heavy and superheavy elements, Phys. Lett. B 387 (1996) 449–254.

[95] P. Marmier, E. Sheldon, Physics of Nuclei and Particles, Vol. 1, Academic Press, New York, 1971.

[96] G. Audi, F. G. Kondev, M. Wang, B. Pfeiffer, X. Sun, J. Blachot, M. MacCormick, The Nubase2012 evaluation of nuclear properies, Chinese Phys. C 36 (2013) 1157.

[97] G. A. Lalazissis, M. M. Sharma, P. Ring, Y. K. Gambhir, Superheavy nuclei in the relativistic mean-field theory, Nucl. Phys. A 608 (1996) 202–226.

[98] S. K. Patra, C. L. Wu, C. R. Praharaj, R. K. Gupta, A systematic study of superheavy nuclei for $Z = 114$ and beyond using the relativistic mean field approach, Nucl. Phys. A 651 (1999) 117–139.

[99] A. T. Kruppa, M. Bender, W. Nazarewicz, P.-G. Reinhard, T. Vertse, S. Ćwiok, Shell corrections of superheavy nuclei in self-consistent calculations, Phys. Rev. C 61 (2000) 034313.

[100] L.-S. Geng, J. Meng, H. Toki, W.-H. Long, G. Shen, Spurious shell closures in the relativistic mean field model, Chin. Phys. Lett. 23 (2006) 1139.

[101] W. H. Long, T. Nakatsukasa, H. Sagawa, J. Meng, H. Nakada, Y. Zhang, Non-local mean field effect on nuclei near $Z = 64$ sub-shell, Phys. Lett. B 680 (2009) 428–431.

[102] W. H. Long, P. Ring, J. Meng, N. Van Giai, C. A. Bertulani, Nuclear halo structure and pseudospin symmetry, Phys. Rev. C 81 (2010) 031302.

[103] S. Shen, H. Liang, P. Zhao, S. Zhang, J. Meng, Pseudospin symmetry in supersymmetric quantum mechanics. II. spin-orbit effects, Phys. Rev. C 88 (2013) 024311.

[104] A. V. Afanasjev, S. Frauendorf, Central depression in nuclear density and its consequences for the shell structure of superheavy nuclei, Phys. Rev. C 71 (2005) 024308.

[105] A. V. Afanasjev, T. L. Khoo, S. Frauendorf, G. A. Lalazissis, I. Ahmad, Cranked relativistic Hartree-Bogoliubov theory: Probing the gateway to superheavy nuclei, Phys. Rev. C 67 (2003) 024309.

[106] A. V. Afanasjev, Superheavy nuclei: a relativistic mean field outlook, Phys. Scr. T 125 (2006) 62–67.

[107] E. V. Litvinova, A. V. Afanasjev, Dynamics of nuclear single-particle structure in covariant theory of particle-vibration coupling: From light to superheavy nuclei, Phys. Rev. C 84 (2011) 014305.

[108] E. Litvinova, Quasiparticle-vibration coupling in a relativistic framework: Shell structure of $Z = 120$ isotopes, Phys. Rev. C 85 (2012) 021303.

[109] J. C. Pei, F. R. Xu, P. D. Stevenson, Density distributions of superheavy nuclei, Phys. Rev. C 71 (2005) 034302.

[110] M. Bender, K. Rutz, P.-G. Reinhard, J. A. Maruhn, W. Greiner, Potential energy surfaces of superheavy nuclei, Phys. Rev. C 58 (1998) 2126–2132.

[111] S. Ćwiok, J. Dobaczewski, P. Heenen, P. Magierski, W. Nazarewicz, Shell structure of the superheavy elements, Nucl. Phys. A 611 (1996) 211–246.

[112] A. Bohr, B. R. Mottelson, Nuclear structure, Vol. 1, World Scientific Publishing, 1998.

[113] J. Dechargé, J. F. Berger, K. Dietrich, M. S. Weiss, Superheavy and hyperheavy nuclei in the form of bubbles or semi-bubbles, Phys. Lett. B 451 (1999) 275–282.

[114] J. N. Ginocchio, Pseudospin as a relativistic symmetry, Phys. Rev. Lett. 78 (1997) 436–439.

[115] J. Meng, K. Sugawara-Tanabe, S. Yamaji, P. Ring, A. Arima, Pseudospin symmetry in relativistic mean field theory, Phys. Rev. C 58 (1998) 628–631.

[116] P. Alberto, M. Fiolhais, M. Malheiro, A. Delfino, M. Chiapparini, Pseudospin symmetry as a relativistic dynamical symmetry in the nucleus, Phys. Rev. C 65 (2002) 034307.

[117] J.-P. Ebran, E. Khan, D. Peña Arteaga, D. Vretenar, Relativistic Hartree-Fock-Bogoliubov model for deformed nuclei, Phys. Rev. C 83 (2011) 064323.

[118] D. N. Poenaru, R. A. Gherghescu, W. Greiner, Heavy-particle radioactivity of superheavy nuclei, Phys. Rev. Lett. 107 (2011) 062503.

[119] D. N. Poenaru, R. A. Gherghescu, W. Greiner, Cluster decay of superheavy nuclei, Phys. Rev. C 85 (2012) 034615.

[120] I. Tanihata, H. Hamagaki, O. Hashimoto, Y. Shida, N. Yoshikawa, K. Sugimoto, O. Yamakawa, T. Kobayashi, N. Takahashi, Measurements of interaction cross sections and nuclear radii in the light p-shell region, Phys. Rev. Lett. 55 (1985) 2676–2679.

[121] T. Minamisono, T. Ohtsubo, I. Minami, S. Fukuda, A. Kitagawa, M. Fukuda, K. Matsuta, Y. Nojiri, S. Takeda, H. Sagawa, H. Kitagawa, Proton halo of ^{8}B disclosed by its giant quadrupole moment, Phys. Rev. Lett. 69 (1992) 2058–2061.

[122] I. Tanihata, H. Savajols, R. Kanungo, Recent experimental progress in nuclear halo structure studies, Prog. Part. Nucl. Phys. 68 (2013) 215–313.

[123] M. Moreno-Torres, M. Grasso, H. Liang, V. De Donno, M. Anguiano, N. Van Giai, Tensor effects in shell evolution at Z, $N = 20$, and 28 using nonrelativistic and relativistic mean-field theory, Phys. Rev. C 81 (2010) 064327.

[124] M. Anguiano, M. Grasso, G. Co', V. De Donno, A. M. Lallena, Tensor and tensor-isospin terms in the effective Gogny interaction, Phys. Rev. C 86 (2012) 054302.

[125] A. A. Saldanha, A. R. Farhan, M. M. Sharma, Superheavy nuclei with the vector self-coupling of the omega-meson in relativistic mean-field theory, J. Phys. G.: Nucl. Part. Phys. 36 (2009) 115103.

[126] T. Lesinski, M. Bender, K. Bennaceur, T. Duguet, J. Meyer, Tensor part of the Skyrme energy density functional: Spherical nuclei, Phys. Rev. C 76 (2007) 014312.

[127] A. Ozawa, T. Kobayashi, T. Suzuki, K. Yoshida, I. Tanihata, New magic number, $N = 16$, near the neutron drip line, Phys. Rev. Lett. 84 (2000) 5493–5495.

[128] R. Kanungo, I. Tanihata, A. Ozawa, Observation of new neutron and proton magic numbers, Phys. Lett. B 528 (2002) 58–64.

[129] M. O. Frégeau, D. Jacquet, M. Morjean, et al., X-ray fluorescence from the element with atomic number $Z = 120$, Phys. Rev. Lett. 108 (2012) 122701.

[130] M. Morjean, D. Jacquet, J. L. Charvet, et al., Fission time measurements: A new probe into superheavy element stability, Phys. Rev. Lett. 101 (2008) 072701.

[131] H. Sagawa, G. Colò, Tensor interaction in mean-field and density functional theory approaches to nuclear structure, Prog. Part. Nucl. Phys 76 (2014) 76–115.

[132] D. M. Brink, G. R. Satchler, Angular momentum, 3rd Edition, Clarendon Press, Oxford, 1994.

[133] T. Otsuka, T. Suzuki, R. Fujimoto, H. Grawe, Y. Akaishi, Evolution of nuclear shells due to the tensor force, Phys. Rev. Lett. 95 (2005) 232502.

[134] T. Otsuka, T. Matsuo, D. Abe, Mean field with tensor force and shell structure of exotic nuclei, Phys. Rev. Lett. 97 (2006) 162501.

[135] B. A. Brown, T. Duguet, T. Otsuka, D. Abe, T. Suzuki, Tensor interaction contributions to single-particle energies, Phys. Rev. C 74 (2006) 061303.

[136] G. Colò, H. Sagawa, S. Fracasso, P. Bortignona, Spin-orbit splitting and the tensor component of the Skyrme interaction, Phys. Lett. B 646 (2007) 227–226.

[137] D. M. Brink, F. Stancu, Evolution of nuclear shells with the Skyrme density dependent interaction, Phys. Rev. C 75 (2007) 064311.

[138] G. Lalazissis, S. Karatzikos, R. Fossion, D. Pena Arteaga, A. Afanasjev, P. Ring, The effective force NL3 revisited, Phys. lett. B 671 (2009) 36–41.

[139] T. Otsuka, T. Suzuki, M. Honma, Y. Utsuno, N. Tsunoda, K. Tsukiyama, M. Hjorth-Jensen, Novel features of nuclear forces and shell evolution in exotic nuclei, Phys. Rev. Lett. 104 (2010) 012501.

[140] N. A. Smirnova, B. Bally, K. Heyde, F. Nowacki, K. Sieja, Shell evolution and nuclear forces, Phys. Lett. B 686 (2010) 109–113.

[141] O. Sorlin, M.-G. Porquet, Nuclear magic numbers: New features far from stability, Prog. Part. Nucl. Phys 61 (2008) 602–673.

[142] H. Nakada, Shell structure in neutron-rich Ca and Ni nuclei under semi-realistic mean fields, Phys. Rev. C 81 (2010) 051302.

[143] M. Grasso, Magicity of the ^{52}Ca and ^{54}Ca isotopes and tensor contribution within a mean-field approach, Phys. Rev. C 89 (2014) 034316.

[144] E. Yüksel, N. Van Giai, E. Khan, K. Bozkurt, Effects of the tensor force on the ground state and first 2^+ states of the magic ^{54}Ca nucleus, Phys. Rev. C 89 (2014) 064322.

[145] L. J. Jiang, S. Yang, B. Y. Sun, W. H. Long, H. Q. Gu, Nuclear tensor interaction in a covariant energy density functional, Phys. Rev. C 91 (2015) 034326.

[146] L. L. Foldy, S. A. Wouthuysen, On the dirac theory of spin 1/2 particles and its non-relativistic limit, Phys. Rev. 78 (1950) 29–36.

[147] T. Otsuka, R. Fujimoto, Y. Utsuno, B. A. Brown, M. Honma, T. Mizusaki, Magic numbers in exotic nuclei and spin-isospin properties of the *NN* interaction, Phys. Rev. Lett. 87 (2001) 082502.

[148] X. Roca-Maza, X. Viñas, M. Centelles, P. Ring, P. Schuck, Relativistic mean-field interaction with density-dependent meson-nucleon vertices based on microscopical calculations, Phys. Rev. C 84 (2011) 054309.

[149] J. J. Li, W. H. Long, J. Margueron, N. Van Giai, Superheavy magic structures in the relativistic Hartree-Fock-Bogoliubov approach, Phys. Lett. B 732 (2014) 169–173.

[150] H. Grawe, K. Langanke, G. Martínez-Pinedo, Nuclear structure and astrophysics, Rep. Prog. Phys. 70 (2007) 1525–1582.

[151] N. Schwierz, I. Wiedenhover, A. Volya, Parameterization of the Woods-Saxon potential for shell-model calculations, arXiv:0709.3525.

[152] V. I. Isakov, K. I. Erokhina, H. Mach, M. Sanchez-Vega, B. Fogelberg, On the difference between proton and neutron spin-orbit splittings in nuclei, Eur. Phys. J. A 14 (2002) 29.

[153] A. Oros, Ph.D. thesis, University of Köln, 1996.

[154] B. G. Todd-Rutel, J. Piekarewicz, P. D. Cottle, Spin-orbit splitting in low-j neutron orbits and proton densities in the nuclear interior, Phys. Rev. C 69 (2004) 021301.

[155] V. Bernard, N. Van Giai, Effects of collective modes on the single-particle states and the effective mass in ^{208}Pb, Nucl. phys. A 348 (1980) 75–92.

[156] M. Baldo, P. F. Bortignon, G. Colò, D. Rizzo, L. Sciacchitano, Beyond the mean field in the particlevibration coupling scheme, J. Phys. G: Nucl. Part. Phys. 42 (2015) 085109.

[157] M. Grasso, Z. Y. Ma, E. Khan, J. Margueron, N. Van Giai, Evolution of the proton *sd* states in neutron-rich Ca isotopes, Phys. Rev. C 76 (2007) 044319.

[158] H. Nakada, K. Sugiura, J. Margueron, Tensor-force effects on single-particle levels and proton bubble structure around the Z or $N = 20$ magic number, Phys. Rev. C 87 (2013) 067305.

[159] H. Liang, J. Meng, S.-G. Zhou, Hidden pseudospin and spin symmetries and their origins in atomic nuclei, Phys. Rep. 570 (2015) 1.

[160] H. Hergert, S. K. Bogner, T. D. Morris, S. Binder, A. Calci, J. Langhammer, R. Roth, *Ab initio* multireference in-medium similarity renormalization group calculations of even calcium and nickel isotopes, Phys. Rev. C 90 (2014) 041302.

[161] A. Ekström, et al., Optimized chiral nucleon-nucleon interaction at next-to-next-to-leading order, Phys. Rev. Lett. 110 (2013) 192502.

[162] F. Wienholtz, et al., Masses of exotic calcium isotopes pin down nuclear forces, Nature 498 (2013) 346–349.

[163] D. Steppenbeck, et al., Evidence for a new nuclear magic number from the level structure of ^{54}Ca, Nature 502 (2013) 207–210.

[164] T. Duguet, G. Hagen, *Ab initio* approach to effective single-particle energies in doubly closed shell nuclei, Phys. Rev. C 85 (2012) 034330.

[165] T. Duguet, H. Hergert, J. Holt, V. Somà, Non-observable nature of the nuclear shell structure. meaning, illustrations and consequences, Phys. Rev. C 92 (2015) 034313.

[166] M. Wang, G. Audi, A. H. Wapstra, F. G. Kondev, M. MacCormick, X. Xu, B. Pfeiffer, The Ame2012 atomic mass evaluation, Chinese Phys. C 36 (2012) 1603.

[167] T. R. Rodríguez, J. L. Egido, New beyond-mean-field theories: Examination of the potential shell closures at $N = 32$ or 34, Phys. Rev. Lett. 99 (2007) 062501.

[168] D. Steppenbeck, et al., Low-lying structure of ^{50}Ar and the $N = 32$ subshell closure, Phys. Rev. Lett. 114 (2015) 252501.

[169] C. R. Hoffman, et al., Determination of the $N = 16$ shell closure at the oxygen drip line, Phys. Rev. Lett. 100 (2008) 152502.

[170] K. Tshoo, et al., $N = 16$ spherical shell closure in ^{24}O, Phys. Rev. Lett. 109 (2012) 022501.

[171] E. Melby, L. Bergholt, M. Guttormsen, M. Hjorth-Jensen, F. Ingebretsen, S. Messelt, J. Rekstad, A. Schiller, S. Siem, S. W. Ødegård, Observation of thermodynamical properties in the ^{162}Dy, ^{166}Er, and ^{172}Yb nuclei, Phys. Rev. Lett. 83 (1999) 3150–3153.

[172] U. Agvaanluvsan, A. Schiller, J. A. Becker, L. A. Bernstein, P. E. Garrett, M. Guttormsen, G. E. Mitchell, J. Rekstad, S. Siem, A. Voinov, W. Younes, Level densities and γ-ray strength functions in ^{170,171,172}Yb, Phys. Rev. C 70 (2004) 054611.

[173] Y. Kalmykov, C. Özen, K. Langanke, G. Martínez-Pinedo, P. von Neumann-Cosel, A. Richter, Spin- and parity-resolved level densities from the fine structure of giant resonances, Phys. Rev. Lett. 99 (2007) 202502.

[174] H. K. Toft, A. C. Larsen, U. Agvaanluvsan, A. Bürger, M. Guttormsen, G. E. Mitchell, H. T. Nyhus, A. Schiller, S. Siem, N. U. H. Syed, A. Voinov, Level densities and γ-ray strength functions in Sn isotopes, Phys. Rev. C 81 (2010) 064311.

[175] M. Guttormsen, A. C. Larsen, F. L. B. Garrote, et al., Shell-gap-reduced level densities in ^{89,90}Y, Phys. Rev. C 90 (2014) 044309.

[176] R. Balian, H. Flocard, M. Véneroni, Variational extensions of BCS theory, Phys. Rep. 317 (1999) 251–358.

[177] S. Liu, Y. Alhassid, Signature of a pairing transition in the heat capacity of finite nuclei, Phys. Rev. Lett. 87 (2001) 022501.

[178] M. Guttormsen, M. Hjorth-Jensen, E. Melby, J. Rekstad, A. Schiller, S. Siem, Heat capacity and pairing transition in nuclei, Phys. Rev. C 64 (2001) 034319.

[179] D. J. Dean, M. Hjorth-Jensen, Pairing in nuclear systems: from neutron stars to finite nuclei, Rev. Mod. Phys. 75 (2003) 607–656.

[180] U. Agvaanluvsan, A. C. Larsen, M. Guttormsen, R. Chankova, G. E. Mitchell, A. Schiller, S. Siem, A. Voinov, Evidence for the pair-breaking process in ^{116,117}Sn, Phys. Rev. C 79 (2009) 014320.

[181] N. Sandulescu, Nuclear superfluidity and specific heat in the inner crust of neutron stars, Phys. Rev. C 70 (2004) 025801.

[182] M. Fortin, F. Grill, J. Margueron, D. Page, N. Sandulescu, Thermalization time and specific heat of the neutron stars crust, Phys. Rev. C 82 (2010) 065804.

[183] A. Pastore, S. Baroni, C. Losa, Superfluid properties of the inner crust of neutron stars, Phys. Rev. C 84 (2011) 065807.

[184] J. Margueron, E. Khan, Suppression, persistence, and reentrance of superfluidity near and beyond the neutron drip, Phys. Rev. C 86 (2012) 065801.

[185] A. Pastore, J. Margueron, P. Schuck, X. Viñas, Pairing in exotic neutron-rich nuclei near the drip line and in the crust of neutron stars, Phys. Rev. C 88 (2013) 034314.

[186] A. Sedrakian, T. Alm, U. Lombardo, Superfluidity in asymmetric nuclear matter, Phys. Rev. C 55 (1997) R582–R584.

[187] A. Sedrakian, U. Lombardo, Thermodynamics of a n-p condensate in asymmetric nuclear matter, Phys. Rev. Lett. 84 (2000) 602–605.

[188] N. Q. Hung, N. D. Dang, Pairing reentrance in hot rotating nuclei, Phys. Rev. C 84 (2011) 054324.

[189] M. Sano, S. Yamasaki, Phase transition and level density of atomic nuclei, Prog. Theor. Phys. 29 (1963) 397–417.

[190] A. L. Goodman, Finite-temperature Hartree-Fock-Bogoliubov calculations in rare earth nuclei, Phys. Rev. C 34 (1986) 1942–1949.

[191] C. Reiß, M. Bender, P.-G. Reinhard, Nuclear shell gaps at finite temperatures, Eur. Phys. J. A 6 (1999) 157–165.

[192] E. Khan, N. Van Giai, N. Sandulescu, Pairing interactions and vanishing pairing correlations in hot nuclei, Nucl. Phys. A 789 (2007) 94–102.

[193] Z. M. Niu, Q. Liu, Y. F. Niu, W. H. Long, J. Y. Guo, Nuclear effective charge factor originating from covariant density functional theory, Phys. Rev. C 87 (2013) 037301.

[194] Y. K. Gambhir, J. P. Maharana, G. A. Lalazissis, C. P. Panos, P. Ring, Temperature dependent relativistic mean field for highly excited hot nuclei, Phys. Rev. C 62 (2000) 054610.

[195] J. L. Egido, L. M. Robledo, V. Martin, Behavior of shell effects with the excitation energy in atomic nuclei, Phys. Rev. Lett. 85 (2000) 26–29.

[196] B. K. Agrawal, T. Sil, S. K. Samaddar, J. N. De, Shape transition in some rare-earth nuclei in relativistic mean field theory, Phys. Rev. C 63 (2001) 024002.

[197] V. Martin, J. L. Egido, L. M. Robledo, Thermal shape fluctuation effects in the description of hot nuclei, Phys. Rev. C 68 (2003) 034327.

[198] D. Gambacurta, D. Lacroix, N. Sandulescu, Pairing and specific heat in hot nuclei, Phys. Rev. C 88 (2013) 034324.

[199] J. Dobaczewski, H. Flocard, J. Treiner, Hartree-Fock-Bogolyubov description of nuclei near the neutron-drip line, Nucl. Phys. A 422 (1984) 103–139.

[200] M. Stoitsov, P. Ring, D. Vretenar, G. A. Lalazissis, Solution of relativistic Hartree-Bogoliubov equations in configurational representation: Spherical neutron halo nuclei, Phys. Rev. C 58 (1998) 2086–2091.

[201] N. Schunck, J. L. Egido, Continuum and symmetry-conserving effects in drip-line nuclei using finite-range forces, Phys. Rev. C 77 (2008) 011301.

[202] T. Nikšić, N. Paar, D. Vretenar, P. Ring, DIRHB — a relativistic self-consistent mean-field framework for atomic nuclei, Comput. phys. Comm. 185 (2014) 1808–1821.

[203] S. E. Agbemava, A. V. Afanasjev, D. Ray, P. Ring, Global performance of covariant energy density functionals: Ground state observables of even-even nuclei and the estimate of theoretical uncertainties, Phys. Rev. C 89 (2014) 054320.

[204] U. Lombardo, Nuclear Methods and the Nuclear Equation of State, World Scientific, Singapore, 1999, Ch. Superfluidity in Nuclear Matter.

[205] S. Goriely, A new nuclear level density formula including shell and pairing correction in the light of a microscopic model calculation, Nucl. Phys. A 605 (1996) 28–60.

[206] G. F. Bertsch, C. A. Bertulani, W. Nazarewicz, N. Schunck, M. V. Stoitsov, Odd-even mass differences from self-consistent mean field theory, Phys. Rev. C 79 (2009) 034306.

[207] T. Nikšić, D. Vretenar, P. Finelli, P. Ring, Relativistic Hartree-Bogoliubov model with density-dependent meson-nucleon couplings, Phys. Rev. C 66 (2002) 024306.

[208] S. Typel, H. H. Wolter, Relativistic mean field calculations with density-dependent meson-nucleon coupling, Nucl. Phys. A 656 (1999) 331–364.

[209] G. A. Lalazissis, J. König, P. Ring, New parametrization for the lagrangian density of relativistic mean field theory, Phys. Rev. C 55 (1997) 540–543.

[210] Y. Sugahara, H. Toki, Relativistic mean-field theory for unstable nuclei with non-linear σ and ω terms, Nucl. Phys. A 579 (1994) 557–572.

[211] Y. Tian, Z. Y. Ma, P. Ring, A finite range pairing force for density functional theory in superfluid nuclei, Phys. Lett. B 676 (2009) 44–50.

[212] G. D. Mahan, Many-Particle Physics, Plenum Press, New York, 2000.

[213] J. Erler, N. Birge, M. Kortelainen, W. Nazarewicz, E. Olsen, A. M. Perhac, M. Stoitsov, The limits of the nuclear landscape, Nature 486 (2012) 509–512.

[214] J. Erler, C. J. Horowitz, W. Nazarewicz, M. Rafalski, P.-G. Reinhard, Energy density functional for nuclei and neutron stars, Phys. Rev. C 87 (2013) 044320.

[215] S. Hilaire, M. Girod, Large-scale mean-field calculations from proton to neutron drip lines using the D1S Gogny force, Eur. Phys. J. A 33 (2007) 237–241.

[216] J. P. Delaroche, M. Girod, J. Libert, H. Goutte, S. Hilaire, S. Péru, N. Pillet, G. F. Bertsch, Structure of even-even nuclei using a mapped collective Hamiltonian and the D1S Gogny interaction, Phys. Rev. C 81 (2010) 014303.

[217] A. V. Afanasjev, S. E. Agbemava, D. Ray, P. Ring, Nuclear land scape in covariant density functional theory, Phys. Lett. B 726 (2013) 680–684.

[218] O. Sorlin, S. Leenhardt, C. Donzaud, et al., ${}^{68}_{28}Ni_{40}$: Magicity versus superfluidity, Phys. Rev. Lett. 88 (2002) 092501.

[219] A. Pastore, Superfluid properties of the inner crust of neutron stars. II. Wigner-Seitz cells at finite temperature, Phys. Rev. C 86 (2012) 065802.

[220] J. Dobaczewski, I. Hamamoto, W. Nazarewicz, J. A. Sheikh, Nuclear shell structure at particle drip lines, Phys. Rev. Lett. 72 (1994) 981–984.

[221] M. Kleban, B. Nerlo-Pomorska, J. F. Berger, J. Dechargé, M. Girod, S. Hilaire, Global properties of spherical nuclei obtained from Hartree-Fock-Bogoliubov calculations with the gogny force, Phys. Rev. C 65 (2002) 024309.

[222] M. Yamagami, J. Margueron, H. Sagawa, K. Hagino, Isoscalar and isovector density dependence of the pairing functional determined from global fitting, Phys. Rev. C 86 (2012) 034333.

[223] J. Meng, H. Toki, J. Y. Zeng, S. Q. Zhang, S.-G. Zhou, Giant halo at the neutron drip line in Ca isotopes in relativistic continuum Hartree-Bogoliubov theory, Phys. Rev. C 65 (2002) 041302.

[224] K. Bennaceur, J. Dobaczewski, M. Płoszajczak, Continuum effects for the mean-field and pairing properties of weakly bound nuclei, Phys. Rev. C 60 (1999) 034308.

[225] A. Pastore, N. Chamel, J. Margueron, Heat capacity of low-density neutron matter: from quantum to classical regimes, Mon. Not. Roy. Astron. Soc. 448 (2015) 1887–1892.

[226] A. Gilbert, A. G. W. Cameron, A composite nuclear-level density formula with shell corrections, Can. J. Phys. 43 (1965) 1446–1496.

[227] A. Schiller, A. Bjerve, M. Guttormsen, M. Hjorth-Jensen, F. Ingebretsen, E. Melby, S. Messelt, J. Rekstad, S. Siem, S. W. Ødegård, Critical temperature for quenching of pair correlations, Phys. Rev. C 63 (2001) 021306.

[228] K. Tanabe, K. Sugawara-Tanabe, H. J. Mang, Theory of the cranked temperature-dependent Hartree-Fock-Bogoliubov approximation and parity projected statistics, Nucl. Phys. A 357 (1981) 20–44.

[229] C. Esebbag, J. L. Egido, Number projected statistics and the pairing correlations at high excitation energies, Nucl. Phys. A 552 (1993) 205–231.

[230] N. Dinh Dang, A. Arima, Modified Hartree-Fock-Bogoliubov theory at finite temperature, Phys. Rev. C 68 (2003) 014318.

[231] A. Pastore, P. Schuck, M. Urban, X. Viñas, J. Margueron, Pairing correlations of cold fermionic gases at overflow from a narrow to a wide harmonic trap, Phys. Rev. A 90 (2014) 043634.

[232] F. Grill, J. Margueron, N. Sandulescu, Cluster structure of the inner crust of neutron stars in the Hartree-Fock-Bogoliubov approach, Phys. Rev. C 84 (2011) 065801.

[233] J. Margueron, N. Sandulescu, Neutron Star Crust, World Scientific, Singapore, 2012, Ch. Pairing Correlations and Thermodynamic Properties of Inner Crust Matter.

[234] D. A. Varshalovich, A. N. Moskalev, V. K. Khersonskii, Quantum theory of angular momentum, World Scientific, 1988.

[235] E. N. E. van Dalen, H. Müther, Relativistic description of finite nuclei based on realistic nn interactions, Phys. Rev. C 84 (2011) 024320.